

Christian Klein-Bösing

Production of Neutral Pions
and Direct Photons in
Ultra-Relativistic Au + Au Collisions

— 2004 —

Experimentelle Physik

Production of Neutral Pions
and Direct Photons in
Ultra-Relativistic Au + Au Collisions

Inauguraldissertation
zur Erlangung des Doktorgrades
der Naturwissenschaften im Fachbereich Physik
der Mathematisch-Naturwissenschaftlichen Fakultät
der Westfälischen Wilhelms-Universität Münster

vorgelegt von
Christian Klein-Bösing
aus Rheine

— 2004 —

Dekan: Prof. Dr. H. Zacharias
Erster Gutachter: Prof. Dr. R. Santo
Zweiter Gutachter: Prof. Dr. J. P. Wessels

Tag der Disputation:
Tag der Promotion:

FÜR MELA

Contents

1	Theoretical Basics	5
1.1	Quarks, Gluons, and the Quark-Gluon Plasma	5
1.1.1	Deconfinement	7
1.1.2	Chiral Symmetry Restoration	10
1.2	Ultra-Relativistic Heavy Ion Collisions	12
1.2.1	Nucleon-Nucleon Reactions	12
1.2.2	Space-Time Evolution	15
1.2.3	Model Descriptions	16
1.2.4	Signatures of a Quark-Gluon Plasma Phase	17
1.3	Jets and Jet Quenching	20
1.3.1	The Nuclear Modification Factor	20
1.3.2	Effects of Cold Nuclear Matter	21
1.3.3	Nuclear Shadowing	23
1.3.4	Parton Energy Loss	25
2	Direct Photons	27
2.1	Thermal Photons from a QGP	27
2.2	Thermal Photons from a Hadron Gas	32
2.3	Non-Thermal Photons	35
2.4	Photon Spectra	35
2.5	Earlier Results on Direct Photon Production	40
3	The PHENIX Experiment	43
3.1	The Relativistic Heavy Ion Collider	43
3.2	Experiments at RHIC	44
3.2.1	STAR	44
3.2.2	PHOBOS	46

3.2.3	BRAHMS	46
3.3	PHENIX	46
3.3.1	Inner Detectors and the ZDC	46
3.3.2	Detectors of the Central Arms	48
3.3.3	Detectors of the Muon Arms	49
3.3.4	PHENIX Data Acquisition	50
4	The Electromagnetic Calorimeter	55
4.1	Lead-Glass Calorimeter	55
4.1.1	Mode of Operation	55
4.1.2	PbGl Setup	58
4.2	Lead-Scintillator Calorimeter	59
4.3	EMCal Frontend Modules	60
4.4	Processing of the EMCal signals	62
4.4.1	Zero Suppression in the DCMs	62
4.4.2	Calibrated Modules	64
4.5	EMCal Photon Triggers	65
4.5.1	EMCal-RICH Level-1 Trigger	65
4.5.2	Level-2 Trigger for the EMCal	68
5	Data Analysis	71
5.1	Data Selection	71
5.1.1	Minimum Bias Events	72
5.1.2	Events with Highly Energetic Photons	72
5.1.3	Trigger Bias	75
5.1.4	Centrality Determination	77
5.2	Processing of EMCal Data	78
5.2.1	DST Level	79
5.2.2	MicroDST Level	84
5.2.3	Analysis Level	85
6	Measurement of Neutral Pions in Au + Au and d + Au Collisions	93
6.1	Extraction of the π^0 Signal	93
6.1.1	Invariant Mass Analysis	93
6.1.2	Mixed Events	95

6.1.3	Triggered Data	100
6.2	Fully Corrected Spectra	107
6.3	Geometrical Acceptance	109
6.4	Detection Efficiency	110
6.4.1	Efficiency from Embedding	111
6.4.2	Efficiency Calculation with a Fast Monte Carlo	121
6.5	Calibration Based on the π^0 Peak Position	123
6.6	Production of Neutral Pions in Au + Au Collisions	127
6.6.1	Statistical Error	127
6.6.2	Sources of Systematic Errors	128
6.6.3	Bin Shift Correction	131
6.6.4	Combination of the PbGl and PbSc Result	132
6.7	Production of Neutral Pions in d + Au Collisions	136
6.8	Analysis of the Scaling Behavior of the π^0 Production	140
6.8.1	Comparison to Theoretical Descriptions	147
6.8.2	Control Measurement in d + Au Collisions	150
7	Measurement of Direct Photons	153
7.1	Inclusive Photons	153
7.1.1	Single Photon Acceptance and Efficiency	154
7.1.2	Charged Particle Background	156
7.1.3	Background from Neutrons and Antineutrons	161
7.1.4	Conversion Correction	166
7.1.5	Spectra	167
7.2	Direct Photon Yields	171
7.2.1	Background from Radiative Decays	172
7.2.2	γ/π^0 Double Ratio	177
7.3	Final Direct Photon Spectra	182
7.3.1	Comparison with Theoretical Models	184
7.3.2	Comparison of the π^0 and the Direct Photon Production	187
	Summary	191
	Zusammenfassung	195
A	Kinematic Variables	199

B	Lists of Analyzed Runs	201
C	Excluded Modules and FEMs	203
D	Countsheets	207
E	Conversion Studies	217
F	Results of the Glauber Calculations	219
G	NLO pQCD results for direct photons in p + p collisions	221
H	Data Tables	223
	H.1 π^0 Production in Au + Au Collisions	223
	H.2 π^0 Production in d + Au Collisions	238
	H.3 Reference Data: π^0 Production in p + p Collisions	239
	H.4 Inclusive Photon Production in Au + Au Collisions	240
	H.5 Direct Photon Yield in Au + Au Collisions	255
	Danksagung	271

1. Theoretical Basics

In the late nineteenth century the atomic theory of matter was not yet fully established, though it was promoted by physicists like Ludwig Boltzmann, one of the founders of modern thermodynamics. It had been first proposed by Leukipp and Demokrit (460 – 370 BC) based on the philosophical argumentation that after repeated division of matter one encounters a fundamental, indivisible unit, the atom (*atomos* (Greek) = indivisible). In the early nineteenth century John Dalton used the idea of atoms to establish quantitative rules for chemical reactions. Nevertheless, it took till the beginning of the twentieth century until the atomic theory was firmly established by Einstein's paper on Brownian motion and soon thereafter Rutherford, Geiger and Marsden demonstrated by the scattering of α -particles off gold foil that the atom contains a positively charged nucleus, where most of its mass is concentrated. At the same time quantum theory evolved and performed strongly, e.g. with the explanation of the line spectra of the hydrogen atom.

However, the discovery that even the atomic nuclei are composed of smaller entities, the proton and the neutron, and other experimental observations such as the radioactive β -decay with its continuous energy spectrum, posed a problem for a comprehensive theoretical description with the forces known at this time, electromagnetism and gravity. This, among other experimental findings, lead to the postulation of new particles, e.g. the pion as the carrier of the nuclear interaction and the neutrino, and to the introduction of two new fundamental forces the weak and the strong interaction.

1.1 Quarks, Gluons, and the Quark-Gluon Plasma

The abundance of strongly interacting particles and antiparticles, the hadrons (*hadros* (Greek) = thick), discovered at accelerator facilities and in cosmic rays, was first only subdivided according to the particle weight into baryons (*barys* (Greek) = heavy) and mesons (*mesos* (Greek) = middle). The particles only interacting weakly or via the electromagnetic force were called leptons (*leptos* (Greek) = thin).

In 1964 Gell-Mann and Zweig introduced the idea that the hadrons with all their quantum numbers can be constructed from smaller entities, the *quarks*, with fractional charge and baryon number [GM64, Zwe64]. Though the physical meaning of quarks was first controversial, deep-inelastic scattering of muons and electrons on protons and neutrons revealed the sub-structure of the nucleons of pointlike particles, first called *partons* and later identified with the quarks.

Leptons			Quarks		
	Charge	Mass		Charge	Mass
e	$-1e$	$0.511 \text{ MeV}/c^2$	u	$+2/3e$	$1.3 - 4 \text{ MeV}/c^2$
ν_e	0	$< 3 \text{ eV}/c^2$	d	$-1/3e$	$4 - 8 \text{ MeV}/c^2$
μ	$-1e$	$105.7 \text{ MeV}/c^2$	c	$+2/3e$	$1.15 - 1.35 \text{ GeV}/c^2$
ν_μ	0	$< 0.19 \text{ MeV}/c^2$	s	$-1/3e$	$80 - 130 \text{ MeV}/c^2$
τ	$-1e$	$1777 \text{ MeV}/c^2$	t	$+2/3e$	$\approx 174 \text{ GeV}/c^2$
ν_τ	0	$< 18.2 \text{ MeV}/c^2$	b	$-1/3e$	$4.1 - 4.4 \text{ GeV}/c^2$

Table 1.1: Properties of the three generations of fundamental fermions [Eid04].

To present knowledge the quarks and the leptons are elementary particles with spin $1/2$. These fundamental fermions are grouped into three generations as shown in Table 1.1. Each generation contains a charged lepton (electron, μ , or τ), the corresponding neutrino, which only interacts weakly, as well as two kinds of strongly interacting quarks. The associated antiparticles are identical in mass and spin but with opposite charge-like quantum numbers, such as charge, baryon or lepton number. The six different kinds of quarks, also called *flavors*, and their antiquarks allow to construct most of the known hadrons, with a baryon containing a combination of three quarks (qqq) and a meson built up by a quark-antiquark pair ($q\bar{q}$). The fact that the quark model predicted the existence of baryons containing three identical quarks, e.g. three s quarks, and the experimental verification of this prediction, the discovery of the Ω^- , motivated the introduction of a new quantum number to satisfy the Pauli principle. This new quantum number is called color charge or color and each quark carries one of three colors, *blue*, *red*, or *green*. The experimental observation that no single, free quarks are observed leads to the assumption that only color neutral objects exist in nature.

Based on concepts of the description of electrically charged particles in quantum-electrodynamics (QED), the theory of the strongly interacting quarks is quantum-chromodynamics (QCD). But while in the electromagnetic interaction the neutral photon mediates the force between electric charges, the gauge bosons of QCD, the gluons, are color-charged and can act amongst themselves. In QCD eight different gluons exist, each a combination of color and anticolor. In addition to the self-interaction of the gauge bosons, the coupling constant of the strong interaction α_s is two orders of magnitude larger than the electromagnetic coupling $\alpha = 1/137$, hence of the order of one, so

that multiple gluon exchanges ($\alpha_s^2, \alpha_s^3, \dots$) contribute significantly to the interaction amplitudes, making a perturbative treatment similar to QED inadequate in most situations.

However, α_s shows a strong dependence on the momentum transfer Q^2 in a collision. For large momentum transfer the leading order perturbative approximation for the *running* coupling constant [Roe96] is given by:

$$\alpha_s(Q^2) \approx \frac{12\pi}{(33 - 2 \cdot N_f) \cdot \ln \frac{Q^2}{\lambda^2}}, \quad (1.1)$$

where N_f is the number of accessible quark flavors ($N_f \leq 6$) and λ a QCD scale parameter, which has to be determined experimentally and is found to be $\lambda \approx 200 - 400 \text{ MeV}/c$, depending on the number of massless quark flavors compared to the available energy and the exact definition of λ , for more details see e.g. [Cas98]. Equation (1.1) is only valid for $Q^2/\lambda^2 \ll 1$, but it illustrates that for increasing momentum transfer, or equivalent short distances, the coupling becomes weaker and at asymptotically large values of Q^2 the quarks behave as if they were free. This phenomenon is known as *asymptotic freedom*. For low Q^2 , when $Q \approx \lambda$, α_s becomes large and a perturbative treatment becomes inaccurate. This strong coupling between the quarks at large distances is probably related to the *confinement* of quarks in hadrons.

The effect of confinement can also be illustrated with the phenomenological potential for the strong interaction [Per00]:

$$V_s = -\frac{4}{3} \frac{\alpha_s}{r} + kr, \quad (1.2)$$

where the first term dominates at small distances r and is similar to the Coulomb potential. The second term is dominant at large distances and is associated with the confinement: The color field between a $q\bar{q}$ pair is restricted to a small tube or *string* because of the gluon-gluon interaction. When trying to separate two quarks the stored energy kr increases and it is energetically more favorable to form a new $q\bar{q}$ pair. The result is that there are two shorter strings. Thus separating two quarks is not possible, only new, color-neutral particles are produced.

1.1.1 Deconfinement

Because of the non-perturbative character of QCD at large distances and small momentum transfer it is very difficult to derive quantities of bound quark-gluon states, hadrons and the atomic nuclei, based on first principles. A useful phenomenological description of quarks in hadrons is provided by *bag models*, e.g. in the MIT bag model, in which the quarks are treated as massless inside a bag of finite temperature and as infinitely massive outside the

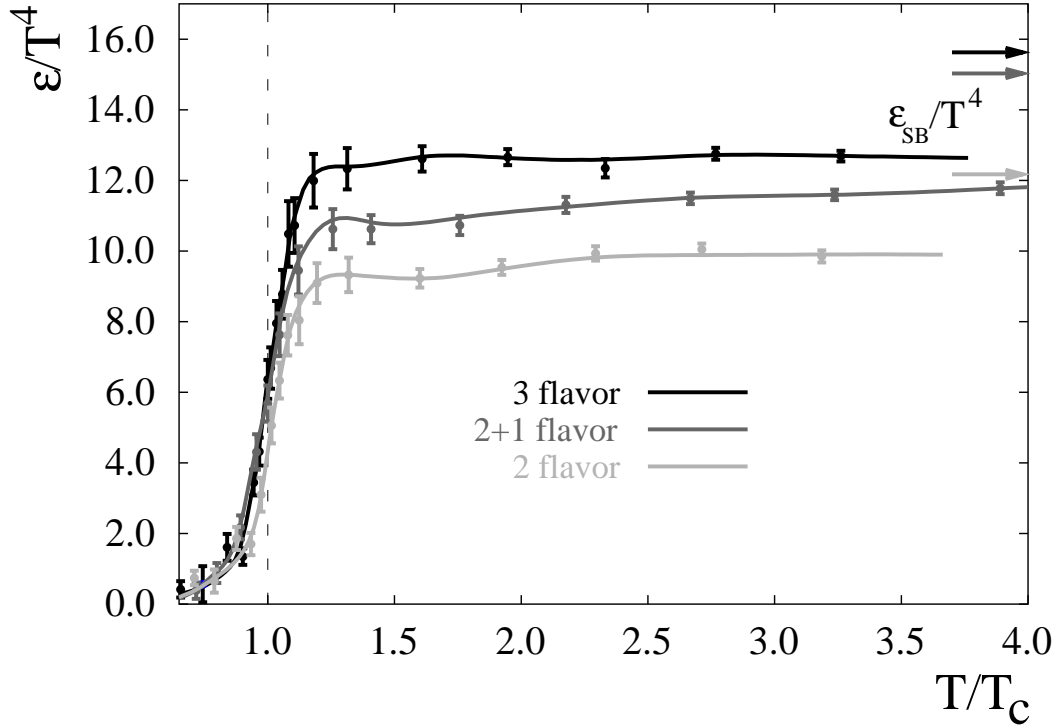


Figure 1.1: Result of a lattice QCD calculation on the dependence of the energy density ϵ on the temperature for three different quark configurations [Kar02]: two degenerate flavors, two degenerate light flavors plus one heavy, and three degenerate flavors. The expectation for an ideal gas with quark and gluon degrees of freedom, the Stefan-Boltzmann limit, is also shown.

bag [Cho74, Won94]. In this model confinement results from the balance between the *bag pressure*, directed inward, and the stress arising from the kinetic energy of the quarks. If this balance is distorted and the pressure of the quarks is larger than the bag pressure, a new phase of matter containing *deconfined* quarks and gluons is formed, the quark-gluon plasma (QGP).

To reach this new phase, two extreme scenarios can be considered: a quark-gluon system in thermal equilibrium with a large temperature $T > T_c$, where the kinetic energy of the quarks and the gluons with corresponding pressure P exceeds the bag pressure, or a system at $T = 0$ with high baryon density n_B or baryo-chemical potential μ_B , where the Pauli principle forces the quarks into states with increasing momenta as they get closer, leading to a degenerative pressure that may exceed the bag pressure.

Typical values for the critical temperature and the critical baryon number density in these two extreme scenarios derived from the bag model in [Won94] are $T_c \approx 144$ MeV

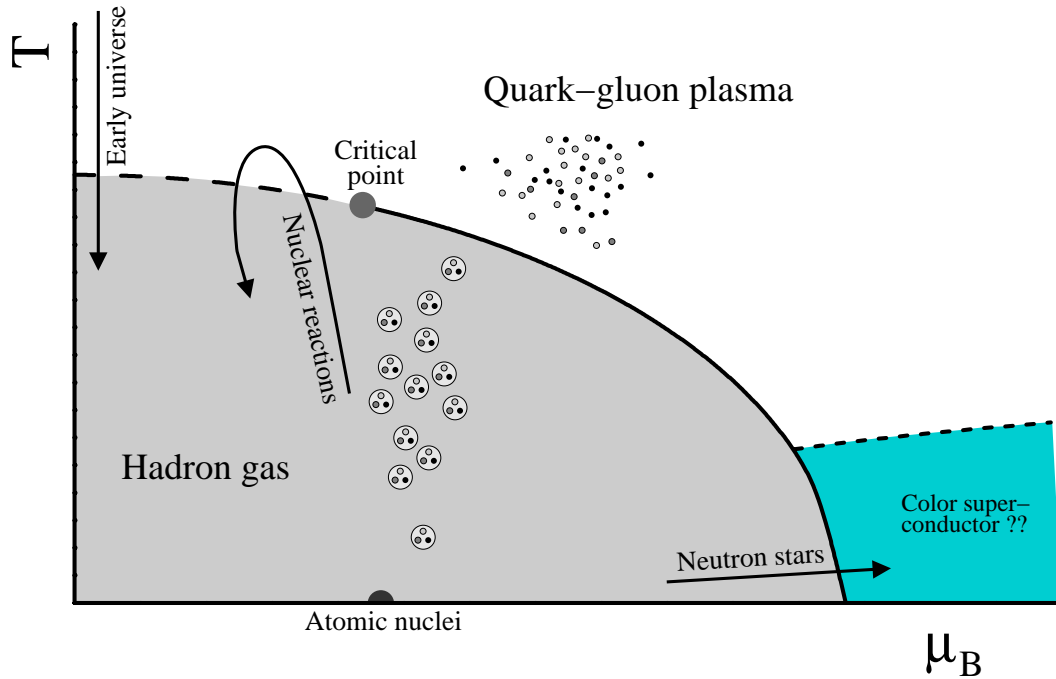


Figure 1.2: A schematic phase diagram of strongly interacting matter. The solid line indicates the first order phase transition from hadronic matter to the quark-gluon plasma. The dashed line at small baryon density represents a crossover transition.

for $n_B = 0$ and $n_B = 0.72/\text{fm}^3$ for $T = 0$, respectively. This can be compared to the baryon number density of normal, cold nuclear matter of $n_B \approx 0.14/\text{fm}^3$.

The treatment of the non-perturbative regime of QCD is not limited to phenomenological models. It is also accessible in a more fundamental way by lattice QCD (LQCD) calculations [Wil74], where the gauge theory of QCD is formulated on a discrete lattice of space-time. This approach has the advantage that it retains the fundamental characteristics of QCD and makes it accessible to computational methods in order to calculate the properties of quarks and gluons, e.g. the thermodynamic equation of state for strongly interacting matter, based on first principles.

LQCD calculations are heavily limited by computing resources, making it difficult to use physical quark masses m_q and negligible lattice spacing a , the *chiral limit* $m_q \cdot a \rightarrow 0$, as well as finite baryo-chemical potential. Nevertheless, already early lattice calculations predicted a phase transition into a deconfined phase at high temperature and vanishing baryo-chemical potential [Cre77], similar to the expectation from phenomenological models. A recent calculation is shown in Figure 1.1. It illustrates the sudden rise of the energy density ϵ/T^4 at a critical temperature $T_c \approx 170 \text{ MeV}$ for different numbers of quark

flavors¹. This is interpreted as the phase transition into the deconfined quark-gluon plasma phase [Kar02]. The expectation for an ideal gas with quark and gluon degrees of freedom, the Stefan-Boltzmann limit of the energy density, is also shown in Figure 1.1. It is not reached even for temperatures four times larger than the critical temperature, indicating that the often used description of the QGP as a free gas of weakly interacting quarks and gluons may not be applicable at these temperatures [Kar02].

Another ongoing discussion to which LQCD provides valuable insight is the nature of the phase transition. Recent developments in LQCD indicate that the equation of state shows a critical point at finite baryo-chemical potential at which the phase transition turns from a rapid crossover to a first order phase transition [Fod02].

A sketch of the current understanding of the phase diagram for the transition from a hadron gas to the QGP is shown in Figure 1.2. This transition is also interesting for cosmology and astrophysics. In the Big Bang scenario for the origin of the universe the elementary particles were produced in the freeze-out from a QGP phase with high temperature and low baryon density on the order of $1 \mu\text{s}$ after the Big Bang. On the other hand the high baryon density needed for the phase transition to the QGP, or to even more exotic states of matter at zero temperature, may today still be reached in the center of neutron stars.

1.1.2 Chiral Symmetry Restoration

In addition to the phase transition to a deconfined phase, a second type of phase transition is expected from LQCD calculations, the restoration of *chiral symmetry*. This shall be explained briefly in the following. For a more detailed description see e.g. [Koc97, Tho01].

For each propagating particle with spin \vec{s} and momentum \vec{p} it is possible to define the helicity:

$$h = \frac{\vec{s} \cdot \vec{p}}{|\vec{p}|}, \quad (1.3)$$

which is the projection of the spin onto the direction of the particle motion. For example, for spin- $1/2$ particles like quarks the helicity has two possible eigenstates $h = \pm \frac{1}{2}$, also called left- and right-handed. In QCD helicity cannot be changed by emission or absorption of gluons. This would imply that the number of left-handed quarks B_L is conserved for the strong interaction separately from the number of right-handed quarks B_R , and one needs two descriptions of QCD related by a mirror transformation or chirally symmetric to each other.

¹The quoted critical temperature refers to the $2 + 1$ case of two light quarks (u,d) and one heavy quark (s) in the calculation. The same result is obtained for only two degenerate quark flavors [Kar02].

However, this is only true for massless particles. For a massive quark, propagating slower than the speed of light, it is possible to find a reference frame where the momentum of the quark changes its sign, hence transforming a left-handed quark into a right-handed one and vice versa. As quarks do have finite mass, chiral symmetry is *explicitly* broken and only the total number of quarks $B = B_L + B_R$ is conserved. One might argue that the breaking of chiral symmetry is weak, as the current quark masses of u and d are small compared to the QCD scale parameter λ given in Equation (1.1). But due to the strength of the interaction between quarks there is an additional dynamical effect, which leads to a *spontaneous* symmetry breaking.

It can be shown that the vacuum expectation value for a quark-antiquark pair, the QCD ground state, is non-zero [Tho01] even for vanishing quark masses²:

$$\langle 0 | \bar{\psi}\psi | 0 \rangle = \langle \bar{\psi}\psi \rangle \neq 0 \quad (1.4)$$

This basically indicates that the ground state is restructured in a way that the chiral symmetry of the underlying QCD Lagrangian is lost. The situation is very similar to the well known phenomenon of ferromagnetism in metals with an unpaired electron carrying magnetic moment or spin ($\langle \uparrow \rangle$ or $\langle \downarrow \rangle$). The spins of neighboring atoms tend to align, even though quantum mechanical exchange forces, i.e. the Lagrangian, do not prefer any direction of the alignment. Nevertheless, below the Curie temperature, near the *ground state*, a macroscopic fraction of the spins is aligned, leading to a spontaneous magnetization of the sample $M \neq 0$, i.e. the original symmetry of the Lagrangian is broken.

The consequences of Equation (1.4), the spontaneously broken chiral symmetry, are rather interesting. It means, that the QCD vacuum contains at any given time a certain number of $q\bar{q}$ pairs, the so-called *chiral condensate*. These $q\bar{q}$ pairs can interact with a (massless) quark traversing the vacuum and change its helicity, as if it has mass. Simply speaking the helicity, hence the momentum, is flipped back and forth by the vacuum, the quark "slows" down, as if it gained mass. This is most likely the origin of the so-called *constituent* quark masses of $m_{u,d} \approx m_{\text{nucleon}}/3$, which are two orders of magnitude larger compared to the current quark masses derived for asymptotically free quarks.

An additional consequence of each spontaneously broken global symmetry is the existence of massless bosons, the so-called Goldstone bosons. They can be identified with the eight pseudo-scalar mesons ($\pi^\pm, \pi^0, K^\pm, K^0, \bar{K}^0, \eta$), the eight lightest hadrons. The fact that they are not massless reflects that the masses of the three lightest quarks are small, but non-zero, the explicit breaking of the symmetry.

The transition into a chirally symmetric phase, which is expected from LQCD for high temperatures or densities, can occur at the same time as the deconfinement phase

²With non-vanishing, realistic quark masses one obtains $\langle \bar{\psi}\psi \rangle = \langle \bar{q}q \rangle \approx -(225 \text{ MeV})^3 \approx -1.5 \text{ fm}^{-3}$ [Tho01].

transition or later. It is already clear from the simplistic view of the bag model that a confined phase, such as a hadron, cannot be chirally symmetric, as the quarks have to reverse their momentum, hence their helicity, at the bag surface. This is only possible if the vacuum outside the bag contains a non-vanishing density of $q\bar{q}$ pairs for helicity exchange. Thus confinement implies chiral symmetry breaking, but note that deconfinement does not imply chiral symmetry restoration.

1.2 Ultra-Relativistic Heavy Ion Collisions

Ultra-relativistic heavy ion collisions, reactions with center of mass energies for each nucleon-nucleon pair $\sqrt{s_{NN}} \gtrsim 10\text{GeV}$, provide the opportunity to study strongly interacting matter at high temperatures and densities in the laboratory and to reach energy densities which might be sufficient to create a quark-gluon plasma. However, a single indisputable signature for the creation of a quark-gluon plasma in such collisions is not known. This is partially due to the lack of an exact definition of the new phase. Nevertheless, a number of observables has been proposed which should show a behavior distinctly different from usual nuclear matter. The detection of a QGP phase is additionally complicated by the fact that it has only a fleeting existence, which is followed by return to a phase of hot hadronic matter. It is an experimental challenge to find observables that reflect the hot and dense quark-gluon plasma phase, not entirely diluted by the later stages of the reaction, in the detected products of the nuclear collision.

1.2.1 Nucleon-Nucleon Reactions

For the interpretation of results from heavy ion collisions a basic understanding of the more elementary nucleon-nucleon reactions is crucial. Above a center of mass energy of $\sqrt{s} \approx 10\text{ GeV}$ the total cross section for $p+p$ collisions is roughly constant at $\sigma_{\text{tot}} \approx 40\text{ mb}$ [Cas98]. The cross section at these energies is dominated by inelastic reactions, where the colliding particles lose energy, with the deposited energy resulting in the production of new particles. The mean number of produced particles (mostly pions) increases only slowly with the center of mass energy and is dominated by particles with small transverse momenta.

Soft Processes

The total number of produced particles is dominated by the particles with low transverse momentum ($p_T < 2\text{ GeV}/c$), as the mean transverse momentum e.g. for pions produced in $p+p$ collisions is $\langle p_T \rangle \approx 0.3\text{ GeV}/c$. As seen in Figure 1.3 the spectral shape in this

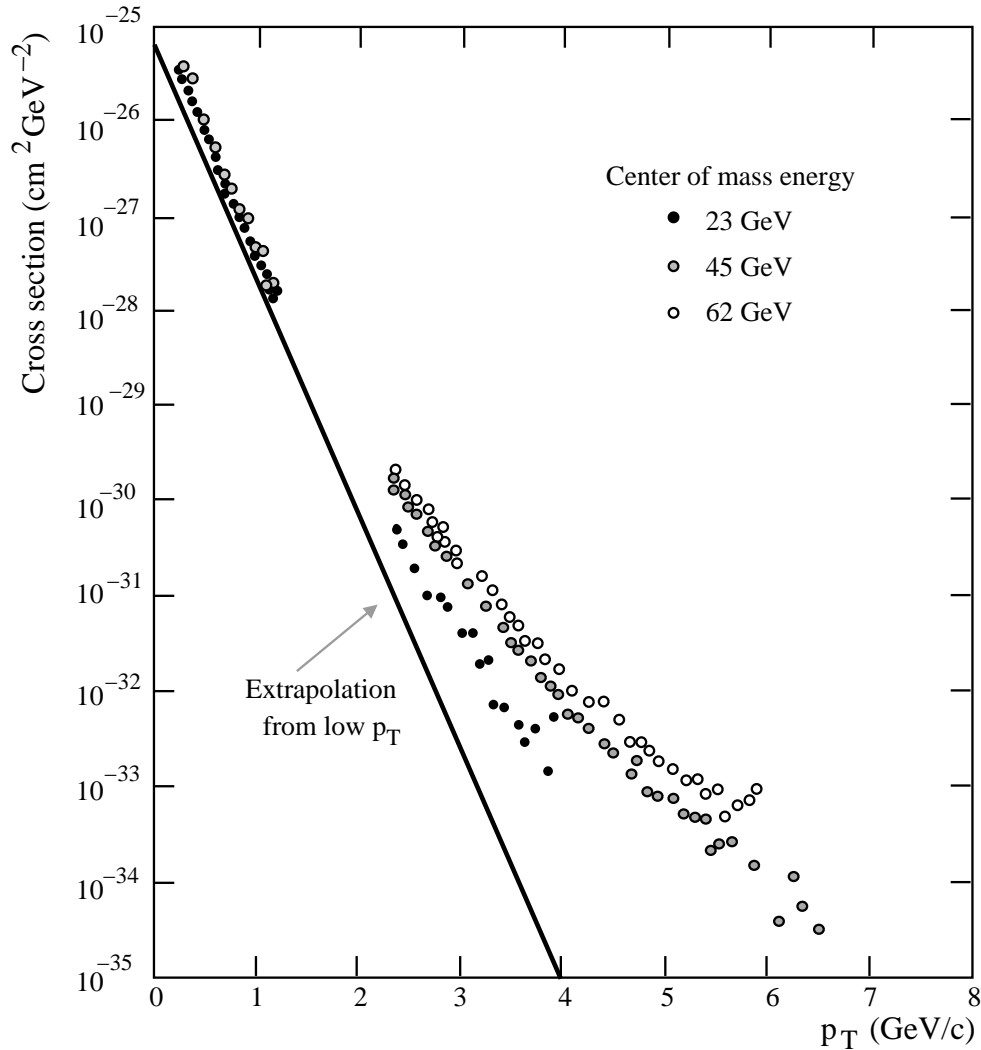


Figure 1.3: Particle production at different energies measured in $p + p$ collisions at the CERN ISR [Jac80].

region is well described by an exponential $e^{-\alpha p_T}$, with $\alpha \approx 6/(\text{GeV}/c)$. The particle production at such low momenta is dominated by so-called *soft* processes, where the momentum transfer Q^2 is on the order of the QCD scales. Soft processes cannot be treated in perturbative QCD; the quarks inside the hadrons cannot be considered as asymptotically free.

Instead the description of the bulk of particles produced e.g. in $p + p$ collisions by soft processes is described by phenomenological models, such as the different types of string models [Won94]. In such models an excited $q\bar{q}$ pair is described as an elastic band, the string, with tension k already introduced in Equation (1.2). If the quarks are separated the potential energy stored in the string increases until it breaks and fragments into smaller

strings. Hence new $q\bar{q}$ pairs are produced which can fragment further, until their potential energy is too small and the strings can be considered as real hadrons.

String models can be tested against the process $e^+e^- \rightarrow q\bar{q}$ at high energies. This allows to study string fragmentation without the uncertainties introduced from a hadronic initial state. Nucleon-nucleon collisions are then described by fragmentation of strings of the form $(q - qq)$, i.e. nucleons excited in the inelastic collisions. The mechanisms for excitation are different in the various models but involve usually momentum or color exchange between the quarks of the colliding nucleons.

Hard Processes

The extrapolation of the exponential shape from low transverse momenta of the particle production fails for large p_T , as seen in Figure 1.3, and the distribution is better described by a power law. In this kinematical region the particle production is governed by *hard* processes with large Q^2 and the quarks can be treated to be asymptotically free.

The inelastic hard scattering of the nucleons can be described in the framework of perturbative QCD in terms of the scattering of the pointlike partons (quarks or gluons) inside the nucleons. This leads to the characteristic *jets* of particles produced along the direction of the scattered partons. The characteristic time and length scale of the parton-parton interaction is short compared to the soft interactions between the bound partons in the initial state and to those of the fragmentation process of the scattered partons in the final state. Therefore the hard inelastic cross section for the production of a given hadron h can be factorized [Col85]:

$$E \frac{d^3\sigma_{NN \rightarrow h}^{\text{hard}}}{dp^3} = \sum_{a,b,c} f_a(x, Q^2) \otimes f_b(x, Q^2) \otimes \frac{d\sigma_{ab \rightarrow c}^{\text{hard}}}{d^3p} \otimes D_{c/h}(z, Q^2). \quad (1.5)$$

The different factors are:

- The non-perturbative distribution functions $f_{q,g}(x, Q^2)$ of partons in the colliding nucleons, which depend only on the momentum transfer and the parton fractional momentum x . They can be determined e.g. in deep-inelastic electron-nucleus reactions,
- The short-distance, perturbatively computable parton-parton scattering $ab \rightarrow c$,
- The universal but non-perturbative fragmentation function $D_{c/h}(z, Q^2)$ of the scattered parton c into the hadron h carrying a fraction $z = p^h/p^c$ of the parton momentum. It also needs to be determined experimentally. If a photon is produced in the hard scattering the fragmentation function reduces to a $\delta(1 - z)$ function.

It should be noted that the calculation of total cross sections via Equation (1.5) suffers from uncertainties due to the arbitrary choice of factorization, renormalization, and fragmentation scales. The different scales are usually chosen identical and on the order of the transverse momentum.

1.2.2 Space-Time Evolution

In ultra-relativistic heavy ion collisions the de-Broglie wavelength of the individual nucleons is so small that the nuclei can be seen as an independent accumulation of nucleons. This simplistic view implies that the Lorentz-contracted nuclei interact only in the region of geometrical overlap, determined by the impact parameter b as shown in Figure 1.4. The corresponding nucleons are called *participants*, while the nucleons outside the geometrical overlap, the *spectators*, are basically unaffected by the collision.

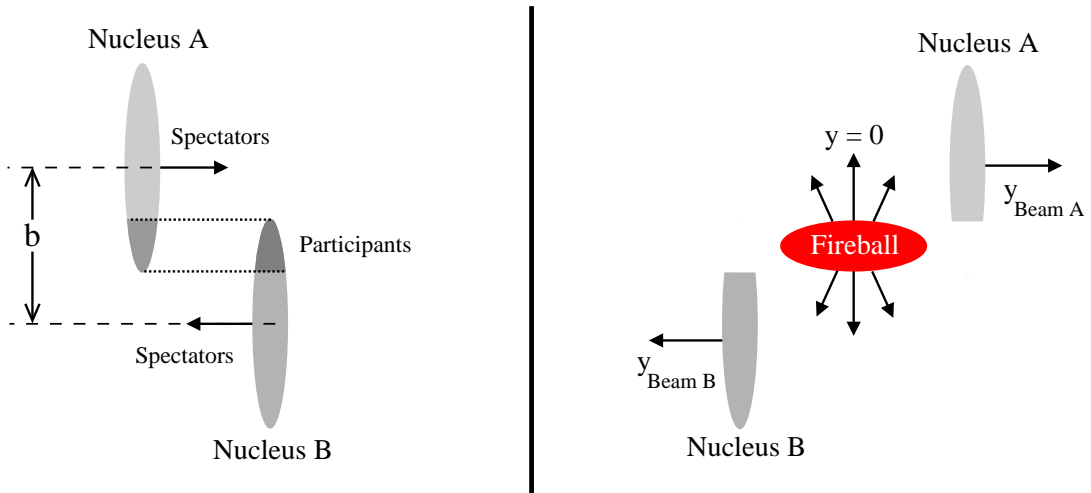


Figure 1.4: Schematic view of two colliding nuclei in the geometrical participant-spectator model. The distance between the centers of the two Lorentz contracted nuclei is the impact parameter \vec{b} .

The participants interact with each other in the reaction zone, leading to the formation of a hot and dense region, the *fireball*. There are two basic scenarios for the formation of the fireball depending on the nuclear *stopping* in the reaction. For large stopping, described in the *Landau* model, the complete kinetic energy of the nucleons is converted into thermal energy and a baryon-rich fireball is formed. The characteristic rapidity distribution of produced particles in such a reaction has a maximum at mid-rapidity³. In the

³The rapidity y is equivalent to the momentum component in the direction of the beam axis. The exact definition is given in Appendix A.

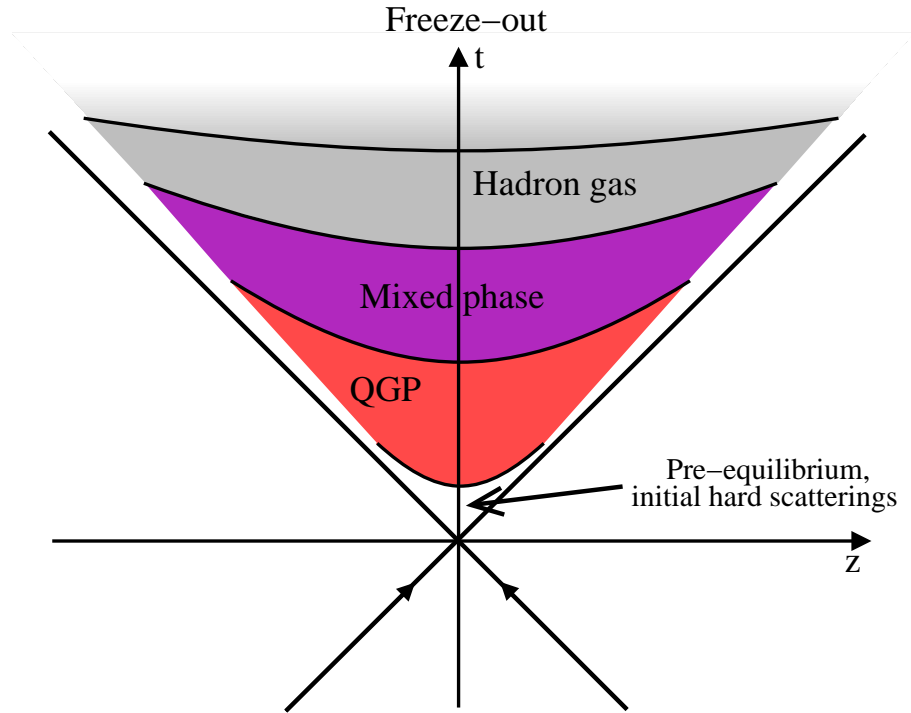


Figure 1.5: The schematic space-time picture of a nucleus-nucleus collision.

Bjorken-McLerran scenario the stopping is limited and the nucleons penetrate each other, they exhibit transparency. This leads to a fireball with low baryo-chemical potential as the baryon number remains concentrated near the beam rapidity. The rapidity distribution in this case should be essentially flat in the rapidity region between the two beams.

The space-time evolution of two colliding nuclei is illustrated in Figure 1.5. The two nuclei approach each other with a velocity close to the speed of light. After the first initial interactions between the nucleons the reaction zone contains highly excited matter, far from thermal equilibrium. After thermalization of the system, provided that the temperature and lifetime is sufficient, a quark-gluon plasma is formed. Due to the rapid expansion into the surrounding vacuum the system cools and the quarks recombine into hadrons. The formation of the hot hadron gas possibly occurs via a mixed phase with domains of co-existing QGP. The final step of the reaction is the complete decoupling (*freeze-out*) of the hadrons after further expansion of the system.

1.2.3 Model Descriptions

The models used to describe an ultra-relativistic heavy ion collision can be divided into two classes: microscopic models, which try to incorporate the individual interactions be-

tween all particles in a reaction, and macroscopic models, which try to describe the complete system in a hydrodynamical approach treating the fireball as ideal fluid, under the presumption of local thermal equilibrium,

Most microscopic models start with the description of the elementary process of a nucleon-nucleon collision and extend it to large nuclei by an incoherent superposition of the elementary reaction with additional effects of nuclear matter. One disadvantage of microscopic models is that they do not consider the phase transition to a quark-gluon plasma, only particular properties of the plasma phase can be incorporated as free parameters. For example, the HIJING model⁴ combines the model description of hard parton-parton processes, inspired by perturbative QCD, with a string model for soft processes and additional effects of cold and hot nuclear matter, such as *shadowing* and *jet quenching* discussed in Section 1.3.

Hydrodynamical models describe the hadronic or partonic matter as an ideal fluid, with thermal equilibrium assumed. The conservation of energy-momentum and baryon number governs the space-time evolution of this fluid via the equation of state (EOS), where pressure, energy density, and chemical potential are related. The advantage of such macroscopic models is that the different scenarios with and without formation of a QGP can be tested with different equations of state and compared to experimental data. However, the results of hydrodynamical models depend strongly on the choice of the initial conditions. A simple hydrodynamical model is described in the context of direct photon spectra in Section 2.4.

1.2.4 Signatures of a Quark-Gluon Plasma Phase

The convincing evidence for the creation of a quark-gluon plasma phase needs to take into account a variety of signatures. They can usually be divided further into:

- Change of thermodynamical and hydrodynamical properties characterizing a phase transition,
- Signals from a deconfined phase,
- Observables influenced by the restoration of chiral symmetry.

Most of the single signatures mentioned below can be described in different models without a phase transition. But a simultaneous description of all signatures without assuming a phase transition is not available.

The experimental search for the QGP is complicated by the fact that it has only a fleeting existence and that any signal from the QGP phase has to compete with the background

⁴Heavy Ion Jet INteraction Generator [Gyu94a]

from the hadron gas following the hadronization of the plasma. It shall also be noted that for the interpretation of many of the promising signatures discussed below, the comparison to more elementary $p + p$ reactions and to $p + A$ collisions, the control experiment for medium effects in cold nuclear matter, at the same energy is crucial.

Kinematical and Hydrodynamical Probes

Thermodynamical properties such as the temperature, the pressure, the energy density, and the entropy of a system as well as their mutual dependence are directly influenced by a phase transition. For example, a change in the number of the degrees of freedom, when going from a quark-gluon plasma back to a hadron gas, can have a direct impact on the dependence of the energy density on the temperature. However, most thermodynamical properties show a distinct behavior only in the case of a first order phase transition.

The average transverse momentum of particles $\langle p_T \rangle$ in the QGP phase is in principle related to the temperature of the system. However, hadrons do interact after the chemical freeze-out from the QGP in the hadron gas so that the direct connection to the temperature is distorted. A better probe may be provided by thermally produced dileptons and photons, which do not suffer from strong final state interactions, as discussed below.

The entropy and energy density of the system is usually related to the measured particle multiplicity dN/dy and the transverse energy dE_T/dy at mid-rapidity. The hydrodynamical properties and the equation of state of the system can be studied through collective flow effects arising from pressure gradients in the asymmetric reaction zone, while the system size and lifetime of the reaction zone can be inferred from interferometry of identical particles, known as Hanbury-Brown-Twiss or HBT interferometry.

Electromagnetic Probes

The main advantage of electromagnetic probes, i.e. direct photons and lepton pairs, is that they are not influenced by the strongly interacting medium. They are created basically throughout all stages of the reaction, in initial hard scattering as well as by thermal production in the QGP and the hadron gas, and can provide a direct measure of the evolution of the fireball. Since the production of direct photons is one of the main topics of this work it is discussed in detail in Chapter 2.

Dileptons are produced in a QGP phase by quark-antiquark annihilation $q\bar{q} \rightarrow l^+l^-$, which is governed by the thermal distribution of quarks and antiquarks in the plasma. This production channel has to be disentangled from the Drell-Yan production, which is the annihilation process of a valence quark with a sea quark, already present in nucleus-nucleus collisions, and the production in a hadron gas via the process $\pi^+\pi^- \rightarrow l^+l^-$, for a more detailed description see e.g. [Won94].

Besides the analysis of the continuum mass spectrum, the study of dileptons allows the measurement of the ρ , ω and Φ mesons via their dilepton decay branch. Measurement of these mesons also provides an interesting probe for the QGP phase, as their mass might be influenced by chiral symmetry restoration and especially the Φ ($s\bar{s}$) is sensitive to strangeness enhancement (see below).

Signatures from the Deconfined Phase

The creation of the deconfined QGP phase should enhance the production of strange quarks because for the creation of a $s\bar{s}$ pair only the current quark mass of approximately $300 \text{ MeV}/c^2$ is needed. By contrast, in the associated production of strange particles in a hadron gas the larger constituent quark mass of the strange quark becomes important and a higher energy is needed. For example, for the simplest reaction $pp \rightarrow \lambda^0 K^+ p$ the threshold is $700 \text{ MeV}/c^2$. This should be directly visible in the enhanced production rate of strange particles compared to proton-proton collisions.

Another promising signature for deconfinement is the J/ψ suppression. The J/ψ , a bound $c\bar{c}$ state, is primarily produced in hard parton-parton scatterings due to its large mass ($m_{J/\psi} = 3097 \text{ MeV}/c^2$). In a QGP the attractive potential between a $c\bar{c}$ is screened by the large density of free color charges in the medium. At hadronization time the dissociated charm quarks couple with a larger probability to the abundant lighter quarks than recombining to a J/ψ .

The deconfined phase of a QGP, with its large color charge density, should also induce an energy loss of quarks and gluons produced in initial hard scatterings. This is discussed separately in Section 1.3.

Indications of Chiral Symmetry Restoration

As discussed in Section 1.1.2 the deconfined phase of the QGP can prelude the restoration of chiral symmetry. A possible signal for the chiral symmetry restoration is the creation of the so-called disoriented chiral condensate (DCC). When the transition occurs very rapidly from a phase with restored chiral symmetry back into the chirally broken ground state, the chiral condensate may populate an energetically less favorable state than usual nuclear matter, the disoriented chiral condensate. One possible signature for the creation of a DCC is random fluctuations between the production amplitudes of the pion isospin-triplet (π^+ , π^0 , π^-), different from the usual value of $N_{\pi^x}/(N_{\pi^+} + N_{\pi^0} + N_{\pi^-}) \approx 1/3$, as discussed in [Pei97].

An additional signal for the chiral symmetry restoration is a modification of the mass and decay width of the light vector mesons ρ , ω , and Φ , which are usually detected via their e^+e^- decay channel.

1.3 Jets and Jet Quenching

Particles with large transverse momenta are predominantly produced in hard parton-parton collisions as discussed above. In $p + p$ collisions the scattered partons fragment directly in the QCD vacuum and are visible as *jets* of particles along the direction of motion of the primordial parton. In heavy ion collisions the hard scattering processes occur in the initial stage of the reaction, as shown in Figure 1.5. The scattered partons may now have to traverse the hot and dense medium before they fragment into hadrons. Thus they can probe matter produced in the later stages of the reaction. A large energy loss in a colored medium was predicted in [Gyu90, Bai95]. It should distort the back-to-back correlation of particle jets and lead to a suppression of particle production at high p_T compared to $p + p$ reactions, the *jet quenching*.

1.3.1 The Nuclear Modification Factor

For the large momentum transfer in initial hard scatterings the partons can be considered as asymptotically free, as for $p + p$ collisions, and the cross section in a collision of two nuclei $A + B$ should be connected to the $p + p$ cross section by a scaling factor, the number of inelastic, binary nucleon-nucleon collisions N_{coll} in the reaction.

For $A + B$ collisions at a fixed impact parameter N_{coll} is proportional to the nuclear thickness function $T_{AB}(b)$, which is analogous to an integrated "nucleon luminosity" for the two overlapping nuclei, as illustrated in Figure 1.6. Since each centrality selection by the experiment samples a different distribution of impact parameters the cross section for a high- p_T particle h produced in an $A + B$ collision with centrality f is linearly connected to the $p + p$ cross section via the average nuclear thickness $\langle T_{AB} \rangle_f$:

$$\frac{1}{N_{AB}^{\text{evt}}} \left. \frac{d^2 N_{AB}^h}{dp_T dy} \right|_f = \langle T_{AB} \rangle_f \cdot \frac{d^2 \sigma_{pp}^h}{dp_T dy}, \quad (1.6)$$

with:

$$\begin{aligned} \langle T_{AB} \rangle_f &= \frac{\int_f T_{AB}(b) d^2 b}{\int_f (1 - e^{-\sigma_{\text{NN}} T_{AB}(b)}) d^2 b} \\ &= \frac{\langle N_{\text{coll}} \rangle_f}{\sigma_{\text{NN}}}, \end{aligned} \quad (1.7)$$

where $\langle N_{\text{coll}} \rangle_f$ is the average number of inelastic, binary nucleon-nucleon collisions with an inelastic cross section σ_{NN} . The average nuclear thickness function and $\langle N_{\text{coll}} \rangle_f$ for a given centrality can be calculated via a Glauber Monte Carlo calculation taking into

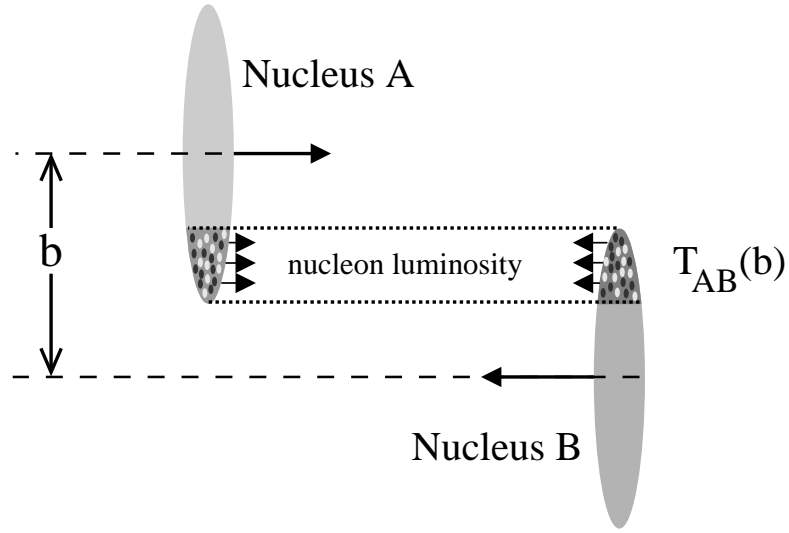


Figure 1.6: The concept of binary scaling: a heavy ion collision as incoherent superposition of nucleon-nucleon collisions.

account the experimental centrality selection, as described in detail in [Kel00, Rey03b] for the PHENIX experiment.

As the factorization of the cross section given in Equation (1.5) implies, the scaling with the number of binary collisions described by Equation (1.6) can be modified when the initial parton distribution is changed in the nuclear environment or the fragmentation process of the hard-scattered partons is modified, e.g. when the partons lose energy prior to fragmentation. Such medium effects are usually studied by means of the *nuclear modification factor* R_{AB} :

$$\begin{aligned}
 R_{AB} &= \frac{dN_{AB}^h}{\langle T_{AB} \rangle_f \cdot d\sigma_{NN}^h} \\
 &= \frac{dN_{AB}^h}{\langle N_{\text{coll}} \rangle_f \cdot dN_{NN}^h},
 \end{aligned} \tag{1.8}$$

which is expected to be unity above a certain p_T , where hard scattering is the dominant source of particle production, and in the absence of any medium effects.

1.3.2 Effects of Cold Nuclear Matter

In order to identify parton energy loss or jet quenching, which should lead to $R_{AB} < 1$, it is crucial to know all other medium effects leading to a modification of the particle production compared to nucleon-nucleon reactions. Possible medium effects are particle

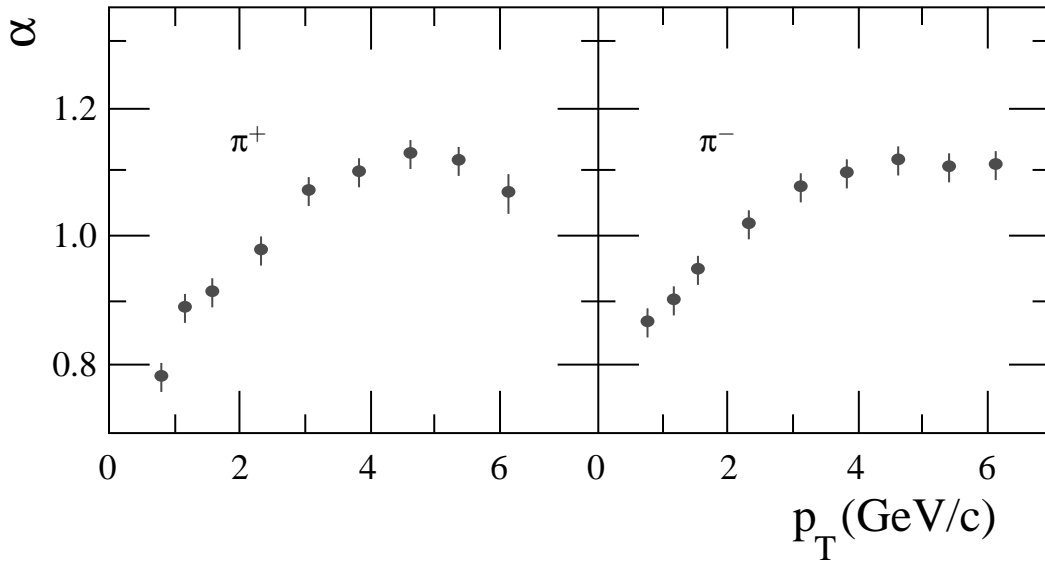


Figure 1.7: Dependence of the exponent α defined in Equation (1.9) on the transverse momentum, the nuclear enhancement for charged pion production as reported in [Cro75].

absorption or energy loss already for the passage through cold nuclear matter, enhanced particle production by multiple soft scattering, or a modification of the parton distribution function in the initial state.

Cronin Effect

One experimental observation, when comparing elementary $p + p$ collisions to $p + A$ reactions, is that the cross section does not simply scale with the number of target nucleons A in a $p + A$ collision. This was first shown by Cronin et al. in 1974 [Cro75] with a proton beam on beryllium, titanium, and tungsten targets. They found that the cross section for a given p_T scales like:

$$E \frac{d^3\sigma}{dp^3}(p_T, A) = E \frac{d^3\sigma}{dp^3}(p_T, 1) \cdot A^{\alpha(p_T)}, \quad (1.9)$$

with $\alpha > 1$ for transverse momenta larger than approximately $2 \text{ GeV}/c$ as shown in Figure 1.7. Hence there was observed an enhancement of particle production compared to the expectation from $p + p$ reactions. This effect is usually referred to as the *Cronin effect* and is attributed to multiple soft scattering of the incoming nucleons, leading to an additional broadening of their transverse momentum.

1.3.3 Nuclear Shadowing

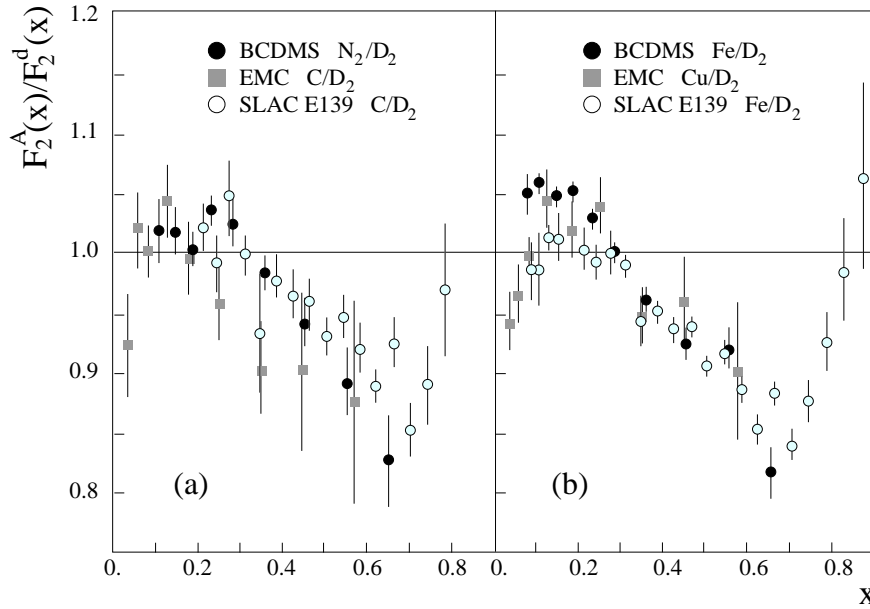


Figure 1.8: The ratio of structure functions $F_2^A(x)/F_2^d(x)$ for nuclear targets A compared to deuterium d , measured in deep-inelastic electron (SLAC-139) and muon (BCDMS, EMC) scattering: (a) medium-weight targets, (b) heavier-weight targets [Roe96].

For the modification of particle production going from protons to heavy ions not only final state effects such as the Cronin effect can be responsible. *Initial state* effects, such as a modification of the nuclear wave function in nuclei, can also have an effect on particle production.

A highly energetic hadron has contributions to its wavefunction from gluons, quarks, and antiquarks each with a probability to carry some fraction of the momentum of the hadron, up to its full momentum. A convenient variable to describe the contribution of a parton to the total hadron momentum is the fractional momentum x , already introduced above. Results on the nuclear structure functions $F_2^{IN}(x, Q^2)$ in various deep-inelastic lepton-nucleon scattering experiments (see e.g. [Roe96, Per00]) can then be used to derive the individual parton distribution functions for quarks and antiquarks also used in Equation (1.5). Any change in the nuclear structure function implies also a change in the underlying parton distributions, hence a changed number of scattering centers, which has a direct impact on the particle production.

For the comparison of nuclear structure functions the deep-inelastic scattering off deuterium is often used as the reference, as it represents an isospin-averaged nuclear structure function. A collection of data for different nuclei is shown in Figure 1.8 where the

nuclear effects are clearly seen: For $x < 0.2$ one observes a reduction of $R_{F_2}^A = F_2^A/F_2^d$, the so-called *nuclear shadowing*. A small enhancement is seen between $0.1 < x < 0.2$, sometimes referred to as *anti-shadowing*. The dip for $0.2 < x < 0.8$ has been first reported by the EMC collaboration [Aub83] and is usually called the *EMC effect*, while the rise for larger x can be associated with Fermi motion of the nucleons inside the nucleus [Pil00]. Similar effects are also expected for the gluon distributions, which are not directly accessible with leptonic probes.

The relevant x -region of the scattered parton can be estimated by the transverse momentum of the *leading hadron*, which is the hadron carrying the largest momentum fraction of the original scattered parton:

$$x \approx \frac{2p_T}{\sqrt{s_{NN}}}, \quad (1.10)$$

so that for RHIC energies and for transverse momenta up to 10 GeV/c the shadowing region $x < 0.1$ is most relevant. Early predictions for jet quenching at RHIC energies already considered this effect which can reduce the nuclear modification factor by approximately 30%, though with a large uncertainty due to the poorly known gluon contribution [Wan92].

The Color Glass Condensate

In addition to the nuclear shadowing effects discussed above, saturation effects may influence the parton density in a nucleus. The gluon density for different momentum transfers inferred by the ZEUS experiment at HERA from deep-inelastic scattering via a QCD fit [Che03] is shown in Figure 1.9. It is seen that for a given x the gluon density rises with the resolution, the momentum transfer of the exchanged virtual photon Q^2 , and that for low x the gluon density rises rapidly without leveling off. This experimental observation has been accompanied by theoretical calculations that predicted a rise of the gluon density which would lead to a violation of the *Froissart* unitarity bound for the total cross section.⁵ This is known as the *small- x problem*.

The model of the *color glass condensate* (CGC) provides a solution for this problem which also has implications for particle production in heavy ion collisions. For a recent review of the topic see e.g. [Ian03]. The basic idea of the color glass condensate is that at sufficiently high gluon densities, when the separation between the gluons becomes small, not only the coupling α_s becomes weak, but the gluons can also start to fuse ($gg \rightarrow g$), which basically limits the gluon density at small x .

⁵On the basis of very general arguments invoking unitarity Froissart has shown that the total cross section for strong interactions grows at most as fast as $\ln^2 s$ as $s \rightarrow \infty$ [Fro61].

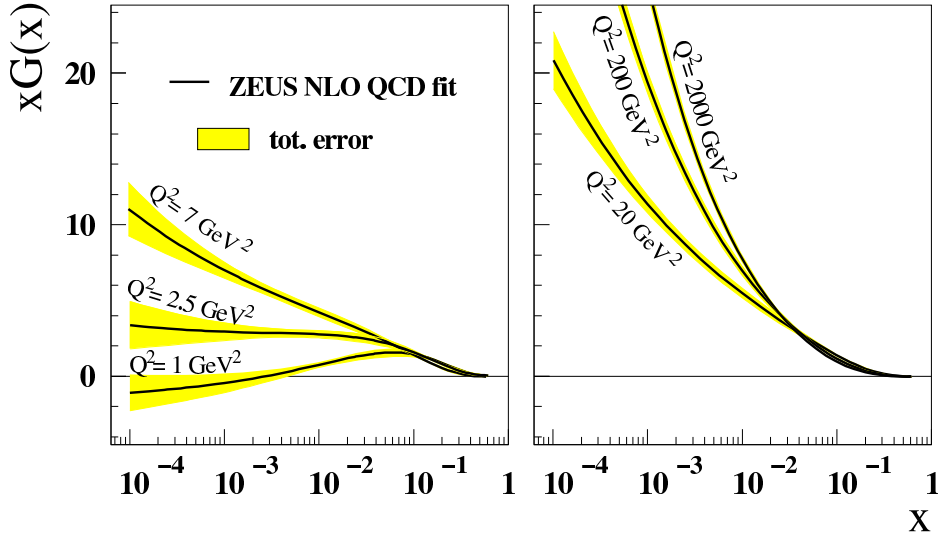


Figure 1.9: The gluon density $xG(x)$ determined by a NLO QCD fit to the ZEUS data from deep-inelastic scattering [Che03].

As discussed e.g. in [Kha03] these effects become important starting at the saturation scale Q_s which depends on the size of the nucleus, basically the "gluon thickness" or the number of gluons as seen by a hadronic probe when traversing the nucleus A , which is proportional to $A^{1/3}$. Q_s depends also on the rapidity region since the probed x region decreases with $x \sim e^{-y}$. In the case that the saturation scale is reached in RHIC collisions at large transverse momenta the depletion of the gluon density implies a reduction of the nuclear modification factor already in $d + Au$ collisions.

1.3.4 Parton Energy Loss

When a parton traverses a colored medium it loses energy predominantly by radiating soft gluons, similar to electromagnetic Bremsstrahlung of an electron passing through matter [Wan92]. The theoretical treatment of the energy loss is complicated by the fact that one has to consider destructive interference effects of the emitted gluons if the formation time of the gluon $\tau \approx \hbar/E_g$ is large compared to its mean free path λ/c in the medium (see e.g. [Gyu94b]). This effect was first studied for the passage of highly energetic electrons or photons through matter and is known as the Landau-Pomeranchuk-Migdal (LPM) effect [Mig56].

This quantum interference can produce an energy loss $\Delta E/\Delta x$ that grows faster than linearly with the path length L of the parton in the medium [Bai97]:

$$\frac{\Delta E}{\Delta x} \sim \frac{L}{\lambda} \ln \frac{L}{\lambda}. \quad (1.11)$$

However, this growth of the energy loss is only valid for a static medium. In a heavy ion collision the rapid decrease of energy density and color charge density in the expanding fireball has to be taken into account.

The most commonly used description of the parton energy loss is the GLV formalism (see e.g. [Gyu00] for details), which is the perturbative treatment of the energy loss by an expansion in the *opacity* L/λ . In this formalism the fractional energy loss varies for large jet energies E as $\ln E/E$. However, the numerical calculation of the fractional energy loss at RHIC energies produces a nearly constant $\Delta E/\Delta x$ below $E = 20 \text{ GeV}$ [Gyu03].

The energy loss can also be implemented in an effective way in the factorized cross section, given by Equation (1.5), via a changed fragmentation process. This is done by shifting the fractional parton energy prior to hadronization:

$$z = p_h/p_c \rightarrow z^* = z/(1 - \epsilon), \quad \text{with } \epsilon \in [0, 1[. \quad (1.12)$$

The shift can be directly related to the parton energy loss as discussed in [Wan02, Vit02]. This procedure facilitates the calculation of particle production in the energy loss scenario, employing well known techniques.

As mentioned above the expansion of the system in a heavy ion collision leads to a rapid decrease of the color charge density. This is usually taken into account by considering a longitudinally expanding fireball, any transverse expansion is neglected. The color charge density ρ then decreases as a function of proper time τ [Vit02]:

$$\rho(\tau) = \frac{\rho_0 \tau_0}{\tau}, \quad (1.13)$$

where τ_0 is the formation time of the partons from which the fireball is composed and ρ_0 is their initial number density.

2. Direct Photons

Similar to the analysis of virtual photons via dileptons, the examination of direct photons provides a tool to study the different stages of a heavy ion collision, especially the formation of a quark-gluon plasma, without being influenced by the strong interaction and hadronization processes. *Direct* photons are all photons not originating from hadronic decays, e.g. $\pi^0, \eta \rightarrow \gamma\gamma$. They are usually further classified into *prompt* photons produced in early hard scatterings, and *thermal* photons emitted from a thermally equilibrated phase.

Prompt and thermal photons cannot be separated experimentally, but it is expected that at intermediate transverse momenta $p_T = 1 - 3 \text{ GeV}/c$ the thermal signal is the largest contribution to the total direct photon yield, while prompt photons dominate at large transverse momenta. As the interpretation of the direct photon results relies on the understanding of the different sources of photons during all stages of a heavy ion collision, a short theoretical survey is given in the following. For more details see e.g. [Won94, Pei02, Arl03, Rap04].

2.1 Thermal Photons from a QGP

A QGP emits photons, as does every thermal source, but while e.g. in stars the photons themselves are thermalized, the mean free path of photons in the QGP phase is large and so the photons are not likely to interact, although the quarks and gluons should be thermalized. In leading order (LO) perturbation theory real photons are produced via quark-antiquark annihilation ($q\bar{q} \rightarrow g\gamma$) and by quark-gluon Compton scattering ($qg \rightarrow q\gamma$). The corresponding Feynman graphs are shown in Figure 2.1 together with an example of a higher order Bremsstrahlung process, in which a quark radiates a photon.

For the calculation of the corresponding emission rates the transition matrix elements for the two LO contributions can be determined analogous to the equivalent QED processes $e^+e^- \rightarrow \gamma\gamma$ and $e\gamma \rightarrow e\gamma$. Together with the introduction of the Mandelstam variables s, u and t this leads to the differential cross section for the two processes [Won94]:¹

$$\frac{d\sigma}{dt}(q\bar{q} \rightarrow g\gamma) = \left(\frac{e_q}{e}\right)^2 \cdot \frac{8\pi\alpha_s\alpha}{s(s-4m_q^2)} \left\{ \left(\frac{m_q^2}{t-m_q^2} + \frac{m_q^2}{u-m_q^2} \right)^2 \right.$$

¹The Mandelstam variables for the process $1,2 \rightarrow 3,4$ are determined by the corresponding four-momenta $P_{1\dots 4}$: $s = (P_1 + P_2)^2$, $t = (P_1 - P_3)^2$, and $u = (P_1 - P_4)^2 = (P_2 - P_3)^2$. We will refer to such processes also as $2 \rightarrow 2$ processes in the following.

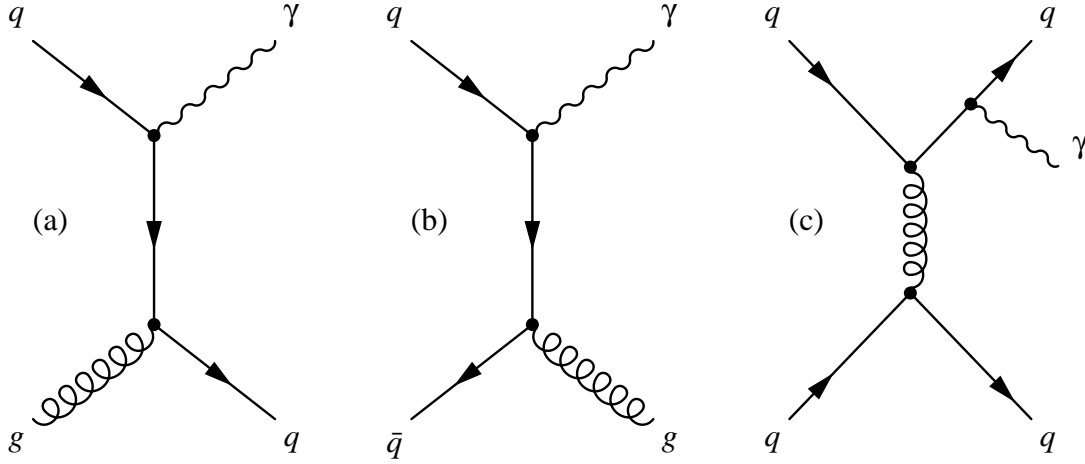


Figure 2.1: Feynman graphs of the main production processes for direct photons in initial hard scatterings as well as in a thermalized quark-gluon plasma phase: (a) quark-gluon Compton scattering of order $\alpha_s\alpha$, (b) quark-antiquark annihilation of order $\alpha_s\alpha$, (c) Bremsstrahlung of order $\alpha_s^2\alpha$.

$$+ \left(\frac{m_q^2}{t - m_q^2} + \frac{m_q^2}{u - m_q^2} \right) - \frac{1}{4} \left(\frac{t - m_q^2}{u - m_q^2} + \frac{u - m_q^2}{t - m_q^2} \right) \Bigg\}, \quad (2.1)$$

$$\frac{d\sigma}{dt}(qg \rightarrow q\gamma) = \left(\frac{e_q}{e} \right)^2 \cdot \frac{8\pi\alpha_s\alpha}{(s - m_q^2)^2} \left\{ \left(\frac{m_q^2}{s - m_q^2} + \frac{m_q^2}{u - m_q^2} \right)^2 + \left(\frac{m_q^2}{s - m_q^2} + \frac{m_q^2}{u - m_q^2} \right) - \frac{1}{4} \left(\frac{s - m_q^2}{u - m_q^2} + \frac{u - m_q^2}{s - m_q^2} \right) \right\}, \quad (2.2)$$

where m_q is the quark mass and e_q is the quark charge.

It is very instructive to consider the case where m_q becomes negligible or the quarks are massless. Then only the last term in each sum remains. In this limit the cross section for the annihilation process, Equation (2.1), is maximal when either u or t are minimal. This corresponds to the case where $P_\gamma \approx P_q$ or $P_\gamma \approx P_{\bar{q}}$. Hence the annihilation process can be visualized as a conversion of one of the annihilating quarks into a photon, and the momentum distribution of the photon is directly related to the (thermal) distribution of quarks and antiquarks in the QGP. For the Compton process a similar argumentation holds. The dominant contribution comes from the region of small u where $P_\gamma \approx P_q$.

For the calculation of the total emission rate for each process the initial distributions of quarks $f_q, \bar{q}(E)$ and gluons $f_g(E)$ in thermal equilibrium at temperature T are needed.

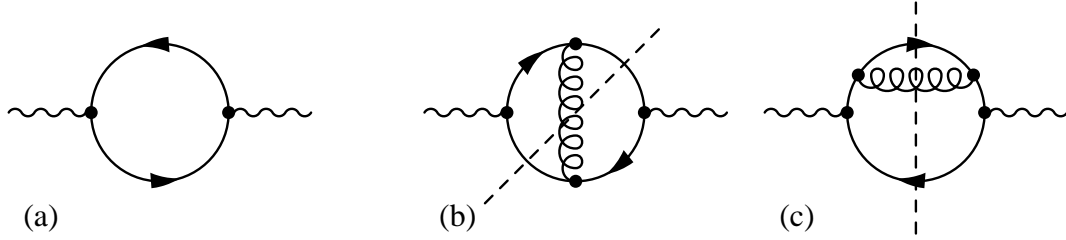


Figure 2.2: Feynman graphs of the photon self-energy: (a) 1-loop polarization tensor, (b) and (c) 2-loop polarization tensor. The dashed lines indicate cuts through the diagram corresponding to the processes in Figure 2.1.

They obey the Fermi-Dirac and the Bose-Einstein statistics, respectively. For vanishing baryo-chemical potential holds:

$$f_{q, \bar{q}}(E) = \frac{1}{e^{E/T} + 1}, \quad (2.3)$$

$$f_g(E) = \frac{1}{e^{E/T} - 1}. \quad (2.4)$$

After phase-space integration of the elementary photon production processes with these thermal distributions the total production rate for a quark-gluon plasma with u and d quarks ($N_f = 2$) in the QGP is given by [Won94]:

$$E_\gamma \frac{dN_\gamma}{d^3p d^4x} = \frac{5}{9} \frac{\alpha_s \alpha}{2\pi^2} f_q(\vec{p}_\gamma) T^2 \left\{ \ln \left(\frac{4E_\gamma T}{m_q^2} \right) + \frac{C_{\text{ann}} + C_{\text{Comp}}}{2} \right\}, \quad (2.5)$$

where C_{ann} and C_{Comp} are numerical integration constants. The close relation between the photon production in the plasma and the quark distribution $f_q(\vec{p}_\gamma)$ is directly seen. However, Equation (2.5) contains the quark mass as a parameter which basically defines a cutoff when the momentum transfer goes to zero. A similar calculation in [Kap91] uses massless quarks and explicitly introduces a cutoff parameter k_c to account for the infrared divergence of Equation (2.1) and (2.2) in the phase-space integration.

To calculate the infrared contribution not considered in Equation (2.5) one can make use of the fact that the thermal emission rate of photons is also given by the imaginary part of the photon self-energy at finite temperature [Gal91, Kap91].

The photon self-energy is determined via loop diagrams as shown in Figure 2.2. The imaginary part is obtained by cuts through the loops: A cut through Figure 2.2(a) gives no contribution because the process $q\bar{q} \rightarrow \gamma$ has no phase space. The familiar Feynman

graphs for the Compton and the annihilation process as in Figure 2.1 correspond to certain cuts through the two loop diagrams as shown in Figure 2.2(b) and (c).

The infrared contribution can now be calculated by using a technique proposed by Braaten and Pisarski [Bra90]. The bare vertices and propagators as in Figure 2.1 or Figure 2.2 can be replaced by so-called *effective* vertices and propagators. The effective propagators and vertices are the bare ones plus one-loop corrections. They are represented as shown in Figure 2.3. The introduction of such effective vertices and propagators basically represents a reordering of perturbation theory to take into account higher order diagrams, containing an infinite number of loops (screening effects), which can contribute to the same order in the coupling constant (see also [Tho00, Pei02]). The LO diagrams with effective propagators are again obtained by the imaginary part of the self-energy or cuts through the diagram, respectively. Such diagrams are also called hard thermal loops (HTLs), as they are used where the momentum of the propagator is soft (thermal) and the corrections are evaluated for hard loop momentum.

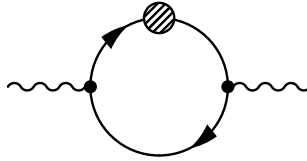


Figure 2.3: Photon self-energy containing a HTL-resummed propagator indicated by the circle. Cuts through the diagram lead to the processes in Figure 2.1(a) and (b) with an effective propagator.

With this technique the infrared contribution has been determined in [Kap91]. Together with the photon production rate corresponding to Equation (2.5) this leads to a photon production rate that does not depend on cutoff parameter or quark mass [Kap91]²:

$$E_\gamma \frac{dN_\gamma}{d^3 p d^4 x} \Big|_{2 \rightarrow 2} = \frac{5}{9} \frac{\alpha \alpha_s}{2\pi^2} e^{-E_\gamma/T} T^2 \ln \left(\frac{2.912 E_\gamma}{4\pi \alpha_s T} \right). \quad (2.6)$$

One would expect that higher order diagrams, such as Bremsstrahlung shown in Figure 2.1(c) and $q\bar{q}$ annihilation with additional scattering (AWS), contribute only to higher order compared to the leading order diagrams. However, it has been shown in [Aur98] that the contribution of 2-loop HTL corrections, corresponding e.g. to Bremsstrahlung, is of order $\alpha_s \alpha$. Although the rate was initially overestimated by a factor of four, it is

²In [Kap91] a Boltzmann distribution has been used instead of Equation (2.3) and (2.4) to make an analytic solution possible.

still found that the 2-loop contribution enhances the photon spectrum from the QGP by a factor of two. It can be parameterized as [Ste01]:

$$E_\gamma \frac{dN_\gamma}{d^3 p d^4 x} \Big|_{\text{Brems}} = 0.0219 \cdot \alpha \alpha_s T^2 e^{-E_\gamma/T}, \quad (2.7)$$

$$E_\gamma \frac{dN_\gamma}{d^3 p d^4 x} \Big|_{\text{AWS}} = 0.0105 \cdot \alpha \alpha_s E_\gamma T e^{-E_\gamma/T}, \quad (2.8)$$

for the contribution from Bremsstrahlung and annihilation with rescattering, respectively. The contribution to the total photon rate is shown in Figure 2.4(a). It is seen that the photon production via Bremsstrahlung surpasses the $2 \rightarrow 2$ processes of the 1-loop calculation by a factor of two.

Investigations on 3-loop corrections in [Aur00] showed that they also can contribute to order $\alpha_s \alpha$ indicating that the thermal photon production may not be calculable via perturbative techniques [Ste01].

When calculating the thermal photon production from a QGP an additional complication is introduced by the consideration of the Landau-Pomeranchuk-Migdal effect already discussed for the parton energy loss. A calculation considering all processes contributing to the order $\alpha_s \alpha$, including Bremsstrahlung, inelastic pair annihilation, as well as the LPM effect, has been performed for the first time in [Arn01]. The photon rates in [Arn01] are given in a slightly different notation compared to Equation (2.6) – (2.8). They can be rewritten to the same notation for two quark flavors ($N_f = 2$) and are given by:

$$E_\gamma \frac{dN_\gamma}{d^3 p d^4 x} \Big|_{2 \rightarrow 2} = \frac{5 \alpha \alpha_s}{9 2\pi^2} \cdot T^2 \cdot e^{-E_\gamma/T} \left\{ \log \left(\frac{3}{2\pi\alpha_s} \cdot E_\gamma/T \right) + 2.02 \cdot e^{-1.35E_\gamma/T} - 0.6328 + \frac{0.082}{E_\gamma/T} \right\}, \quad (2.9)$$

$$E_\gamma \frac{dN_\gamma}{d^3 p d^4 x} \Big|_{\text{Brems}} = \alpha \alpha_s \cdot T^2 \cdot e^{-E_\gamma/T} \left\{ \frac{0.0411 \cdot \log \left(12.28 + \frac{1}{E_\gamma/T} \right)}{(E_\gamma/T)^{3/2}} \right\}, \quad (2.10)$$

$$E_\gamma \frac{dN_\gamma}{d^3 p d^4 x} \Big|_{\text{aws}} = \alpha \alpha_s \cdot E_\gamma T \cdot e^{-E_\gamma/T} \left\{ \frac{7.49 \cdot 10^{-3}}{\sqrt{1 + \frac{E_\gamma/T}{16.27}}} \right\}, \quad (2.11)$$

where Equation (2.9) is a more general expression for Equation (2.6) with improved accuracy at low photon energies. The contribution from $2 \rightarrow 2$ processes (the 1-loop HTL rates), can serve as a reference when comparing the different contributions to the rate. As seen in Figure 2.4(b), the inclusion of the LPM effect as in [Arn01] leads to a contribution from inelastic annihilation to the total photon rate that is reduced by a factor of two. It is of the same order of magnitude as the rate from $2 \rightarrow 2$ processes. The photon rate

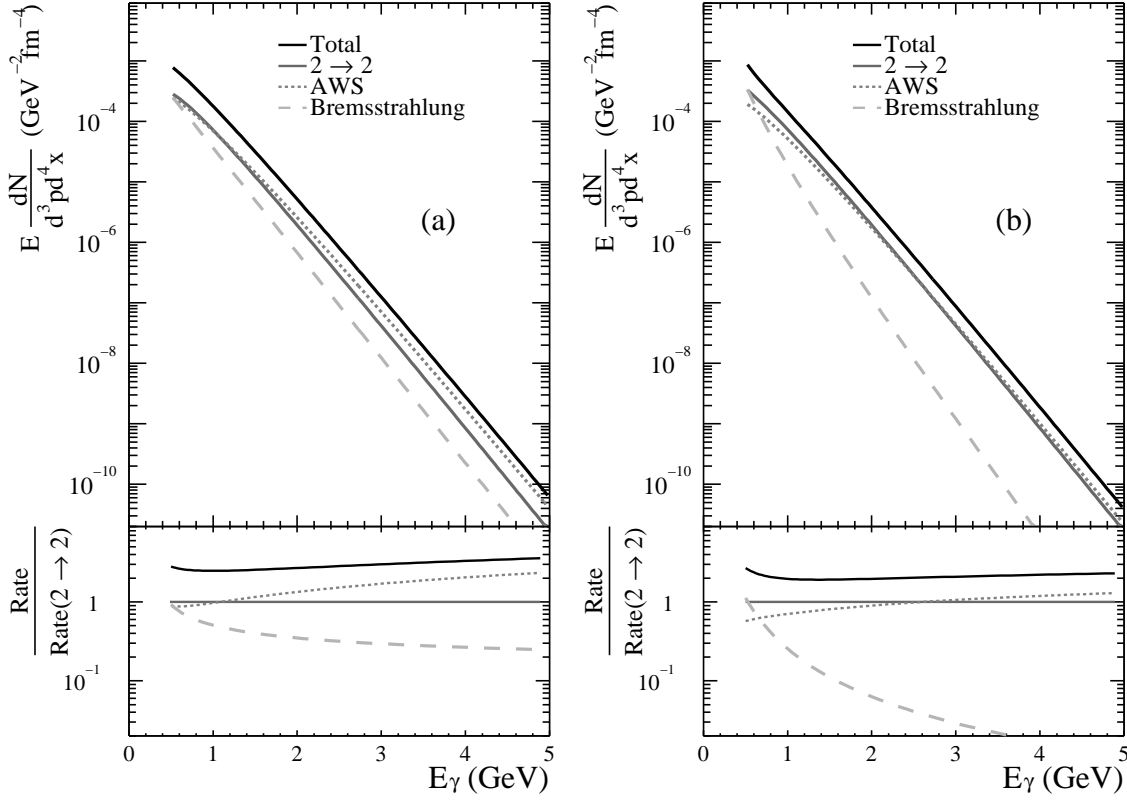


Figure 2.4: The static photon emission rates for a QGP with $T = 250 \text{ MeV}$, $N_f = 2$, and $T_c = 170 \text{ MeV}$. The strong coupling constant is given by the parameterization $\alpha_s(T) = \frac{6\pi}{(33-2N_f)\log(8T/T_c)}$ [Kar88]. The different contributions are calculated with: (a) Equation (2.6)–(2.8) considering contributions up to 2-loop order [Kap91, Ste01], (b) Equation (2.9)–(2.11) considering the LPM effect for Bremsstrahlung and inelastic pair annihilation, and $2 \rightarrow 2$ processes [Arn01].

from Bremsstrahlung decreases strongly with the photon energy, in contrast to the 2-loop calculation.

In the future one hopes to get more definitive answers on the static photon emission rates in a thermalized QGP from non-perturbative methods such as lattice QCD.

2.2 Thermal Photons from a Hadron Gas

The calculation of the thermal photon spectrum from the fireball produced in heavy ion collisions involves also the contribution from the hot hadron gas (HHG) phase following the QGP. It is also needed as reference for a scenario without a phase transition, to see if the thermal photon spectrum can be used as a signature for the QGP.

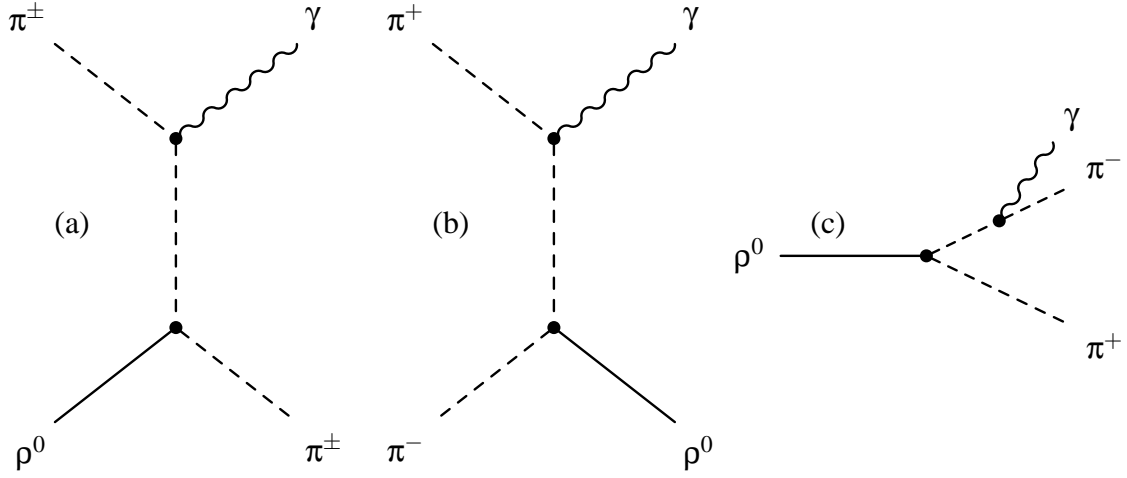


Figure 2.5: Examples of processes for the production of photons in a hadron gas: (a) $\pi\rho$ Compton scattering, (b) $\pi^+\pi^-$ annihilation, (c) ρ decay.

The emission rate of thermal photons from the HHG can be treated very similar to the QGP case, discussed above. Again the rate is proportional to the imaginary part of the photon self-energy, with the difference that pions, η s, and the ρ mesons constitute the loop corrections instead of quarks and gluons [Kap91]. The coupling between the different vertices of the loop is determined by experimental observations, such as the decay rate for $\rho \rightarrow \pi\pi$. This *effective* coupling already considers higher-order effects, e.g. vertex corrections. The cuts through the loop diagrams can be identified with the relevant hadronic processes, e.g.:

- $\pi^\pm\rho^0 \rightarrow \pi^\pm\gamma$, Compton scattering shown in Figure 2.5(a),
- $\pi^+\pi^- \rightarrow \rho^0\gamma$, the annihilation process shown in Figure 2.5(b),
- $\rho^0 \rightarrow \pi^+\pi^-\gamma$, ρ^0 decay shown in Figure 2.5(c),
- $\omega \rightarrow \pi^0\gamma$, ω decay.

The first estimate of the emission rate from a hot hadronic gas has been presented in [Kap91] together with the already discussed emission rate from a QGP phase. The comparison of the rates at $T = 200$ MeV lead to the surprising result that "The hadron gas shines as brightly as the quark-gluon plasma" [Kap91]. This would make direct photons a good thermometer of the fireball but not a signature for a phase transition. However, apart from the fact that the space-time evolution of a hadron gas and a QGP can be different, it has been already discussed that the QGP rates need to incorporate higher-order processes and the LPM effect. It was also found that the inclusion of the production of photons via

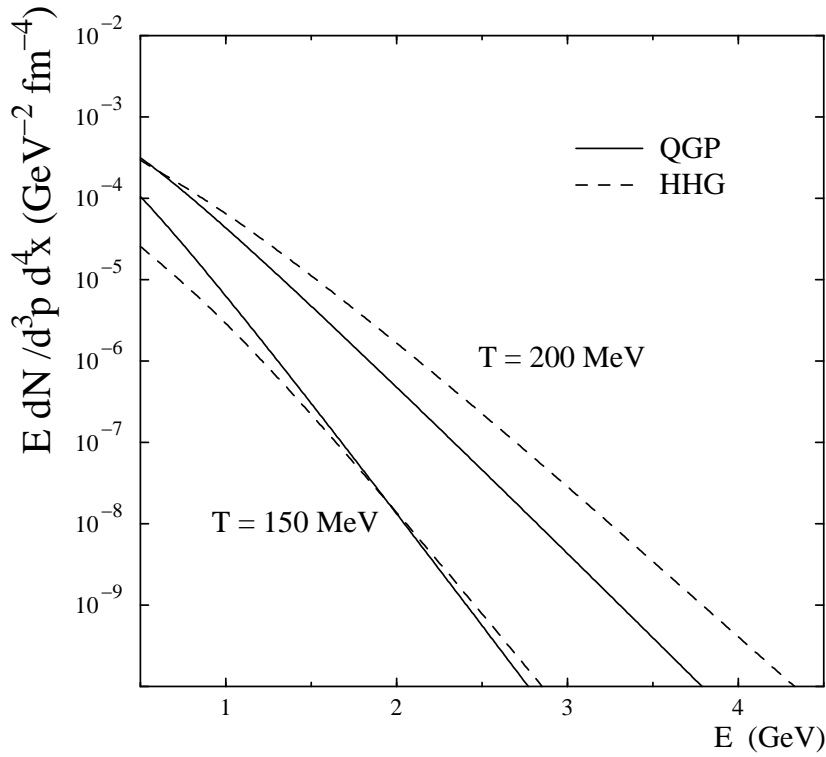


Figure 2.6: Comparison of the photon production rate from the quark-gluon plasma and the hadron gas at two different temperatures and for two quark flavors [Ste01].

the $a_1(1260)$ resonance in the hadron gas ($\pi\rho \rightarrow a_1 \rightarrow \pi\gamma$) strongly enhances the rate from the hadron gas [Xio92].

A recent parameterization of the rate for thermal photon production in the hot hadron gas is given in [Ste01]. It considers the exact expression for the decay $\omega \rightarrow \pi\gamma$ from [Kap91] and parameterizations for the processes $\pi\pi \rightarrow \rho\gamma$, $\pi\rho \rightarrow \pi\gamma$, and $\rho \rightarrow \pi\pi\gamma$ from [Son93, Son98], where the a_1 meson is taken into account:

$$E_\gamma \frac{dN_\gamma}{d^3p d^4x} \Big|_{\text{HHG}} = 4.6 \cdot T^{2.15} \cdot e^{-1/(1.35TE_\gamma)^{0.77}} \cdot e^{-E_\gamma/T}. \quad (2.12)$$

This can be compared to the rates obtained for the QGP, considering the Bremsstrahlung and inelastic annihilation contribution from [Aur98], for different temperatures. As seen in Figure 2.6, the agreement between the rates of QGP and HHG may be a coincidence at a certain temperature, but it cannot be ruled out especially given the current uncertainties of the calculations.

2.3 Non-Thermal Photons

The main source of non-thermal direct photons are the prompt photons. They are produced in early hard scatterings, similar to hadrons with large transverse momenta and are calculable via perturbative QCD invoking the factorization theorem Equation (1.5). The basic underlying processes are the same as in the QGP (see Figure 2.1), with the main difference that the initial parton distribution is not given by the thermal distributions in the QGP, but by the parton distributions in the incoming nuclei. The photon production in hard scattering is in principle not influenced by the uncertainty in the fragmentation function as in the case of hadron production, since it is a δ -function for photons. However, photons can also be produced during the fragmentation process of scattered partons.

For the production of photons in $p + A$ collisions the same effects become important as for the hadron production: the nuclear p_T -broadening, the Cronin effect, the shadowing of the parton distribution function, and possible saturation effects. Especially the Cronin effect can be a rather significant contribution to the total yield in the intermediate p_T range, where the largest thermal signal is expected. This has been demonstrated for the measurement of direct photons at SPS energies and for RHIC energies in [Dum01].

An additional source of non-thermal direct photons arises from the pre-equilibrium phase, where the theoretical description is rather difficult due to the uncertainties in the formation time of the thermalized phase. It is often treated in parton cascade models for photon production, which combine perturbative QCD with relativistic transport models (see e.g. [Sri98, Bas03]). The passage of high energy quark jets through the QGP leads to Compton scattering with the thermal gluons and annihilation with thermal antiquarks. This has also been considered as a source for direct photons, which may dominate in the region below $p_T = 6 \text{ GeV}/c$ for Au + Au collisions at RHIC [Fri03].

2.4 Photon Spectra

In the experiment, only photons from the entire space-time evolution of the heavy ion collision can be observed. Therefore thermal and non-thermal production rates have to be convoluted with the entire evolution of the reaction.

The elementary thermal photon rate depends basically on the temperature at a given space-time point $T(x)$, hence the observed photon spectrum is given by:

$$E_\gamma \frac{dN_\gamma}{d^3 p_\gamma} = \int d^4 x \frac{dN_\gamma}{d^3 p_\gamma d^4 x} (T(x)). \quad (2.13)$$

The evolution of the fireball is usually described as an ideal fluid in terms of relativistic hydrodynamics (for a more detailed description on this topic see e.g. [Bla90]). The hy-

hydrodynamic equations of motions are basic conservation laws, e.g. the local conservation of energy-momentum:

$$\partial_\mu T^{\mu\nu}(x) = 0, \quad (2.14)$$

where $T^{\mu\nu}(x)$ now denotes the relativistic energy-momentum tensor, which is given for an ideal fluid by:

$$T^{\mu\nu}(x) = (\varepsilon(x) + P(x))u^\mu u^\nu - P(x)g^{\mu\nu}, \quad (2.15)$$

where $\varepsilon(x)$ denotes the energy density, $u^\mu(x)$ the four-velocity field, $P(x)$ the pressure, and $g^{\mu\nu}$ the Minkowski metric tensor. In addition, for any conserved scalar quantity, such as baryon number, a continuity equation holds locally:

$$\partial_\mu (\rho(x)u^\mu(x)) = 0, \quad (2.16)$$

where $\rho(x)$ is the volume density. In order to solve the equations of motions given by Equation (2.14) and (2.16), only the relation between pressure, energy density, and density is needed, i.e. the equation of state (EOS) $\varepsilon(P, \rho)$.

The hydrodynamic description of the system depends strongly on the initial conditions. A first simplification of the problem is to follow Björken's approach [Bjo83] and consider only a longitudinal expansion, any transverse expansion is neglected. The fireball is treated as a longitudinally expanding tube of strongly interacting matter. The expansion is best expressed in terms of the proper-time τ and the rapidity y here given by:

$$\tau = \sqrt{t^2 - z^2}, \quad (2.17)$$

$$y = \frac{1}{2} \log \frac{t+z}{t-z}, \quad (2.18)$$

where t and z are the time and the longitudinal position in the center-of-mass frame. The point where the two colliding nuclei have maximum overlap can be chosen as the origin. This notation has already been used in Figure 1.5 where the hyperbolas are curves of constant proper-time for individual fluid cells of the evolving fireball. The rapidity y indicates the position of the fluid-cells on those hyperbolas.

A further simplification used by Björken is the *boost invariance* of the initial conditions [Bjo83]. Motivated by the plateau-like structure in the rapidity distribution of nucleon-nucleon collisions one can choose the initial conditions independent of the rapidity ($\varepsilon(\tau), P(\tau)$). In this picture the *scaling ansatz* for the four-velocity can be made:

$$u^\mu = \frac{1}{\tau} (t, 0, 0, z). \quad (2.19)$$

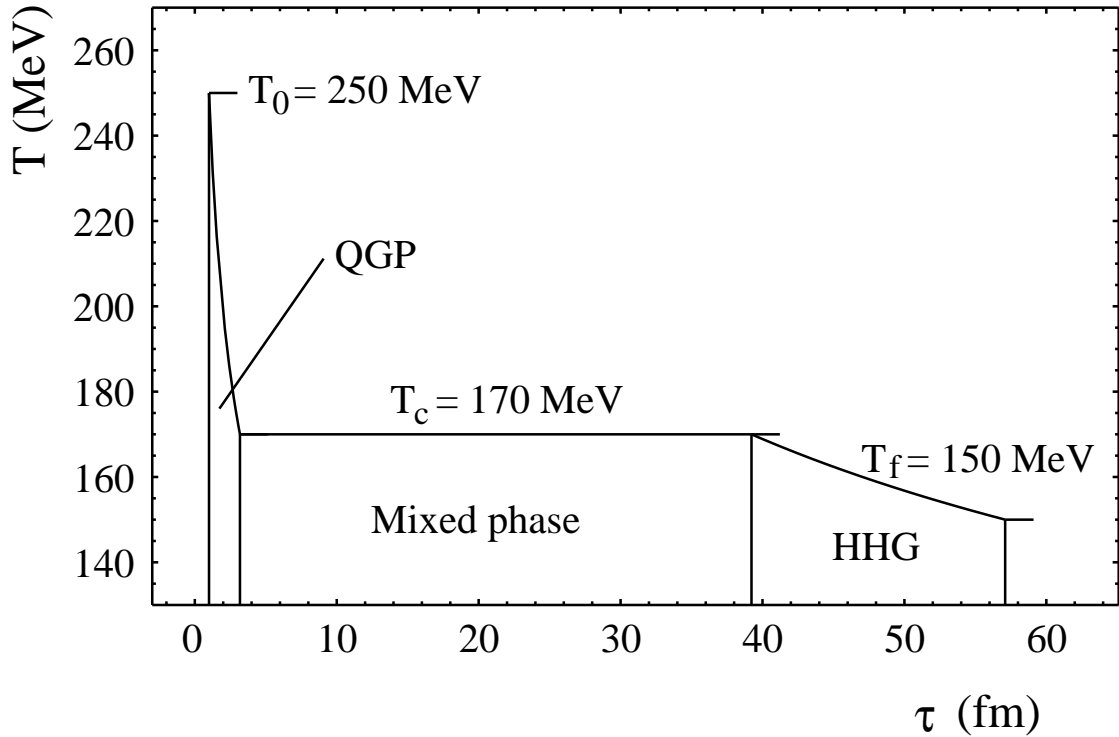


Figure 2.7: Sketch of the temperature evolution for Bjorken expansion in the phase transition scenario from an ideal gas of massless quarks and gluons in the QGP to an ideal hadron gas of massless pions [Pei02].

Together with the conservation of energy-momentum given in Equation (2.14) this leads to the basic differential equation of Bjorken's hydrodynamical model.

$$\frac{d\varepsilon}{d\tau} + \frac{\varepsilon + P}{\tau} = 0. \quad (2.20)$$

The equation of state depends on model assumptions. Usually the QGP phase and the hot hadron gas are treated separately, with the EOSs matched at the phase transition according to the order of the phase transition. The EOS for the QGP in most hydrodynamic models is from simple bag models with quarks and gluons described as an ideal gas. One obtains e.g. for a QGP with baryo-chemical potential $\mu_B = 0$ [Bla02]:

$$P_{\text{QGP}} = g_{\text{QGP}} \frac{\pi^2}{90} T^4 - B, \quad (2.21)$$

$$\varepsilon_{\text{QGP}} = g_{\text{QGP}} \frac{\pi^2}{30} T^4 + B, \quad (2.22)$$

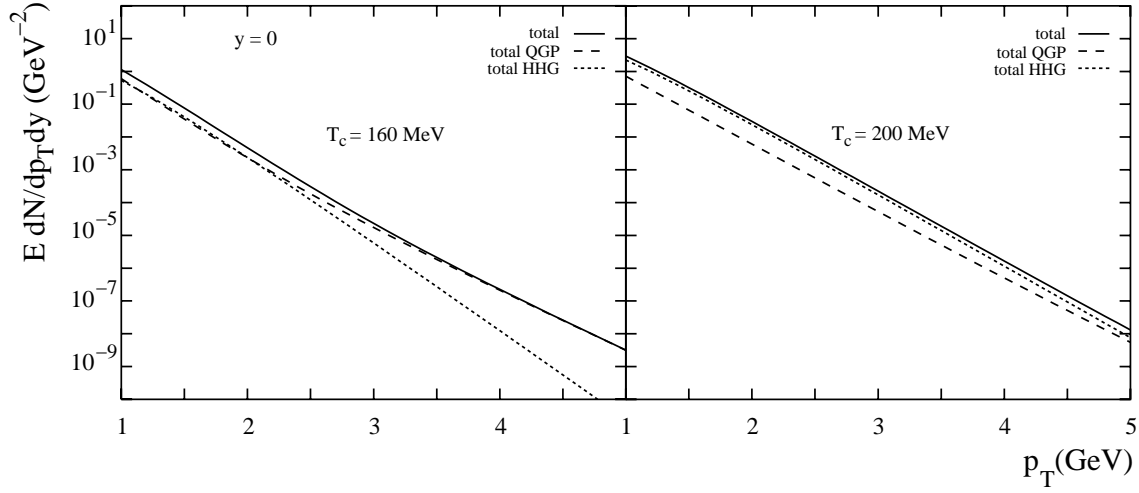


Figure 2.8: Total thermal photon emission from a QGP phase and a hot hadron gas for different critical temperatures [Pei02].

where g_{QGP} is the effective number of degrees of freedom of gluons (8 color-anticolor combinations and 2 spin states) and quarks (3 colors, 2 spin states, e.g. 2 flavors, q and \bar{q}):

$$g_{\text{QGP}} = 8 \times 2 + \frac{7}{8} \times 3 \times 2 \times 2 \times 2 = 37, \quad (2.23)$$

and B is the bag constant. It determines the energy density of the QCD vacuum necessary for the confinement of quarks and gluons in the hadron bag. It is typically of the order of $B^{1/4} \approx 200 \text{ MeV}$. From Equation (2.21) and (2.22) one can derive the EOS of a QGP in the bag model:

$$\epsilon_{\text{QGP}} = 3P_{\text{QGP}} + 4B. \quad (2.24)$$

Similarly, the pressure and the energy density of a hadron gas can be determined for an ideal gas of massless pions [Bla02]:

$$P_{\text{HG}} = g_{\text{HG}} \frac{\pi^2}{90} T^4, \quad (2.25)$$

$$\epsilon_{\text{HG}} = g_{\text{HG}} \frac{\pi^2}{30} T^4, \quad (2.26)$$

where g_{HG} is the number of degrees of freedom in the hadron gas, which is $g_{\text{HG}} = 3$ for a pion gas. The EOS is given by:

$$\epsilon_{\text{HG}} = 3P_{\text{HG}}. \quad (2.27)$$

The critical temperature T_c for the phase transition from a QGP into a hadron gas, in this simple model with first order phase transition, is determined by the Gibbs Criteria ($T_{\text{QGP}} = T_c = T_{\text{HG}}$ and $P_{\text{QGP}} = P_c = P_{\text{HG}}$) and the two EOS:

$$T_c = \left(\frac{90B}{(g_{\text{QGP}} - g_{\text{HG}})\pi^2} \right)^{\frac{1}{4}}. \quad (2.28)$$

The initial conditions of the QGP are given by the formation time τ_0 and the initial temperature T_0 . The phase transition is characterized by the critical temperature, which is $T_c \approx 150\text{MeV}$ for $B^{1/4} \approx 200\text{MeV}$. The kinetic decoupling of the hadrons is where the thermodynamic treatment of the fireball is no longer valid. It is characterized by the *freeze-out* temperature T_f .

For the first order phase transition, which is implied by this simple model but probably not realistic [Fod02], a mixed phase of QGP and hadron gas exists during which the temperature stays constant at the critical temperature. The lifetimes of the three different phases in this simple model are determined by the evolution given by the Björken scenario together with the different EOS, as discussed in [Ste99]:

$$\Delta\tau_{\text{QGP}} = \tau_0 \left\{ \left(\frac{T_0}{T_c} \right)^3 - 1 \right\}, \quad (2.29)$$

$$\Delta\tau_{\text{mixed}} = \tau_0 \left(\frac{T_0}{T_c} \right)^3 \left\{ \frac{g_{\text{QGP}}}{g_{\text{HG}}} - 1 \right\}, \quad (2.30)$$

$$\Delta\tau_{\text{HG}} = \tau_0 \left(\frac{T_0}{T_c} \right)^3 \left\{ \left(\frac{T_c}{T_f} \right)^3 - 1 \right\}. \quad (2.31)$$

The lifetimes of the different phases for an initial temperature of $T_0 = 250\text{MeV}$, critical temperature $T_c = 170\text{MeV}$, and freeze-out temperature $T_f = 150\text{MeV}$ are shown in Figure 2.7. The emission of thermal photons is now given by the convolution of this temperature evolution with the corresponding static emission rates following Equation (2.13)³. The resulting (thermal) photon spectra are shown in Figure 2.8 for two different assumptions for the critical temperature. An increase of the critical temperature obviously leads to a larger contribution from the hadron gas, as this leads to a decrease in the lifetime of the QGP.

The simple one-dimensional hydrodynamic expansion discussed in this section should only serve as an example, more complex scenarios are given in the literature (see e.g. [Hir04] and references therein). The uncertainty from the description of the space-time evolution, together with the unknown initial condition, is another source of uncertainty

³In the mixed phase the contributions from the QGP and the hadron gas have to be weighted accordingly.

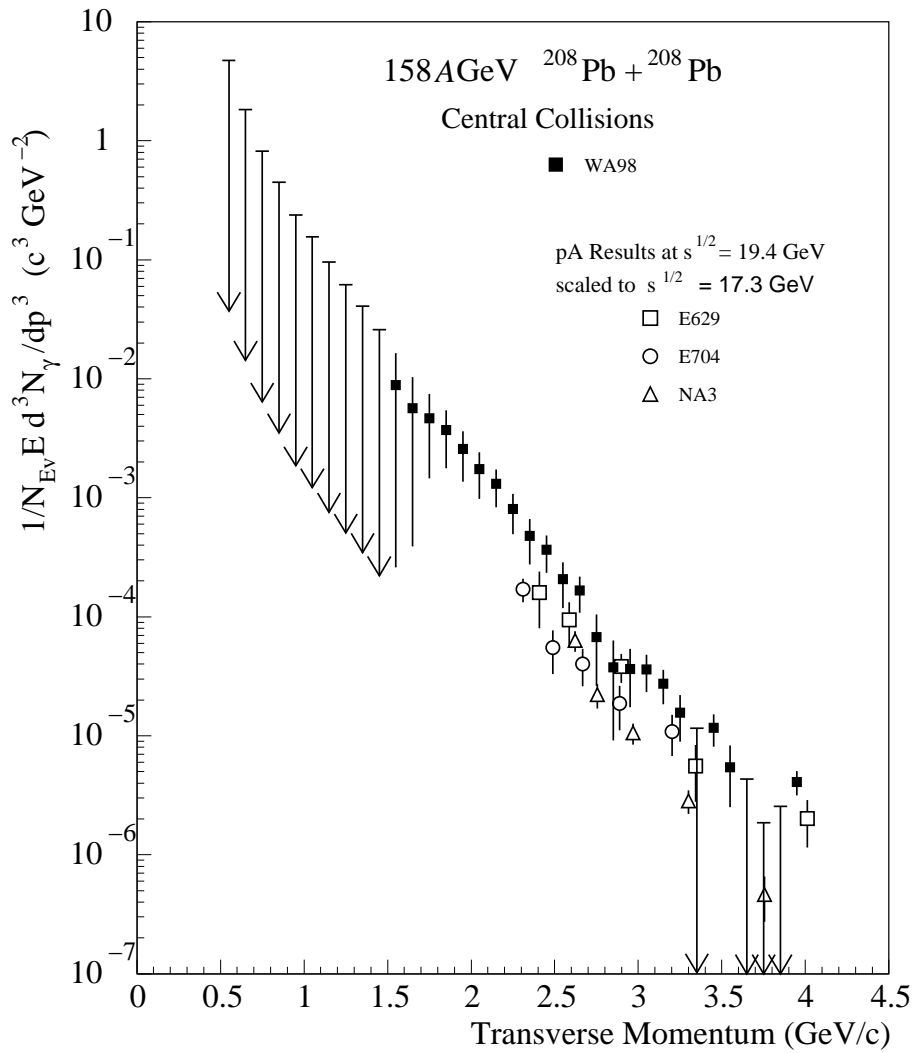


Figure 2.9: First measurement of direct photons in heavy ion collisions reported by the WA98 experiment together with scaled results from p + A collisions [Agg00].

for the theoretical description of the direct photon production in heavy ion collisions, in addition to the uncertainties in the static rates. Results from other models are presented in Section 7.2 in the comparison with experimental data.

2.5 Earlier Results on Direct Photon Production

The first measurement of direct photons in heavy ion collisions has been reported by the WA98 experiment at the CERN SPS in central Pb + Pb collisions at $\sqrt{s_{NN}} = 17.2$ GeV

[Agg00, Buc99]. It is shown in Figure 2.9 together with scaled results from $p + A$ collisions. The comparison with proton induced reactions suggests a modification of the direct photon production in heavy ion collisions. Whether this is due to quark-gluon plasma formation or other nuclear effects is still debated. A recent review of different theoretical models, which describe the WA98 data, partially without a phase transition scenario, is given in [Pei02].

3. The PHENIX Experiment

The PHENIX¹ detector at RHIC, the Relativistic Heavy Ion Collider at Brookhaven National Laboratory, is designed to study nuclear matter under extreme conditions. The variety of sub-detectors within the PHENIX experiment allows to explore possible signatures of a deconfined phase of quarks and gluons in heavy ion collisions as well as the spin structure of the nucleon in polarized p + p reactions and the effects of cold nuclear matter in d + Au collisions.

3.1 The Relativistic Heavy Ion Collider

RHIC started operation in the year 2000 with colliding gold nuclei at a center of mass energy of $\sqrt{s_{\text{NN}}} = 130$ GeV. The collider consists of two rings, denoted as *yellow* and *blue*, which accelerate the colliding species in opposite directions. The energy per nucleon in each ring ranges from 30 to 100 GeV/nucleon for heavy ions and up to 250 GeV for protons (for a detailed description of RHIC see also [Hah03]).

The ion source and the initial acceleration process are different for polarized protons and heavy ions, as described here for the case of gold ions. The different stages of the acceleration are also illustrated in Figure 3.1.

Negatively charged gold ions are generated within a pulsed sputter source and injected into a Tandem van de Graaff accelerator, where a fraction of their electrons is removed by so-called *stripping foils*. The Tandem accelerates the ions to about 1 MeV/nucleon followed by further ionization, selection of the Au⁺³² state, and transfer to the *AGS Booster*. The Booster synchrotron captures the ions after multiple injections into six bunches and accelerates them to 95 MeV/nucleon. The Alternating Gradient Synchrotron (AGS) is filled in four Booster cycles after further stripping to Au⁺⁷⁷. The energy of the ions is increased to 8.86 GeV/nucleon, and on exit from the AGS they are completely ionized by the last stripper before they are injected into one of the two RHIC rings, where they are accelerated to their colliding energy.

Polarized protons are injected directly with an energy of 200 MeV into the Booster by the linear accelerator LINAC and experience the same acceleration steps as heavy ions thereafter.

As the two rings of RHIC are operated independently and the beam injection has two Tandem Van De Graaff accelerators at its disposal, RHIC is also ideally suited to

¹Pioneering High Energy Nuclear Interaction EXperiment

Run	Date	Species	$\sqrt{s_{NN}}$	Integrated luminosity
1	6/2000 – 9/2000	Au + Au	130 GeV/c	$1 \mu\text{b}^{-1}$
2	9/2001 – 11/2001	Au + Au	200 GeV/c	$24 \mu\text{b}^{-1}$
	12/2001 – 1/2002	p + p	200 GeV/c	0.15pb^{-1}
3	11/2002 – 3/2003	d + Au	200 GeV/c	2.7nb^{-1}
	4/2003 – 6/2003	p + p	200 GeV/c	0.35pb^{-1}

Table 3.1: Collected data by the PHENIX experiment during the first three RHIC beam periods.

study asymmetric collisions. This happened during the third RHIC beam period, where d + Au collisions have been examined to study the effects of cold nuclear matter at $\sqrt{s_{NN}} = 200 \text{ GeV}$ (see Section 1.3.2). The choice of deuterons instead of protons was mainly motivated by technical reasons. The mass/charge ratio is similar to gold, this makes it possible to adopt many accelerator settings from Au + Au. An overview over the first three beam times of RHIC and the amount of data collected by PHENIX is given in Table 3.1.

3.2 Experiments at RHIC

The positions of the four experiments at RHIC are shown in Figure 3.1. Besides PHENIX there is a second, in terms of size and cost of construction, large experiment STAR², as well as the two smaller experiments BRAHMS³ and PHOBOS⁴.

3.2.1 STAR

The main component of the STAR detector [Ack03] is a large cylindrical Time Projection Chamber (TPC), with a diameter and length of 4 m. The TPC is installed inside a large solenoid magnet and covers the pseudo-rapidity region $|\eta| < 1$, allowing the simultaneous tracking of a couple of thousand charged particles in Au + Au collisions and their identification over a broad momentum range via their energy loss dE/dx . The tracking system is completed by a Silicon Vertex Detector (SVD) surrounding the beam pipe. The SVD improves the momentum resolution of the system and facilitates the reconstruction of secondary vertices of short-lived particles. Capability for photon and electron detection as well as energy measurement is added in a STAR upgrade by calorimeters surround-

²Solenoidal Tracker At RHIC

³Broad RAnge Hadron Magnetic Spectrometer

⁴PHOBOS is not an acronym.

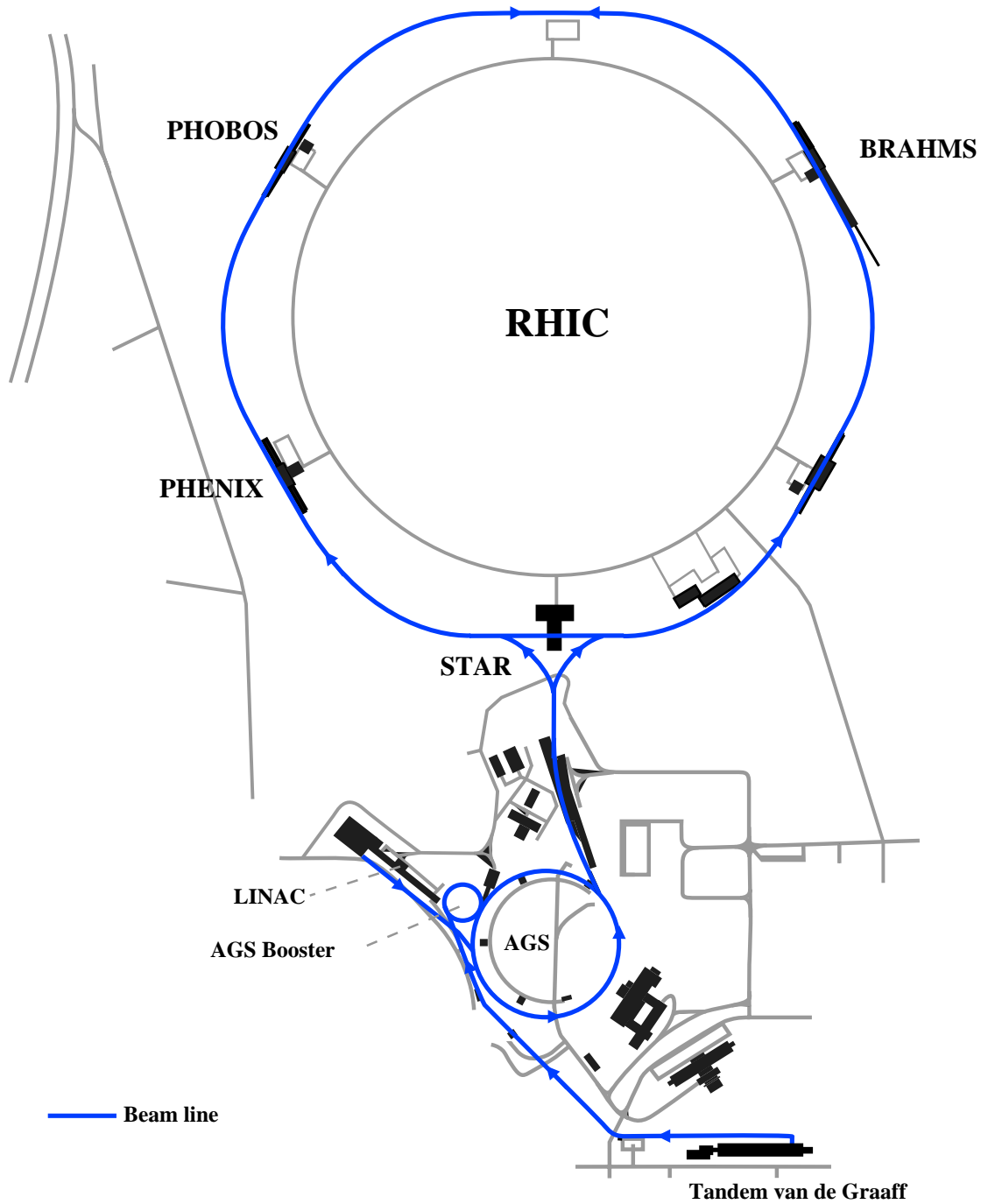


Figure 3.1: RHIC complex with its four experiments. The arrows indicate the direction of the ions through the different stages of acceleration.

ing the TPC: the Barrel Electromagnetic Calorimeter and the End-cap Electromagnetic Calorimeter.

3.2.2 PHOBOS

The PHOBOS detector [Bac03] employs different types of Silicon Pad Detectors, which allow the measurement of charged particle multiplicities with a pseudo-rapidity coverage of $|\eta| < 5.4$. Together with the spectrometry of charged particles near mid-rapidity ($0 \leq \eta \leq 2$) PHOBOS offers the possibility to study particle production in a broad kinematical region of the colliding nuclei.

3.2.3 BRAHMS

Like the PHOBOS experiment, BRAHMS [Ada03] covers a broad pseudo-rapidity range, though by means of two movable spectrometer arms. The spectrometers can be positioned at an angle ϑ with respect to the beam axis in the intervals $2.3^\circ \leq \vartheta \leq 90^\circ$ and $30^\circ \leq \vartheta \leq 95^\circ$, respectively.

3.3 PHENIX

In the following, a short survey of the PHENIX experiment [Adc03b] will be given. As the focus of this work is the search for direct photons and the measurement of neutral pions with the Electromagnetic Calorimeter (EMCal), this subsystem is treated separately and in more detail in Chapter 4.

The setup of the PHENIX experiment as shown in Figure 3.2 can be subdivided into the inner detectors close to the beam pipe and the four spectrometer arms, the east and west central arm at mid-rapidity, and the north and south muon arm at forward and backward rapidity, respectively.

3.3.1 Inner Detectors and the ZDC

The inner detectors are the *Beam-Beam Counters* (BBC) and the *Multiplicity Vertex Detector* (MVD) [All03]. The BBC comprises two detectors, each with an array of 64 Cherenkov counters, located 1.44 m north and south from the nominal collision vertex. The Cherenkov counters are arranged in rings around the beam pipe just outside the poles of the central magnet. The BBCs detect charged particles in the pseudo-rapidity region of $3.1 < |\eta| < 3.9$ and allow the determination of the primary vertex of the collision and the start time for the time-of-flight system. Furthermore, the BBC plays a major role within

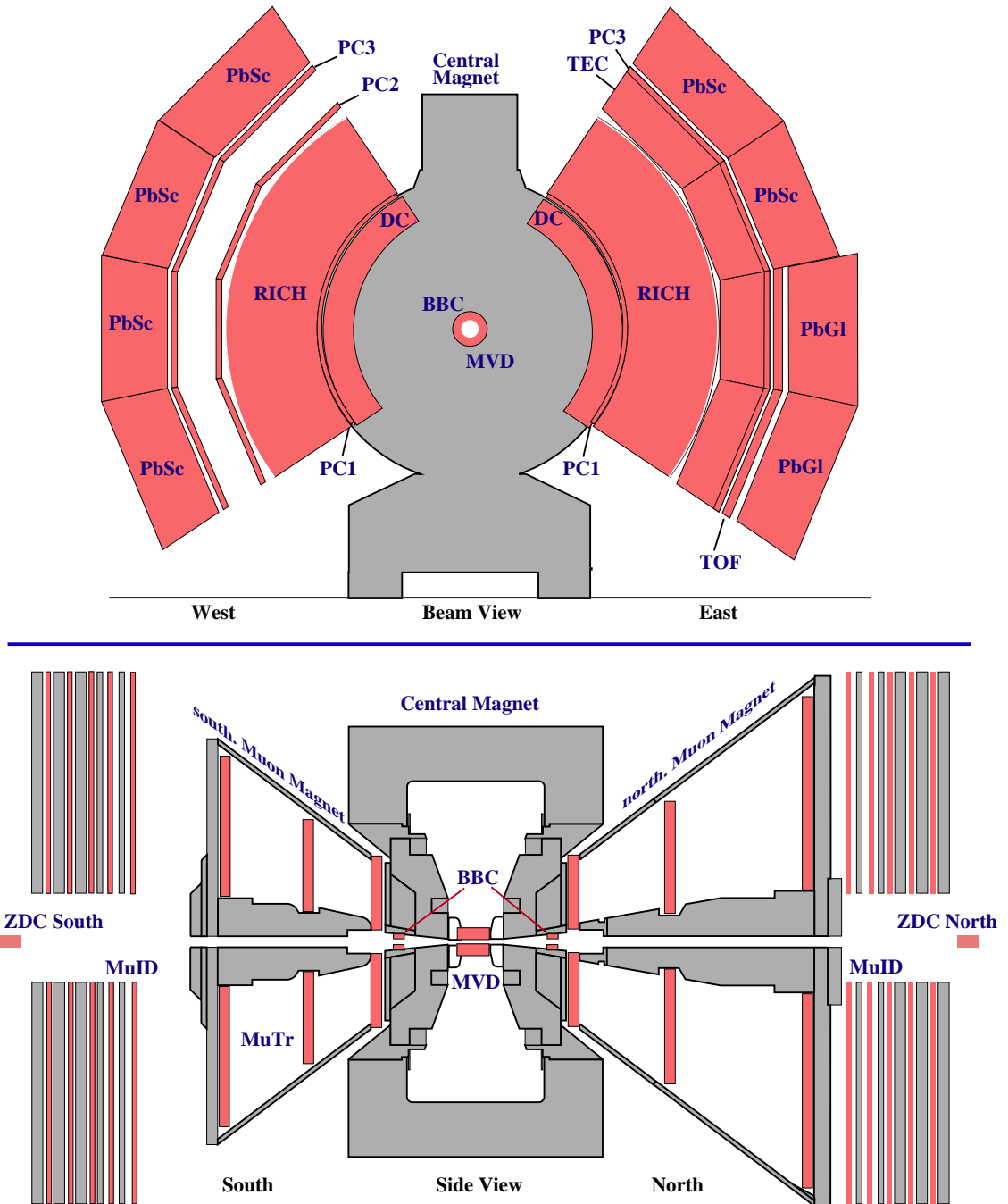


Figure 3.2: The PHENIX setup during the third RHIC beam period.

the *Level-1* triggering system (see Sec. 3.3.4), to decide whether an inelastic collision occurred and, in combination with the ZDC, for the centrality determination.

The MVD consists of two concentric barrels of Silicon Strip Detectors around the beam pipe and two disk shaped end caps of Silicon Pad Detectors. The detector provides event characterization via measurement of the charged particle multiplicity within $|\eta| < 2.64$ and an improved determination of the collision vertex.

Zero Degree Calorimeters (ZDCs) are positioned at each of the four RHIC experiments [Adl03a]. This allows a common event characterization for monitoring of the collider performance. For PHENIX the ZDCs serve as trigger detectors, for vertex and centrality determination. The ZDCs consist of two hadron calorimeters located at ± 18.25 m from the primary vertex between deflecting dipole magnets of the RHIC magnet system. For this reason mainly spectator neutrons with an angle $\vartheta < 2^\circ$ with respect to the beam axis are detected.

3.3.2 Detectors of the Central Arms

The detectors of the east and west arms of the PHENIX experiment are arranged concentric at different distances around the beam pipe and cover the pseudo-rapidity range of approximately $|\eta| \lesssim 0.35$ and 90° in azimuth each.

Additionally, a magnetic field in the interaction region is produced by the *Central Magnet* (CM) for momentum separation of charged particles [Aro03]. Its two concentric coils can be operated independently and provide, depending on the currents and the polarity, an axial magnetic field with $\int Bdl = 0.43\text{--}1.15$ Tm in radial direction. To prevent the influence of the magnetic field on the different detector components, e.g. the photomultiplier tubes of the EMCal and the *Ring Imaging Cherenkov Counters* (RICH), the exterior field integral over $r > 2$ m from the vertex is required to be minimal. This is achieved by an appropriate arrangement of the flux return yoke, leading to a residual field integral of less than $\int_{l=2.4\text{m}}^{l=4\text{m}} Bdl = 0.01$ Tm.

Tracking and Particle Identification

The *Drift Chamber* (DC) is located in each arm in the region $2\text{ m} < r < 2.4\text{ m}$. It measures the deflection of charged particles in the magnetic field of the CM with a resolution of about $150\ \mu\text{m}$ in the $r\text{--}\phi$ plane to determine the momentum of single particles and the invariant mass of particle pairs. The DC also provides position information for pattern recognition and tracking of charged particles through the various detectors of the central arms [Adc03a].

Multi-wire Proportional Chambers at different radii from the beam axis form the three layers of the *Pad Chambers* (PC), also called PC1, PC2, and PC3. The PC1 is located in

the east and west arm between the RICH and the DC. Similarly, the PC3 is installed in both arms close to the sectors of the EMCal. The PC2 is only positioned in the west arm behind the RICH (see also Figure 3.2).

The *Time Expansion Chamber* (TEC) is mounted only in the east arm between the RICH and PC3 and provides in addition to position information an energy loss measurement to separate electrons and charged pions with $250 \text{ MeV}/c \leq p \leq 2.5 \text{ GeV}/c$. A possible future upgrade for e/π separation at larger momenta is to operate the TEC as a Transition Radiation detector.

The *Time-Of-Flight Spectrometer* (TOF), with its timing resolution of about 100 ps, allows to distinguish between kaons and protons up to $p = 4 \text{ GeV}/c$ and pion/kaon separation up to $p = 2.4 \text{ GeV}/c$ [Aiz03]. As the TOF is only installed in front of the two sectors of the lead-glass calorimeter, it covers only a small angular range of $\Delta\phi \approx 45^\circ$. Therefore the identification of charged particles is supported by a time-of-flight measurement of the larger acceptance lead-scintillator calorimeter with a nominal timing resolution of approximately 270 ps [Aph03a].

The *Ring Imaging Cherenkov Detector* (RICH) plays a major role for electron identification. Located in both arms, it is composed of gas volumes of 40 m^3 . Charged particles with velocities larger than the speed of light within the gas medium emit Cherenkov radiation in a light cone that falls as ring on the RICH mirror system and is reflected onto photomultipliers. Due to different thresholds for electrons and pions to generate Cherenkov radiation, with CO_2 as radiator gas no pions are detected below $p = 4.65 \text{ GeV}/c$, the RICH provides good separation of the two particle species [Aiz03].

Electromagnetic Calorimeter

The outermost detector of the central arms, with a radial distance of more than 5 m, is the *Electromagnetic Calorimeter* (EMCal) [Aph03a]. It consists of six sectors of lead-scintillator sandwich calorimeter (PbSc) and two sectors of lead-glass Cherenkov calorimeter (PbGl), each sector covering 22.5° in azimuth. With their fine segmentation ($\delta\eta \times \delta\eta \approx 0.01 \times 0.01$) both calorimeters provide a good energy and position resolution for the detection of photons and electrons. The calorimeters are described thoroughly in Chapter 4.

3.3.3 Detectors of the Muon Arms

The investigation of dileptons and the J/ψ , at mid-rapidity by the detection of electrons, is completed by the measurement of muons at $1.2 < |\eta| < 2.4$ with the *Muon Tracker* (MuTr) and the *Muon Identifier* (MuID) in the north and south muon arms [Aki03].

The MuTr of each arm is composed of three so-called stations, tracking chambers with cathode-strip readout, mounted inside the conical shaped *Muon Magnets* with radial field (see Figure 3.2). The tracking of charged particles with a position resolution of approximately $100\ \mu\text{m}$ facilitates the reconstruction via the invariant mass of a muon pair with a resolution of $6\%/\sqrt{m_{\mu\mu}}$, and thus the separation of the heavy mesons J/ψ and ψ' , $\Upsilon(1S)$ and $\Upsilon(2S,3S)$, as well ρ/ω and ϕ .

The largest background in the measurement of muons is formed by mis-identified pions and by muons from pion decays. The suppression of this background is achieved by the absorption of hadrons in the dense material of the Central Magnet and by the identification of muons by range within the MuID. The MuID consists of a sequence of steel absorber plates and streamer tube detectors. The thickness of the plates is chosen such that only muons with an energy above 2.9 GeV penetrate the MuID completely. The material in front of the MuID, e.g. a 30 cm steel backplate of the Muon Magnet, ensures that only muons with an energy larger than 1.9 GeV reach the detector. The combination of MuID and different absorbers leads to a pion/muon separation of $2 \cdot 10^{-4}$ to $3.9 \cdot 10^{-3}$ in the momentum region $2\ \text{GeV}/c < p < 10\ \text{GeV}/c$ [Aki03].

3.3.4 PHENIX Data Acquisition

The investigation of different colliding species, ranging from polarized protons to gold, requires not only a versatile detector with specialized subsystems, but also a flexible data acquisition (DAQ) and a triggering system that can handle the high interaction rates of approximately 500 kHz in $p + p$ collisions and the large event sizes in high multiplicity $\text{Au} + \text{Au}$ events at a rate of a few kHz [Adl03d].

To cover the broad range of signatures of a possible QGP in heavy ion collisions and to explore the regime of hard scattering at large transverse momenta it is also necessary to select and enhance rare events via specialized triggers, e.g. on highly energetic photons.

The trigger decisions within the PHENIX experiment are implemented in two different layers, *Level-1* triggers (LVL1) and *Level-2* triggers (LVL2). The fully pipelined LVL1 triggers and the lower levels of the parallel readout are driven by the 9.43 MHz RHIC beam clock⁵, while the higher levels of the readout and the LVL2 triggers are data-driven, which means that the results are propagated to the next level only after the processing of a given event is completed. The PHENIX DAQ is shown schematically in Figure 3.3 and will be discussed briefly below, for more details see [Adl03d].

⁵The beam clocks provide a central time signal synchronized with the ion bunches in each of the RHIC rings (*Yellow Clock* and *Blue Clock*) and are delivered to each experiment. The time of 106 ns for each clock tick already accounts for the maximum of 120 bunches in each ring.

Front End Modules

The Front End Modules (FEMs) differ in detail for the various subsystems but their general layout is very similar. They consist of the Front End Electronics (FEE), which digitize the analog signals from the detector elements and buffer the data to wait for LVL1 trigger decisions. The FEMs also include a Heap Manager (HM), which controls the FEE, formats and communicates accepted data to the DCMs, and manages readout requests.

The different subsystems use two approaches to digitize and collect the data. In the first approach, used e.g. for the EMCal, the data are sampled and stored in analog form in switched capacitor arrays called Analog Memory Units (AMUs) and are digitized only after the receipt of the LVL1 accept. The second approach is to digitize the data directly and buffer it in Digital Memory Units (DMUs).

Data Collection Modules

After a LVL1 accept the data from the FEMs are transferred via optical fibers from the interaction region to the counting room, where the Data Collection Modules (DCMs) are located (see Figure 3.3). The uncompressed data from about 350 000 channels are formatted, zero suppressed⁶, and checked in parallel in the DCMs. The DCMs also provide buffering for up to five events for output to the Event Builder and are able to control the readout of the FEMs via the Granule Timing Module (GTM). The GTM passes the RHIC clock to the different detector combinations (*Granules*) and manages the *busy* and *accept* signals from the trigger.

Event Builder

The main purpose of the Event Builder (EvB) is the final stage of event assembly. It also provides the environment for the LVL2 trigger system (see below). The parallel data streams received from the DCM are transferred to a set of Sub-Event Buffers (SEBs). This modular structure allows easy scalability and maintains the possibility that different collections of detector data streams (*Granules*) can be read out independently. The data in the SEB are checked and transferred on request to the Assembly/Trigger Processor modules (ATPs), where the LVL2 trigger algorithms can decide whether an event is finally assembled from the different data streams and stored on disk for online monitoring and subsequent archiving in tape archives of the RHIC Computing Facility (RCF).

⁶The ADC values corresponding to no signal are removed from the data stream to allow better compression.

Level-1 Trigger

The task of the LVL1 is to select interesting events and to control the rate for the PHENIX DAQ. The Local Level-1 system (LL1) receives parallel input via fibers from different detector subsystems such as BBC, ZDC, MuID, RICH, and EMCal. This information is converted into a bit pattern for each RHIC beam crossing and gets summarized by the *Global Level-1 System* (GL1). The GL1 generates a *raw* trigger from the input trigger vectors and checks whether a trigger system or the DAQ is busy, if the raw trigger passes this test it is called a *live* trigger. This bit pattern is compared to a scaledown counter and only if this *scaled* trigger generates an accept, the GL1 initiates the readout of the FEMs via the GTM.

The trigger for an inelastic collision, the minimum bias condition, is usually given by the BBC. Other LVL1 trigger decisions facilitate the search for rare events, e.g. events containing a highly energetic photon, electron, or muon. The role of the EMCal within the LVL1 trigger is discussed in Section 4.5.1.

Level-2 Trigger

The PHENIX DAQ is capable of handling Au + Au collisions with a rate of approximately 1400 Hz, this corresponds to a data rate of 224 Mbyte/s [Adl03d]. However, archiving the data on disk in the early PHENIX runs was only possible at a rate of about 35 Mbyte/s. The necessary reduction of the data volume was achieved by the Level-2 triggers.

The Level-2 system is located in the ATPs (see above) and consists of a set of different algorithms, which analyze, depending on the Level-1 trigger decision, different detector information and release an event for archiving if a certain trigger condition is satisfied. Unlike the hardware triggers of the LVL1, the software triggers of the LVL2 support more complicated operations, e.g. the reconstruction of particle tracks, and thus provide a more precise selection of interesting events. The Level-2 trigger for the EMCal is described in Section 4.5.2.

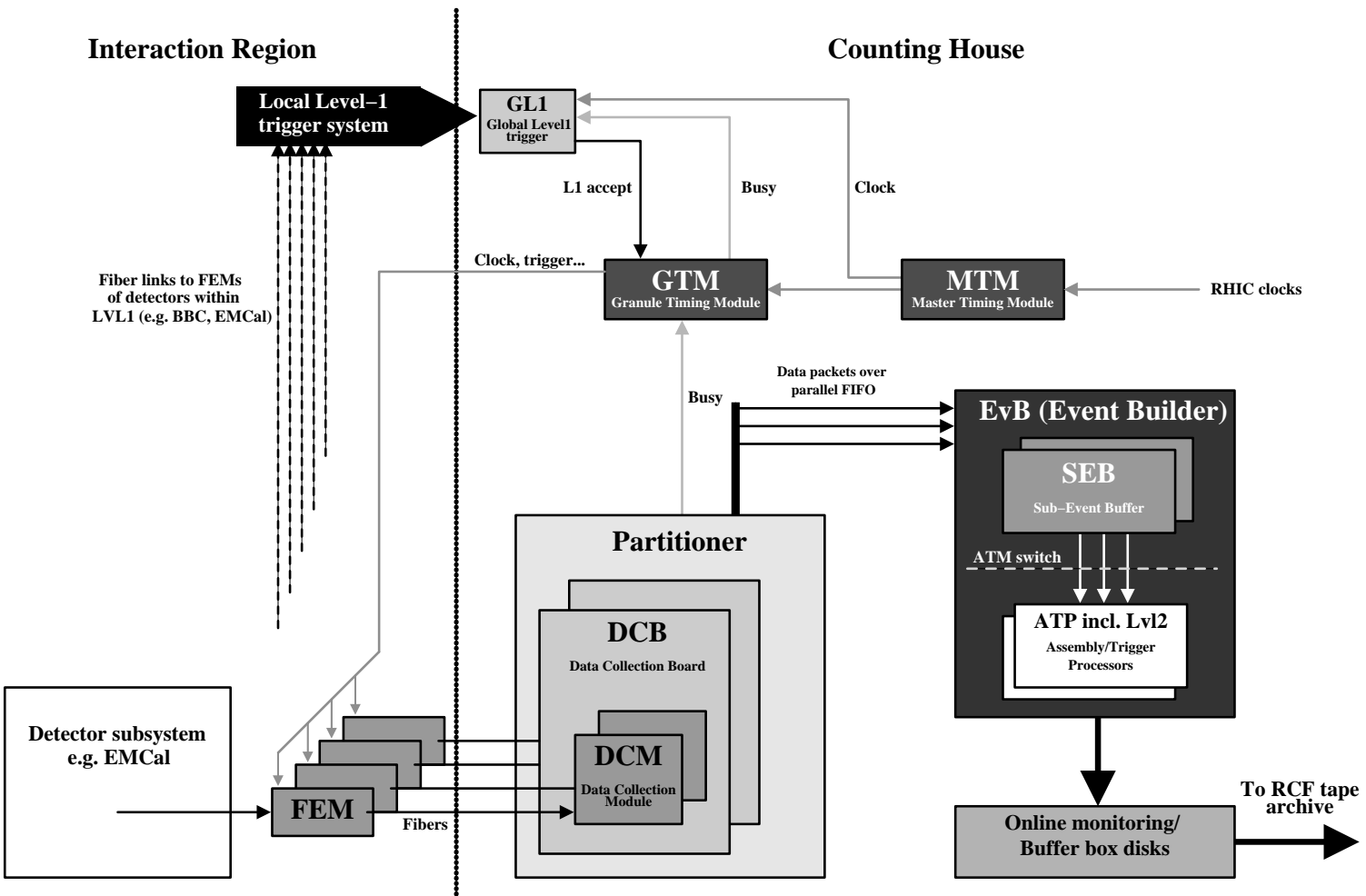


Figure 3.3: Sketch of the PHENIX online system without voltage control, alarm systems, and serial interface to FEMs.

4. The Electromagnetic Calorimeter

The Electromagnetic Calorimeter (EMCal) [Aph03a] is the major detector subsystem used for the analyses presented in this work. While only three EMCAL sectors were operational during the first year of PHENIX operation, the PHENIX setup since the second RHIC run comprises eight fully equipped sectors each covering $\Delta\phi = 22.5^\circ$ in azimuth (see Figure 3.2).

The two different detector types, six sectors of lead-scintillator sandwich calorimeter (PbSc) and two sectors of lead-glass Cherenkov calorimeter (PbGl), with their different systematics provide a good possibility for internal cross-checks of each EMCAL measurement. The main purpose of the EMCAL is the measurement of electrons and photons and thereby, in addition, the reconstruction of neutral mesons via an invariant mass analysis of particle pairs. The EMCAL can also be used for determination of the total transverse energy E_T , which is a measure for the energy density in a heavy ion collision [Adc01b, Ste02], and for particle identification. Particle identification is made possible by the excellent timing resolution for hadrons in the PbSc that complements the measurement by the TOF detector with its smaller acceptance. The EMCAL also offers the unique opportunity to identify antineutrons within PHENIX by measuring their annihilation energy deposited in the calorimeter [Pin04].

4.1 Lead-Glass Calorimeter

The lead-glass calorimeter was previously used in the WA98 experiment at CERN, where direct photons were measured successfully for the first time in heavy ion collisions [Buc99, Agg00]. After the disassembly of the WA98 experiment 9216 elements of the former LEDA¹ calorimeter were transported to BNL and reassembled in two sectors of the EMCAL. The two PbGl sectors reside in the east arm of the PHENIX experiment behind the TOF wall at a radial distance of 5.4 m from the nominal beam axis.

4.1.1 Mode of Operation

Electromagnetic Showers

Highly energetic photons incident on the PbGl interact mainly via electron-positron pair production. Other processes such as photoelectric effect and Compton scattering play only

¹LEad-Glass Detection Array

a minor role in this energy regime. The produced electrons and positrons subsequently lose their energy in the electric field of the atomic nuclei by radiating Bremsstrahlung. These photons can again produce e^+e^- pairs, resulting in the formation of an electromagnetic shower. The distance where the energy of an electron decreases by a factor of e is called the radiation length X_0 and also determines the probability for a photon to convert into an e^+e^- pair within the range X :

$$p_{\text{conv}} = 1 - e^{-7/9 \cdot X/X_0}. \quad (4.1)$$

The further propagation of the shower is stopped when the energy of the individual particles falls below the critical energy E_c , where the energy loss via ionization begins to dominate over the energy loss by Bremsstrahlung.

Except for the first step, electrons and positrons form an electromagnetic shower in the same way as photons do. The depth of the shower maximum depends on the initial energy E_0 of the incoming particle and can be expressed in units of the radiation length [Eid04]:

$$\frac{X_{\text{max}}}{X_0} \approx \ln\left(\frac{E_0}{E_c}\right) + t \quad (4.2)$$

($t = 0.5$ for photons, $t = -0.5$ for electrons).

The lateral extension of an electromagnetic shower is determined by multiple scattering of the shower particles. It is characterized by the Molière radius:

$$R_M \approx \frac{21 \text{ MeV} \cdot X_0}{E_c}. \quad (4.3)$$

Hadronic Showers

Strongly interacting particles, such as pions and protons, form a so-called hadronic shower. Its characteristic quantity is the nuclear interaction length λ , the distance where 63% of the hadrons suffer an inelastic interaction and form further hadrons, mostly pions. Charged hadrons that do not participate in an inelastic reaction and deposit only a small fraction of their energy by ionization and possibly Cherenkov radiation are called *Minimum Ionizing Particles* (MIPs). Their energy loss is given by the Bethe-Bloch equation (see e.g. [Eid04]). It is constant over a wide energy range leading to the formation of the characteristic MIP peak.

Cherenkov Radiation

Charged particles with a velocity v larger than the speed of light within a medium $v > c/n$, where n is the index of refraction of the medium, emit light. This phenomenon is known

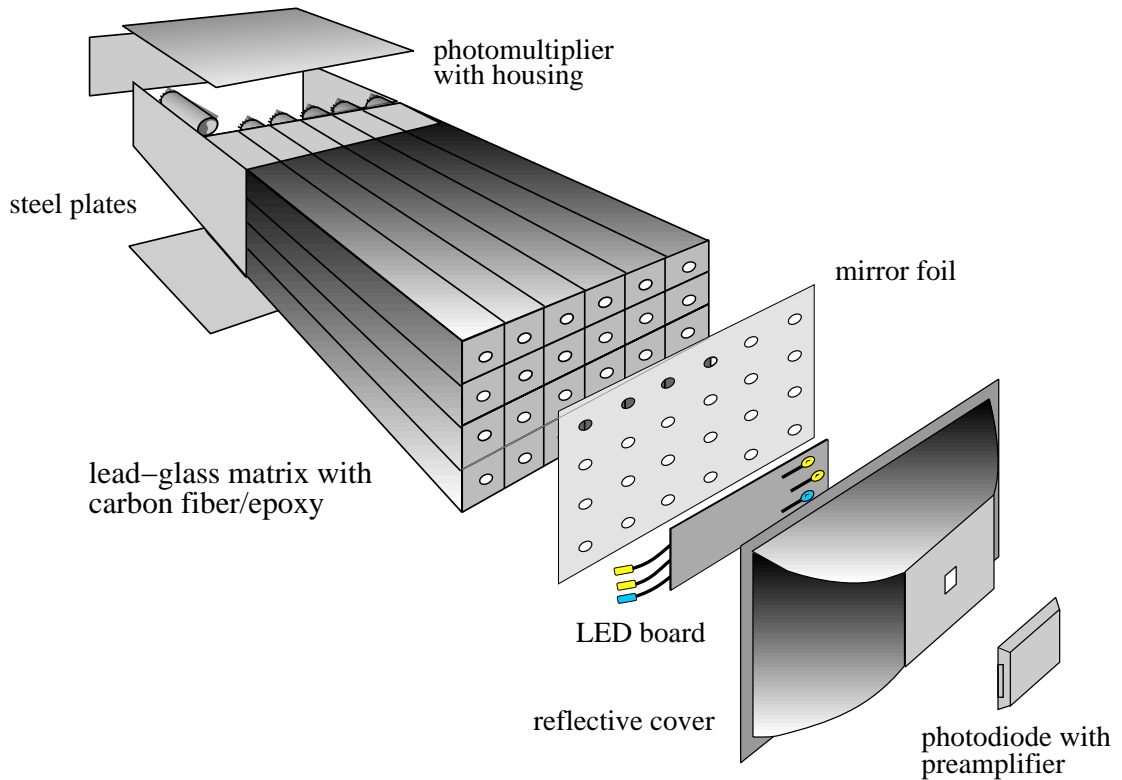


Figure 4.1: Exploded view of a lead-glass supermodule including the reference system.

as Cherenkov radiation. The light is emitted with an angle to the incident direction of the particle given by:

$$\cos \theta_{\text{Ch}} = \frac{c}{vn}. \quad (4.4)$$

Thus the measurement of the angle of the Cherenkov cone allows the determination of the velocity of a particle.

Though Cherenkov radiation is a negligible source of energy loss, it is very useful for particle detection and energy measurements because the number of produced Cherenkov photons per unit length is constant, and the total length of all positron and electron tracks of a shower is connected linearly to the energy of the primary particle [Kle92]. This linearity is no longer preserved when the Cherenkov photons reach the photomultiplier, mainly due to absorption of light and due to the fact that the shower may not deposit its complete energy within the detector (*leakage*). Both effects depend on the shower depth and have to be compensated by a linearity correction in the analysis (see Section 5.2.1).

Index of refraction	\bar{n}	1.648
Radiation length	X_0	2.8 cm
Molière radius	R_M	3.68 cm
Interaction length	λ	38 cm
Critical energy	E_c	16 MeV

Table 4.1: Physical parameters of the lead-glass TF1 [Aph03a].

4.1.2 PbGl Setup

Each lead-glass sector consists of 192 so-called supermodules, each forming a self-contained detector with its own reference system (see Figure 4.1), which allowed the easy reassembly of the detector in a different geometry and without a completely new calibration. One supermodule is formed by an array of 6×4 lead-glass modules, each with a size of $4 \times 4 \times 40 \text{ cm}^3$ and wrapped in reflecting mylar foil and shrink tube. The modules are glued together with carbon fiber and epoxy resin to form the self-supporting supermodule. The properties of the employed lead-glass type TF1 are summarized in Table 4.1.

Each lead-glass module is read out via a *FEU-84* photomultiplier, which is controlled individually by a custom VME based control system (*HIVOC*) [Neu95].

The reference system consists of three LEDs, chosen to emulate different aspects of the spectral and temporal behavior of a highly energetic photon that showers in the detector. The Avalanche Yellow LED (AY) generates a short signal of about 50 ns with a pulse shape similar to the Cherenkov light of an electromagnetic shower and with a fixed intensity. It is used to monitor the gain variations during datataking and for timing calibration. The Variable Yellow LED (VY) is served by a pulser that allows variation of the intensity. It is used to sample the dynamic range of the ADC and the transition between different amplification regions (see below). The third LED, emitting blue light with wavelength similar to the Cherenkov light, is intended to monitor the light attenuation of the lead-glass. To compensate for variations of the light output the LEDs are monitored by a photodiode. For a more detailed description of the lead-glass and the reference system see [Sch94a, Sch94b, Pei96].

The modular setup including the reference system allowed a simple reassembly of the lead-glass calorimeter for the PHENIX EMCal. The energy calibration from the WA98 experiment has been mostly transferred for use within PHENIX (see [Büs02]). Additionally, the response of the PbGl to electrons with energies up to 80 GeV was measured in a beam test at CERN [Mex99, Awe02]. The different readout electronics for the PHENIX experiment made a different logical grouping of the supermodules necessary. In PHENIX

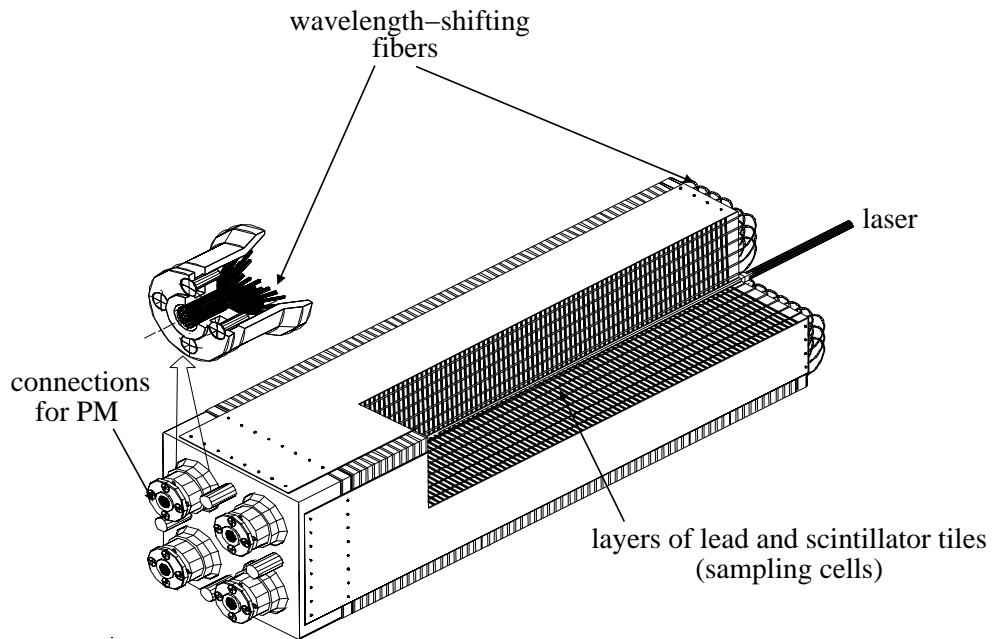


Figure 4.2: Interior view of one PbSc module, consisting of four towers.

144 channels, a matrix of 2×4 supermodules, are read out by one FEM (see Section 4.3) and are called one *SM144*.

4.2 Lead-Scintillator Calorimeter

The lead-scintillator calorimeter is formed by four sectors in the west arm and two sectors in the east arm of the PHENIX experiment positioned directly behind the PC3 at a radial distance of 5.10 m (see Figure 3.2). The PbSc allows to determine the energy deposit of a particle by collecting scintillation light produced at various depths of the detector.

A PbSc module consists of four towers, each with 66 cells of 0.15 cm lead absorber and 0.4 cm scintillator and a size of $5.535 \times 5.535 \times 37.5 \text{ cm}^3$ (see Figure 4.2).²

The cells are optically connected via wavelength-shifting fibers for light collection by a photomultiplier. Some physical parameters of this sandwich structure are summarized in Table 4.2. Though the hadronic interaction length is larger compared to the PbG1, the PbSc provides a better energy measurement for hadrons, as it also measures low energy shower particles via scintillation that would not emit Cherenkov light. This is advantageous for the determination of the total transverse energy E_T , but it means a larger background contribution from hadrons when measuring photons.

²The smallest unit within the PbG1 is called a module, while one PbSc module consists of four towers. In the following chapters *module* and *tower* are used always as synonym for the smallest unit in the PbSc as well as in the PbG1 to avoid confusion.

Active sampling cells		66
Scintillator		0.4 cm Polystyrene (1.5% PT/0.01% POPOP)
Absorber		0.15 cm Pb
Radiation length	X_0	2.02 cm
Interaction length	λ	44.2 cm
Cell size		0.56 cm (0.277 X_0)
Active depth		37.5 cm (18 X_0)

Table 4.2: Physical parameters of the lead-scintillator sandwich calorimeter [Aph03a].

Groups of 6×6 modules are connected mechanically to a self-supporting supermodule, with 3×6 PbSc supermodules forming one sector. In the case of the PbSc one mechanical supermodule contains 144 towers and is read out by one FEM. It corresponds to the logical SM144, already introduced for the PbGl.

The initial calibration of the PbSc has been established with cosmic muons as well as with electron beams, where the behavior of highly energetic electromagnetic showers was studied [Dav98]. During operation the calibration is monitored by an UV laser. The laser light is transported to each PbSc module by a series of optical splitters and fibers and is injected by a plastic fiber that penetrates the center of the module. This fiber is grated such that the exiting light emulates the depth profile and energy deposit of a 1-GeV electromagnetic shower.

4.3 EMCal Frontend Modules

The EMCal data contain timing and pulse height signals from the photomultiplier tubes. Analog processing of this data is done on a custom built ASIC chip³ that serves 2×2 photomultiplier channels. Within this ASIC a specially developed discriminator provides, together with the beam clock, the Time to Amplitude Conversion (TAC) used for the measurement of the arrival time of a particle at the detector. The integrated pulse height signal or energy signal is put through a Variable Gain Amplifier (VGA). As the resolution of the employed 12-bit Analog to Digital Converter (ADC) is not sufficient to obtain a good signal resolution at lower energies and to facilitate energy measurements up to 20 GeV at the same time, the VGA signal is split into a *Low Gain* (LG) signal, which is converted directly from the VGA, and a *High Gain* signal (HG), which is converted after additional amplification by a factor of 16. Each ASIC chip also calculates the analog trigger sum of

³Application Specific Integrated Circuit

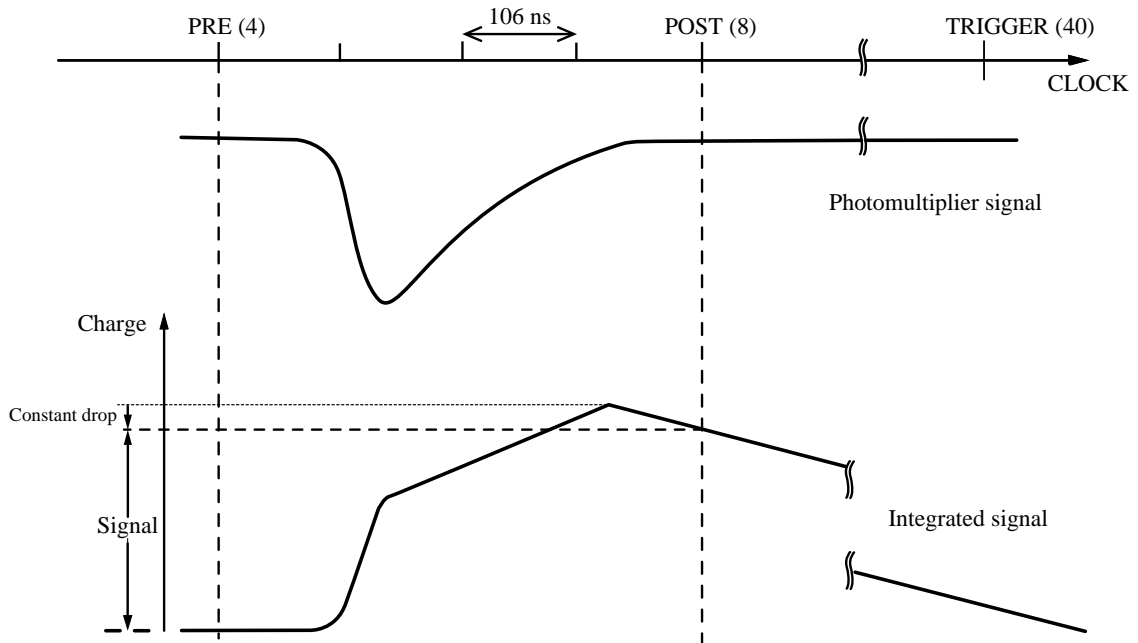


Figure 4.3: Illustration of the AMU sampling.

its 2×2 photomultipliers and a 4×4 sum with the input from three neighboring ASICs as needed for the LVL1 trigger (see Section 4.5.1).

The TAC, HG, and LG signals from the ASICs are sampled and stored in Analog Memory Units (AMUs) to allow for the latency of the LVL1 decision as described in Section 3.3.4. One AMU consists of 64 capacitors or AMU *cells* and samples the input signal at the rate given by the RHIC beam clock, thus preserving the signal for 64 clock ticks or about $7 \mu\text{s}$, enough to cover the LVL1 trigger latency of 40 clock ticks.

After the LVL1 accept, the appropriate AMU cells are read out and converted in the ADC. To compensate for constant offset voltages two AMU cells are read out: one corresponding to a time before the energy signal starts (*pre* cell) and one shortly after the integrated signal reaches its maximum (*post* cell), as illustrated in Figure 4.3. The height of the signal can then be determined by subtraction of the ADC values for pre and post cell as discussed in Section 4.4.

Six pre-amp ASIC chips together with four AMU/ADCs form one ASIC card that serves 2×12 photomultipliers. One EMCal FEM consists of six ASIC cards together with the Heap Manager, a Data Formatter, which sends the data via fibers to the DCMs, and a Trigger Board, which summarizes the trigger sums and communicates them to the LVL1 system. Each FEM serves 144 channels corresponding to one SM144.

4.4 Processing of the EMCAL signals

The EMCAL data from the FEMs are passed upon the receipt of the accept signal from the GL1 to the DCMs by optical fibers as described in Section 3.3.4, where they are checked, reformatted, and zero suppressed. The data are assembled in the EvB to events in the PHENIX Raw Data Format (PRDF) and can be converted and corrected offline into actual physical information, such as time-of-flight and energy in case of the EMCAL.

4.4.1 Zero Suppression in the DCMs

While 192 channels are sent from each FEM only 144 are data channels, the remaining channels are sometimes used for voltage reference and monitoring. They may be dropped in the DCMs. An additional possibility to reduce the data volume is to drop the channels that contain values corresponding to energy values on the level of the *pedestal* noise.

When subtracting the values of the pre and post cells to obtain the energy signal of the photomultiplier, a constant offset from zero can remain, even when no real input signal from the photomultiplier is present. These offsets are called pedestals and fluctuate around a mean value for a given channel depending on the cell number of the AMU. The pedestals have to be subtracted before converting the difference signal to energy information (see below). The DCMs allow the suppression of channels for which the HG difference between the pre and the post cell value does not pass a certain threshold (zero suppression). The thresholds are determined in so-called pedestal runs without any physical input to the photomultipliers, by determining the pedestals and the fluctuations for each channel.

The very broad double peak structures in the single PbGl pedestal distribution as shown in Figure 4.4(a) lead to larger values for the root-mean-square deviation (RMS) compared to the PbSc (Figure 4.4(c)). The reason for this behavior is attributed to the photomultiplier bases, as the three production models used in the PbGl calorimeter correspond to three regions of the width distribution in Figure 4.4(b). The large RMS values make it necessary to limit the thresholds for the PbGl, in order not to exceed the energy threshold of the cluster routine (see Section 5.2.1). For the PbSc it is sufficient to calculate the thresholds for each ASIC card individually as the RMS are very similar within one ASIC card and quite small. The DCM thresholds for the zero suppression of data channels are finally given by:

$$(HG_{\text{post}} - HG_{\text{pre}})_{\text{min}} = \begin{cases} \min(\text{mean}_{\text{ch}} + 2.5 \cdot \text{RMS}_{\text{ch}}, 300) & \text{for PbGl,} \\ \text{mean}_{\text{ASIC}} + 10 & \text{for PbSc.} \end{cases} \quad (4.5)$$

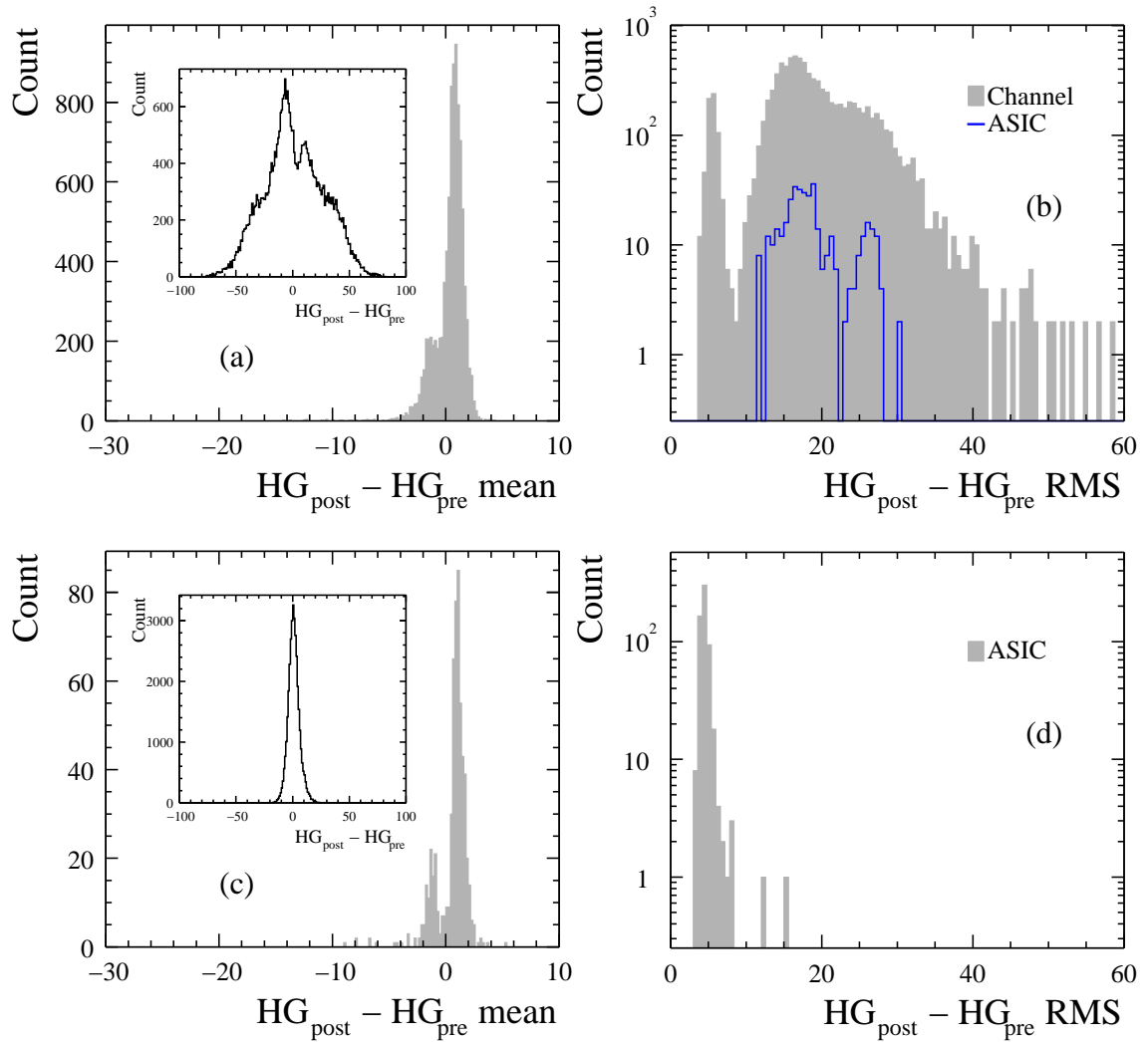


Figure 4.4: The mean pedestal values for (a) PbGl on a channel-by-channel basis and (c) PbSc on ASIC basis (2×12 channels). The inserted pictures show a typical distribution in a single channel. The right plots show the RMS of the pedestals in (b) the PbGl for single channels and ASIC cards, and (d) in the PbSc only for ASIC cards.

4.4.2 Calibrated Modules

The offline conversion of the EMCal raw data format from the EvB into energy for each module takes several steps and shall be described briefly. More details can be found in [Büs02].

As mentioned above the actual difference between the values of the read out pre and post cell of an AMU shows a constant offset from zero. This offset can be different if a cell is read out as pre or post, so it has to be determined twice for each of the 64 cells before it can be subtracted:

$$\begin{aligned} HG_{\text{corr}} &= (HG_{\text{post}} - HG_{\text{pre}}) - (PED_{\text{post}}^{HG} - PED_{\text{pre}}^{HG}), \\ LG_{\text{corr}} &= (LG_{\text{post}} - LG_{\text{pre}}) - (PED_{\text{post}}^{LG} - PED_{\text{pre}}^{LG}). \end{aligned} \quad (4.6)$$

Additionally, the transition between the two amplification regions has to be carried out. The transition factors V_i are close to the nominal amplification of 16 and are determined for each module by comparing the two regions in special calibration runs that sample the dynamic range of both high and low gain ADC, as described in [Büs02]. The switch-over from high to low gain is done at a value of 128 low gain ADC channels for PbGl and PbSc:

$$ADC_i = \begin{cases} HG_{\text{corr}_i} & \text{for } LG_{\text{corr}_i} < 128 \text{ ADC channels,} \\ LG_{\text{corr}_i} \cdot V_i & \text{for } LG_{\text{corr}_i} \geq 128 \text{ ADC channels.} \end{cases} \quad (4.7)$$

The final energy calibration of each module is given by a set of different factors that have to be applied to the calculated ADC value:

$$E = ADC \cdot C_0 \cdot C_T(t) \cdot \kappa \cdot \lambda. \quad (4.8)$$

In this simplified equation C_0 describes the calibration and the reference system at initial time t_0 , $C_T(t)$ compensates for time dependent changes of the calibration compared to t_0 observed with the reference system, κ compensates, in the case of the PbGl, for the changes in the reference system due to different readout electronics in PHENIX compared to WA98, and λ summarizes additional corrections to the overall calibration for which the reference system could not account.

For the PbGl calorimeter the calibration factors are given as:

$$C_0 = \frac{PM_{AY}}{PIN_{AY}} \Big|_{\text{calibration}} \cdot \frac{PIN_{AY}}{PM_{AY}} \Big|_{t=t_0-t_{\text{PHENIX}}} \cdot F_{\text{WA98}}, \quad (4.9)$$

$$C_T(t) = \frac{PM_{AY}}{PIN_{AY}} \Big|_{t=t_0-t_{\text{PHENIX}}} \cdot \frac{PIN_{AY}}{PM_{AY}} \Big|_t. \quad (4.10)$$

At a given time, the response of a photomultiplier to the signal from the Avalanche Yellow LED is given by PM_{AY} , while PIN_{AY} is the response of the photodiode, located in the hut of each supermodule. This scheme allows to track differences in the photomultiplier gains compared to the time of initial calibration, even when the light output of the LED has changed. The factor F_{WA98} summarizes all other correction factors from the WA98 final calibration, which have been transferred to PHENIX at time $t = t_{PHENIX}$ (see also [Büs02]). In principle all these correction factors can be combined into a single conversion factor $F_{ADC \Rightarrow E}$ that expresses the energy equivalent of one ADC channel at a given time:

$$E = ADC \cdot F_{ADC \Rightarrow E}(t). \quad (4.11)$$

4.5 EMCal Photon Triggers

4.5.1 EMCal-RICH Level-1 Trigger

The EMCal-RICH Trigger (ERT) is a part of the Level-1 system since the beginning of the third RHIC beam time. The combination of calorimetry and electron identification facilitates the search for lepton pairs and the J/ψ . For this analysis only the trigger for highly energetic photons is relevant.

The EMCal provides the trigger information to the ERT by special hardware, the Trigger Board, which summarizes the information from the 144 channels connected to one FEM. The information is summarized as the logical OR of thresholds placed on each of the individual analog sums of 2×2 and 4×4 photomultiplier signals at interaction time. The trigger sums are provided by the ASICs as described above and are passed to three neighboring ASICs as shown in Figure 4.5, allowing the sum over 4×4 channels to cover overlapping areas, even across different FEMs.

Since the ERT works with the analog sums of the single EMCal channels, differences in the photomultiplier gains become important because they cannot be compensated by different calibration factors. To ensure a good response of the trigger, equivalent to a quick rise of the trigger efficiency at the predefined threshold to hundred percent, it is important that the photomultiplier gains are similar. This is achieved by the *gain balancing* described below.

The different settings for the nominal trigger threshold of the EMCal LVL1 trigger during the d + Au run are summarized in Table 4.3. During datataking only the ERT_4×4a (ERT_Gamma1) and the ERT_4×4b (ERT_Gamma2) in coincidence with the minimum bias condition of the BBC (BBCLL1) have been run with a sufficiently small prescale factor to gather a considerable amount of data. The prescale factor or *prescale* is used to regulate the fraction of each trigger decision that is passed to the DAQ (see Section 3.3.4).

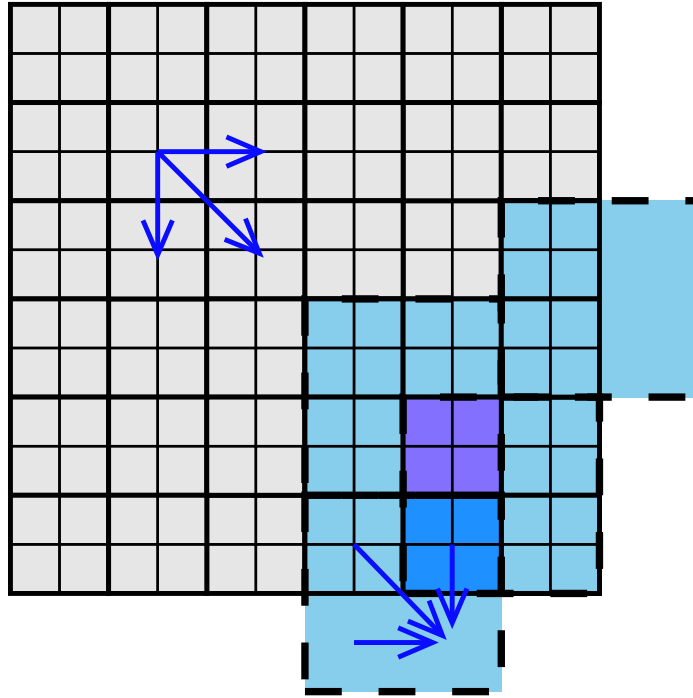


Figure 4.5: Sketch of the 36 2×2 tiles and four of the 36 plus 11 overlapping 4×4 tiles used for the analog trigger sums within one SM144. The arrows indicate the directions in which the ASICs pass their individual trigger sums to their neighbors.

ERT_2 \times 2	$E_{2 \times 2} > 0.8 \text{ GeV}$
ERT_4 \times 4a	$E_{4 \times 4} > 2.1 \text{ GeV}$
ERT_4 \times 4b	$E_{4 \times 4} > 2.8 \text{ GeV}$
ERT_4 \times 4c	$E_{4 \times 4} > 1.4 \text{ GeV}$

Table 4.3: The different types of EMCal Level-1 triggers during the d + Au run.

For the analysis only the trigger condition ERT_Gamma1&&BBCLL1 is used to extend the photon and π^0 spectra to larger p_T . It shall be denoted simply as *Gamma1* in the following.

Gain Balancing

One possibility to adjust the photomultiplier gains is by changing the high voltage on the photomultiplier bases directly. This can only be done on a module-by-module basis in the case of the PbGl, as the high voltage for each photomultiplier is created directly on the base by Cockcroft Walton Generators, which are controlled individually [Neu95].

In the PbSc 48 photomultipliers share the same high voltage supply and variations in the gain can only be compensated by changing the amplification of the VGA for each photomultiplier in the range from $\times 4$ to $\times 12$ with a 5-bit resolution.

As described in Section 4.4.2 the total calibration factor used to compute the energy equivalent of one ADC channel includes a factor to account for variations in the gain. So with an updated $\left. \frac{PIN_{AY}}{PM_{AY}} \right|_t$ ratio in Equation (4.10) the gain balancing does not affect the overall calibration. Only the energy equivalent per ADC channel $F_{ADC \Rightarrow E}$ changes.

Within each photomultiplier tube there are several dynodes which are responsible for the multiplication process of the photoelectrons from the cathode. The increase in the number of electrons is proportional to the potential difference between two dynodes. Thus the amplification A is expected to obey a power law within the operating region of the photomultipliers from voltages U of approximately 1300 V to 2000 V:

$$\frac{A_1}{A_2} = \left(\frac{U_1}{U_2} \right)^\gamma. \quad (4.12)$$

If the voltage is evenly divided among the dynodes, γ should roughly correspond to the number of dynodes.

For the PbGl γ has been determined by comparing the response of each photomultiplier to the signal from the Avalanche Yellow LED for different high voltage settings. The values for γ as shown in Figure 4.6 have been determined by decreasing the default voltages by 100 V.⁴

For known γ and given start voltage the amplification of each photomultiplier can be optimized toward a common value by altering the voltage as given by Equation (4.13), where $F_{ADC \Rightarrow E}$ is the energy equivalent per ADC channel, which is anti-proportional to the gain A .

$$U_{i+1} = \left(\frac{F_{iADC \Rightarrow E}}{F_{\text{wanted}ADC \Rightarrow E}} \right)^{\gamma^{-1}} \cdot U_i \quad (4.13)$$

The initial conversion factors for each module are shown as the zeroth iteration in Figure 4.7. Since the mean of the distribution is close to 0.4 MeV/(ADC channel), this value is a natural choice for the desired value $F_{\text{wanted}ADC \Rightarrow E}$. During the iterative optimization process one has to take care that the newly calculated voltage does lie in the operating region of the photomultipliers. In some cases the gains could not be adjusted due to this natural limitation of the voltage range. Nevertheless already after two iterations the overall gains were identical within few percent as shown in Figure 4.7.

⁴The deviation of γ from 12 (the number of dynodes within the PMT FEU-84) can be explained by the fact that the potential differences between the dynodes are not the same (they are divided roughly 3 : 2 : 2 : 2 : 2 : 2 : 2 : 3 : 4 : 5 [Neu95]) and by the non-linear dependence of the electron yield at each dynode on the potential difference.

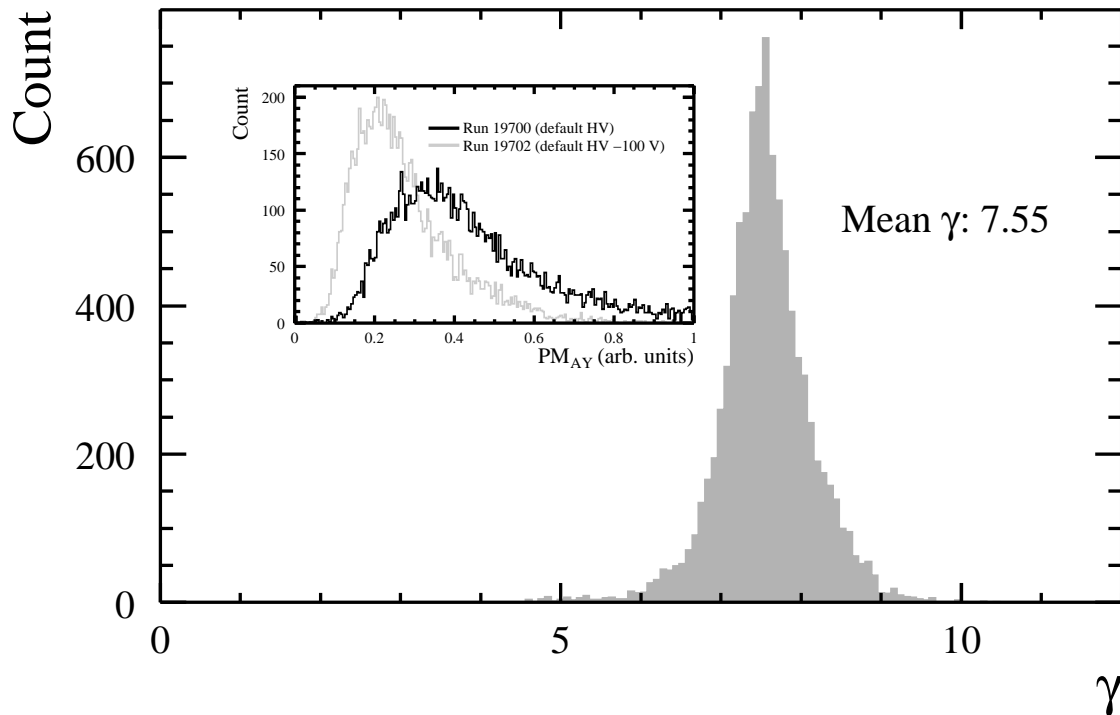


Figure 4.6: The power γ obtained by comparing the individual photomultiplier response to the AY LED for two different voltages (inlaid picture).

4.5.2 Level-2 Trigger for the EMCal

The Level-2 trigger is part of the PHENIX data acquisition (see also Section 3.3.4 and [Adl03d]) and acts on the results of the fast electronic triggers of the Level-1. During the last part of the second beam time all data accepted by Level-1 were passed to the Level-2 system, partially reconstructed, and analyzed. A fraction of the data were kept as a minimum bias sample (so-called *forced accepts*), from the remaining data only the part satisfying one of the Level-2 trigger conditions was kept.

The Level-2 triggers used for the EMCal are basically triggers on highly energetic electromagnetic particles with different boundary conditions (see Table 4.4). They convert the raw data of each EMCal module into the calibrated energy information. The conversion factors have been determined once from the EMCal calibration at the beginning of datataking with Level-2 and remained constant until the end of the second run. Similar to the EMCal LVL1 trigger the energy in 4×4 modules, a *tile*, is summed under consideration of a list of bad modules. The tiles can overlap within one sector and thus provide already a basic kind of energy clustering. The trigger condition is satisfied if one of the tiles shows an energy sum greater than a predefined threshold and the event remains in the data stream, if it is not suppressed by a prescale for this trigger.

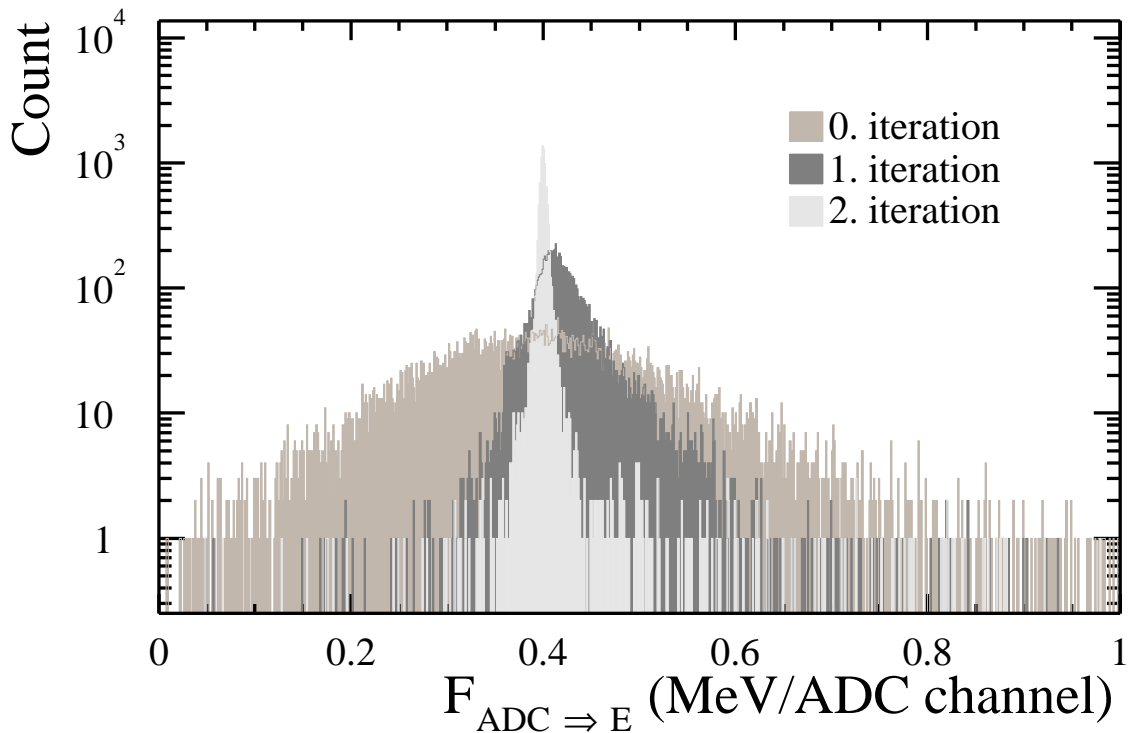


Figure 4.7: The distribution of total calibration factors within the PbGl for different iterations of the gain balancing.

L2EMCHighPtTileTrigger	$E_{\text{Tile}} > 3.5 \text{ GeV}$
L2EMCHighPtTilePeriphTrigger	$E_{\text{Tile}} > 1.5 \text{ GeV}$ and centrality $> 52\%$
L2EMCHighPtTileTriggerRecut	$E_{\text{Tile}} > 2.5 \text{ GeV}$

Table 4.4: The three different EMCal Level-2 trigger.

In general, the LVL2 triggers allow more accurate trigger decisions compared to similar LVL1 triggers. For the EMCal this is due to the possibility to perform a better energy determination via the actual correction factors, compared to the analog trigger sum of the LVL1. The faster LVL1 triggers are better suited for collisions with a large event rate such as $p + p$ or $d + \text{Au}$, compared to $\text{Au} + \text{Au}$ collisions, where the data volume of each event is the limiting factor for data acquisition.

The three types of LVL2 *EMCHighPtTile* triggers, with their different thresholds used during the second RHIC run, are summarized in Table 4.4. In the following we will always refer to the L2EMCHighPtTileTrigger as the Level-2 EMCal trigger. It was the only LVL2

EMCal trigger used in the analysis because it showed the largest suppression due to the high threshold and was operated with the smallest prescale.

5. Data Analysis

After the description of the detector setup in Chapters 3.3 and 4, we now discuss in detail the necessary steps toward the actual analysis. This includes the selection of events and their division into centrality classes, and also the conversion of the EMCal raw data into quantities with physical meaning and their correction. The main focus of this thesis is the analysis of Au + Au collisions with center of mass energy of $\sqrt{s_{NN}} = 200$ GeV from the second RHIC beam time, which will be described thoroughly. In addition, we will address the particular details in the analysis of the d + Au data.

5.1 Data Selection

All raw data coming from the detectors have been assembled by the Event Builder in the PHENIX Raw Data Format (PRDF). Collections of events over a certain period of time (usually 30 minutes up to 2 hours) represent the individual runs. Within one run the global settings of the data acquisition, e.g. the prescale factors of the triggers, and of the detectors remain unchanged. Runs are subdivided into segments to keep the size of the output files low, and to make parallel processing during the offline DST¹ production possible, where the raw data are converted into quantities with more physical meaning.

Both in the analysis of Au + Au and d + Au data, two different types of events have been analyzed: minimum bias events, which are only biased by the limited BBC efficiency, and events specially selected because they contain a highly energetic photon.

In addition to the trigger selection, we require that the vertex z of a given event lies within the range $-30 \text{ cm} \leq z \leq 30 \text{ cm}$, in order to exclude regions that are shadowed by the pole tips of the central magnet and to minimize the background of scattered particles.

The analyzed runs are also required to meet certain quality criteria. For example, the EMCal and PC3 multiplicity, as well as the BBC and ZDC response, is monitored during the data analysis. All runs showing a large deviation from the average behavior are excluded during the next analysis pass. We also exclude runs where the PHENIX setup was changed, e.g. due the addition of photon converters. To maximize the number of analyzed events all settings of the central magnet are considered. A list of all analyzed runs can be found in Appendix B.

¹Data Summary Table

5.1.1 Minimum Bias Events

The condition for accepting an inelastic Au + Au reaction is given by the BBC and the ZDC. The collision has to trigger at least two photomultipliers at a time in both BBCs and cause a signal in both ZDCs. Only this allows a determination of the collision vertex and the centrality of the event. This trigger accepts 92% of the geometrical cross section for Au + Au collisions.

Because of the lower multiplicity and the asymmetric reaction, the minimum bias trigger in d + Au requires only a signal of at least one photomultiplier within each BBC. This condition allows the measurement of 88% of the geometrical d + Au cross section.

Due to the limited bandwidth of the PHENIX data acquisition, usually only a fraction of all minimum bias events is recorded. This fraction is determined by the prescale factor, which is specified at the beginning of a run for each trigger. In addition, only those events for which the data acquisition is active can be accepted (see Section 3.3.4).

The bandwidth that is freed by scaling down the number of accepted minimum bias events is used to enrich rare events in the data by means of special triggers, e.g. for highly energetic photons.

5.1.2 Events with Highly Energetic Photons

Because of the different production processes for direct photons and neutral pions in different regions of transverse momentum, it is essential to cover a broad p_T range. This is only possible with the help of specialized triggers for high p_T photons, which are conceptually similar but operationally different for d + Au and Au + Au, the LVL1 and the LVL2 triggers. The technical details are described in Section 4.5.1 and 4.5.2, respectively. In the following we will concentrate on the specialties when analyzing data with different trigger conditions.

When data from different triggers are combined it is particularly important to pay attention to two points. First, the normalization to the number of unbiased events has to also take into account the events rejected by the trigger. Second, the calculation of the particle yields has to account for the sensitivity or efficiency of the trigger to the respective particle species, which can be different compared to minimum bias triggers and depends on the energy of the measured particle, because of the effective trigger thresholds. For the determination of the trigger efficiencies refer to Section 6.1.3 and [Fra04b].

To calculate the number of underlying minimum bias events $\tilde{N}_{\text{evt}}^{\text{mb}}$ for a given photon trigger, one usually starts with a sample of minimum bias events and determines the

fraction of events for which the trigger condition, including the prescale condition, is satisfied:

$$\epsilon_{\text{evt}}^{\text{trig}} = \frac{N_{\text{evt}}^{\text{mb} \wedge \text{trig}}}{N_{\text{evt}}^{\text{mb}}}. \quad (5.1)$$

The number of underlying minimum bias events is then given by correcting the number of measured triggered events for the total rejection factor ($1/\epsilon_{\text{evt}}^{\text{trig}}$) of the trigger:

$$\tilde{N}_{\text{evt}}^{\text{mb}} = \frac{1}{\epsilon_{\text{evt}}^{\text{trig}}} \cdot N_{\text{evt}}^{\text{trig}}. \quad (5.2)$$

It is important to mention that the trigger conditions can change on a run-by-run basis, e.g. by changed prescale factors or modification of the gains, and it is not always possible to determine the factor $\epsilon_{\text{evt}}^{\text{trig}}$ by simple count of the number of the triggers in the minimum bias sample.

Event Counting for the Level-2 Photon Trigger

As described in Section 3.3.4, the Level-2 system performs a partial analysis of the data for a given Level-1 trigger. During the second RHIC run only those Au + Au events were passed to the Level-2 system that satisfy the Level-1 minimum bias condition. Such events may satisfy one or more Level-2 trigger conditions and be accepted. Because of the different rejection power for each trigger, the number of recorded events is regulated as in the Level-1 system by a prescale factor S^{L2} , e.g. with a prescale of two every second LVL2-triggered event is kept.

The Level-2 system keeps a fraction of all sampled events as a control sample unbiased by any Level-2 trigger decision. The number of these events is given by the forced accept rate F in the LVL2. When the LVL2 rejection is active the event sample satisfying the forced accept condition represents the minimum bias sample:

$$N_{\text{forced}}^{\text{L2}} = \frac{N_{\text{sampled}}^{\text{L2}}}{F} \equiv N^{\text{mb}}. \quad (5.3)$$

The number of sampled events $N_{\text{sampled}}^{\text{L2 scaled}}$ for a given LVL2 trigger, considering the prescale factor S^{L2} for this trigger, can be derived based on the number of those minimum bias events:

$$\begin{aligned} N_{\text{sampled}}^{\text{L2 scaled}} &= \frac{N_{\text{sampled}}^{\text{L2}}}{S^{\text{L2}}} \\ &= N^{\text{mb}} \frac{F}{S^{\text{L2}}}. \end{aligned} \quad (5.4)$$

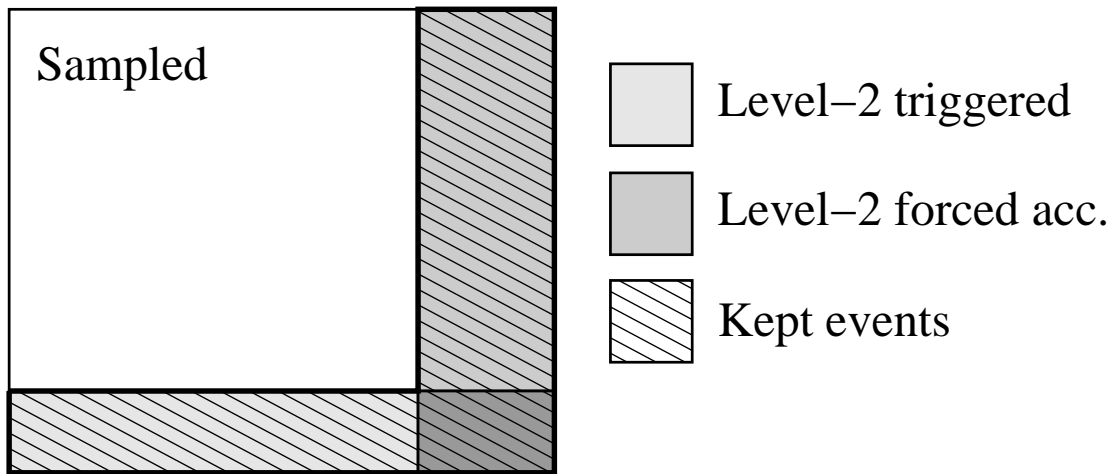


Figure 5.1: Schematic sketch of the event samples for the Level-2 trigger.

The event selection for the Level-2 system is illustrated schematically in Figure 5.1. The minimum bias sample recorded due to forced accepts and the fraction of events that fired a Level-2 trigger may partially overlap, as the recorded minimum bias events contain e.g. highly energetic photons as well. Usually it is desirable to analyze the complete minimum bias sample separately from the triggered data. This allows to apply trigger specific corrections only where necessary. For this reason we exclude events that also satisfy the forced accept condition in the analysis of the triggered data. Thus we have to subtract the number of recorded minimum bias events from the number of events sampled for the trigger when computing the number of sampled minimum bias events for the analysis of the LVL2-triggered data. This leads with Equation (5.4) to:

$$\begin{aligned}\tilde{N}_{\text{evt}}^{\text{mb}} &= N_{\text{sampled}}^{\text{L2 scaled}} - N^{\text{mb}} \\ &= N^{\text{mb}} \cdot \frac{(F - 1)}{S^{\text{L2}}},\end{aligned}\quad (5.5)$$

where the forced accept rate F and the scaledown factor S^{L2} are obtained from the PHENIX database during the analysis.

Event Counting for the Level-1 Photon Trigger

Most of the data used in the analysis of d + Au collisions come from specially filtered runs for which only events satisfying the ERT Gamma1 trigger condition (see Section 4.5.1) have been considered in the DST production. This makes it necessary to determine the scaling factor for each event from the PHENIX database, where the number of trigger

	$N_{\text{evt}}^{\text{mb}}$	$N_{\text{evt}}^{\text{trig}}$	$(\tilde{N}_{\text{evt}}^{\text{mb}})$
Au + Au	28.3 M	0.643 M	(43.1 M)
d + Au	18.7 M	10.4 M	(156 M)

Table 5.1: Number of analyzed events for the minimum bias sample in d + Au and Au + Au as well as for the events accepted because of a photon trigger.

counts for each run is recorded. The rejection power of the trigger for a given run is simply given by the comparison of the raw trigger counts for the Gamma1 and for the minimum bias condition given by the BBC, leading to the effective rejection power of the trigger. Additionally, the scaledown S^{L1} of the Gamma1 trigger has to be considered:

$$\epsilon_{\text{evt}}^{\text{trig}} = \frac{N_{\text{raw}}^{\text{G1}}}{N_{\text{raw}}^{\text{BBC}}} \cdot \frac{1}{S^{\text{L1}} + 1}. \quad (5.6)$$

The number of recorded triggers stored in the database refers to whole runs, and the sets of analyzed run segments are not necessarily complete. This is addressed by averaging the values of $\epsilon_{\text{evt}}^{\text{trig}}$ weighted by the number of actually analyzed events in each run.

5.1.3 Trigger Bias

An additional problem when analyzing data with any kind of trigger is a bias toward certain types of events. For example, it has been demonstrated that the BBC LVL1 minimum bias condition in p + p collisions is sensitive to $p_{\text{inel}}^{\text{BBC}} = (52 \pm 6)\%$ of the total inelastic cross section [Bel03], while this trigger condition accepts about $p_{\pi^0}^{\text{BBC}} = (75 \pm 2)\%$ of all events containing a π^0 reconstructed within the EMCal acceptance. This has been shown in [Rey03c] by comparison of the π^0 raw yield in minimum bias events to an event sample that is unbiased for the π^0 measurement above a certain p_{T} , as the only trigger requirement is a hit in the EMCal above the trigger threshold.

To consider this effect for the determination of the total inclusive π^0 cross section in p + p collisions, the number of measured minimum bias events $N_{\text{evt}}^{\text{mb}}$ and the number of measured π^0 s have to be corrected accordingly to the total number of inelastic events $N_{\text{evt}}^{\text{inel}}$ and to the total number of π^0 s $N_{\pi^0}^{\text{inel}}$, respectively:

$$\begin{aligned} N_{\text{evt}}^{\text{inel}} &= \frac{N_{\text{evt}}^{\text{mb}}}{p_{\text{inel}}^{\text{BBC}}}, \\ N_{\pi^0}^{\text{inel}} &= \frac{N_{\pi^0}^{\text{mb}}}{p_{\pi^0}^{\text{BBC}}}. \end{aligned} \quad (5.7)$$

Leading to an overall correction factor κ_1 for this effect:

$$\begin{aligned} \frac{N_{\pi^0}^{\text{inel}}}{N_{\text{evt}}^{\text{inel}}} &= \frac{p_{\text{inel}}^{\text{BBC}}}{p_{\pi^0}^{\text{BBC}}} \cdot \frac{N_{\pi^0}^{\text{mb}}}{N_{\text{evt}}^{\text{mb}}} \\ &= \kappa_1 \cdot \frac{N_{\pi^0}^{\text{mb}}}{N_{\text{evt}}^{\text{mb}}}. \end{aligned} \quad (5.8)$$

In the case of d + Au and Au + Au collisions a direct determination of the trigger bias and its correction is not possible because all EMCal triggers have been taken in coincidence with the minimum bias trigger condition, thus an unbiased event sample is not available.

For Au + Au the trigger bias is only a minor problem. It affects solely the very peripheral events. Due to the large multiplicity compared to p + p the BBC trigger efficiency for an inelastic Au + Au collision is basically 100% in each centrality class. This is not the case in d + Au, where even at zero impact parameter the multiplicity can be so low that the minimum bias trigger condition is not satisfied.

The correction to the inclusive π^0 yield in d + Au collisions can be determined based on the p + p corrections and some simple assumptions, as discussed in [Tan03]:

- The measurement of one p + p collision is equivalent to one binary nucleon-nucleon collision.
- For $N_{\text{coll}} = n$ binary nucleon-nucleon collisions only one π^0 is detected. This is justified by the low multiplicity in d + Au collisions.

The correction factor for a given number of collisions κ_n is then given by:

$$\begin{aligned} \kappa_n &= \frac{1 - (1 - p_{\text{inel}}^{\text{BBC}})^n}{1 - (1 - p_{\pi^0}^{\text{BBC}}) (1 - p_{\text{inel}}^{\text{BBC}})^{n-1}} \\ &\equiv \frac{p_{\text{inel},n}^{\text{BBC}}}{p_{\pi^0,n}}. \end{aligned} \quad (5.9)$$

Together with the probability distribution $P(n)$ for n binary collisions from a Glauber calculation, the correction factor for the inclusive π^0 yield measured in minimum bias d + Au reactions with the requirement that the BBC was struck is given by:

$$\langle \kappa \rangle_{\text{BBC}} = \frac{\sum_{n=1}^{n_{\text{max}}} \kappa_n P(n) p_{\text{inel},n}^{\text{BBC}}}{\sum_{n=1}^{n_{\text{max}}} P(n) p_{\text{inel},n}} = 0.95. \quad (5.10)$$

The correlation of the BBC trigger decision and the measurement of a π^0 in the EMCal acceptance must also be taken into account when determining the average number of binary collisions N_{coll} for the selected event sample as discussed in [Tan03].

From the above considerations it becomes also clear that for Au + Au collisions the corrections are negligible. Due to the increased number of binary collisions compared to d + Au the correction factor approaches unity quickly.

5.1.4 Centrality Determination

The events, selected by the trigger decisions described above, are analyzed for different impact parameters of the colliding nuclei or centralities to follow the transition from small energy densities and few participants in peripheral events to the hot and dense phase in central collisions.

The centrality for Au + Au collisions within PHENIX is determined via the correlation between the energy deposit in the ZDC and the charge deposit in the BBC. The BBC measures the multiplicity of charged particles in the pseudo-rapidity region $3.1 < |\eta| < 3.9$, while the ZDC detects the energy of neutral particles, mostly neutrons, close to the beam axis as described in Section 3.3.1. With increasing centrality the multiplicity and thereby the detected charge in the BBC increases. The relation between ZDC response and centrality is more complex. The ZDC is also sensitive to reactions where the nuclei miss each other but neutrons are emitted via the Coulomb interaction², such events are excluded by requiring the BBC and ZDC coincidence. Going from peripheral to central events the excited spectator fragments emit an increasing number of neutrons, which can be detected in the ZDC. If the centrality increases further most neutrons stay bound, e.g. within deuterons, and are deflected in the magnetic field. In addition, the total number of spectators decreases, leading to less free neutrons that are detected by the ZDC. This behavior is illustrated in Figure 5.2 for the complete minimum bias sample. The distribution is divided into the different centralities by an angle ϕ_{cent} in the BBC–ZDC plane defined as:

$$\phi_{\text{cent}} = \arctan\left(\frac{(Q_{\text{BBC}} - Q_0)/Q_{\text{max}}}{E_{\text{ZDC}}/E_{\text{max}}}\right), \quad (5.11)$$

where E_{max} represents the maximum energy of 4500 GeV deposited in the ZDC and $Q_{\text{max}} = 1700$ the maximum charge-equivalent measured by the BBC.

The value of Q_0 , as well as the choice of the angular cuts shown in Figure 5.2, is based on a simple simulation of the BBC and ZDC signal together with a Glauber model of the

²In Au + Au collisions at $\sqrt{s_{\text{NN}}} = 200$ GeV approximately one third of all ZDC coincidences are produced by mutual Coulomb excitation of the gold nuclei [Nys01].

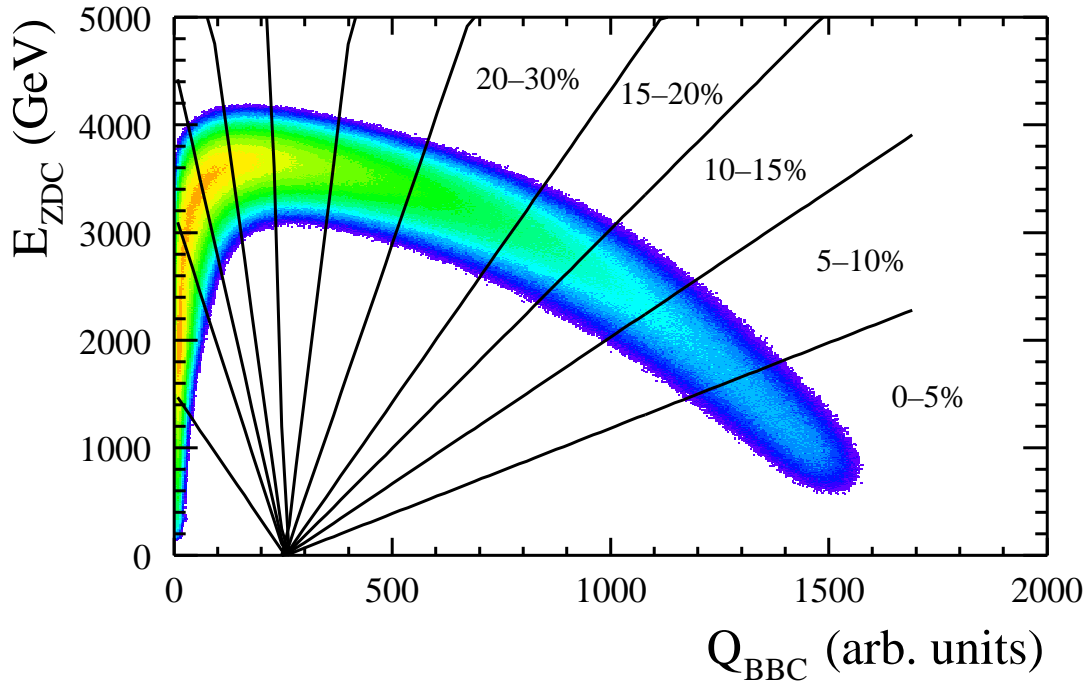


Figure 5.2: Total ZDC signal versus total charge measured by the BBC and the division into different centralities based on this distribution.

Au + Au collision as described in [Kel00]. The cut is chosen in a way that the selected event sample represents a specified fraction of the total geometrical cross section σ_{tot} .

The main centrality classes used in the analysis are shown in Table 5.2 together with the respective number of binary nucleon-nucleon collisions N_{coll} , the number of participants N_{part} , and the nuclear overlap function T_{AB} as defined in Section 1.3.1. In the analysis of the d + Au data only the minimum bias sample is used for this work.

5.2 Processing of EMCal Data

During the DST production the raw data information of each detector is converted into physical quantities, such as energy, time-of-flight, and position. Usually these quantities are analyzed further and stored in the DST as information on e.g. particle tracks and momenta.

The DST information is further condensed in the form of *microDSTs*, which basically represent a reduced set of variables for each detector compared to the DST. At this

Centrality Class		N_{coll}	N_{part}	$T_{AB} \text{ (mb}^{-1}\text{)}$
Au + Au				
Minb	0-92%	257.8 ± 25.4	109.1 ± 4.1	6.14 ± 0.45
Cent	0-10%	955.4 ± 93.6	325.2 ± 3.3	22.75 ± 1.56
Peri	60-80%	20.4 ± 5.9	19.5 ± 3.3	0.49 ± 0.14
d + Au				
Minb	0-88%	8.3 ± 0.5	9.1 ± 0.4	0.198 ± 0.012

Table 5.2: The main centrality classes used in the analysis. For all other centralities refer to Appendix F. The Glauber results are from [Rey03b, dV04].

point the information of all detectors is still kept together in one file. In the last step of specialization, the *nanoDSTs*, the data important for different types of analysis are split into different files, which may also contain certain cuts tested during the analysis of the microDSTs.

Since this work is based on the analysis of microDSTs, the production chain up to the level of microDSTs shall be explained in detail for the EMCal, together with the corrections applied to the data during the analysis, and the particle identification (PID) cuts used to suppress the contamination by hadrons in the photon measurement.

5.2.1 DST Level

The first step in the DST production for the EMCal data is the conversion of the raw module information into energy and timing information as described in Chapter 4.4.2, referred to as *calibrated towers* in the following. Because an electromagnetic shower usually spreads over more than one module this calibrated towers are passed to the *Cluster routine*, which summarizes associated areas of towers into the so-called clusters. The algorithm of the cluster routine can be divided into the following steps:

- Find a cluster, which is a group of adjacent towers each with an energy above the noise threshold (see Table 5.4).
- Find the local maxima of the cluster. A local maximum is a module above the peak threshold, given in Table 5.4, with the maximum amplitude in the 3×3 region surrounding it.
- If more than one local maximum is found, split the cluster according to amplitude and positions of the maxima.

- Calculate the first and second moments of the clusters as the seed for the determination of the impact position.
- Compare the shape of the cluster with the expectation for an electromagnetic shower for particle identification (χ^2 method described below).
- Compute and correct the total energy for the cluster.

For each cluster the newly computed values such as corrected energy and position are stored in a list of clusters that can be used in the analysis. They represent the reconstructed properties of hits in the EMCal.

Position Reconstruction

The lateral segmentation of the EMCal permits conclusion on the impact position of a particle based on the center of gravity or first moment of a cluster given by:

$$\bar{x} = \frac{\sum_i E_i x_i}{\sum_i E_i} \quad \text{and} \quad \bar{y} = \frac{\sum_i E_i y_i}{\sum_i E_i}, \quad (5.12)$$

where (x_i, y_i) is the position within a sector of the i^{th} module of the cluster and E_i is its energy.

For non-zero angular incidence the projection of the shower maximum on the detector surface does not correspond to the impact position x_0 . Additionally, the connection between the center of gravity of a shower and x_0 is influenced by the finite size of the modules as described in [Büs97, Mit02]. During the clustering process the center of gravity is corrected for these dependencies based on test beam results and simulations to the actual impact point on the detector surface, assuming that the particle is a photon. In addition to the impact position, the module coordinates of the tower with the highest energy within the cluster are also stored. This information is used later to determine a list of bad modules, which are excluded in the final analysis (see Section 5.2.3).

Photon Identification

To facilitate the measurement of photons within the EMCal, certain variables for their identification are also computed and associated with the cluster. The main tool to suppress the background from hadrons is a cut on the shower shape, as a hadronic shower usually spreads over more modules than an electromagnetic shower, whose lateral extension is given by Equation (4.3).

	PbGl	PbSc
PID 0	No cuts	
PID 1	TOF cut (Au + Au)	$ t < 2.0 \text{ ns}$
	TOF cut (d + Au)	$ t < 5.0 \text{ ns}$
PID 2	Shower shape cut	$\max(D_{\text{corr},x}, D_{\text{corr},y}) < D_{\text{cut}}(\theta)$
PID 3	TOF and shape cut	$\chi^2 < 3$

Table 5.3: The parameters of the different cuts used during the analysis.

In the case of the PbGl the second moment or *dispersion* D of a cluster is calculated as a measure of the width of the shower. For the x -direction the dispersion is given as:

$$D_x = \frac{\sum_i E_i x_i^2}{\sum_i E_i} - \left(\frac{\sum_i E_i x_i}{\sum_i E_i} \right)^2. \quad (5.13)$$

The same holds for the y -direction. Because the dispersion is limited by the finite size of the modules, the second moment has to be corrected with the first moment of the cluster as given by Equation (5.12) [Sch94b]:

$$D_{\text{corr},x} = D_x - (|\bar{x}| - \bar{x}^2). \quad (5.14)$$

Finally, the maximum of the dispersion in x - and y -direction is used in the analysis. Since a shower, electromagnetic as well as hadronic, spreads over an increasing number of modules with increasing incident angle θ , the cut on the dispersion is chosen as a function of angle as given by Equation (5.15). For more details see [KB00].³

$$D_{\text{cut}}(\theta) = 0.27 - 0.145 \cdot \theta + 0.00218 \cdot \theta^2, \quad \text{with } \theta \text{ in degrees.} \quad (5.15)$$

For the PbSc the shower shape cut is based on a comparison of the deposited energy E_i^{meas} in each module of the measured cluster to the expectation for a cluster formed by an electromagnetic shower of the same cluster energy.

The expected energy deposit E_i^{ideal} for a given tower is determined by a parameterization of the shower shape based on test beams and simulation studies [Baz99, Baz03b]. It depends on the total energy E of the cluster, the distance to the center of gravity of the shower r_{cog} , and the angle of incidence θ :

$$\frac{E_i^{\text{ideal}}}{E} = p_1(E, \theta) \cdot \exp\left(\frac{-r_{\text{cog}}^3}{p_2(E, \theta)}\right) + p_3(E, \theta) \cdot \exp\left(\frac{-r_{\text{cog}}}{p_4(E, \theta)}\right). \quad (5.16)$$

³Here and in the following the incident angle θ always denotes the angle with respect to a perpendicular on the detector surface.

This parameterization is also the basis to unfold overlapping electromagnetic showers into separate clusters. For this purpose the clustering routine contains also a parameterization of the electromagnetic shower shape in the PbGl (see [Baz01]), but it is not used for photon identification.

The ideal energy deposit as given by Equation (5.16) represents only a mean value for many measurements or simulations of the electromagnetic shower form, but the individual value can deviate. This is described by the variance σ_i given in Equation (5.17), which provides the dependence of the fluctuations on the energy and angle of incidence, $f(E, \theta)$, and on losses to the total energy due to the thresholds used in the clustering, $q(E)$.

$$\sigma_i^2 = q(E) + C \cdot E_i^{\text{ideal}} \cdot \left(1 + a_1 \cdot \frac{E_i^{\text{ideal}}}{E} + a_2 \left(\frac{E_i^{\text{ideal}}}{E} \right)^2 + f(E, \theta) \cdot \left(1 - \frac{E_i^{\text{ideal}}}{E} \right) \right) \quad (5.17)$$

Based on Equation (5.16) and (5.17) a measure for the electromagnetic character of a cluster with N towers can be defined as:

$$\chi^2 = \frac{1}{N} \sum_{i=1}^N \frac{(E_i^{\text{ideal}} - E_i^{\text{meas}})^2}{\sigma_i^2}. \quad (5.18)$$

During the analysis of the PbSc data only clusters with a value of $\chi^2 < 3$ are considered as electromagnetic showers.

Finally we make use of a time-of-flight cut. In the DST the arrival time for the tower with the largest energy within the cluster is stored and can be compared to the calculated time-of-flight for a photon. However, in the analysis we use only a loose TOF cut and the main rejection of hadrons comes from the shower shape cut. The four different PID criteria used during the analysis of the Au + Au and d + Au data are summarized in Table 5.3.

Energy Corrections

As described in Section 4.1.1 the measured energy E is not linearly related to the energy of the incoming particle E_0 because a shower might not deposit all of its energy in the calorimeter and due to light absorption. The *non-linearity* of the PbGl and the PbSc has been determined in electron test beam measurements and by simulation studies [Aph03a, KB00].

For the PbGl the linearity correction is shown in Figure 5.3(a) and is given by:

$$\frac{E_0}{E_{\text{det}}} = a_1 + a_2 \cdot \ln \frac{E_{\text{det}}}{\text{GeV}} + a_3 \cdot \ln^2 \frac{E_{\text{det}}}{\text{GeV}}, \quad (5.19)$$

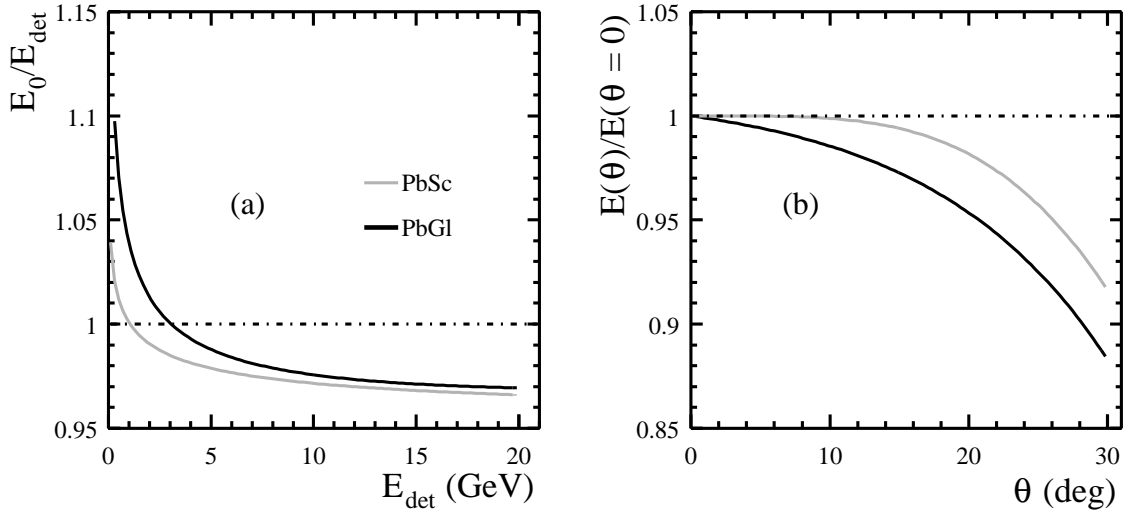


Figure 5.3: The energy correction applied during clustering for PbGl and PbSc: (a) the linearity correction, (b) the angular correction for a photon with an energy of 10 GeV.

	PbGl	PbSc
Minimum tower energy	14 MeV	10 MeV
Minimum cluster energy	60 MeV	15 MeV
Minimum peak energy	80 MeV	80 MeV
Linearity correction	$a_1 = 1.0386$ $a_2 = -0.0414$ $a_3 = 0.00061$	$a_1 = 0.0033$ $a_2 = 2$ $a_3 = 120$
Angular correction	$b_1 = -0.01204$ $b_2 = 0.07791$	$b_1 = 0.918$ $b_2 = 1.35$ $b_3 = 0.003$

Table 5.4: The parameters used by the clustering algorithm.

with parameters summarized in Table 5.4.

As the pathlength through the calorimeter is larger for large angular incidence, the additional light absorption leads to a further reduction of the measured energy. This has been studied for the PbGl by simulating photons under different angles of incidence θ [KB00]. The result is shown in Figure 5.3(b) and leads to the correction function:

$$\frac{E(\theta)}{E(\perp)} = 1 + b_1 \cdot (e^{b_2 \cdot \theta} - 1), \quad \text{with } \theta \text{ in degrees.} \quad (5.20)$$

For the PbSc the situation is a little bit more complex, as two different types of energy variables can be used: on the one hand the usual sum of all energy amplitudes within the cluster, on the other hand the energy of the electromagnetic *core* of the cluster E_{core} . As E_{core} is the energy used in the following analysis we will concentrate on its determination and correction.

Based on the parameterization of the electromagnetic shower profile given by Equation (5.16) the energy in each tower is predicted. The prediction is based on the center of gravity and the total energy of the cluster. If the predicted fractional energy deposit in a tower is larger than 2%, the tower energy is included in the energy summation for E_{core} .

The energy is finally corrected in a similar way as in the PbGl for linearity and angular dependence. In the case of the PbSc a correction for the 2% cut-off for a module contributing to E_{core} is folded into the angular correction⁴, which is applied before the linearity correction:

$$\frac{E_{\text{core}}}{E} = b_1 \cdot (1 - b_2 \sin^4 \theta \cdot (1 - b_3 \cdot \ln E_{\text{core}})), \quad (5.21)$$

$$\frac{E}{E_0} = \left(2 - \sqrt{1 + a_1 \cdot \ln^2(1 + E)}\right) \cdot \left(e^{\frac{\ln E \cdot a_2}{a_3}}\right). \quad (5.22)$$

The parameters are again given in Table 5.4. The comparison of the energy corrections in Figure 5.3 shows that the PbSc is less sensitive to angular variations and the linearity correction in the PbGl is more pronounced at lower energies, while at larger energies the corrections in PbGl and PbSc are similar.

5.2.2 MicroDST Level

The microDSTs basically represent a reduced set of information compared to the DST. In the case of the EMCal the information on the calibrated towers had been dropped for the PbSc but kept for the PbGl, because studies on the calibration had not been finished before the microDST production. The microDST framework also allows to rewrite a microDST with substituted information, leading to the concept of *afterburners*, which can be applied to a microDST for corrections not known during the DST production.

In case of the EMCal these afterburners mainly incorporated corrections to the measured energy and the timing (see [Chi02]), while other variables remained unchanged. In the following we will concentrate on corrections to the energy.

The energy corrections for the afterburner in the case of the PbSc have been determined by the position of the MIP peak in each individual module and were confirmed by

⁴This can also be considered as a correction for effects introduced by the tower threshold of 10 MeV during the clustering, as long as the energy of the photon is larger than $E_\gamma = 10 \text{ MeV} / 0.02 = 500 \text{ MeV}$.

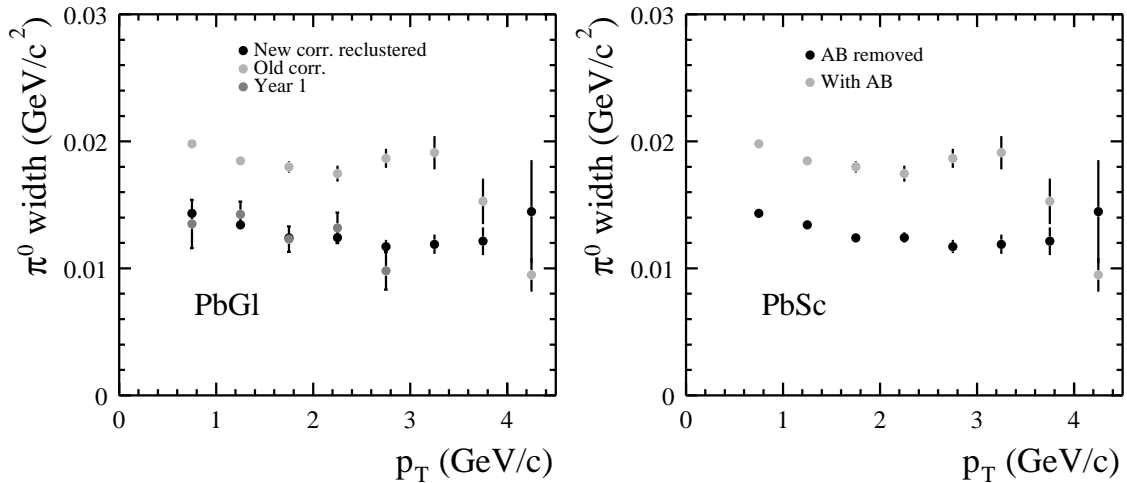


Figure 5.4: Improvement in the width of the π^0 peak in peripheral events after applying all corrections mentioned in the text. For the PbG1 the width in the analysis of peripheral Au + Au collisions at $\sqrt{s_{NN}} = 130$ GeV is also shown.

the comparison of the measured energy of identified electrons to their momentum (E/p matching). In case of the PbG1 the corrections were based on the comparison of the slopes of the energy spectra in each individual module as described below.

One disadvantage of the afterburner is that corrections on a tower-by-tower basis cannot directly be applied to one cluster, which usually consists of several towers. As an approximation, the energy correction valid for the tower with the largest contribution to the cluster is used for the whole cluster. Since in the case of the PbG1 the information of the tower energies is still available in the microDST, the afterburner-corrected clusters are not used. Instead a completely new list of clusters is calculated during the analysis based on the corrected tower information (*reclustering*).

5.2.3 Analysis Level

During the analysis different corrections to the energy are applied to account for miscalibrations during the DST or microDST production. The energy corrections can generally be split up into those affecting the relative calibration between the modules, which basically influence the energy resolution, hence the width of the π^0 peak, and those that influence the overall energy scale, thus determining the measured π^0 peak position.

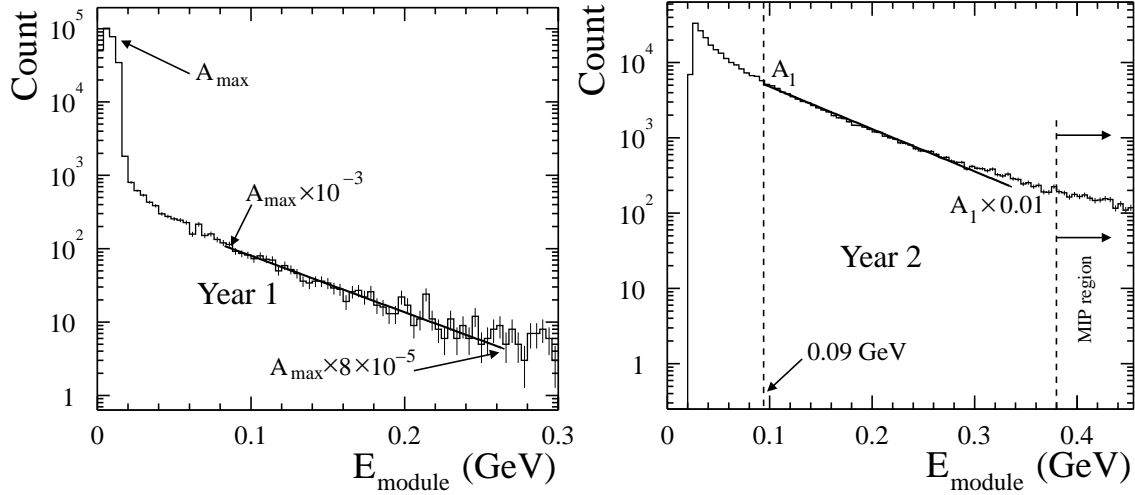


Figure 5.5: Energy spectrum within one PbGl module during the first and second year of physics running together with the fit ranges for the determination of the slope. The pedestal peak is clearly seen on the left plot and is absent on the right.

Relative PbGl Energy Calibration

The initial relative calibration factors used during the DST production were determined exactly in the same way as for the first year of physics running as described in [Awe01], based on the energy spectra in each individual tower. Unfortunately this calibration led to a larger width of the π^0 peak than observed in the analysis of Au + Au collisions from the previous beam time as shown in Figure 5.4, indicating a problem with the procedure. Due to the fact that the calibrated information of each PbGl module is also stored in the microDSTs, it was possible to undo the corrections applied during the DST production and to redo the procedure as described in the following.

The measured energy spectrum in each module is fitted in a given range by an exponential to determine the slope parameter k_i :

$$\frac{dN_i}{dE} = A \cdot e^{k_i \cdot E}. \quad (5.23)$$

Previously the fit range had been determined by the maximum A_{\max} of the spectrum as illustrated in Figure 5.5. This maximum value was basically given by the pedestal noise in each module that was suppressed already in the DCMs during the second RHIC run, as described in Section 4.4.1, leading to a miscalculation of the fit range. To overcome this problem a fixed lower bound was used instead (see Figure 5.5).

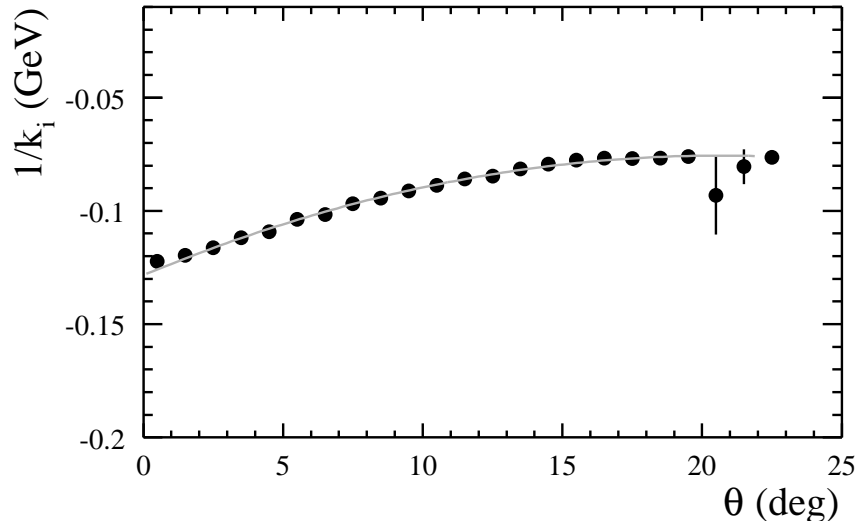


Figure 5.6: Angular dependence of the inverse slopes for the PbGl, the polynomial used to fit this dependence for the calculation of the relative correction factors is also shown.

The slope parameter k_i is different for each module. Based on the assumption that every module should measure the same energy spectrum one can iteratively determine a correction factor λ_i for each module that would adjust all slopes to a common value k_{ref} :

$$\lambda_i = \frac{k_i}{k_{\text{ref}}}. \quad (5.24)$$

However, this would ignore that the slopes show a natural angular dependence due to the fact that a shower spreads its energy over more modules with increasing incident angle θ . This is illustrated in Figure 5.6 for the inverted slopes, which show a more symmetric distribution than the k_i themselves. To account for this behavior the slopes are corrected for the angular dependence by a second order polynomial also shown in Figure 5.6. The improvement for the width of the π^0 peak due to the newly determined corrections is shown in Figure 5.4 and is now comparable to the width from the previous run.

With the large dataset of the second Au + Au run it is also possible to study the stability of the slope method for different sets of events. For this purpose a set of 24 M minimum bias events was divided into subsets of 12 M, 4.8 M, and 2.4 M events. The correction factors are determined for each subset and can be compared to the correction factors obtained with the whole data set on a module-by-module basis. The deviation from unity indicates the change in the absolute energy scale depending on the selected dataset, while the spread of the distribution is a measure for the stability of the method. As seen in Figure 5.7 the energy scale does not change by more than 0.2% regardless of the chosen

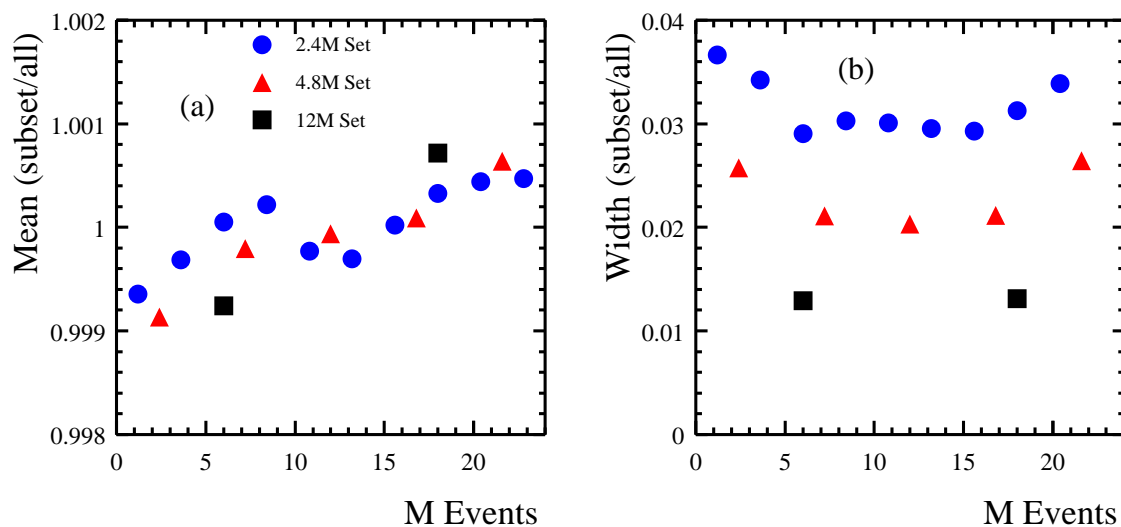


Figure 5.7: Comparison of the correction factors obtained with different subsets of the data. The axis of abscissae represents a running number over 24 M events.

dataset and the relative calibration for each individual module is already for a small dataset of 2.4 M events accurate to within 4%.

In the analysis of the $d + Au$ data no additional corrections to the relative calibration were applied during the analysis. Only an overall correction of the energy scale was used (see below).

Relative Calibration of the PbSc

In the PbSc a problem with the afterburner correction was discovered when the position dependence of the measured energy was examined. It showed an unexpected increase toward the edge of the calorimeter, as seen in Figure 5.8. The presumption that the afterburner corrections had been determined or applied in a wrong way is supported by the fact that the comparison of the measured energy in the PbSc and the reconstructed momentum of identified electrons showed a similar deviation for clusters at the edge of the calorimeter [Fra04b].

Since the afterburner corrections had been applied on the cluster level it was possible to undo this correction simply by dividing out the factor previously applied. This correction was done for the PbSc, together with multiplication by the overall scale corrections described below and summarized in Table 5.5. The number of clusters in a given energy range then showed a flat dependence on the position as shown in Figure 5.8. In addition,

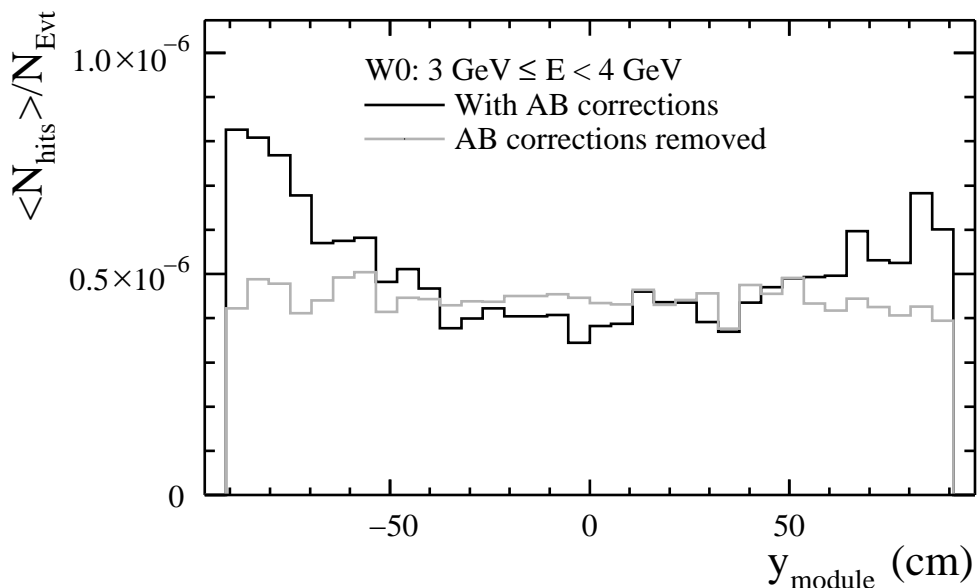


Figure 5.8: Position dependence of clusters with energy between 3 and 4 GeV for one PbSc sector (W0) with and without the afterburner (AB) corrections.

the energy resolution of the PbSc improved as seen in the decreased width of the invariant mass peak of the π^0 shown in Figure 5.4.

Absolute Energy Calibration

An advantage of the invariant mass measurement of π^0 s is that the absolute energy scale is in principle fixed by the measurement of the π^0 peak position and the comparison with the expectation from the efficiency simulation, which is also needed for the correction of the spectra. Since this method is closely related to the efficiency calculation, it is discussed in Section 6.4. Only the correction itself is described here.

To avoid shifts in the reconstructed π^0 mass due to the overlap of clusters in events with large multiplicity, the empirical energy correction for the PbGl in the analysis of the Au + Au cluster data is based on the π^0 peak position measured in p + p collisions during the same beam time. The functional form is given by:

$$E_{\text{corr}} = E (a_1 + a_2 \cdot e^{a_3 \cdot E}), \quad (5.25)$$

with the parameters summarized in Table 5.6.

In the analysis of the d + Au data the same correction for the absolute energy scale is used as in Au + Au. Additionally, a newly determined correction based on the π^0 peak position with parameters given in Table 5.6 is applied.

Sector	Overall correction	Run period correction		
		27808–30109	30110–31335	31336–33614
E0	1.014	1.	1.	1.
E1	1.	1.	1.	1.
E2	0.96	1.035	1.035	1.066
E3	0.967	1.035	1.035	1.066
W0	0.967	1.035	1.035	1.066
W1	0.967	1.035	1.035	1.066
W2	0.984	1.02	1.06	1.09
W3	0.984	1.02	1.06	1.09

Table 5.5: Parameters of the final overall energy corrections applied to the cluster energy in the Au + Au analysis.

Sector	a_1	a_2	a_3 (GeV ⁻¹)
Au + Au			
E0	0.9623	0.1356	-1.109
E1	0.9623	0.1356	-1.109
d + Au additionally to Au + Au			
E0	1.02	0.03	-0.863
E1	1.	0.	0.
E2	0.98	0.07	-0.978
E3	0.99	0.06	-0.877
W0	0.985	0.05	-0.834
W1	0.989	0.04	-0.709
W2	0.98	0.05	-0.921
W3	1.	0.03	-0.359

Table 5.6: Parameters for the linearity correction of the energy as given by Equation (5.25).

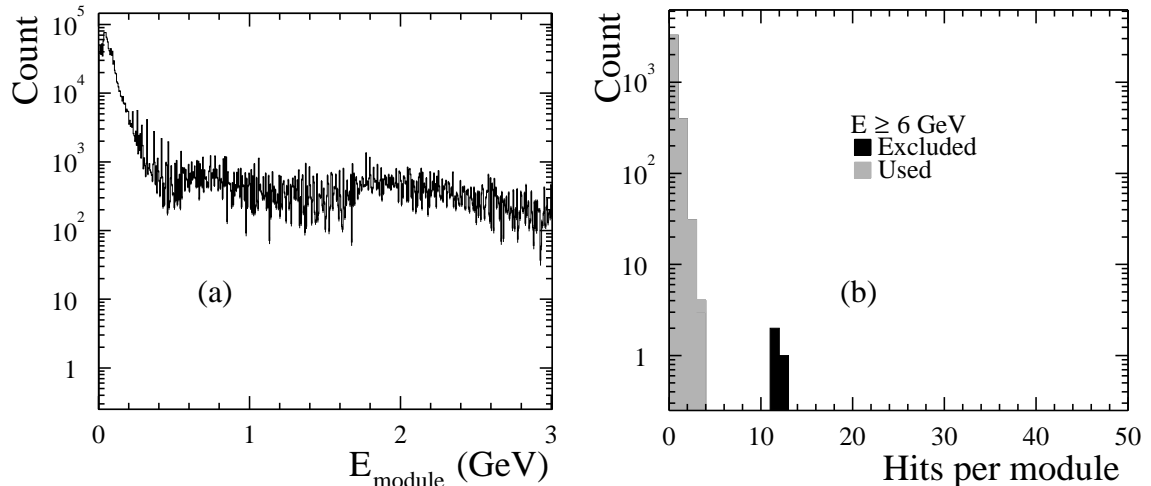


Figure 5.9: (a) Energy spectrum of an obviously bad module, where the relative calibration failed. (b) The hit frequency for each module within E1 with a cluster energy above 6 GeV. The black entries are excluded.

Other corrections applied during the analysis of the Au + Au data are needed to compensate for jumps in the absolute calibration during three different run periods because in the case of the PbSc the time-dependence of the gains was not tracked correctly by the reference system [Chi02], and to balance the energy scale between the PbGl sectors and between the PbSc sectors, respectively. The overall corrections are based on the comparison of the measured π^0 and MIP peak position within those sectors as described in Section 6.4. The energy of a given cluster is multiplied by both correction factors given in Table 5.5.

Identification of Bad Modules

When analyzing the EMCal data one has to apply quality criteria to the clusters to account for modules that distort the energy measurement of a hit. This is of particular importance when detecting single photons. While in the measurement of π^0 s modules leading to a wrong invariant mass are automatically omitted, this *self-exclusion* is not a feature of the photon measurement.

Modules without any energy signal, denoted *dead*, within a cluster lead to a measured energy that is too low. Most of the dead modules are due to faulty photomultipliers, which produce either no signal or are switched off because they show a constantly large energy signal independent of a physics input. Additionally, the edge modules of the detector are

considered to have a dead neighbor to exclude clusters that suffer from leakage at the calorimeter edge.

During the determination of the relative correction factors, as described above, some modules showed suspicious energy spectra as seen in Figure 5.9(a). Those modules are flagged as *bad*. For the photon measurement it is also critical to exclude modules that only sporadically contribute in a wrong way to the signal. Especially at higher energies, where the number of produced photons is small, one single *warm* module can easily distort the measured spectrum. For this reason the search for bad modules is also performed in different energy ranges by looking at the frequency at which a given module is the main contributor to a cluster with an energy falling into this region. For each energy range the mean hit frequency and the RMS are computed and modules showing large deviations from this mean value, as illustrated in Figure 5.9(b) for the PbGl, are also marked as bad modules for the analysis.

The position of the cluster for the bad module cut is not given by the reconstructed impact position; instead, it is determined by the tower with the largest energy deposit within the cluster. During the analysis it is required that this tower does not fall on a module that is either flagged as bad or dead, or is adjacent to one. A map of the excluded area in each detector is shown in Appendix C for the analysis of the Au + Au data as well as for the analysis of the d + Au data.

6. Measurement of Neutral Pions in Au + Au and d + Au Collisions

In this chapter the extraction of the π^0 signal will be discussed together with the necessary corrections to obtain the invariant π^0 yield. The most important corrections are the acceptance correction, which accounts for the limited angular coverage of the EMCal, and the efficiency correction, which corrects for losses due to the finite energy and position resolution of the detector and due to different particle identification cuts.

6.1 Extraction of the π^0 Signal

Neutral pions are detected via their 2γ decay channel. Due to the relatively short mean lifetime of neutral pions of about 10^{-16} s, typical of electromagnetic decays, the pions decay before escaping from the collision region. This makes the decay vertex well known and the pions can be reconstructed via an invariant mass analysis of photon pairs measured by the EMCal (see Chapter 4).

6.1.1 Invariant Mass Analysis

The invariant mass of a particle pair is given by the absolute value of its four-momentum $P_{12} = P_1 + P_2$. As photons are massless particles this reduces to the determination of the energy E and the opening angle θ between the two photons:

$$m_{\gamma\gamma} = \sqrt{(P_{\gamma_1} + P_{\gamma_2})^2} = \sqrt{E_{\gamma_1} \cdot E_{\gamma_2} \cdot (1 - \cos \theta_{12})}. \quad (6.1)$$

For a photon pair originating from a π^0 decay this invariant mass is identical to the π^0 rest mass of $134.9766 \text{ MeV}/c^2$ [Eid04]. However, due to the finite energy and position resolution in the detection of the photon pair, the actual reconstructed value is smeared around a mean value, which can deviate from the nominal value. The reconstructed peak position is also influenced by the high multiplicity in a heavy ion collision, where overlapping clusters can shift the measured energy of the single photon.

With the invariant mass analysis the π^0 cannot be identified uniquely since all possible photon-photon combinations have to be considered. This leads to a large combinatorial background, which increases quadratically with the multiplicity.¹ The π^0 yield is instead

¹For a given multiplicity N the number of possible pair combinations is $N_{\text{pair}} = \frac{N}{2} \cdot (N - 1)$.

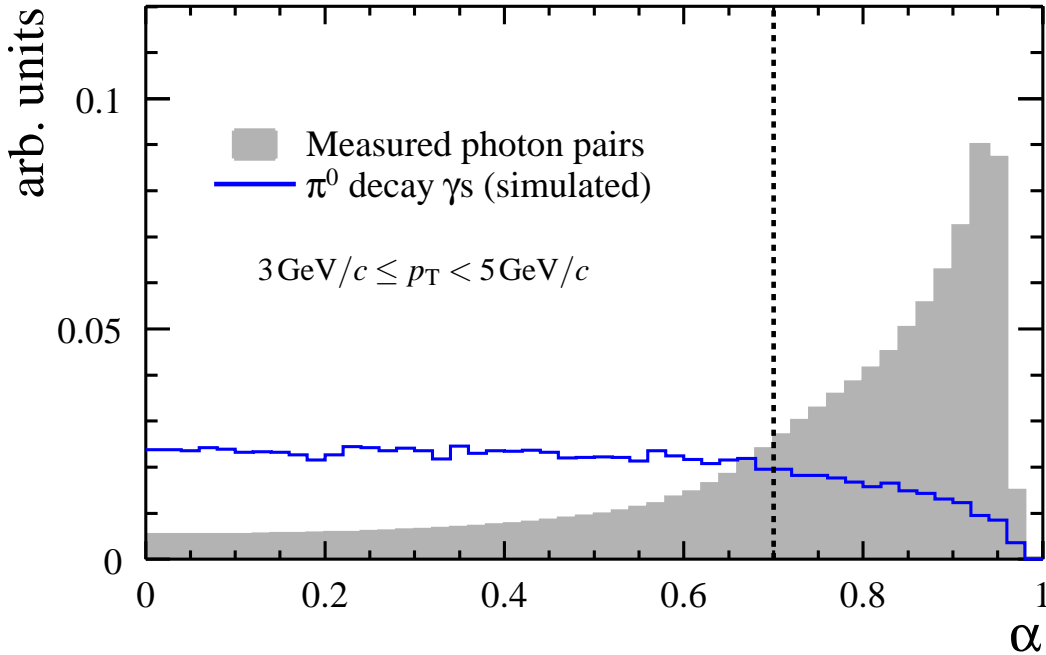


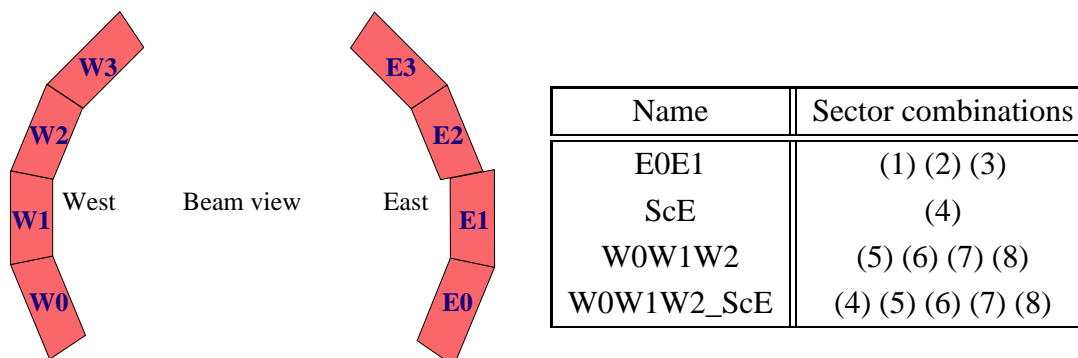
Figure 6.1: Asymmetry of photon pairs with $3 \text{ GeV}/c \leq p_T < 5 \text{ GeV}/c$ from π^0 s within the E1 acceptance (simulated) and measured within minimum bias events. The asymmetry cut used during the analysis is also shown.

determined on a statistical basis, with the background contribution established via a *mixed event* technique as described below.

One possibility to reduce the combinatorial background is to make use of the phase-space distribution of the photons in a π^0 decay. The probability for a decay photon to carry a fraction x of the pions energy is the same for all values of x . Expressed in terms of the *asymmetry* α of the two photon energies defined by Equation (6.2), this is equivalent to a flat distribution of α .

$$\alpha = \left| \frac{E_1 - E_2}{E_1 + E_2} \right| \quad (6.2)$$

For random combinations within one event the asymmetry is not flat. As the energy spectrum of all detected particles is steeply falling, pair combinations containing one hit with lower energy are more probable. This leads to an increase of photon pairs with large asymmetry, as illustrated in Figure 6.1, where the asymmetry distribution for photons from π^0 s in a simulation is compared to the measured asymmetry for photon candidate pairs in real Au + Au collisions.



Sector	E0	E1	E2	E3	W0	W1	W2	W3
E0	(1) (2)	—	—	—	—	—	—	—
E1	(2) (3)	—	—	—	—	—	—	—
E2	—	—	(4) (4)	—	—	—	—	—
E3	—	—	(4) (4)	—	—	—	—	—
W0	—	—	—	—	(5) (8)	(8)	—	—
W1	—	—	—	—	(8) (6)	(8)	—	—
W2	—	—	—	—	(8) (8)	(7)	—	—
W3	—	—	—	—	—	—	—	—

Table 6.1: The notation for the different sectors in the two calorimeter arms and their combinations used for the invariant mass analysis of photon pairs.

For photons originating from π^0 s the distribution shows a slight decrease for large asymmetries due to the limited acceptance of the EMCAL. Decay photons with large asymmetry show a larger opening angle so that one photon can miss the detector.

During the π^0 peak extraction a cut was used that required $\alpha < 0.7$ for all pair combinations. It reduces the background from uncorrelated photon pairs, which show the biggest contribution for large values of α as seen in Figure 6.1.

The eight sector combinations for which invariant mass distributions have been generated for the analysis are given in Table 6.1. No combinations between PbGl and PbSc have been used, nor combinations between east and west arm. In the following we will always refer to the sector combination W0W1W2_ScE as PbSc and E0E1 as PbGl, respectively.

6.1.2 Mixed Events

The *event mixing* method is a widely used technique to determine the combinatorial background of combined particle properties, e.g. the invariant mass of a photon pair. The basic

Mult. class	0	1	2	3	4	5	6	7
	Maximum multiplicity per sector							
PbGl	5	10	15	20	25	30	50	> 50
PbSc	2.9	5.7	8.6	11.4	14.3	17.1	28.6	> 28.6

Table 6.2: The eight multiplicity classes used for the event mixing for PbGl and PbSc in the analysis of the Au + Au data.

Vertex class				
0	1	2	3	4
Maximum z (cm)				
-15	-5	5	15	> 15

Table 6.3: The five vertex classes used for the event mixing.

idea is to compare the result obtained by combining particles within one event to the result for particle combinations from different events, which are a priori not correlated.

In the case of the π^0 invariant mass, the mixed event distribution is determined by combining one photon candidate from the current event with all photon candidates from previous events. The number of previous events used for the pair combinations determines the statistical error of the background and is limited basically by computing resources. In this analysis a buffer of three previous events is used for the event mixing with the current event.

In order to describe the combinatorial background correctly it is essential that the events used for mixing have similar properties as the real event and that they are not biased toward a certain reaction, as e.g. events that are chosen because of a high- p_T photon trigger. For this reason only minimum bias events are considered for the event mixing and different event classes are employed. First the events are divided into eight different multiplicity classes as given in Table 6.2. This ensures that only events with similar centrality and thus similar energy spectra of the particles are combined.

For the calculation of the invariant mass the three momentum components of the particles are needed. The momentum acceptance, and hence the pair mass distribution, changes depending on the vertex position. For this reason the events in each multiplicity class are divided into five vertex classes given in Table 6.3 and the momenta of the two combined particles in the mixed events are recalculated with respect to the new vertex z_{mix} given by:

$$z_{\text{mix}} = \frac{z_{\text{current}} + z_{\text{previous}}}{2}. \quad (6.3)$$

It is self-evident that for the photons used in the event mixing the same criteria are applied as for the pair combinations from one event, such as PID cuts, cuts on bad modules, and the asymmetry cut. Other properties valid a priori for the real photon pairs, e.g. a minimum distance that allows to distinguish them, have to be considered in addition. In the analysis a minimum distance cut of at least 8 cm is required for each photon pair combination, within one event and for mixed events, respectively.

Background Scaling and Subtraction

Before the mixed event background $M(p_T, m_{\text{inv}})$ can be subtracted from the invariant mass distribution for real events $R(p_T, m_{\text{inv}})$, it has to be scaled to account for the increased number of pair combinations in the mixed events. The scale factor or function is determined by dividing the real and the mixed invariant mass distributions as shown in Figure 6.2. Two features of the distributions are remarkable. First, the apparent rise for low transverse momentum of the pair and for low invariant mass. This has already been observed earlier and might be due to two-particle Bose-Einstein correlations as discussed in [Ste94]. However, other explanations such as the correlation of two particles by overlapping clusters, which are not correctly unfolded, need also to be considered. Second, for low p_T the real over mixed ratio shows a residual slope that seems not to be related to the π^0 decay. As a consequence a constant scaling of the mixed event background is not sufficient, instead a scaling function is used:

$$M_{\text{scaled}}(p_T, m_{\text{inv}}) = f(p_T, m_{\text{inv}}) \cdot M(p_T, m_{\text{inv}}). \quad (6.4)$$

The scaling function $f(p_T, m_{\text{inv}})$ is determined by fitting a polynomial in the range $m_{\text{inv}} \in [0.05 \text{ GeV}/c^2, 0.48 \text{ GeV}/c^2]$ with the π^0 peak excluded ($m_{\text{inv}} \notin [m_\pi - 3.5 \cdot \sigma_\pi, m_\pi + 4 \cdot \sigma_\pi]$). The values for the width σ_π and the mean m_π are taken from a centrality- and p_T -dependent parameterization as described below. In the analysis a linear fit is used as the scaling function up to $p_T = 3 \text{ GeV}/c$ and a constant fit above. To cross-check the result, the ratio is also fit by a polynomial plus a Gaussian with the peak region included.

For the determination of the scaling function for large pair- p_T the statistics in the real event sample are too poor to lead to stable results. Instead a constant scaling factor $f(p_T)$ is used if the ratio shows bins with zero entries in the fit region. The scaling factor is determined by integrating the real and the mixed invariant mass distributions in the range with the peak region excluded as given above:

$$f(p_T) = \frac{\int R(p_T, m_{\text{inv}}) dm_{\text{inv}}}{\int M(p_T, m_{\text{inv}}) dm_{\text{inv}}}. \quad (6.5)$$

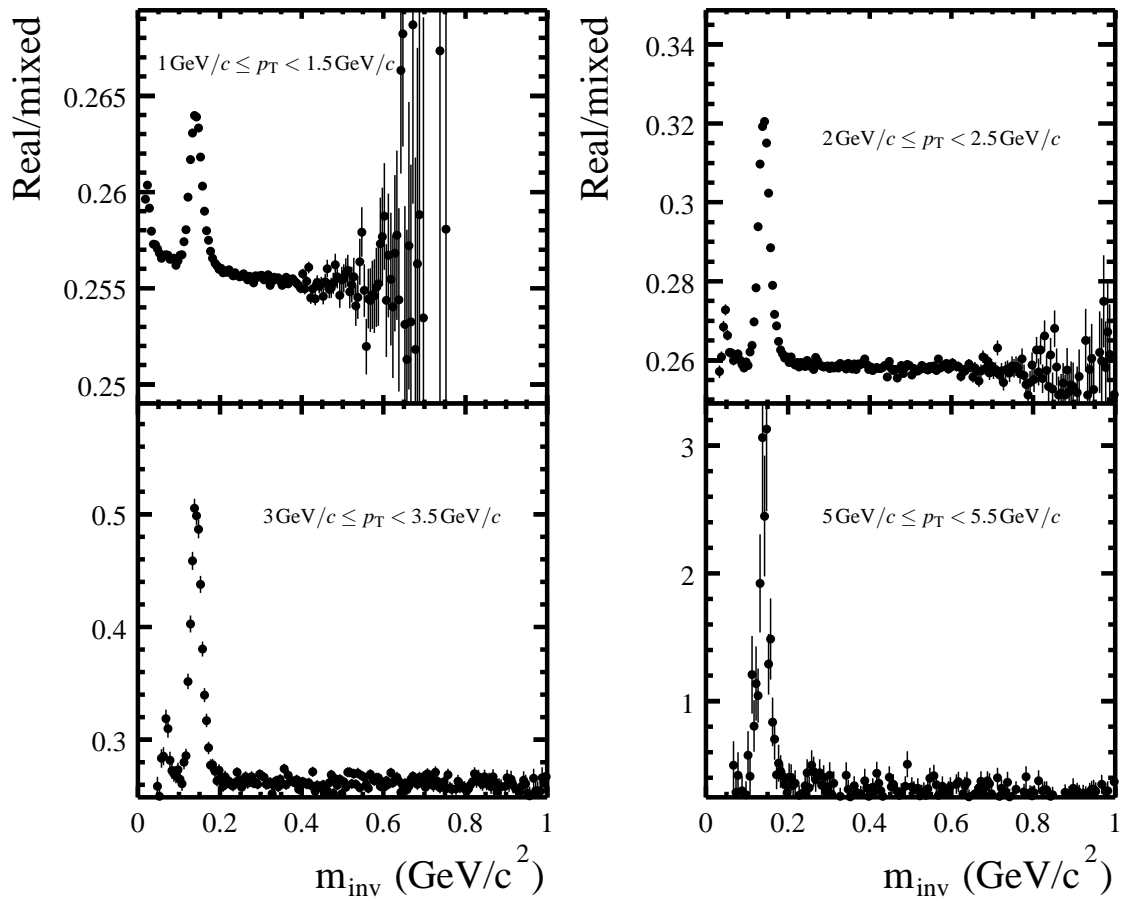


Figure 6.2: The ratio of the invariant mass distributions from real and mixed events for different p_T bins from minimum bias events in the PbPb.

The resulting scaled background for different p_T is shown in Figure 6.3 together with the invariant mass distribution from real events.

After subtraction of the background the remaining distribution is integrated in the peak region to obtain the raw π^0 yield in this transverse momentum range (see Figure 6.4). The integration region is, just as the fit region, determined by the mean and the width of the π^0 peak and given by $m_{\text{inv}} \in [m_\pi - 3 \cdot \sigma_\pi, m_\pi + 3 \cdot \sigma_\pi]$.

The values of the peak width and mean are extracted in one initial analysis of the invariant mass distribution in which a p_T dependent parameterization, as given by Equation (6.6), is determined for different centralities. The p_T dependence for different centralities is shown in Figure 6.5. The observed increase of the peak position in central collisions is due to the high multiplicity. With increasing multiplicity it becomes more probable that two particles are so close to each other that they form only one cluster. Due to the steeply falling spectrum the measured energy for highly energetic photons is most likely influenced by low energetic particles, thus only slightly shifted. The correlation for the decay photons is still retained, but the measured π^0 peak positions are shifted toward higher values and the energy resolution, reflected in the width of the π^0 peak, is worse in more central collisions. This effect also plays an important role for the determination of the detection efficiency as described below.

The use of a predefined value for the position and spread of the π^0 peak as given by:

$$\begin{aligned} m_\pi(p_T) &= a_0 + a_1 \cdot \exp\left(\frac{p_T^2}{2a_3^2}\right) \\ \sigma_\pi(p_T) &= b_0 + b_1 \cdot \exp\left(\frac{p_T^2}{2b_3^2}\right), \end{aligned} \quad (6.6)$$

has the advantage that even in p_T regions where no fit to the subtracted invariant mass distribution is possible, the integration region is well defined just by extrapolation from low p_T . This is illustrated in Figure 6.6 for central Au + Au collisions.

Countsheets

During the analysis the different steps of the peak extraction are documented in so-called *countsheets*. The countsheets contain for each p_T bin the plots for the ratio of real over mixed invariant mass distribution, the scaled mixed distribution, and the invariant mass distribution after background subtraction. Additionally, the fitted functions and integration regions are listed together with the raw count of π^0 s for this p_T . Some examples of countsheets are given in Appendix D. The use of countsheets provides a good visual control of the peak extraction procedure and of the event mixing method. Though the amount of this control output is large due to the different centrality selections, PID criteria, event

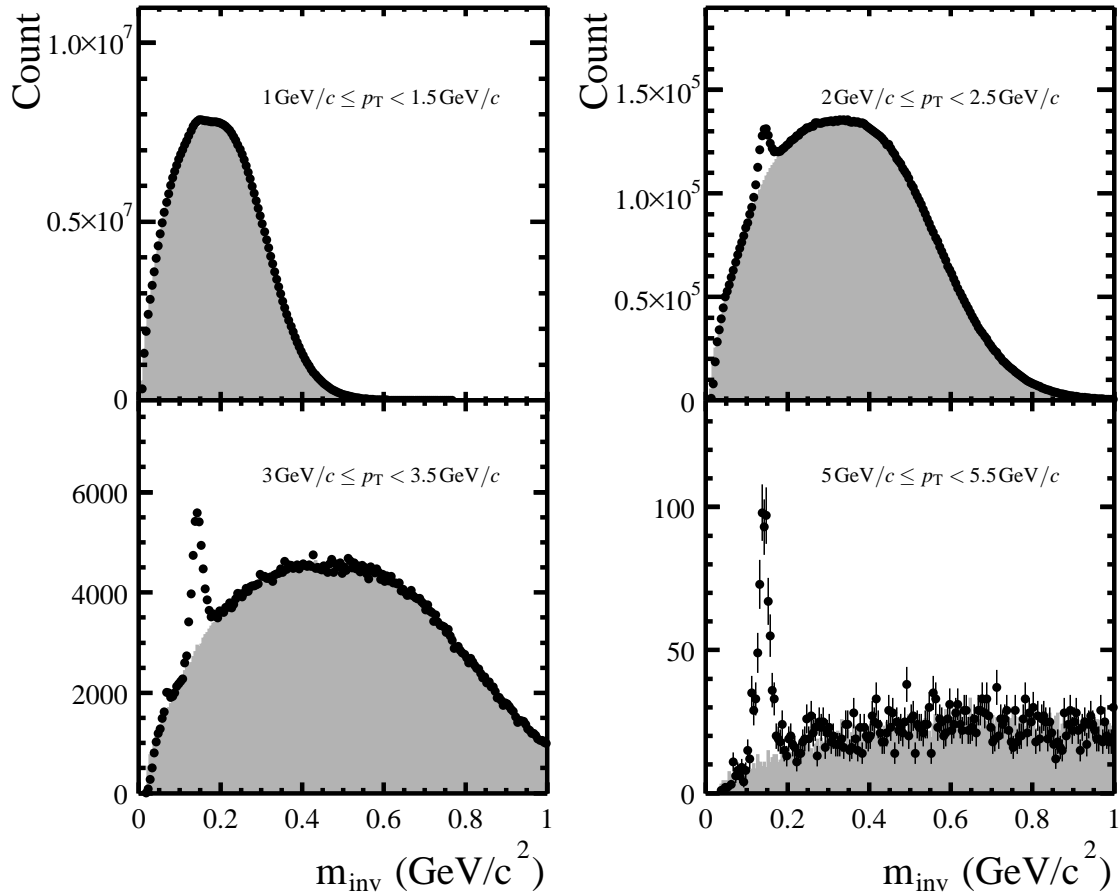


Figure 6.3: Invariant mass distributions for real events (full circles) and scaled background (grey) for minimum bias events as measured with the PbGl.

samples, and sector combinations, it allows the detailed investigation in the case that the extracted raw yields show conspicuous behavior.

6.1.3 Triggered Data

In addition to the minimum bias event sample, we make use of events that are enriched with highly energetic photons. In the case of the Au + Au run this sample has been obtained by the EMCal LVL2 trigger, while in d + Au the LVL1 ERT trigger has been used (see Section 4.5).

As already mentioned, it is important for the correct determination of the background of the invariant mass distribution to use only minimum bias events for the event mixing. For other events, which require at least one highly energetic photon by means of a trigger,

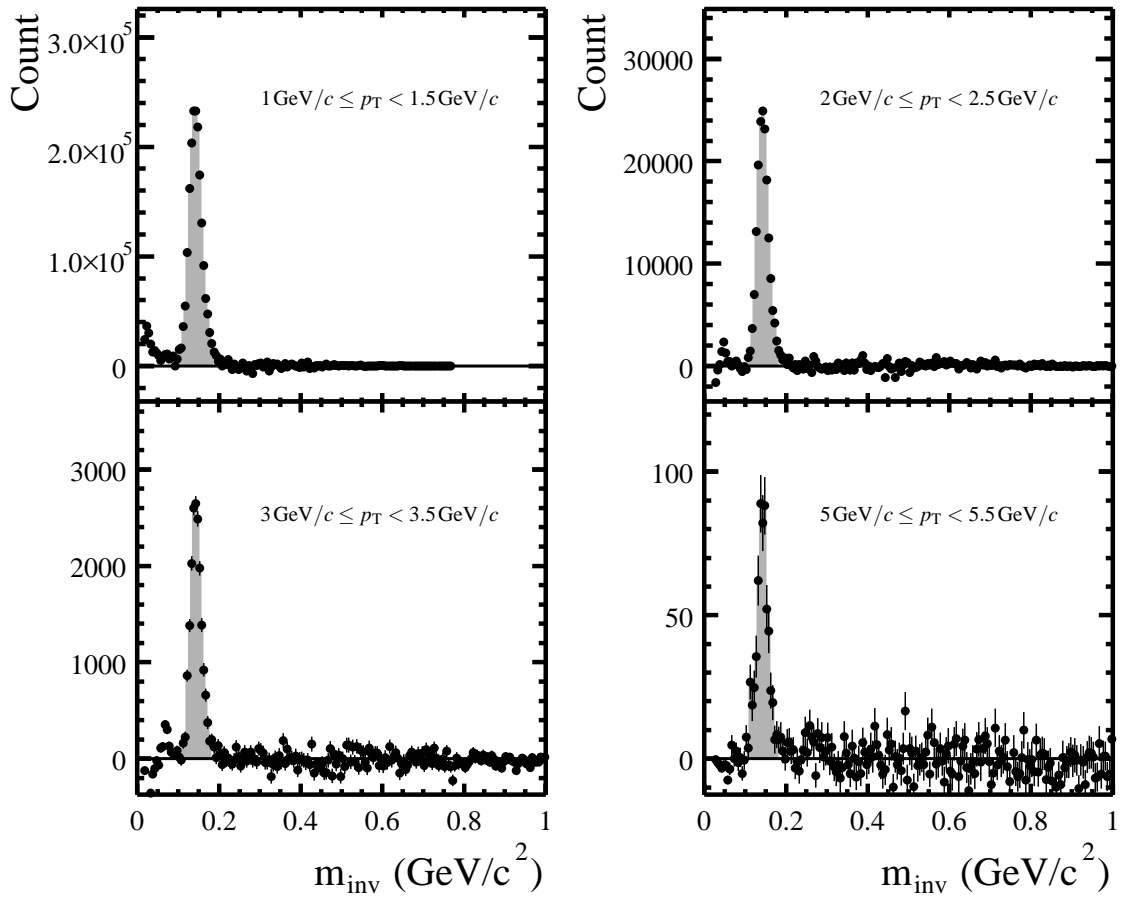


Figure 6.4: π^0 peak after background subtraction (minimum bias events PbPb), the integration region used for yield extraction is shaded grey.

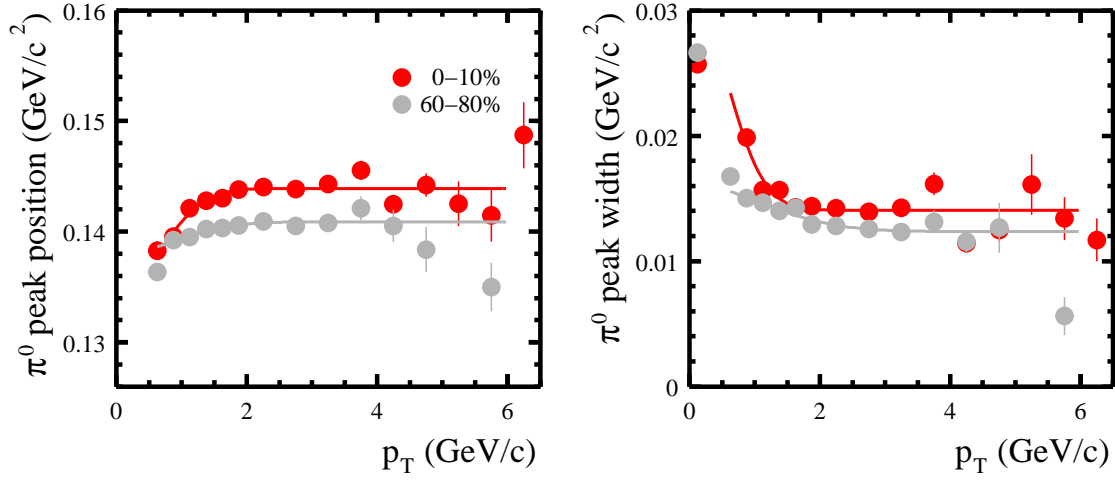


Figure 6.5: Parameterization of the π^0 peak position and width in central and peripheral collisions measured with the PbGl.

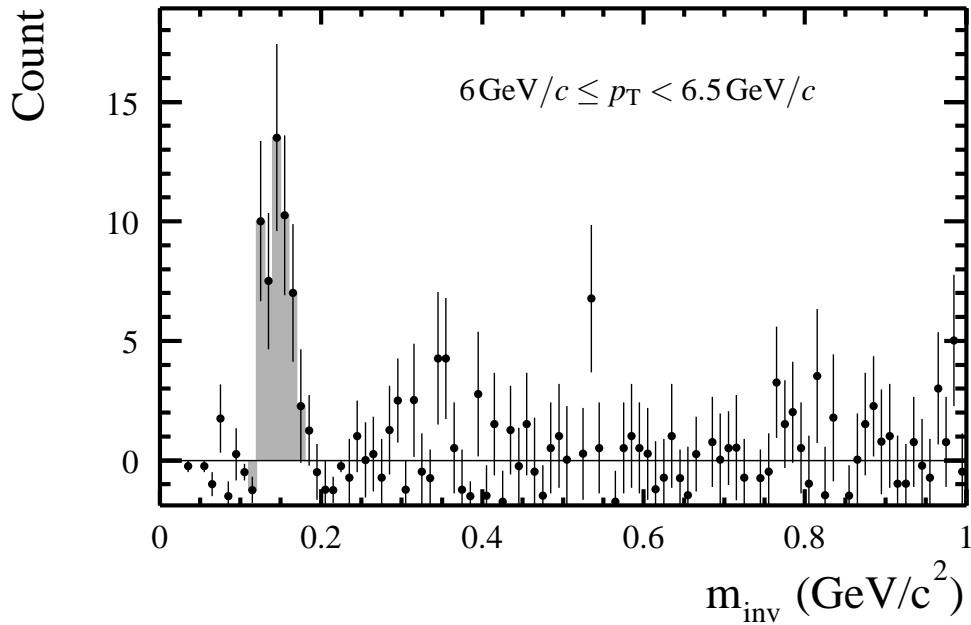


Figure 6.6: Yield extraction for the PbGl with the predefined integration region (grey) in central events. A clear signal is seen in the expected region, but a determination of the position and width is difficult.

the single photon energy spectrum is biased, and the low energetic part of the spectrum is not represented correctly.

One problem in the analysis of the d + Au high- p_T event sample is that most of the runs are filtered for the Gamma1 trigger, and thus they do not contain minimum bias events. For these data a new approach is used that softens the bias of the triggered data and makes them usable for the event mixing. Before a Gamma1 event is considered for the event mixing one highly energetic hit is removed from the event. The hit is chosen randomly from a list of hits that have to satisfy the following conditions:

- The hit has to lie on a FEM that caused a trigger (see Section 4.5.1).
- It has to be the hit with the highest measured energy within the FEM.

This ensures that only hits are removed, which are probably responsible for the acceptance of the event by the trigger. Due to the low multiplicity in d + Au the number of those hits or *trigger particles* is usually one. The mixed event distribution from those *pseudo* minimum bias events provides a good description of the background as illustrated in Appendix D by means of the countsheets. At large transverse momenta, where the Gamma1 data are used for the final result, the combinatorial background plays only a minor role.

Trigger Efficiency

When minimum bias data and data from other triggers are combined it is important to consider the difference in the bias on the event by the trigger devices BBC and ZDC on the one hand and EMCal with ERT or LVL2 system on the other hand. In the π^0 and direct photon analysis the EMCal acts as detector and trigger at the same time. But the identification of highly energetic hits is different for the trigger than in the actual analysis because of different calibration factors and more refined clustering during the offline DST production.

This becomes clear when comparing the energy spectra from minimum bias events, which are not influenced by the trigger settings for the EMCal, with the data from triggered events after scaling with the number of underlying minimum bias events as described in Section 5.1.2. For example, in case of the ERT trigger the predefined analog threshold does not determine a sharp energy cut-off at the nominal value of 2.1 GeV. Instead a slow increase over a broad energy range is observed, which reflects the deviation of the hit energy determined by the analog 4×4 sum and the offline clustering (see Figure 6.7). The energy-dependent trigger efficiency obtained by this comparison and shown in Figure 6.7(a) is expected to reach a plateau at a value of one, if the active detector area considered in the analysis is the same as in the trigger.

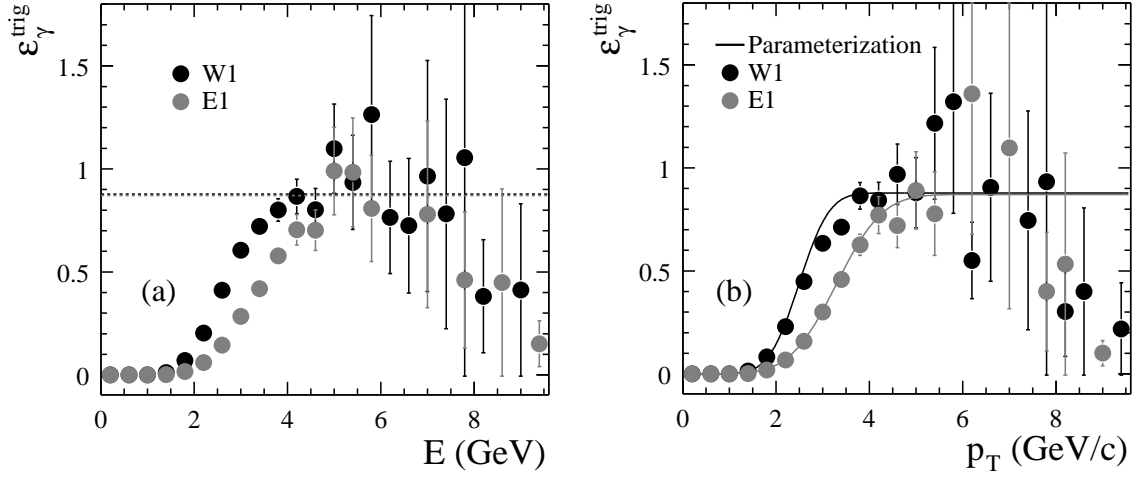


Figure 6.7: Trigger turn-on or trigger efficiency ($\epsilon_{\gamma}^{\text{trig}}$) for two EMCAL sectors determined by the comparison of minimum bias data and Gamma1 data in d + Au collisions. The geometrical limit is shown as well as the parameterization used in the simulation of the π^0 trigger efficiency.

This is not the case for the Gamma1 trigger used in the analysis of the d + Au data. Some FEMs had to be disregarded (*masked*) for the trigger, because they contained bad modules that otherwise would have caused wrong trigger decisions. Effectively this leads to a reduction of the EMCAL acceptance for the trigger and less highly energetic hits compared to minimum bias events. Thus the trigger efficiency is limited by the geometrical limit $\epsilon_{\text{geo}}^{\text{trig}}$ determined by the number of active modules lying within a masked FEM $N_{\text{module}}^{\text{active} \wedge \text{masked FEM}}$ compared to the total geometrical acceptance of the detector given by the number of active modules $N_{\text{module}}^{\text{active}}$:

$$\epsilon_{\text{geo}}^{\text{trig}} = 1 - \frac{N_{\text{module}}^{\text{active} \wedge \text{masked FEM}}}{N_{\text{module}}^{\text{active}}}. \quad (6.7)$$

A map of FEMs masked in the Gamma1 trigger is shown in Appendix C. The resulting geometrical limits of the efficiency are given in Table 6.4 for all sectors.

In the analysis of π^0 s we are interested in the p_T dependence of the trigger efficiency $\epsilon_{\pi^0}^{\text{trig}}$ for the two decay photons. It can be modeled within a simulation by a threshold applied to each individual decay photon. To describe the slow turn-on the threshold fluctuates with a Gaussian distribution $g(p_T)$ around a mean value. The parameters for the individual sectors are given in Table 6.4. They are determined by a fit to the measured trigger efficiency for single particles with an integrated Gaussian distribution:

$$\epsilon_{\gamma}^{\text{trig}}(p_T) = \int_{-\infty}^{p_T} g(p'_T) dp'_T. \quad (6.8)$$

Sector	$\epsilon_{\text{geo}}^{\text{trig}}$ (%)	Mean (GeV/c)	Width (GeV/c)
E0	82.0	3.68	0.91
E1	87.1	3.29	0.78
E2	88.5	2.48	0.47
E3	88.6	2.54	0.48
W0	89.3	2.62	0.62
W1	87.8	2.49	0.51
W2	74.6	2.54	0.55
W3	95.8	2.57	0.54

Table 6.4: The geometrical limits of the ERT trigger efficiency for the different sectors as well as the mean and the width of the assumed Gaussian distribution of the trigger thresholds, which are determined by a fit to the trigger efficiency with Equation (6.7) as shown in Figure 6.7(b).

At large transverse momenta, where the overlap between minimum bias data and Gamma1 triggered events is not sufficient, the fit is fixed to the expectation from the geometrical limit of the trigger efficiency. This is shown in Figure 6.7(b).

To determine the trigger efficiency in the simulation and for the real data in a consistent way, it is required in the analysis that for a given hit pair in a Gamma1 event, the hit with the higher energy lies on a FEM that caused a trigger. In the simulation the hit that passes the threshold has to lie on a FEM that is also active in the trigger. The advantage of this requirement is that the turn-on curve should approach the geometrical efficiency limit for a single photon given by Equation (6.7). The agreement between measured data and the simulation is illustrated in Figure 6.8.

Though the trigger efficiency is well described over a broad p_T range the Gamma1 triggered data are only used above $p_T^{\text{trans}} = 6 \text{ GeV}/c$, where the efficiency approaches the geometrical limit. Since the minimum bias data in this p_T region add little statistics to the measurement, a sharp transition is used for the combined result for the π^0 raw yield in d + Au:

$$\frac{1}{N_{\text{evt}}} \frac{dN_{\text{raw}}}{dp_T} = \begin{cases} \frac{1}{N_{\text{evt}}^{\text{mb}}} \frac{dN_{\text{raw}}^{\text{mb}}}{dp_T} & \text{for } p_T < 6 \text{ GeV}/c, \\ \frac{1}{\epsilon_{\pi^0}^{\text{trig}}} \frac{1}{N_{\text{evt}}^{\text{mb}}} \frac{dN_{\text{raw}}^{\text{Gamma1}}}{dp_T} & \text{for } p_T \geq 6 \text{ GeV}/c. \end{cases} \quad (6.9)$$

In the analysis of the Au + Au data the trigger turn-on is better determined, because the calibration factors employed by the LVL2 algorithm were close to the final calibration factors used in the analysis. In addition, the LVL2 algorithm allows to mask individual

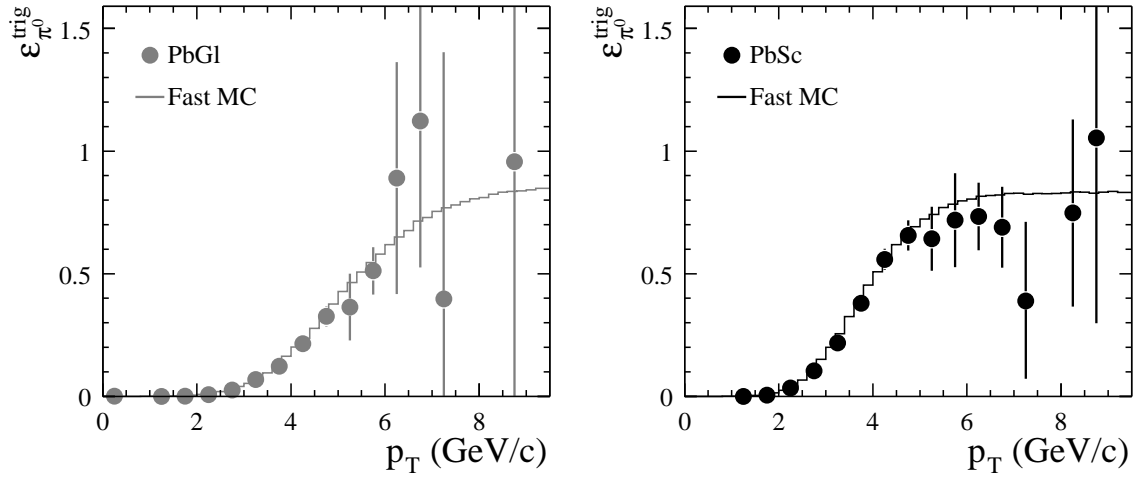


Figure 6.8: Trigger efficiency for π^0 s as modeled in the simulation and determined in real d + Au collisions.

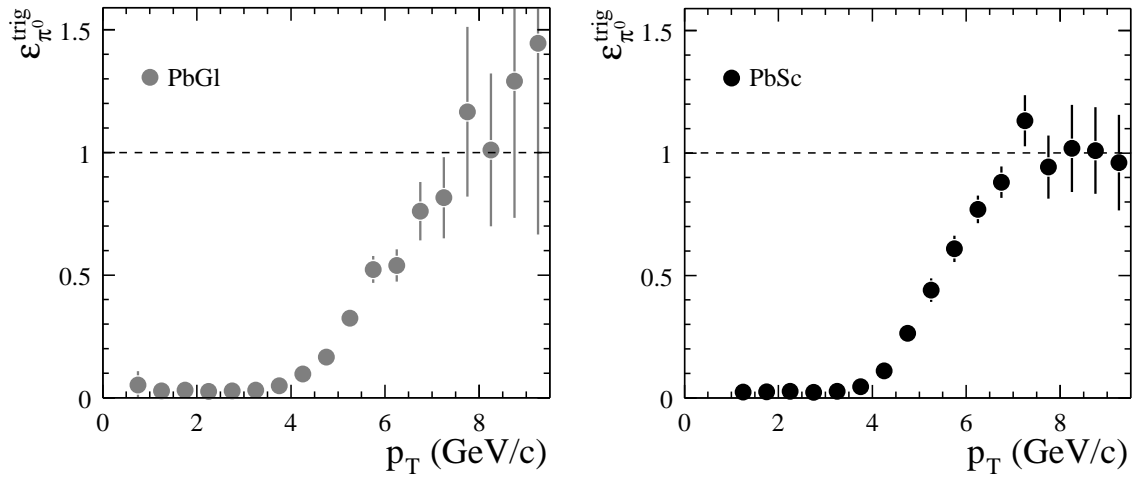


Figure 6.9: Efficiency of the LVL2 EMCAL trigger for π^0 s, determined for the PbG1 and the PbSc by comparison of triggered data with minimum bias events for the centrality selection 0–92%.

modules, which are usually also excluded during the analysis. This leads to a trigger efficiency that reaches the geometrical limit of 100% for large photon transverse momenta (see Figure 6.9). However, for the π^0 measurement the LVL2-triggered data are only considered in the case of the PbSc. For the PbGl the trigger efficiency reaches its plateau value later and the uncertainty introduced by the use of triggered data is not compensated by the additional statistics.

For the Au + Au data the size of the minimum bias event sample and the size of the data set filtered for the LVL2 trigger (the number of underlying minimum bias events, see Table 5.1.2), are of the same order of magnitude. Therefore the results of the two data sets are combined in the case of the PbSc where the trigger becomes fully efficient:

$$\frac{1}{N_{\text{evt}}} \frac{dN_{\text{raw}}}{dp_{\text{T}}} = \begin{cases} \frac{1}{N_{\text{evt}}^{\text{mb}}} \frac{dN_{\text{raw}}^{\text{mb}}}{dp_{\text{T}}} & \text{for } p_{\text{T}} < 6.5 \text{ GeV}/c, \\ \frac{1}{N_{\text{evt}}^{\text{mb}} + N_{\text{evt}}^{\text{LVL2}}} \left(\frac{dN_{\text{raw}}^{\text{LVL2}}}{dp_{\text{T}}} + \frac{dN_{\text{raw}}^{\text{mb}}}{dp_{\text{T}}} \right) & \text{for } p_{\text{T}} \geq 6.5 \text{ GeV}/c. \end{cases} \quad (6.10)$$

6.2 Fully Corrected Spectra

Particle production in ultra-relativistic reactions is usually described in the Lorentz invariant form of the differential particle yield:

$$\frac{1}{2\pi p_{\text{T}} N_{\text{in}}} \cdot \frac{d^2 N^{\text{X}}}{dp_{\text{T}} dy} = \frac{1}{2\pi p_{\text{T}} N_{\text{in}}} \cdot \frac{\Delta N^{\text{X}}}{\Delta p_{\text{T}} \Delta y}, \quad (6.11)$$

with ΔN^{X} the total number of particles (e.g. π^0 s) produced in N_{in} inelastic reactions within the pseudo-rapidity window Δy and the transverse momentum interval $\left[p_{\text{T}} - \frac{\Delta p_{\text{T}}}{2}, p_{\text{T}} + \frac{\Delta p_{\text{T}}}{2} \right]$, which is determined by the bin width in the analysis.

The Lorentz invariant yield is connected to the invariant cross section via the total inelastic cross section σ_{in} :

$$E \frac{d^3 \sigma}{d\vec{p}^3} = \frac{1}{2\pi p_{\text{T}} N_{\text{in}}} \cdot \frac{d^2 N^{\text{X}}}{dp_{\text{T}} dy} \cdot \sigma_{\text{in}}. \quad (6.12)$$

However, the determination of the total inelastic cross section is an experimental challenge already in elementary reactions. It involves precise beam studies for the measurement of the luminosity, which have only been performed for p + p collisions at PHENIX (see [Adl03c, Bel03]), and the determination of the minimum bias trigger efficiency for inelastic reactions.

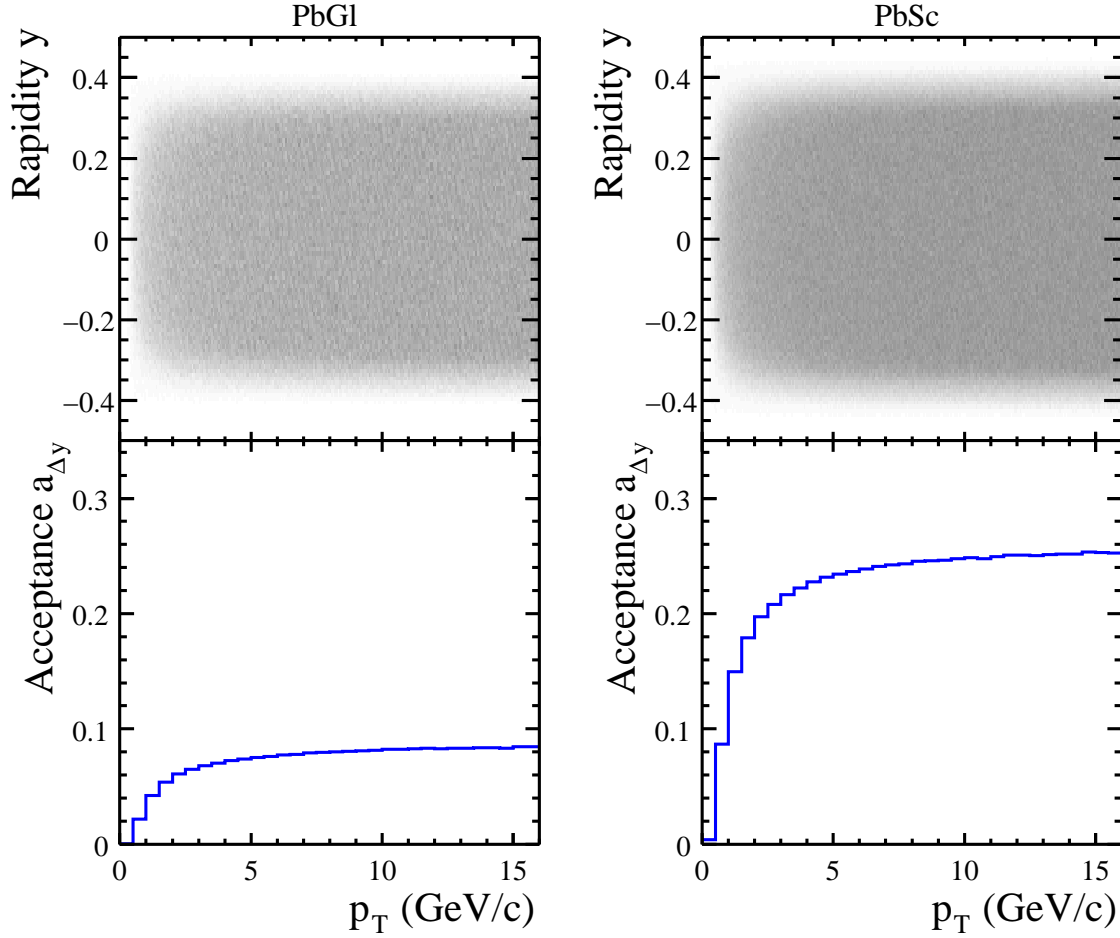


Figure 6.10: Geometrical acceptance of the PbGl and the PbSc for $\pi^0 \rightarrow 2\gamma$ within the rapidity interval $|y| < 0.45$.

To convert the raw yield of π^0 s, determined with the EMCAL as described in Section 6.1, into its Lorentz invariant form and to account for inefficiencies and losses during the detection of the π^0 s several correction factors have to be applied:

$$\frac{1}{2\pi p_T N_{\text{in}}} \cdot \frac{d^2 N^{\pi^0}}{dp_T dy} = \frac{1}{2\pi p_T \tilde{N}_{\text{mb}}} \cdot \frac{1}{a_{\Delta y}(p_T) \epsilon(p_T) c_{\text{conv}} c_{2\gamma}} \cdot \frac{\Delta N_{\text{raw}}^{\pi^0}}{\Delta p_T \Delta y}. \quad (6.13)$$

The determination of the detection efficiency $\epsilon(p_T)$ for each centrality selection and PID cut as well as of the acceptance correction $a_{\Delta y}(p_T)$ is described in detail in the following sections. The factor $c_{2\gamma} = 0.98798 \pm 0.032$ is the branching ratio of the neutral pion decay into two photons [Eid04], which corrects for the fact that the invariant mass analysis is only sensitive to this decay channel. The correction for π^0 s lost due to con-

version of one or both decay photons c_{conv} is also determined as part of the efficiency calculation in Au + Au, but applied separately.

6.3 Geometrical Acceptance

The acceptance of a detector is determined by the number of particles hitting the detector surface compared to the number of particles emitted into the respective phase-space interval. The phase-space interval is usually chosen as a rapidity interval Δy and for full azimuthal coverage ($\Delta\phi = 2\pi$).

For single particles the acceptance is basically the fraction of phase-space covered by the detector in the interval. Within a rapidity interval of $\Delta y = 0.9$ the PbSc (excluding the sector W3) covers 26.4% of the phase-space and the PbGl 9%.

For neutral pions the situation is a bit more complex, as two photons are needed for the detection. In this case the acceptance depends on the kinematics of the π^0 decay, namely the opening angle between the two photons and hence the transverse momentum of the π^0 . In addition the acceptance is influenced by the vertex position, which is restricted for the analysis of real events to $|z_{\text{vtx}}| \leq 30$ cm.

All these aspects are taken into account in a fast Monte Carlo simulation [Rey03a] of the PHENIX setup, which is also used for the efficiency calculation in d + Au (see Section 6.4.2) and in the background determination for direct photon measurement. Within this fast Monte Carlo π^0 s are generated with the following characteristics:

- Flat transverse momentum distribution $0 < p_T \leq 20$ GeV/c,
- Uniform vertex distribution $|z_{\text{vtx}}| \leq 30$ cm,
- Gaussian rapidity distribution around zero in the interval $|y| \leq 0.45$ and width $\sigma_{\text{rap}} = 3$,
- Uniform ϕ distribution.

The π^0 decay is calculated via JETSET routines that are part of the PYTHIA event generator [Sjo01]. For each π^0 it is verified that both decay photons hit the detector. The resulting p_T distribution of accepted π^0 s is divided by the transverse momentum distribution of the generated π^0 s and provides the geometrical acceptance of the PbSc and PbGl, respectively. It is shown in Figure 6.10. For the correct determination of the acceptance it is important that the p_T distributions are weighted according to the real π^0 spectrum, because the center of a transverse momentum interval does not represent the mean p_T very well for wide intervals and the shape of the π^0 output distribution depends on the p_T of

the particle, especially at low transverse momenta. As the opening angle between the two photons increases with decreasing p_T it becomes more probable that one photon misses the detector when the transverse momentum of the π^0 approaches zero. The acceptance drops as seen in Figure 6.10.

The difference in the acceptance for PbGl and PbSc is basically determined by the number of sectors employed for the analysis, leading to a better ϕ coverage for the PbSc. In addition, the distance from the vertex is larger for the PbGl, which is reflected in the rapidity coverage of the detector as seen in Figure 6.10. The cut on bad modules is not taken into account in the acceptance calculation in the analysis of the Au + Au data. It is considered in the efficiency as discussed below.

6.4 Detection Efficiency

The goal of the efficiency determination for a detector is to correct for all detector specific effects and analysis cuts, which make the measured spectrum $f(p_{T_{\text{out}}})$ different from the true input spectrum $f(p_{T_{\text{in}}})$ of particles hitting the detector. This leads to the general definition of the efficiency:

$$\varepsilon(p_T) = \frac{f(p_{T_{\text{out}}})}{f(p_{T_{\text{in}}})}. \quad (6.14)$$

The output spectrum and thereby the efficiency is influenced e.g. by the position and energy resolution of the detector but also by the event multiplicity, which determines the probability for EMCAL clusters to overlap. In addition, the efficiency depends on the various PID and analysis cuts and in case of the π^0 s on the determination of the yield via the invariant mass analysis.

The problem that the input spectrum for the efficiency determination is in principle unknown is circumvented by assuming a spectrum for a first pass, e.g. based on the measured raw spectrum. This spectrum is used to determine the efficiency for a first correction of the raw spectrum, resulting in a new input distribution. Iterative repetition of this procedure leads to a quick convergence of the calculation.

To illustrate two of the major influences on the efficiency, the steeply falling input spectrum and the limited energy resolution, we consider the extreme example of a flat input distribution as illustrated in Figure 6.11(a). A limited energy resolution leads to a redistribution of the yield in one energy or p_T -bin to the neighboring bins. As this is true for any p_T bin, the loss in one bin for a flat input spectrum (and constant energy resolution) is compensated by the gain from the surrounding bins, leading to identical input and output spectra, hence an efficiency of one. For a steeply falling spectrum as shown in Figure 6.11(b) the situation is different. The change of yield in each bin is

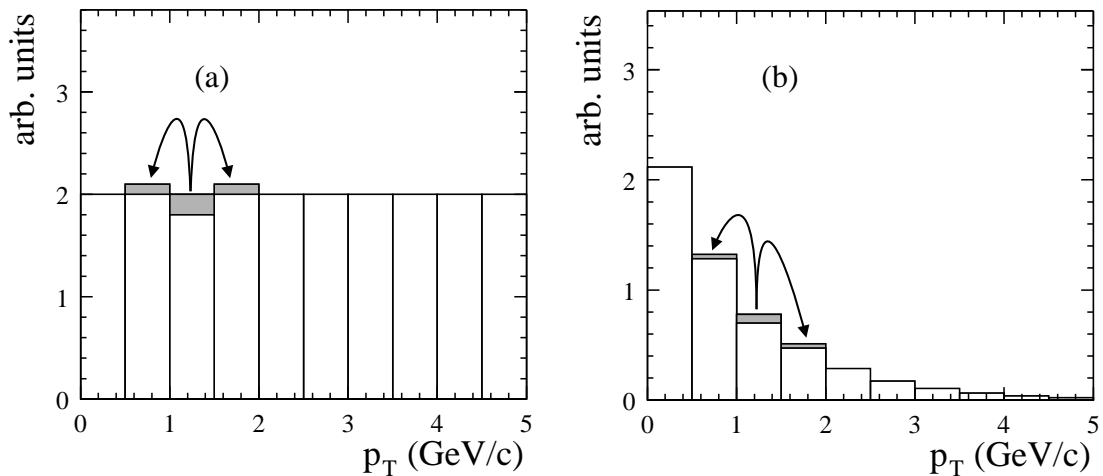


Figure 6.11: Illustration how the efficiency is influenced by different shapes of the input spectrum.

dominated by the gain from lower p_T , which is larger than the loss for this p_T , the feed-down from higher p_T plays only a minor role. This leads to an overall shift of the yield toward higher transverse momenta and an efficiency larger than one.

The determination of the efficiency is done with different approaches in the analysis of the Au + Au and the d + Au data and will be discussed in detail, as it represents the main source of systematic errors. Uncertainties in the π^0 measurement directly affect the extraction of the direct photon signal, as the background is determined mainly by the π^0 decay photons.

6.4.1 Efficiency from Embedding

The general idea of this method is to merge the EMCal data from real events with the data from the simulation of single particles, e.g. π^0 s. Reconstructing the properties of these *embedded* particles allows a detailed study of how the measured spectrum is influenced by the detector and the high-multiplicity environment. The main advantage of this technique is that the merged event can be processed within the same clustering algorithm (see Section 5.2.1) and analyzed within the same framework as the real data. In addition, the combination with the real event provides the measured behavior of the detector in a high multiplicity environment, something no simulation can accomplish as accurately.

The various steps toward a determination of the efficiency shall be discussed in the following. We will concentrate on the efficiency determination for π^0 s. The same procedure is used for the single photon efficiency (see Section 7.1.1). The framework described below is also used for the determination of the detector response to neutron and antineutrons as described in Section 7.1.3.

Simulation of Single Particles

The simulation of single particles is carried out within the PISA framework², a simulation of the complete PHENIX setup based on the GEANT package [Bru93]. The input single particles are generated with the following characteristics using the event generator *EXODUS* [Ave03]:

- Single particle $p_T = 0 - 20 \text{ GeV}/c$, with a flat distribution,
- Pseudo-rapidity $|y| < 0.37$ (flat),
- ϕ isotropic within the EMCal acceptance,
- Flat vertex distribution, $|z_{\text{vtx}}| \leq 30 \text{ cm}$.

The PISA output files generated with the simulation contain the relevant information on the input particles as well as the detector response. They are used to generate the *simulated DSTs*. These DSTs contain the same data fields as the real DSTs such as a list of towers with energy information and lists of clusters. In addition, simulation-specific information is stored in the simulated DSTs, e.g. the ancestry of all particles hitting the detector. During the generation of the simulated DSTs a cut is used, which only accepts the π^0 s decaying into two photons and which requires that both photons are heading toward the calorimeter. This allows to factorize out the effects from Dalitz decays and defines a clear interface between the efficiency and acceptance calculation (see Section 6.3).

Embedding of Simulated Particles

The embedding of the simulated particles into a real event is done within a framework similar to the standard PHENIX framework *ezdstd* used to analyze different kinds of input files ranging from DSTs to nanoDSTs [Pin03]. The main flow of the embedding program as shown in Figure 6.12 is described in the following.

For the embedding, a DST containing real data is read in together with one or more simulated DSTs for different particle species (π^0 , γ , n and \bar{n}). Real events are only considered if they satisfy the minimum bias trigger condition and the same vertex cut used during the analysis. The simulated events are scanned prior to the embedding, and their position within the DST is sorted into one of twelve vertex classes, each 5 cm wide. This allows to select directly a simulated event with the appropriate vertex for combination with the real event. One further advantage of this *prescan* is that the vertex classes can be used as a *ring-array* to recycle the simulated events if the statistics within a vertex class

²PHENIX Integrated Simulation Application [Mag04]

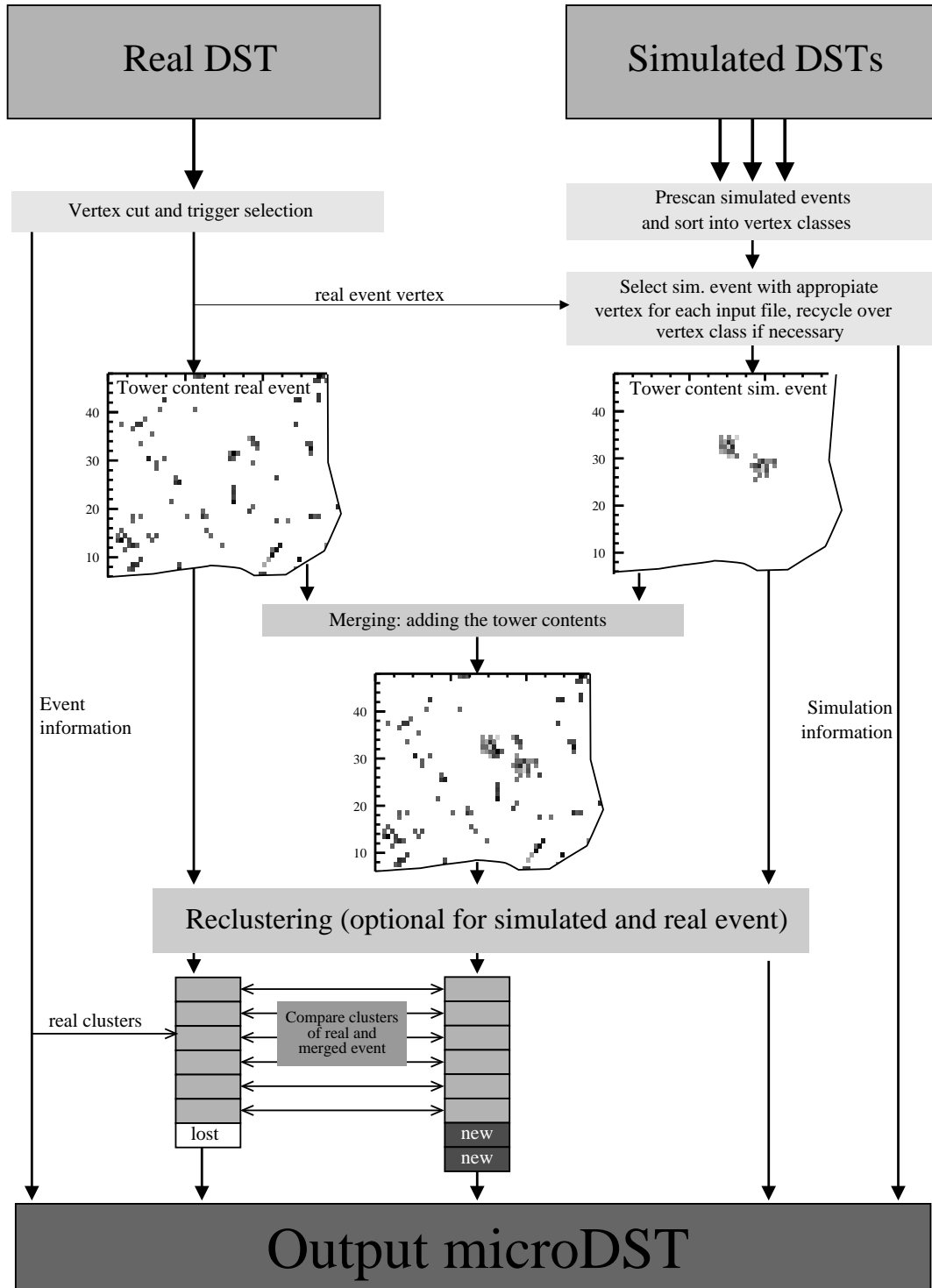


Figure 6.12: Main program flow of the embedding algorithm.

does not cover the number of real events for this vertex class. To avoid the duplication of results if one real DST is used together with the same simulated DST more than once, a randomized offset to the initial access of the array is introduced for each vertex class.

For each selected real event the tower information is extracted from the DST and merged with the tower data from one simulated event. The merging basically involves the addition of the energies as illustrated in Figure 6.12. The list of merged towers is now the basis for a new clustering. Due to the added information from the simulated event, the resulting list of *merged* clusters is different from the list of clusters from the real event. A comparison yields the modified or new clusters in the merged event and the lost clusters from the real event (see Figure 6.12).

In addition to the pure cluster data of the merged events, information from the simulation enter the list of modified clusters on the output level. For example, one piece of information needed later in the direct photon analysis is the distance of the new hit to the closest projection of a charged hit, where the charged hits incorporate the simulated PC3 hits as well as the PC3 hits from the real event.

The embedding output contains also data copied directly from the real and the simulated DST into the microDST format, such as trigger information of the real events and ancestry information of simulated particles. The relevant data used during the evaluation of the embedding output are:

- Event header information from the real event used for embedding (trigger, vertex, etc.),
- Lists of PC3 hits from the real event,
- Lists of EMCal clusters containing the new/modified hits after embedding,
- Lists of EMCal clusters from the pure simulation (the hits on the *empty* detector),
- Lists of PC3 hits from the simulated event,
- Simulated particle information, such as parent particles, primary momentum, and energy.

One optional feature of the embedding framework is to copy all data from the real DST into the output microDST, this allows in principle a complete analysis of the real data based on the embedding output.

Evaluation of the Embedding Output

The microDST output is analyzed with the same program as the real data. This ensures that all PID cuts, cuts on bad modules, and the calculation of the analysis variables are

identical for the evaluation of the embedding output. It also adds the future capability to analyze both real and embedded data at the same time, in case the embedding of simulated particles becomes a part of the DST production process.

Because the embedded particles are simulated with a flat p_T distribution to cover all transverse momenta with the same number of input particles, they have to be weighted with the real dN/dp_T distribution. Since the efficiency is used to determine the distribution this is an iterative process as discussed above. To describe the low p_T part of the spectrum where the particle production is dominated by soft processes and the spectrum for large transverse momenta, dominated by particle production in hard parton-parton scatterings, at the same time, a functional form is chosen that provides a smooth transition between a Hagedorn parameterization and a power law by weighting with a Woods-Saxon type function:

$$\frac{dN}{dp_T} = p_T \cdot a_{WS} \cdot \left(\frac{p_1}{b_1 + p_T} \right)^{b_2} + p_T \cdot (1 - a_{WS}) \cdot \left(\frac{b_3}{p_T} \right)^{b_4}, \quad (6.15)$$

$$\text{with } a_{WS} = \frac{1}{1 + \exp\left(\frac{p_T - a_1}{a_2}\right)}.$$

The weighting functions are determined for each centrality selection and are identical to the ones used for the determination of the decay background from radiative decays, needed for the analysis of direct photons.

The simulation of the PbSc and of the PbGl is basically tuned to test-beam measurements [Aph03a], with a far better energy resolution than during regular operation of the full EMCal over a long time period. This became obvious when comparing the width of the π^0 peak position between embedded simulated π^0 s and the result obtained for real π^0 s. To compensate for the difference, the energies of the new hits from embedding need an additional smearing for both PbGl and PbSc according to a Gaussian distribution around one, with a width σ given by:

$$\sigma_{\text{PbGl}} = 7\% + \frac{4\%}{\sqrt{E/(\text{GeV})}}, \quad (6.16)$$

$$\sigma_{\text{PbSc}} = 5\%. \quad (6.17)$$

The resulting good agreement between the π^0 peak in real and embedded events is shown in Figure 6.13.

In the simulation the time-of-flight (TOF) measurement for a PbGl hit is not implemented very well. In order to model the TOF cut for the efficiency calculation an energy

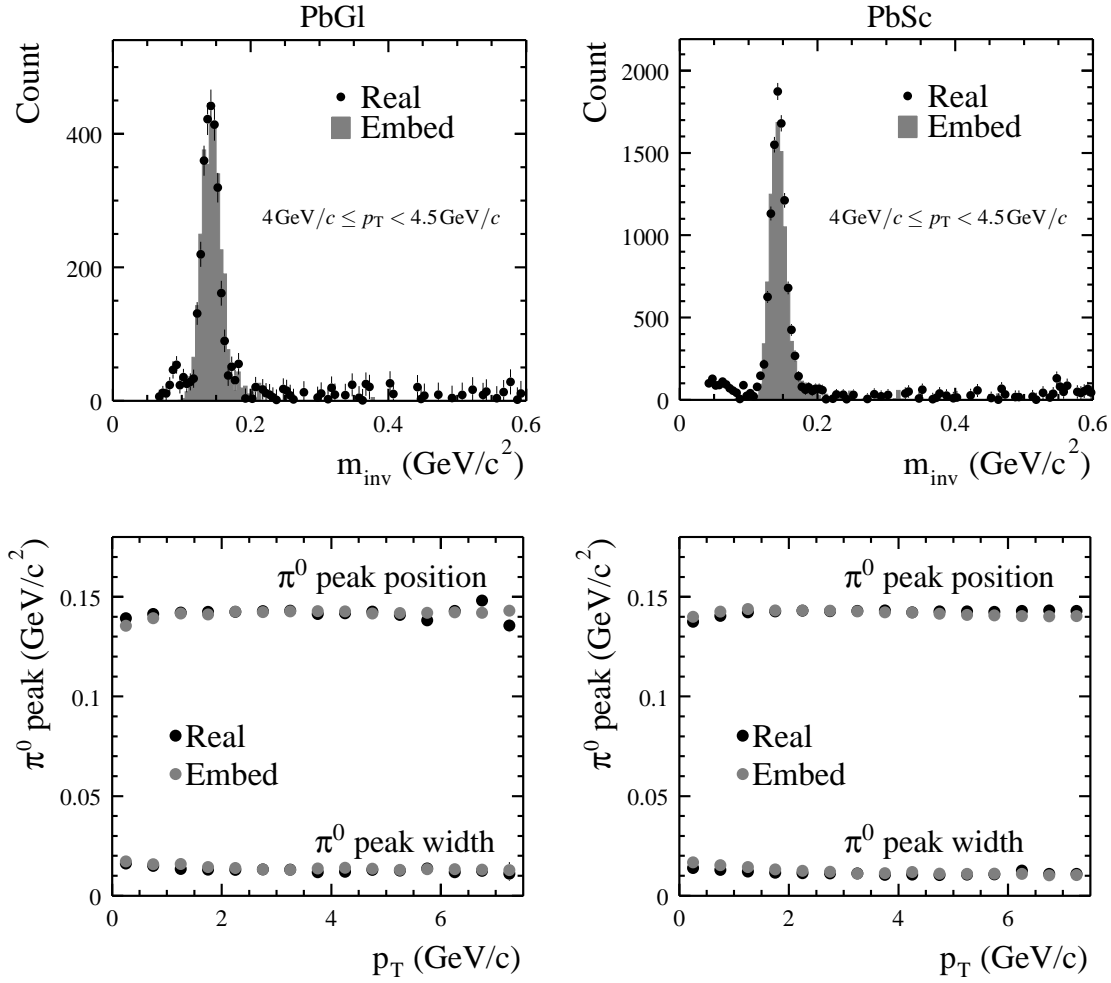


Figure 6.13: Comparison of the π^0 peak position in real events measured with the PbGl and the PbSc with the results obtained for embedded π^0 s.

and centrality dependent survival probability for photons p_γ is introduced. It has been determined by comparing the raw π^0 yields in the real data before (PID0) and after applying the timing cut (PID1). The π^0 s are required to satisfy a tight asymmetry cut ($\alpha < 0.2$), which limits the energy of the two photons to a similar value. The advantage of this method is that the two photons are identified via the π^0 invariant mass and the energy of the single photon can be estimated by the average energy of the two photons. This analysis of the π^0 yields the probability for both photons to survive the TOF cut $p_{2\gamma}$; the survival probability for single photons is simply given by:

$$p_\gamma = \sqrt{p_{2\gamma}}. \quad (6.18)$$

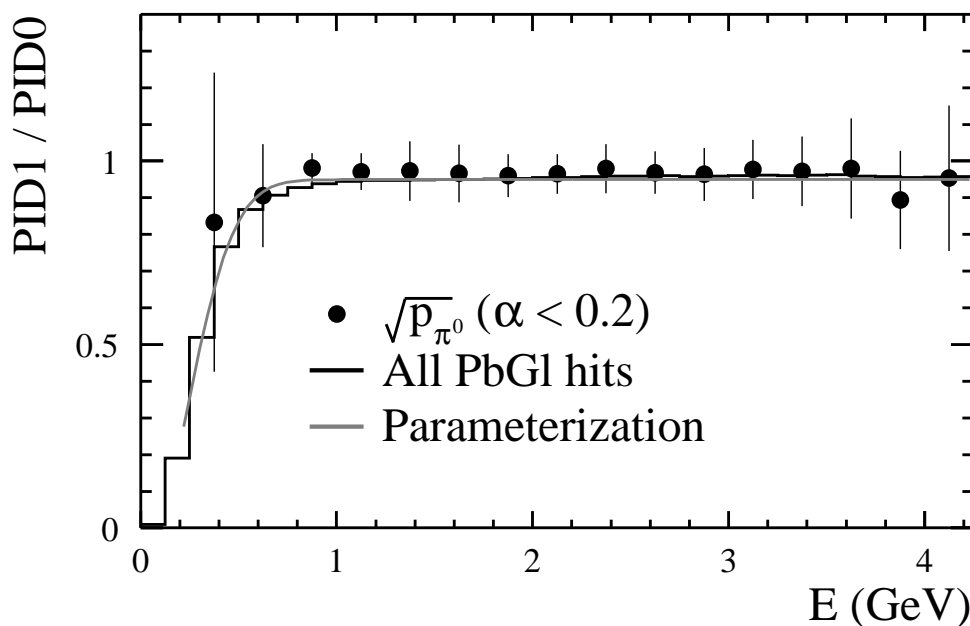


Figure 6.14: TOF survival probability determined via the comparison of the π^0 yields (with $E = 0.5 \cdot (E_1 + E_2)$) and all hits with and without TOF cut, and the parameterization used for the efficiency calculation.

The result for minimum bias events is shown in Figure 6.14, together with the parameterization used during the efficiency calculation. In addition, the ratio between the measured single hit distribution for PID0 and PID1 is shown. It is seen that in principle a comparison on this level is already sufficient to determine the parameterization. At low energies even more information is provided than in the comparison of the raw π^0 yields, due to the limited acceptance of the PbGl for π^0 s in this kinematical region.

Determination of the π^0 efficiency

For the determination of the π^0 efficiency only π^0 s are considered whose decay gammas did not convert. The conversion effect is taken into account separately. Additionally, it is required that the simulated response on the empty detector showed exactly two hits. This approach allows to calculate directly the invariant mass and the p_T of the π^0 before and after the embedding by using the two hits on the empty detector and the two new hits in the merged event that are closest to the hits on the empty detector, respectively. The advantage of this method is that the combinatorial background is negligible and the efficiency algorithm checks only if the embedded π^0 is lost. It does not accidentally count a real π^0 , whose clusters have been only slightly modified by the embedding, so that they can appear in the list of new clusters.

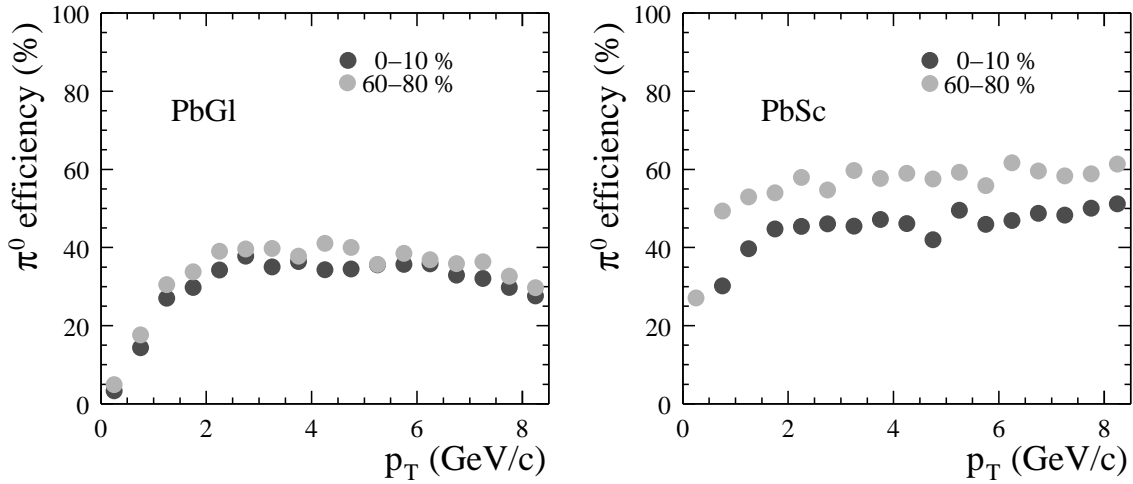


Figure 6.15: Detection efficiencies in Au + Au collisions for $\pi^0 \rightarrow 2\gamma$ for two different centralities and PID3 in the PbG1 and the PbSc.

The output spectrum for the π^0 s for each centrality is then simply determined by integrating the invariant mass distribution in a window of $3\sigma_{\pi^0}$ as in the analysis of the real event. As mentioned above each pair combination in the embedded event has to be weighted with the input p_T distribution given by Equation (6.15), where the transverse momentum is given by the known true p_T of the simulated π^0 .

The resulting efficiencies as defined by Equation (6.14) are shown for the PbG1 and the PbSc in Figure 6.15 for two different centralities and PID3. An efficiency loss in central collisions compared to peripheral events is clearly seen. It can be explained by the increased overlap probability in central events due to the high multiplicity. The increased overlap of clusters makes it more likely that the energy of a single decay photon is altered and the π^0 is not reconstructed within the invariant mass window. The effect is smaller in the PbG1, as its finer segmentation allows a better separation of hits.

For the efficiencies the effect of the bad/dead module and edge cut is already included, although this is in principle an acceptance effect. The reason for this lies in the definition of the cut and the longitudinal profile of an electromagnetic shower. A cluster is not accepted for analysis if the module with the largest energy contribution to the cluster lies on, or is adjacent to a flagged module. This module is basically determined by the maximum energy deposit of an electromagnetic shower, which is reached after a certain depth within the calorimeter as given by Equation (4.2). This leads to the effect that for non-zero angle of incidence the impact position of a particle on the calorimeter is not identical to the module with the largest energy deposit used for the bad module cut. Thus purely geometric effects and detector effects are not cleanly separated and this part of the acceptance

is incorporated into the full simulation of the detector response and the embedding. The acceptance loss for $\pi^0 \rightarrow 2\gamma$ due to the bad module and edge cut in the Au + Au analysis is approximately 20% at large p_T for the PbSc and 40% for the PbGl, respectively.

Conversion Correction

The loss of π^0 s due to conversion of one or both decay photons into an e^+e^- pair is considered separately from the efficiency correction. The probability for conversion of one photon p_γ^{conv} is related via Equation (4.1) to the number of radiation lengths X_0 of material between the collision vertex and the EMCal given in Appendix E. The probability that either decay photon of a π^0 converts is given by:

$$p_{\pi^0}^{\text{conv}} \simeq 2 \cdot p_\gamma^{\text{conv}}. \quad (6.19)$$

However, the conversion of one decay photon is not tantamount to the loss of the π^0 . It is possible that an e^+e^- pair is not separated by the clustering routine and all the energy of the decay photon is contained in one broader cluster, or that one particle after conversion carries a large fraction of the primary photon energy. This allows that the π^0 might be reconstructed within the invariant mass window used for the analysis, even though one decay photon converted.

Thus, in principle the determination of the π^0 loss due to conversion is a task for the efficiency calculation. However, the determination of the π^0 efficiency as described above requires exactly two hits on the empty detector, so that conversions are basically excluded and this method is not suited to account for converted decay photons. For this reason a second method for the efficiency determination is introduced for the evaluation of the embedding output. This method searches for all simulated hits on the empty detector within the new hits of the embedded event. Therefore it includes also the multiple clusters from conversions. The disadvantage of this method is the increased combinatorial background at low transverse momenta. Nevertheless, the efficiencies obtained using all clusters can be compared for two cases, based on the simulation information of the embedding output: for all π^0 s that decay into two photons, or only for π^0 s whose decay photons did not convert. The comparison of the π^0 efficiencies as seen in Figure 6.16 determines the fraction of π^0 s, with one or more converted photons, which is not reconstructed within the invariant mass window. This fraction is influenced by the shower shape cut used in the analysis, since clusters containing an e^+e^- pair from conversion are broader than clusters from single photons.

The correction factors used in the analysis are averaged for all centralities and listed in Table 6.5 together with the comparison to the simplified expectation from the conversion probability for the decay photons. The difference between these two values is obvious in

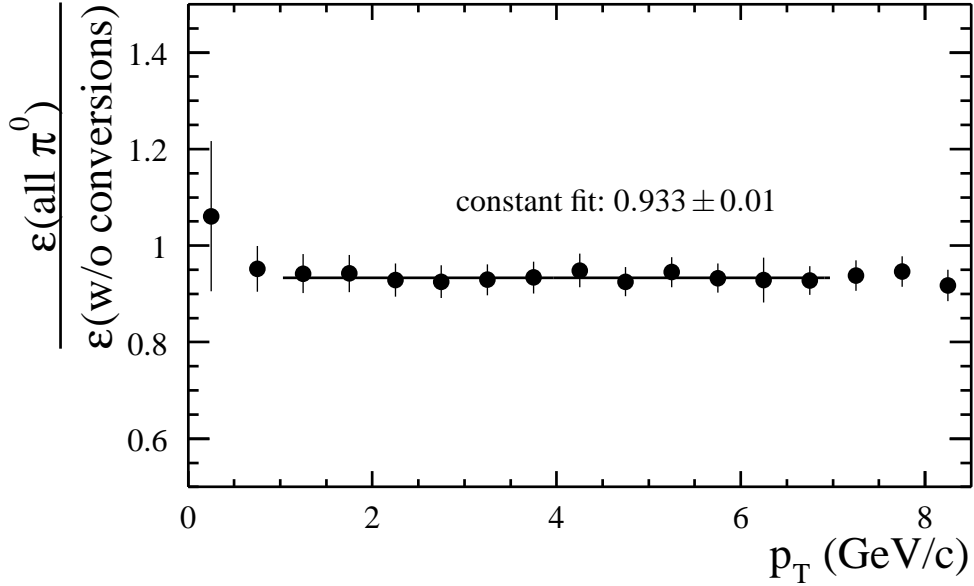


Figure 6.16: π^0 efficiency obtained when considering all π^0 s from the embedding compared to the efficiency when excluding π^0 s with a least one converted decay photon (PbG1, minimum bias events, PID2).

PbG1		
	c_{conv}	$1 - 2p_{\gamma}^{\text{conv}}$
PID0	0.94	0.79
PID2	0.93	
PbSc		
	c_{conv}	$1 - 2p_{\gamma}^{\text{conv}}$
PID0	0.91	0.86
PID2	0.90	

Table 6.5: Correction factors for the loss of π^0 s due to conversion. The application of the TOF cut does not affect the values.

the case of the PbG1. It can be understood by the fact that for the PbG1 many conversions occur directly in front of the detector in the time-of-flight wall (see Appendix E) and the e^+e^- pair is not separated in the PbG1.

6.4.2 Efficiency Calculation with a Fast Monte Carlo

The determination of the efficiency via embedding of simulated particles has the advantage that it provides the best possible description of the real event background and detailed information on the detector response in the simulation. The disadvantages of this method are the resources needed in preparation for the embedding and for the embedding process itself: CPU power for the simulation and embedding, as well as disk space for the storage of the simulation output, the real DSTs, and the embedding output.

For the analysis in the low multiplicity environment of d + Au collisions, where the effects of cluster overlap are negligible, a determination of the detector response within a fast Monte Carlo simulation offers a less time- and disk-space-consuming alternative to the efficiency calculation with embedding.

The simulation code used for the efficiency determination also incorporates the acceptance calculation and the determination of the decay background for the direct photon analysis, see Section 6.3 and Section 7.2.1, respectively. Neutral pions are generated and decay within the Fast Monte Carlo as described in Section 6.3. The energy and position of each decay photon is smeared based on the nominal energy and position resolution given in [Aph03a]. Additional corrections are applied to the position resolution to account for angular incidence and to the energy resolution to reconstruct the observed π^0 peak position and width for each sector:

$$\frac{\sigma_E}{E} = \frac{a_E}{\sqrt{E}/(\text{GeV})} \oplus a_{\text{const}}, \quad (6.20)$$

$$\frac{\sigma_{xy}(\theta = 0^\circ)}{E} = \frac{b_E}{\sqrt{E}/(\text{GeV})} \oplus b_{\text{const}},$$

$$\frac{\sigma_{xy}(\theta)}{E} = 28 \text{ mm} \cdot \sin \theta \oplus \sigma_{xy}(0^\circ). \quad (6.21)$$

In the next step a simple simulation of the shower overlap is performed. The amount of shower overlap is negligible in d + Au collisions but the method shall be discussed briefly for completeness. Based on an overlap probability p_{over} it is decided whether or not the photon is influenced by another hit. In the case of a positive decision a random energy is added to the photon energy based on the sampled energy distribution of real hits on the detector. This approach considers only the two cases of no overlap and complete overlap of two clusters and does not contain the effects introduced by the unfolding of clusters in the clustering algorithm. Nevertheless, it can be seen a reasonable approximation. For the analysis of the d + Au data p_{over} is chosen as zero.

For photons with modified energy and position the same cuts need to be applied as for the real data. For this purpose the effect of the shower shape cut on single photons is parameterized based on the comparison of the π^0 yields for different PIDs, as described

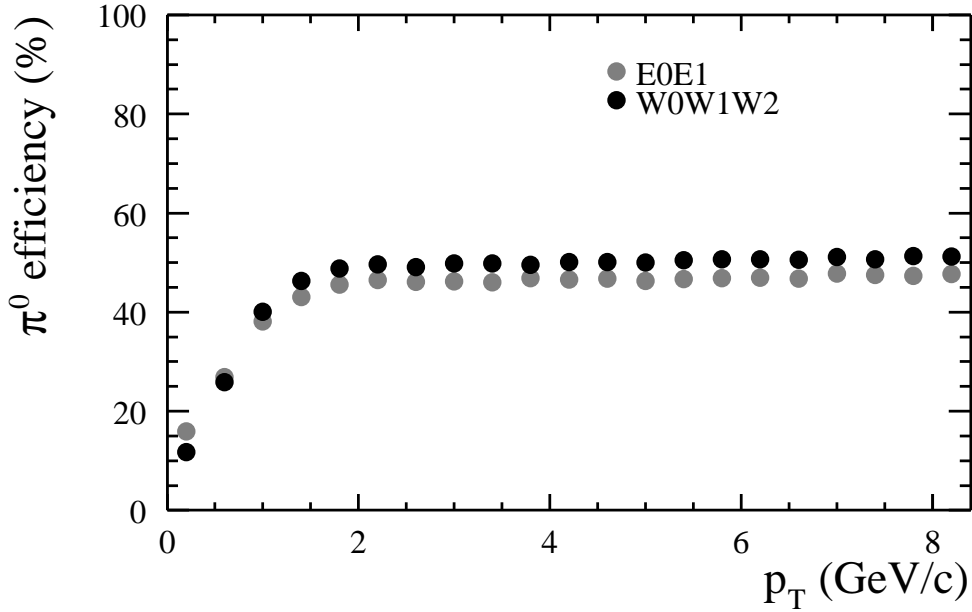


Figure 6.17: Comparison of the π^0 efficiency for the PbGl and PbSc in the analysis of the d + Au data determined with the fast Monte Carlo simulation.

above for the timing cut in embedded events. The probability determined for a photon to survive the shower shape cut is 98% for PbGl and PbSc. The very loose TOF cut used in the analysis of the d + Au data (see Table 5.3) basically introduces an energy threshold, as it only excludes hits with a meaningless timing signal because of an amplitude that is too low. In the simulation this is modeled by an energy threshold of 0.2 GeV.

The cut on bad modules must also be implemented in the fast Monte Carlo. As discussed above, this cut depends on the module with the largest energy deposit within the cluster, hence on the depth of the maximum energy deposit of the shower. In the fast Monte Carlo only the impact position of a photon on the detector surface (x, y) is known. For a more accurate description of the bad module cut this can be corrected with a parameterization obtained from real data by comparing the reconstructed impact position and the position of the tower with maximum energy deposit:

$$r_{\text{shift}} = 0.07 \text{ cm} \cdot \theta \cdot (0.32 + 0.51 \cdot \log(1 + E) + 0.45 \cdot \log^2(1 + E)), \quad (6.22)$$

$$x_{\text{shifted}} = x + r_{\text{shift}} \cdot \cos \varphi,$$

$$y_{\text{shifted}} = y + r_{\text{shift}} \cdot \sin \varphi, \quad (6.23)$$

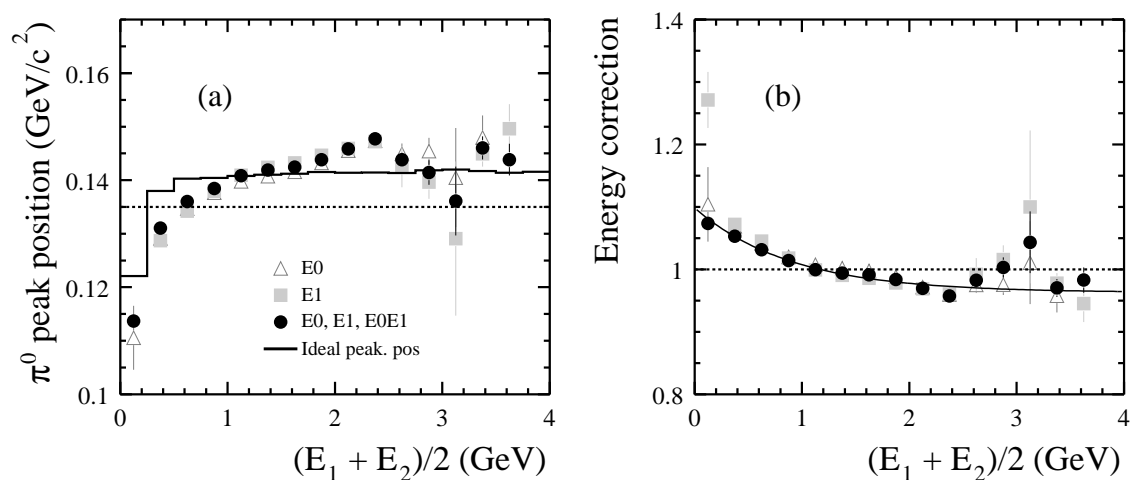


Figure 6.18: (a) Comparison of the π^0 peak positions measured within the PbGl (in $p + p$ events) to the expectation from the simulation. (b) The ratio of the expectation to the measured peak position and the derived energy correction.

where θ is the impact angle in degrees with respect to a perpendicular to the detector surface, and E is the energy of the photon in GeV. The corrected position determines the position of the tower that is compared to the list of bad modules also used during the analysis of the real data (see Appendix C).

If both decay photons survive the above cuts, it is verified that they pass the cuts for photon pairs: the asymmetry cut and the requirement of a minimum distance. Similar to the evaluation of the embedding output the π^0 is counted as accepted if the invariant mass of the photon pair falls into the same window around the π^0 peak as used in the real analysis. The efficiency is then determined again by the comparison of the weighted input spectrum to the spectrum of the reconstructed neutral pions. The result is shown in Figure 6.17. For better a comparison with the result from embedding the loss of π^0 s due to the bad module cut is also included. For the PbGl this loss is about 35% and 30% for the PbSc, different from the result for the Au + Au data due to the changed map of bad modules (see Appendix C).

6.5 Calibration Based on the π^0 Peak Position

One advantage in the analysis of π^0 s is that the energy scale of the calorimeter has direct influence on the position of the π^0 peak. This can be used to determine the correct absolute calibration of the detector. However, due to the finite energy resolution and the steeply

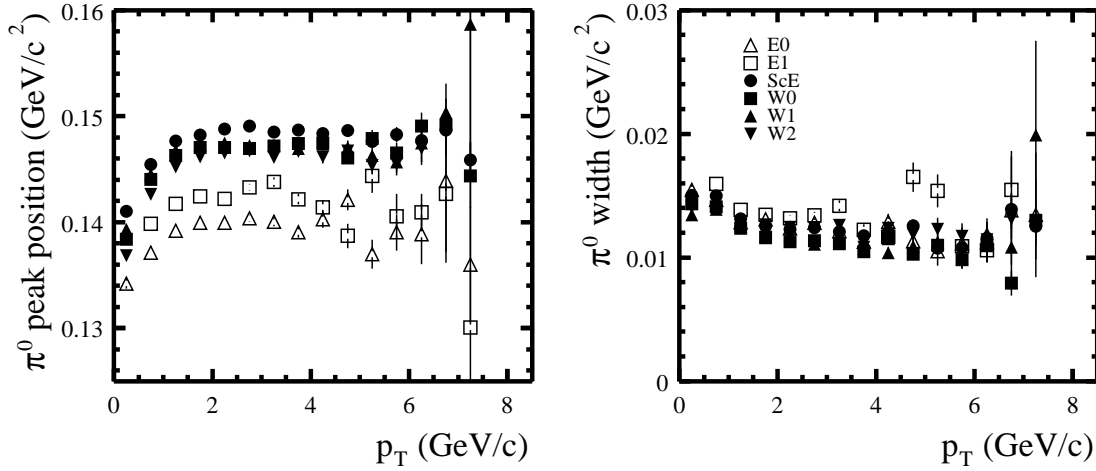


Figure 6.19: π^0 peak position and width for the different sector combinations in Au + Au minimum bias collisions before the final energy scale correction.

falling spectra it is not expected that the π^0 peak position is reconstructed at the nominal value of approximately $135 \text{ MeV}/c^2$. Instead it is shifted to larger values.

To determine the expected peak position, the energy response of the detector needs to be modeled correctly. This is best done with the same methods described above for the efficiency calculation. We will limit the discussion to the fast Monte Carlo, though the method is equally valid for the determination of the π^0 peak position via embedding. It is advisable to use only neutral pions from low multiplicity events, where the influence of overlapping showers on the peak position is negligible and the main task for the simulation is the correct description of the energy resolution. For this reason p + p collisions from the same run as the Au + Au data were used to determine the energy correction for the Au + Au data (see also [Rey03c]).

The energy resolution of the detector is given within the fast Monte Carlo by a smearing of the energy according to Equation (6.20). The parameters are fixed by the comparison of the peak widths from the simulation to the widths obtained in the analysis. Once the peak widths are correctly reproduced in the simulation, the π^0 peak positions from the fast Monte Carlo represent the expectation for a correct energy scale.

Differences in the direct comparison of the simulation and the real data already point to problems with the absolute calibration of the detector. However, the method can be refined further to determine an energy scale correction for single photons. This is done by requiring a small energy asymmetry $\alpha < 0.2$ for the photon pairs. Thereby the energy of the two decay photons is limited to a similar value and the dependence of the π^0 peak position on the average photon energy $E = \frac{E_1 + E_2}{2}$ can be analyzed. The results for the

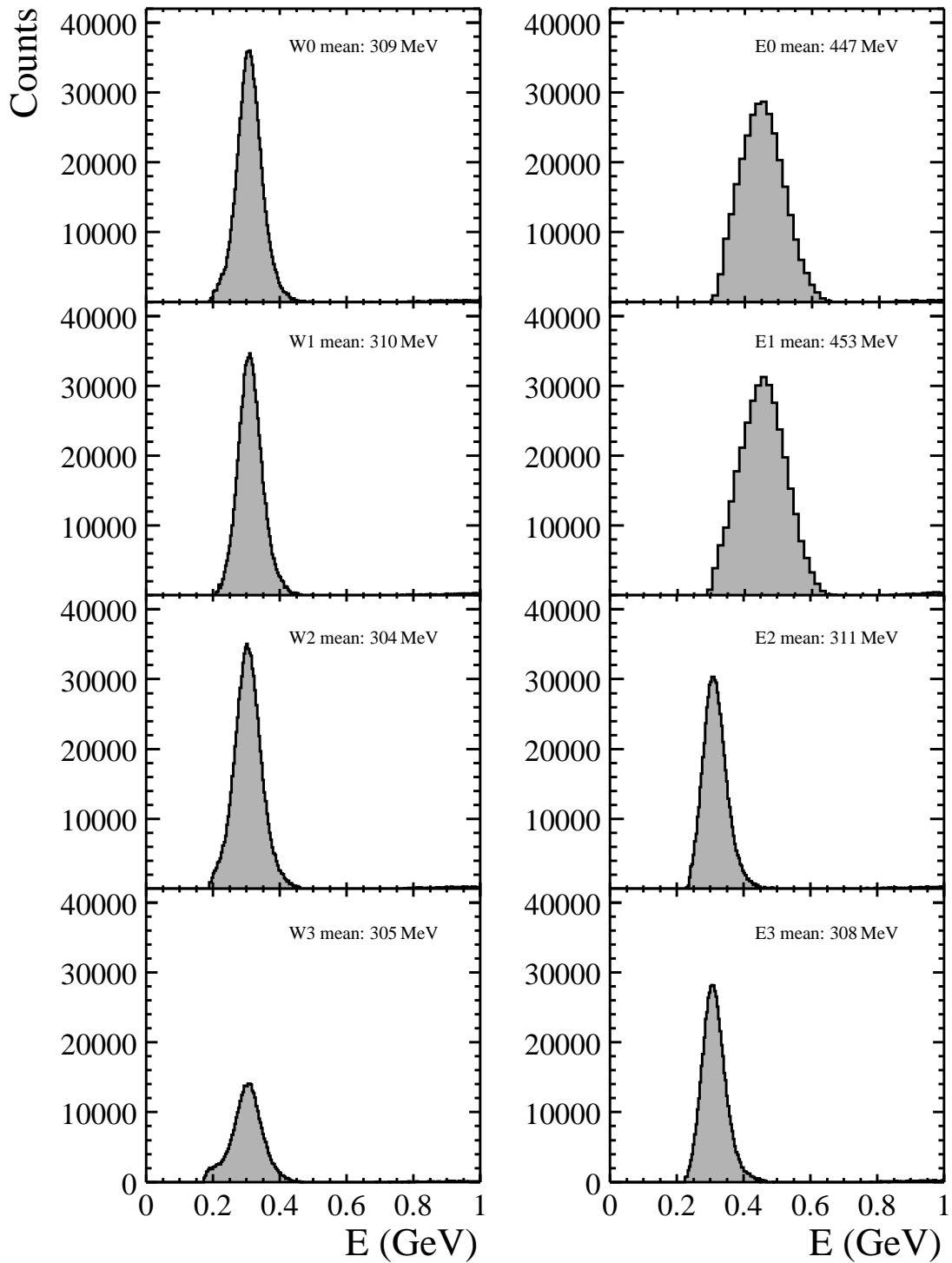


Figure 6.20: MIP peaks in the different EMCAL sectors before the final sector-by-sector energy scale corrections.

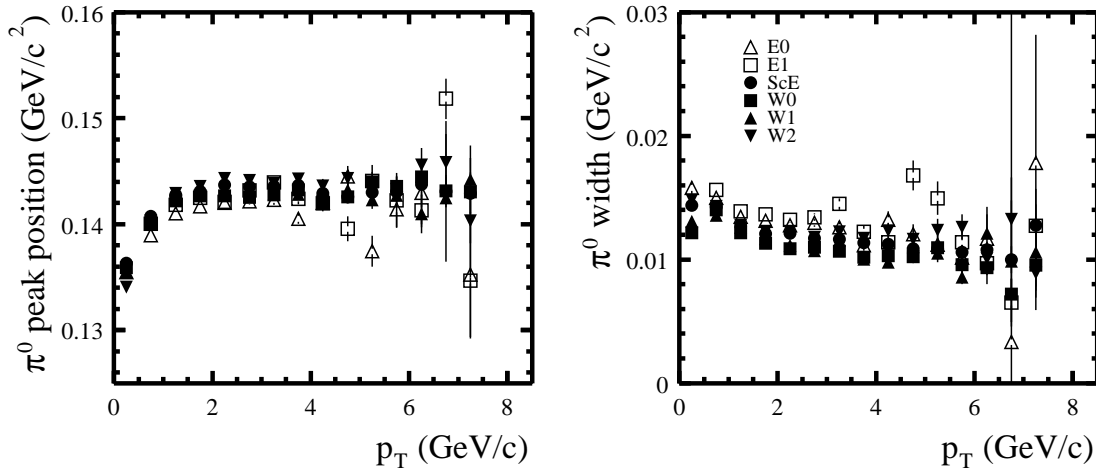


Figure 6.21: π^0 peak position and width for the different sector combinations in Au + Au minimum bias collisions with the final calibration used for the analysis.

PbGl in p + p collisions are shown in Figure 6.18(a). An empirical linearity correction is then simply given by the ratio of the expected to the observed peak position shown in Figure 6.18(b). It can be parameterized by the functional form:

$$E_{\text{corr}} = E (a_1 + a_2 \cdot e^{a_3 \cdot E}), \quad (6.24)$$

with the parameters already given in Table 5.6.

As seen in Figure 6.18(a) the energy scale in both PbGl sectors was similar during the p + p run. This was not the case for the Au + Au run, as seen in Figure 6.19 for minimum bias events. The π^0 peak positions vary among the different PbGl sectors. It is also conspicuous that the peak positions within the PbSc, after removal of the afterburner corrections and application of the run period correction discussed in Section 5.2.3, are drastically different from the values measured with the PbGl, even though the energy resolution reflected in the width of the π^0 peak is similar.

The comparison of the measured π^0 peak position at large p_T with the expectation from the embedded events leads to an overall correction of the absolute energy scale in the PbSc of about 3%. However, due to the lack of statistics for peripheral Au + Au collisions this method is not sensitive to minor variations of the energy scale on a sector-by-sector basis and not suitable to derive an empirical linearity correction as for p + p collisions.

An alternative way to check the energy calibration is to investigate the energy deposit of minimum ionizing particles in each sector for peripheral events. As seen in Figure 6.20 the positions of the MIP peak show the same difference of the energy scale between the various sectors as indicated by the π^0 peak positions. The MIP peak can now be used

to adjust the energy scale within the PbGl sectors and the PbSc sectors, respectively. Together with the overall scale correction of 3% for the PbSc this leads to the energy scale adjustments given in Table 5.5. As seen in Figure 6.21 the π^0 peak positions after this correction agree very well between all sectors.

For the analysis of the d + Au data the procedure for the determination of an empirical linearity correction has been repeated for both PbGl and PbSc, respectively. A further refinement to the previous method used in p + p is that the fast Monte Carlo now supports a different energy resolution for each individual sector, allowing a better determination of the energy scale correction. The parameters for the correction function are listed in Table 5.6.

6.6 Production of Neutral Pions in Au + Au Collisions

After all corrections to the measured raw yield of neutral pions treated in the previous sections, we present and discuss in this section the invariant yield of π^0 s in Au + Au collisions at $\sqrt{s_{\text{NN}}} = 200$ GeV for different centralities. In addition, the sources of systematic errors for this measurement will be discussed, as they are the main source of uncertainty in the determination of the background from radiative decays for the direct photon measurement (see Section 7.2.1).

6.6.1 Statistical Error

The π^0 raw yield is not determined by identifying neutral pions directly as discussed in Section 6.1. The only measured quantity in the real event is the sum R of the π^0 signal S and the random background contribution B within the considered invariant mass region:

$$R = S + B. \quad (6.25)$$

It is obvious that the accuracy of the determination of the number of π^0 s depends on the knowledge of the background and its magnitude compared to the signal. A commonly used estimation for the statistical error of the raw yield is:

$$\sigma^2(S') \approx S' + 2 \cdot B', \quad (6.26)$$

where S' is the estimated number of π^0 s after background subtraction and B' the estimated background. However, this formula does not consider the uncertainties in the determination of the background, which is calculated via the mixed event technique described in Section 6.1.1 and given by:

$$B' = f \cdot M. \quad (6.27)$$

Here, f is the factor used to scale the mixed event background M in the integration region background, so that the π^0 signal is given by:

$$S' = R - B' = R - f \cdot M. \quad (6.28)$$

Based on this, the statistical error of the determined π^0 raw yield can be written as [Bat02]:

$$\sigma^2(S') = S' + B' + \sigma^2(f)M^2 + f^2M. \quad (6.29)$$

The error of the scaling factor $\sigma(f)$ is determined by the error of the fit to the ratio of real and mixed invariant mass distributions. For the case that the fit is not a constant, the fit errors and the fit itself are evaluated at the π^0 peak position. For large p_T , where the scaling factor is calculated by comparing the integrals of the invariant mass distributions, the error is given by the statistical uncertainty of Equation (6.5).

6.6.2 Sources of Systematic Errors

Each correction of the raw yield following Equation (6.13) is afflicted with its own uncertainty, but already the determination of the π^0 raw yield itself is sensitive to the method of extraction. In particular it is sensitive to the choice of the fit function for the background scaling and the extraction window. In principle, both should be taken into account by the detector efficiency, but in the efficiency calculation no background subtraction is necessary. For this reason the systematic error of the peak extraction method is determined in two steps: first via the comparison of the raw yield obtained with two different fits for the background scaling, as also shown in Appendix D, and second through the comparison of the fully corrected spectra for different sizes of the extraction window, for the real data as well as for the efficiency calculation (see Figure 6.22).

The systematic error introduced by the efficiency calculation is estimated by comparing the fully corrected spectra for different PID criteria as well as for different additional smearing. The default additional smearing given by Equation (6.16) is changed in a way that a clear disagreement between the measured π^0 peak width and the peak width from the embedding is observed. As seen in Figure 6.23 the systematic errors can be estimated as 7% and 9%, respectively.

Apart from the uncertainty of the efficiency, the main contribution to the systematic error is the determination of the absolute energy scale. Based on the comparison of the π^0 peak positions as described in Section 6.5 the energy scale can only be determined or confirmed with limited accuracy, $\Delta(E)/E = 1.6\%$ in the PbSc and, because of the smaller acceptance, $\Delta(E)/E = 2\%$ in the PbGl. The consequence of this uncertainty is that the yield for a given p_T might as well represent the yield at a different transverse momentum, shifted by the energy scale error. The influence of the energy scale on the spectrum can

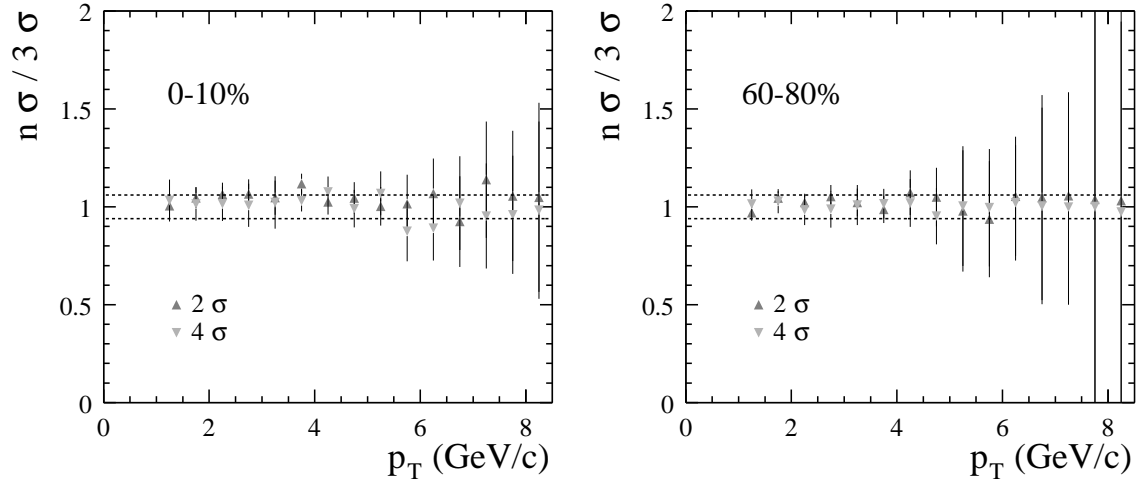


Figure 6.22: Comparison for PID2 in the PbPb and two different centralities of the fully corrected spectra with an extraction window of $2\sigma_\pi$ and $4\sigma_\pi$ to the default window of $3\sigma_\pi$. Only the statistical error of the π^0 yield is shown. The error estimate of 6% used for the analysis is indicated by the dashed lines.

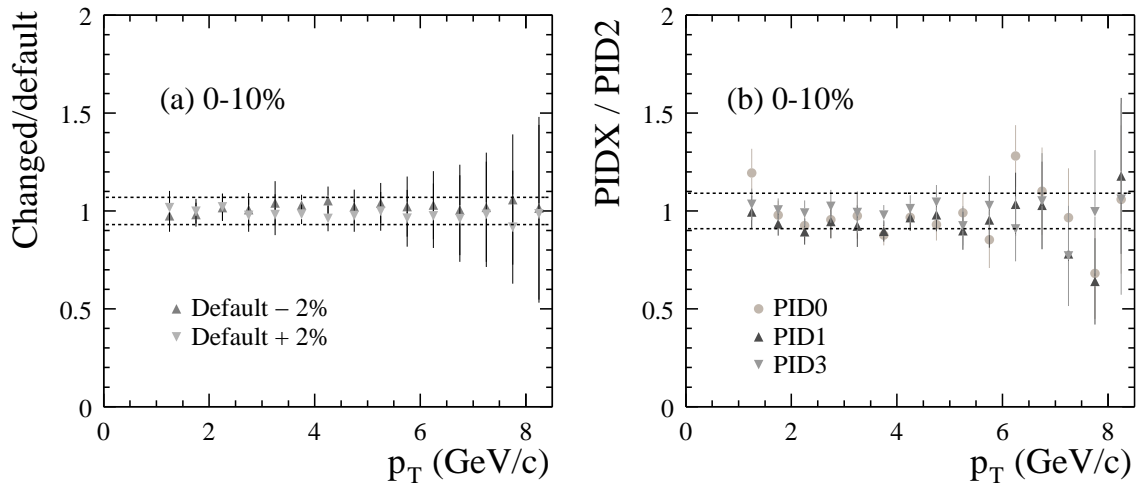


Figure 6.23: Comparison of fully corrected spectra for (a) different additional energy smearing and (b) for different PIDs in central collisions for the PbPb. The error estimates used for the analysis are indicated by the dashed lines.

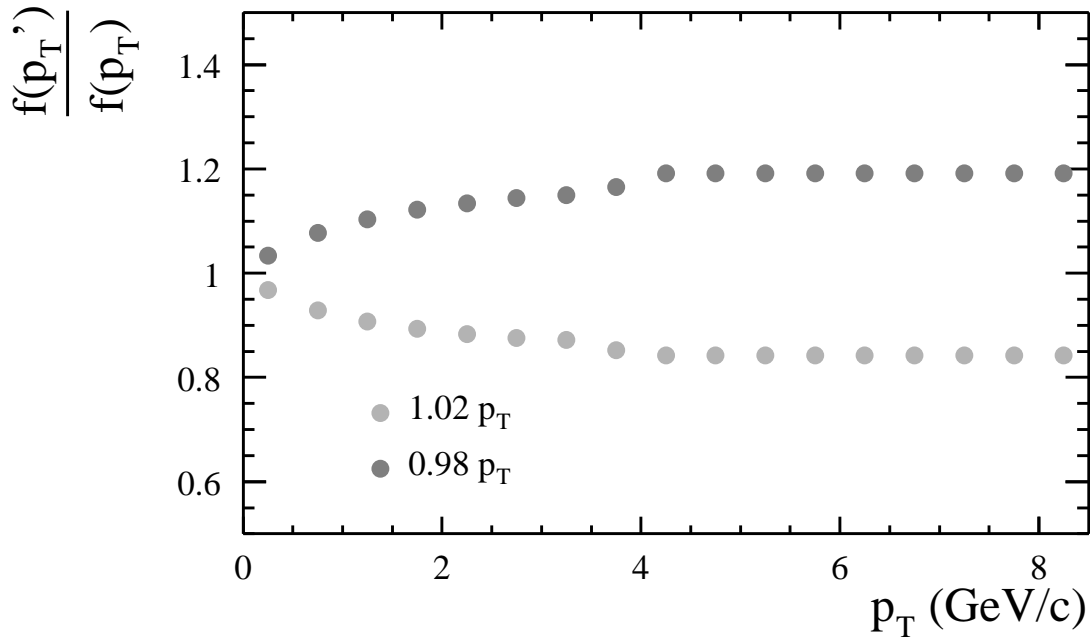


Figure 6.24: Comparison of the parameterization of the invariant yield (Equation (6.15)) for central events assuming different energy scales.

e.g. be studied by changing the a priori correct energy scale of the simulation. However, a simple comparison of the functional form given by Equation (6.15) for different energy scales, p_T and $p_T' = p_T \cdot (1 \pm \frac{\Delta(E)}{E})$, yields the same result. As shown in Figure 6.24 the yield uncertainty due to the energy scale error reaches an asymptotic value above approximately 4 GeV/c. This value is determined by the power-law behavior of the yield at large p_T and given by:

$$\left. \frac{\Delta E(N_{\pi^0})}{N_{\pi^0}} \right|_{p_T \rightarrow \infty} = 1 - \left(1 \pm \frac{\Delta(E)}{E} \right)^n, \quad (6.30)$$

where n is the same parameter as used for Equation (6.15). In the analysis of the Au + Au data $n \approx 7.5 - 8.5$ depending on centrality.

The additional contributions to the systematic error that have not been discussed in detail involve the uncertainty of the conversion correction (2.9%), of the acceptance calculation (2.5%), and the normalization for the LVL2-triggered data ($\approx 5\%$).

For the final systematic error all contributions are added in quadrature. However, for different types of analyses e.g. for the determination of the nuclear modification factor, it is useful to classify the errors, depending on how they affect the data points or if they cancel for certain ratios, as the γ/π^0 comparison in the direct photon analysis. This will be discussed in the corresponding sections. Table 6.6 provides a final overview over the

p_T	PbGl		PbSc	
	3.25 GeV/c	8.50 GeV/c	3.25 GeV/c	8.50 GeV/c
Yield extraction	8.7%	7%	9.8%	7.2%
Efficiency	11.4%	11.4%	11.4%	11.4%
Acceptance	2.5%	2.5%	2.5%	2.5%
Conversions	2.9%	2.9%	2.9%	2.9%
LVL2 data	–	–	–	5.8%
Energy scale	13.8%	14.1%	10.5%	11.4%
Total syst.	20.3%	19.8%	18.7%	19%
Statistical	10.6%	32.5%	8.1%	13.1%

Table 6.6: Summary of the dominant sources of systematic errors on the π^0 yields extracted independently with the PbGl and PbSc electromagnetic calorimeters in central Au + Au events for different p_T .

various contributions to the total error of the π^0 measurement in the PbSc and the PbGl, respectively.

6.6.3 Bin Shift Correction

In the case of steeply falling spectra an error is introduced when plotting the extracted yield for a given transverse momentum at the center of the bin, as it does not represent the center of gravity of the distribution within the bin. This effect becomes worse for larger bin widths and steeper falling spectra. One way to overcome this problem is to shift either the data point horizontally, in p_T , so that it represents the true center of gravity or to move the point vertically, in the yield, so that it represents the true yield of the distribution at the bin center. For comparison of spectra with different shape, e.g. in the nuclear modification factor, it is advantageous to use the shifted yields so the distributions can be divided at the bin center.

In order to derive the shift, a fit to the invariant yield following Equation (6.15) is taken as an approximation of the true spectrum. For this function $f(p_T)$ the average yield in a given bin with center p_T^c and width Δp_T is compared to the value of the function at the center:

$$r = \frac{\frac{1}{\Delta p_T} \int_{p_T^c - \Delta p_T}^{p_T^c + \Delta p_T} f(p_T) dp_T}{f(p_T^c)}. \quad (6.31)$$

The corrected yield is then given by:

$$\left. \frac{dN}{dp_T} \right|_{\text{corrected}} = \frac{dN/dp_T|_{\text{uncorrected}}}{r}. \quad (6.32)$$

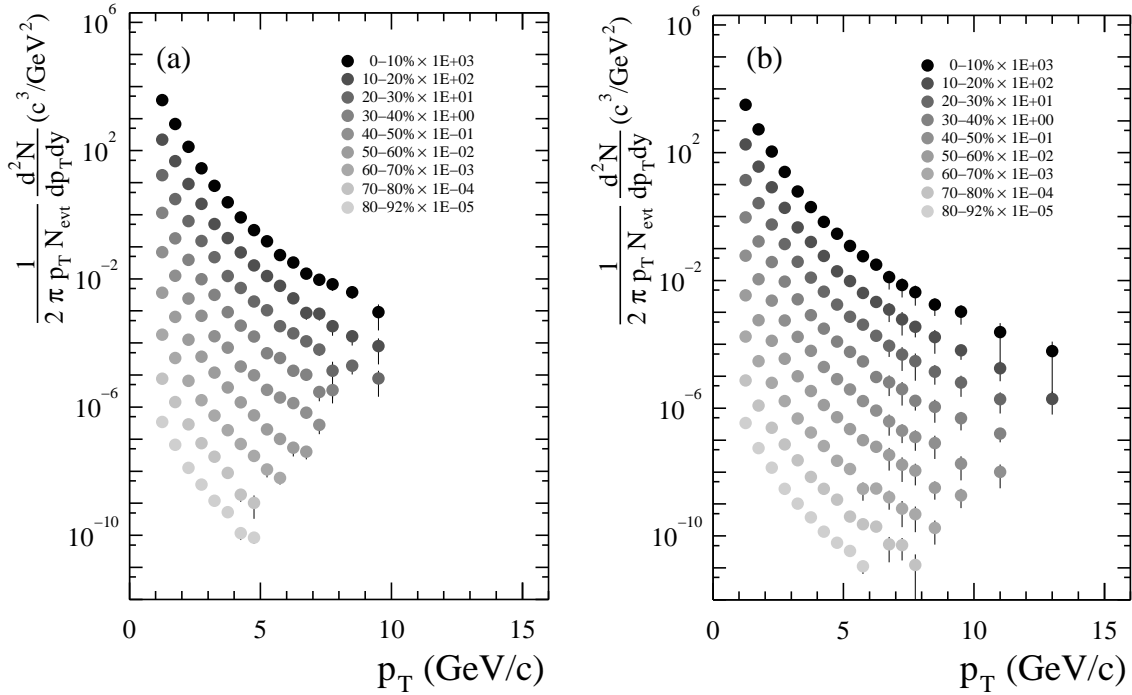


Figure 6.25: Fully corrected spectra for eight different centrality selections as determined (a) with the PbGl and (b) with the PbSc. The error bars represent the combined statistical and systematic errors.

As the shifted data points also lead to a different fit result, the fit procedure and the bin shift need to be repeated until the yield corrections become negligible. Usually two iterations are sufficient, resulting in a total correction of the order of a few percent compared to the original yield.

6.6.4 Combination of the PbGl and PbSc Result

One of the advantages of the EMCAL is the employment of two different detector types, which have been analyzed separately for this work. This provides a good internal consistency check similar to the comparison of the PbGl and the PbSc in the published PHENIX data on π^0 production [Adl03e]. We concentrate on the internal cross-check and compare only the combined results to the published data.

The fully corrected spectra for both detector types and different centralities are shown in Figure 6.25 with the data given in Appendix H. The PID criterion chosen for the final result is only the shower shape cut (PID2). The comparison of the results for both detectors shows an overall agreement within 15%, which improves in more peripheral events as shown in Figure 6.26. The difference is well covered by the error assigned to

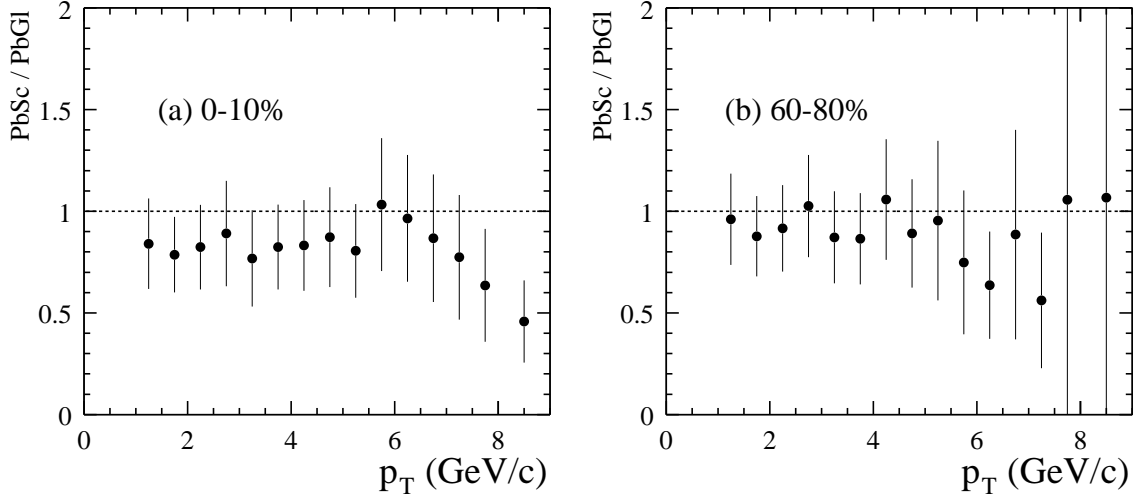


Figure 6.26: Comparison of fully corrected spectra for the PbGl and the PbSc for different centralities.

the individual measurements, so a combination of the results obtained with both detectors is justified. As the analysis of the different detector types provides essentially two independent measurements, the total error of the combined result is reduced.

The combination of the data for PbGl and PbSc is done by a standard weighted least-squares method also described in [Eid04]. Assuming the two measurements are uncorrelated, the average yield $\bar{x}(p_T)$ for each transverse momentum with $1-\sigma$ error $\delta\bar{x}(p_T)$ is given by:

$$\bar{x}(p_T) \pm \delta\bar{x}(p_T) = \frac{\sum_{i=1}^N w_i(p_T) x_i(p_T)}{\sum_{i=1}^N w_i(p_T)} \pm \left(\sum_{i=1}^N w_i(p_T) \right)^{-1/2}, \quad (6.33)$$

where

$$w_i(p_T) = \frac{1}{\delta x_i(p_T)^2}. \quad (6.34)$$

Here, x_i and δx_i are the yield and the total error of the measurement at a given transverse momentum p_T determined with the PbGl ($i = 1$) and with the PbSc ($i = 2$), respectively, and $N = 2$. Since the total error of each individual measurement is given by the quadratic sum of the statistical error $\delta x_i^{\text{stat}}(p_T)$ and the systematic error $\delta x_i^{\text{sys}}(p_T)$, the combined error can be rewritten as:

$$\begin{aligned} \delta\bar{x}(p_T)^2 &= \frac{1}{\sum_{i=1}^N w_i(p_T)} \\ &= \frac{1}{\sum_{i=1}^N w_i(p_T)} \frac{1}{N} \sum_{i=1}^N \frac{\delta x_i(p_T)^2}{\delta x_i(p_T)^2} \end{aligned}$$

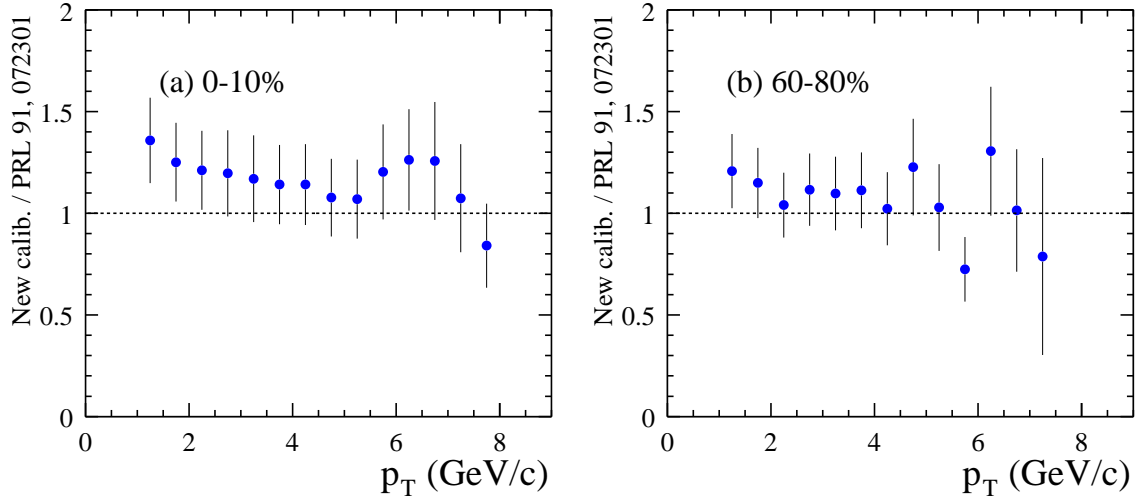


Figure 6.27: Comparison of the combined result to the data published in [Adl03e] for two centrality selections. Please note that the statistical error of the measurement has been considered only once, to account for the overlapping event sets in both analyses.

$$\begin{aligned}
&= \frac{1}{\sum_{i=1}^N w_i(p_T)} \frac{1}{N} \sum_{i=1}^N w_i(p_T) \cdot \delta x_i(p_T)^2 \\
&= \sum_{i=1}^N \frac{1}{N} \frac{w_i}{\sum_{j=1}^N w_j(p_T)} (\delta x_i^{\text{stat}}(p_T)^2 + \delta x_i^{\text{sys}}(p_T)^2) \\
&= (\delta \bar{x}^{\text{stat}}(p_T)^2 + \delta \bar{x}^{\text{sys}}(p_T)^2), \tag{6.35}
\end{aligned}$$

with the statistical error $\delta \bar{x}^{\text{stat}}(p_T)$ and the systematic error $\delta \bar{x}^{\text{sys}}(p_T)$ of the combined result defined as:

$$\begin{aligned}
\delta \bar{x}^{\text{stat}}(p_T)^2 &= \sum_{i=1}^N \frac{1}{N} \frac{w_i}{\sum_{j=1}^N w_j(p_T)} \cdot \delta x_i^{\text{stat}}(p_T)^2, \\
\delta \bar{x}^{\text{sys}}(p_T)^2 &= \sum_{i=1}^N \frac{1}{N} \frac{w_i}{\sum_{j=1}^N w_j(p_T)} \cdot \delta x_i^{\text{sys}}(p_T)^2. \tag{6.36}
\end{aligned}$$

A similar decomposition of the total error of the combined result also holds for the different types of errors contributing to the systematic error. This is especially important for quantities in which a part of the systematic error cancels.

In order to cross-check the combined result we require that the χ^2 value:

$$\chi^2 = \sum_{i=1}^N w_i (\bar{x} - x_i)^2 \tag{6.37}$$

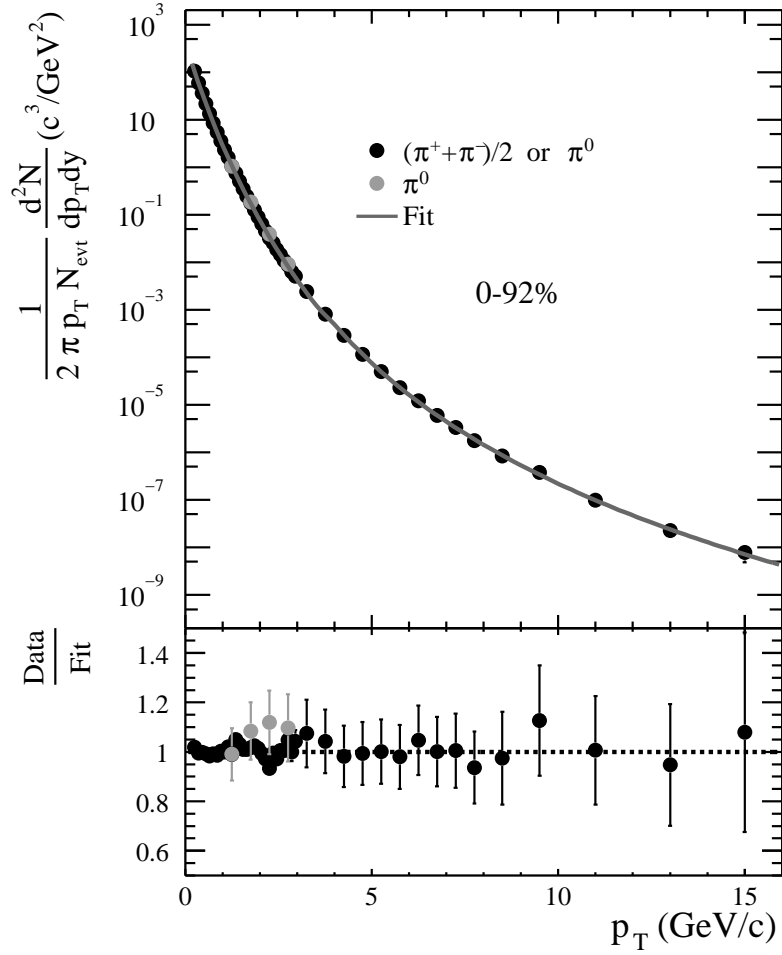


Figure 6.28: Comparison of the combined π^0 result to the measurement of charged pions within the PHENIX experiment in minimum bias events. The fit considers the averaged result of the π^+ and π^- measurement [Adl04] below $p_T = 3 \text{ GeV}/c$ and the π^0 data above.

is smaller than or equal to $N - 1$, which is the expectation value of χ^2 if the measurements follow a Gaussian distribution.

In some rare cases the χ^2 value exceeds this expectation. For such data points the total error $\delta\bar{x}$ of the combined result is increased by a scale factor S given by:

$$S = \sqrt{\chi^2/(N-1)}. \quad (6.38)$$

The resulting combined π^0 spectra are tabulated in Appendix H.

The published data in [Adl03e] do not contain the energy corrections for PbSc and PbGl discussed in Section 5.2.3 and do not incorporate the LVL2-triggered data (see

[KB03, d'E03]). Nevertheless it agrees within errors with the new combined result as seen in Figure 6.27.

A completely independent cross-check of the π^0 measurement is the measurement of identified charged pions within the PHENIX experiment [Adl04]. It is shown exemplarily for minimum bias events in Figure 6.28, which illustrates the overall agreement of the pion measurements within PHENIX. Together the data spans more than eleven orders of magnitude.

6.7 Production of Neutral Pions in d + Au Collisions

In order to disentangle between the effects of the hot and dense nuclear matter produced in Au + Au collisions and the effects of cold nuclear matter, it is essential to study a system where there is no formation of a large medium with high energy density in the final state and only the effects of cold nuclear matter influence the particle production. This type of control is provided by studying the π^0 production in d + Au collisions.

The analysis of the d + Au data has been carried out in a similar manner as the analysis of the Au + Au data. The major differences have already been mentioned. These are the use of a different trigger on high- p_T photons from filtered runs, which do not contain minimum bias data, and the determination of the efficiency corrections based on a fast Monte Carlo simulation of the detector response. In addition, the energy calibration and the list of bad modules changed compared to the Au + Au run.

The determination of the final systematic errors is very similar to the Au + Au case, so we only quote the contributions to the total systematic error in Table 6.6, which can be compared directly to Table 6.6. For a more detailed description see [Aph03b].

As in the Au + Au analysis, the PbGl and PbSc have been analyzed separately. The overall agreement between the two results is seen in Figure 6.29(a). However, the data show a apparent discrepancy at large p_T . Although it is covered by the error bars, for large transverse momenta fewer π^0 s seem to be measured in the PbGl compared to the PbSc.

The cause for this behavior has been tracked down to a problem in the clustering algorithm for the PbGl, leading to a wrong unfolding of overlapping clusters. The error became apparent when looking at the invariant mass distribution for simulated π^0 s, as seen in Figure 6.30(a), which shows a double peak structure for the PbGl starting at $p_T \approx 8 \text{ GeV}/c$, when the opening angle between the two decay photons is small enough. A similar structure, though less obvious, is also seen for real events in Figure 6.30(b). The shower-shape cut rejects most of the photons contributing to the shifted peak and reduces the overall number of detected π^0 s drastically, see Figure 6.30(c) and (d).

p_T	PbGl		PbSc	
	3.25 GeV/c	8.75 GeV/c	3.25 GeV/c	8.75 GeV/c
Yield extraction	5%	5%	5%	5%
Efficiency	4%	4%	4%	4%
Acceptance	3%	2%	3%	2%
Conversions	2.8%	2.8%	2.8%	2.8%
ERT normalization	–	5%	–	5%
Trigger efficiency	–	8%	–	4%
Energy scale	6%	10%	6%	10%
Total syst.	9.7%	15.5%	9.7%	13.9%
Statistical	4%	15.9%	2.3%	9.3%

Table 6.7: Summary of the dominant sources of systematic errors on the π^0 yields extracted independently with the PbGl and PbSc electromagnetic calorimeters in d + Au minimum bias events for different p_T .

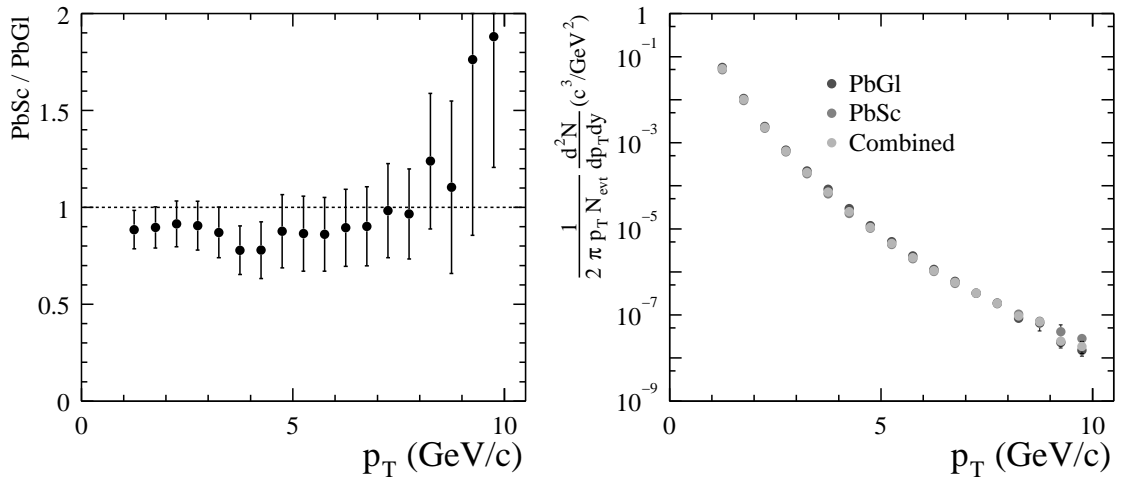


Figure 6.29: Comparison of the minimum bias spectra in d + Au collisions measured with the PbGl and the PbSc as well as the combined spectrum.

Such a behavior, a shift of the π^0 peak to lower invariant mass, is expected when the energy of one decay photon gains a fraction x of the total energy of the two decay photons $E_{\text{tot}} = E_1 + E_2$, while the second photon loses the same amount:

$$\begin{aligned} m_{\text{inv}}^2 &= (E_1 + xE_{\text{tot}}) \cdot (E_2 - xE_{\text{tot}}) \cdot (1 - \cos\theta_{12}) \\ &= (E_1 \cdot E_2 + xE_{\text{tot}} \cdot (E_2 - E_1) \\ &\quad - x^2 E_{\text{tot}}^2) \cdot (1 - \cos\theta_{12}). \end{aligned} \quad (6.39)$$

On the average the second term gives no contribution and compared to Equation (6.1) only the quadratic term remains, leading to a depletion of the reconstructed invariant mass in this simplified model of a wrong cluster splitting.

A more detailed examination of the cluster algorithm revealed that the parameterization of the shower form for the PbGl, which is used to split the energy measured in a module i into separate clusters for overlapping showers, contained an additional offset. It was independent from the distance of the module to the shower center of gravity r_{cog} [Baz03a]:

$$\frac{E_i^{\text{ideal}}}{E} = f(E, \theta, \phi, r_{\text{cog}}) + c(E), \quad (6.40)$$

where E is the total energy contained in a 3×3 region around a local maximum, and θ and ϕ the impact angle and the orientation on the detector surface, see also Section 5.2.1. Due to this constant offset, the integral of the parameterization is not unity, instead it increases with the size of the integration region chosen for r_{cog} . The consequence of this wrong parameterization is that for the outer parts of a cluster the calculated expected energy is too large. For overlapping showers, for which the energy is split between the clusters according to this expectation, this leads to a wrong energy determination and broad clusters. Since at least one of the resulting unfolded clusters is too broad, it is rejected by the dispersion cut, the double peak structure vanishes as seen in Figure 6.30, and the yield is decreased dramatically.

After the constant offset had been removed [KB04b] the clustering was tested again by reconstructing simulated π^0 s with the corrected algorithm. The result showed only a single π^0 peak and a similar yield with and without the dispersion cut. The corrected version of the parameterization is now considered in each new DST production. However, in the current analysis it has not been considered. For the final combined result, given in Appendix H and shown in Figure 6.29, the deviation between the PbGl and the PbSc above $p_T \approx 8 \text{ GeV}/c$ leads to an increased systematic uncertainty, determined by Equation (6.38).

In principle the wrong cluster splitting also has an impact on the analysis of the Au + Au data. However, as the embedding of simulated particles did use the same clustering algorithm also used in the DST production, the effect is compensated by the efficiency.

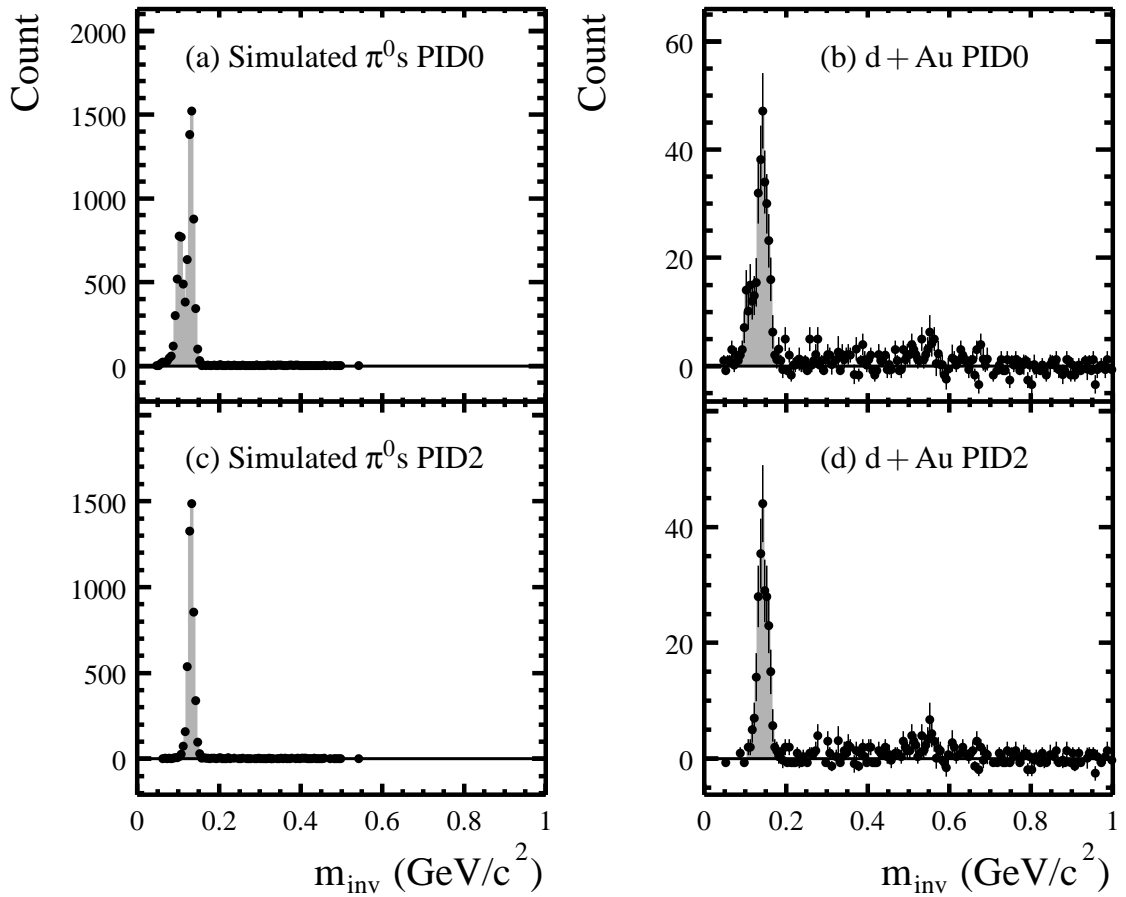


Figure 6.30: Invariant mass for simulated π^0 s and for minimum bias d + Au collisions with $8\text{GeV}/c \leq p_T < 9\text{GeV}/c$ measured with the PbGl. The double peak structure is clearly seen when no PID cut is used for the two photons. The shower-shape cut rejects the photons contributing to the second peak. Please note that the shown simulated π^0 s do not contain the additional energy smearing given by Equation (6.16), which is needed to match the peak width and position in real events.

6.8 Analysis of the Scaling Behavior of the π^0 Production

To search for medium modifications of the particle production, the π^0 yield for different centralities can be compared to the expectation that for large transverse momenta a nucleus-nucleus collision can be described as an independent superposition of nucleon-nucleon collisions (see Section 1.3.1).

In the case of the π^0 measurement the basis for the comparison is provided by the PHENIX measurement of the invariant cross section for the π^0 production in p + p collisions at the same energy [Adl03c]. It is shown in Figure 6.31 together with the comparison to next to leading order (NLO) pQCD calculations. The calculations employ two different kinds of fragmentation functions, from [Kni01] (*KKP*) and from [Kre04] (*Kretzer*), but identical parton distribution functions. It is found that the calculations that employ the *KKP* fragmentation functions, which have a larger contribution for gluons fragmenting into pions, agree better with the data. We will use the direct photon cross section determined within the same calculations as a reference for the comparison of the direct photon production in Au + Au (see Section 7.3 and Appendix G).

As discussed in Section 1.3.1 the differential cross section measured in p + p collisions can be compared to the invariant yield determined in Au + Au reactions of a certain centrality, by scaling with the geometrical factor T_{AB} for this centrality. This nuclear overlap factor accounts for the number of binary nucleon-nucleon collisions N_{coll} in a Au + Au reaction. The comparison is shown in Figure 6.32 for two different centralities. The π^0 production in central Au + Au collisions is strongly suppressed compared to the expectation from p + p reactions, while the particle production in peripheral collisions follows the p + p yield scaled with the number of collisions.

To study the modification of particle production in nuclear matter in more detail, the ratio of the scaled p + p reference and the measurement in the selected centrality is considered. This nuclear modification factor R_{AB} has already been defined by Equation (1.8).

It is useful to classify the different sources of errors for the individual measurements, depending on how they affect the data points and thereby the shape of the nuclear modification factor. We use three different classes of errors:

- Type A: errors that fluctuate from point to point, such as the statistical error, and errors where the p_T correlation is unknown, e.g. the uncertainty in the yield extraction.
- Type B: errors that are correlated in p_T and move all points into the same direction, such as the uncertainty on the efficiency calculation.
- Type C: scale uncertainties, which move all points by the same amount. This error includes e.g. the normalization error of 9.6% in the case of the p + p measurement,

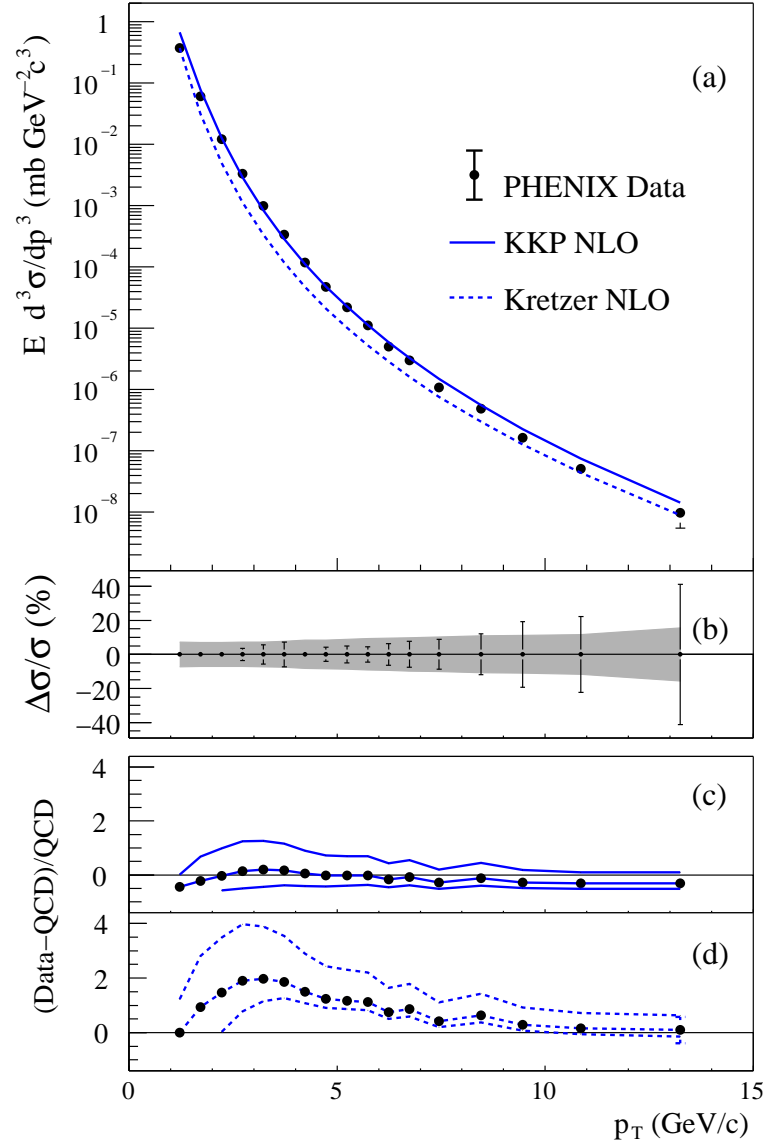


Figure 6.31: (a) The invariant differential cross section for π^0 s measured by the PHENIX experiment in $p + p$ collisions at $\sqrt{s} = 200 \text{ GeV}$ together with the results from NLO pQCD calculations with factorization and renormalization scales of p_T . The NLO calculations use two different sets of fragmentation functions: *Kniehl-Kramer-Pötter* (solid line) [Kni01] and *Kretzer* (dashed line) [Kre04]. (b) The relative statistical (points) and point-to-point systematic (band) errors. (c) and (d) The relative difference between the data and the theory using the two different sets of fragmentation functions with scales $\mu = p_T/2$ (lower curve), p_T , and $2p_T$ (upper curve). The overall normalization error for the measurement of 9.6% is not shown [Adl03c].

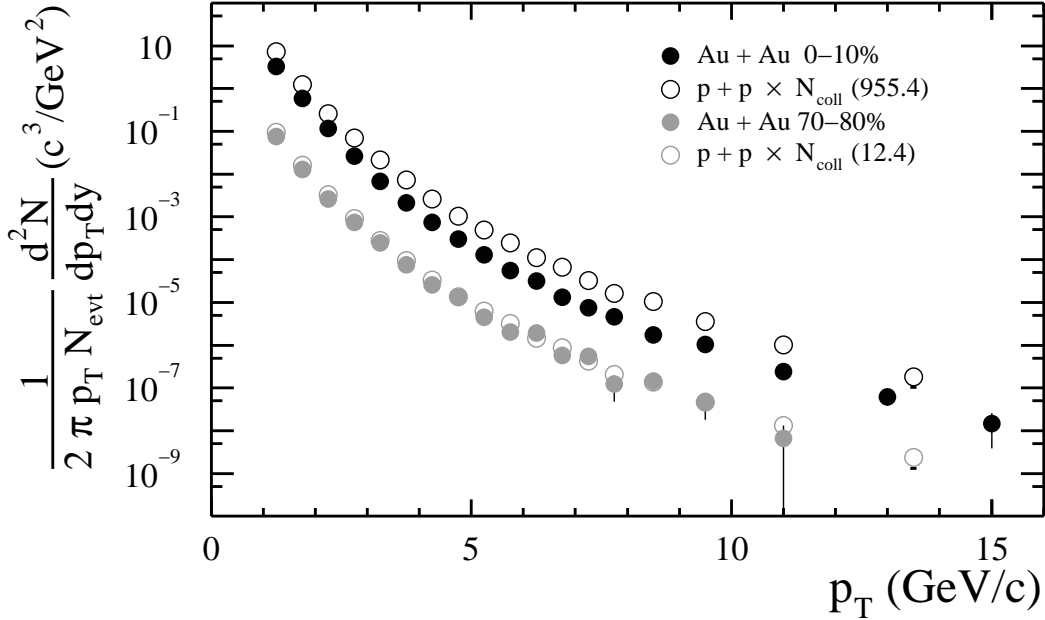


Figure 6.32: The combined result for the π^0 production in central (0-10%) and peripheral (60-80%) Au + Au collisions compared to the expectation from p + p, obtained by scaling with the appropriate number of binary nucleon-nucleon collisions N_{coll} .

as well as the uncertainty in the conversion corrections and the trigger normalization. For the comparison of the spectra within the nuclear modification factor the uncertainty in the determination of N_{coll} is also considered by this error.

For the Au + Au measurement the contributions of the different types to the total error are listed together with the invariant yields in Appendix H. In the comparison of the nuclear modification factor for different centralities shown in Figure 6.33 the uncertainties of type A are given as error bars, while type B and C are given as dark grey and light grey boxes, respectively.

As seen in Figure 6.33 the suppression of the π^0 production is most pronounced in central collisions at large transverse momenta. It amounts to a factor of five for $p_T > 5 \text{ GeV}/c$, indicating a strong final state interaction of the hard-scattered parton. The suppression gradually decreases when going to larger impact parameters. In the three most peripheral centrality selections shown in Figure 6.33 R_{AB} is consistent with unity, which is expected in the absence of any medium effects. In addition, the nuclear modification factor flattens out and becomes basically constant above $p_T = 2 \text{ GeV}/c$, when going from central to more peripheral collisions.

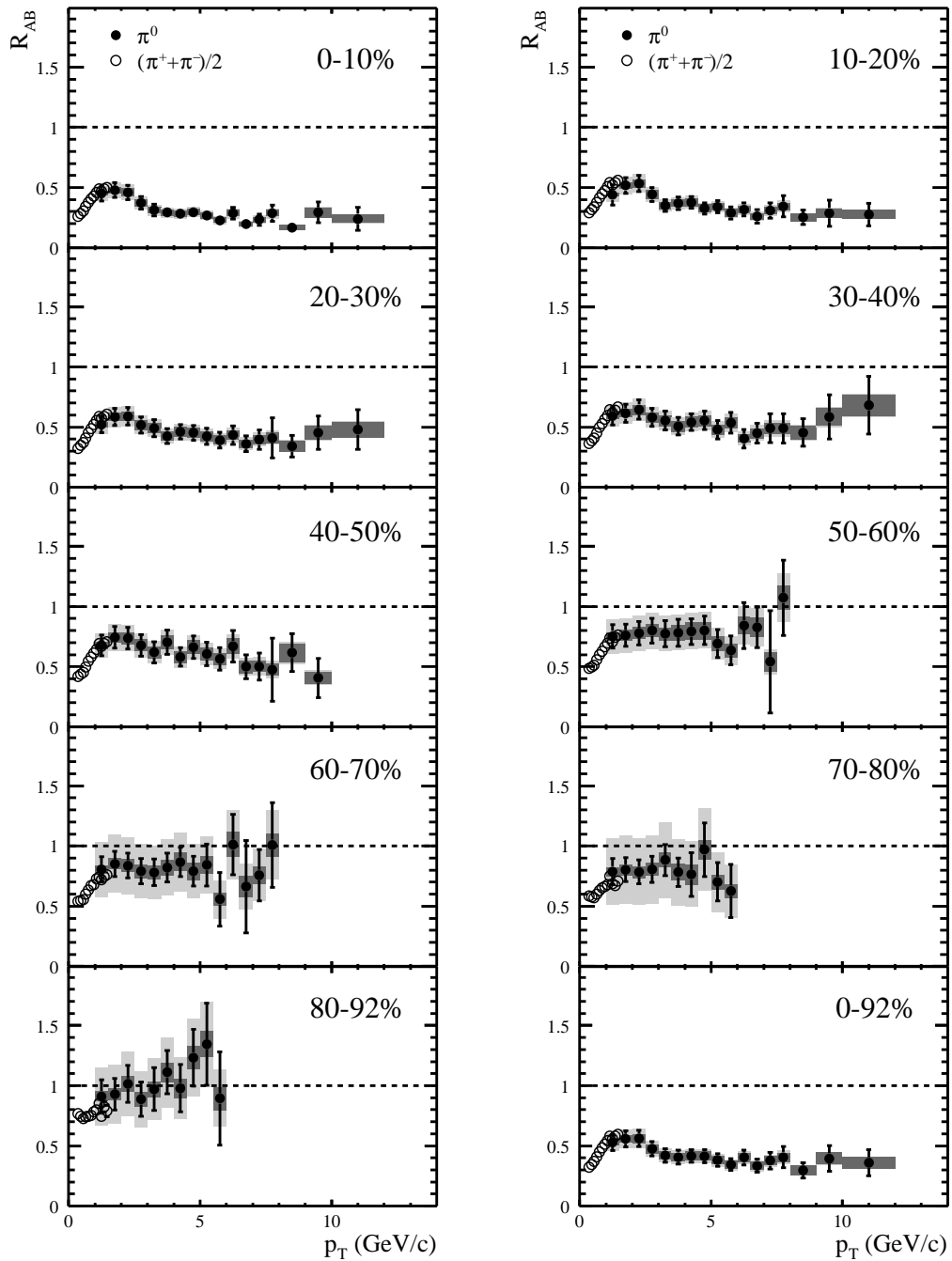


Figure 6.33: The centrality evolution of the nuclear modification factor for π^0 s and charged pions in Au + Au collisions. The π^0 production is suppressed in central collisions compared to p + p reactions, while it follows the scaling with the number of binary nucleon-nucleon collisions in peripheral events. Point-to-point errors (type A) are shown as error bars, errors that move all points in one direction (type B) are shown as dark grey boxes, and overall scale uncertainties (type C) as light grey boxes. In the case of the charged pions the scale uncertainty is not shown for clarity. It is the same as for the π^0 s (light grey boxes).

The measurement of neutral pions in the PHENIX experiment is complemented by the detection of charged pions via the tracking system of the central arms in combination with the time-of-flight measurement (see also Section 3.3). The good agreement of the averaged charged pion result with the neutral pion measurement in minimum bias Au + Au collisions has already been shown in Figure 6.28. Together with the data published in [Adl04] and the p + p reference, which is provided in [Mat04], the measurement of charged pions provides the extension of the nuclear modification to low transverse momenta. This is also shown in Figure 6.33. It nicely illustrates the rise of the nuclear modification factor at low p_T , where the particle production is not expected to scale with the number of binary nucleon-nucleon collisions, as this region is dominated by soft processes. R_{AB} reaches its maximum value in all centralities in the region between $1.5 \text{ GeV}/c \leq p_T \leq 2.5 \text{ GeV}/c$. This maximum value amounts only 50% of the expectation from the scaled p + p yield in central events.

The production of particles via soft processes is expected to scale with the number of participating nucleons. However, it has already been shown in Au + Au collisions at $\sqrt{s_{NN}} = 130 \text{ GeV}$ [Adc01a] that the total multiplicity of charged particles at mid-rapidity $dN_{ch}/d\eta$, which should be dominated by soft processes, does not exhibit this scaling. Instead the dependency of the multiplicity on the number of participants N_{part} can be parameterized as:

$$\left. \frac{dN_{ch}}{d\eta} \right|_{\eta=0} = N_{part}^{\alpha}, \quad (6.41)$$

with $\alpha = 1.16 \pm 0.04$. A similar behavior has been observed at lower energies in Pb + Pb collisions at $\sqrt{s_{NN}} = 17.2 \text{ GeV}$, though with a smaller power $\alpha = 1.07 \pm 0.04$ [Rey99, Agg01]. The deviation from the N_{part} scaling is often interpreted as the increased influence of hard and semi-hard processes on the total particle production. An approximate scaling of semi-hard processes with the number of participants has also been predicted for the case of gluon saturation in the color glass condensate [Kha03].

We will test the scaling of the pion production with the number of participating nucleons by defining the ratio R_{AB}^{part} for the centrality selection f similar to the nuclear modification factor:

$$R_{AB}^{part} = \frac{2 \cdot dN_{AB}}{\langle N_{part} \rangle_f \cdot dN_{NN}}, \quad (6.42)$$

where the factor of two accounts for the participating nucleons in the p + p reference measurement. The evolution of the ratio with centrality is shown in Figure 6.34 for charged and neutral pions. It is seen that the yield of neutral pions per participant in central collisions is enhanced at intermediate p_T by a factor of approximately 2.5 compared to p + p

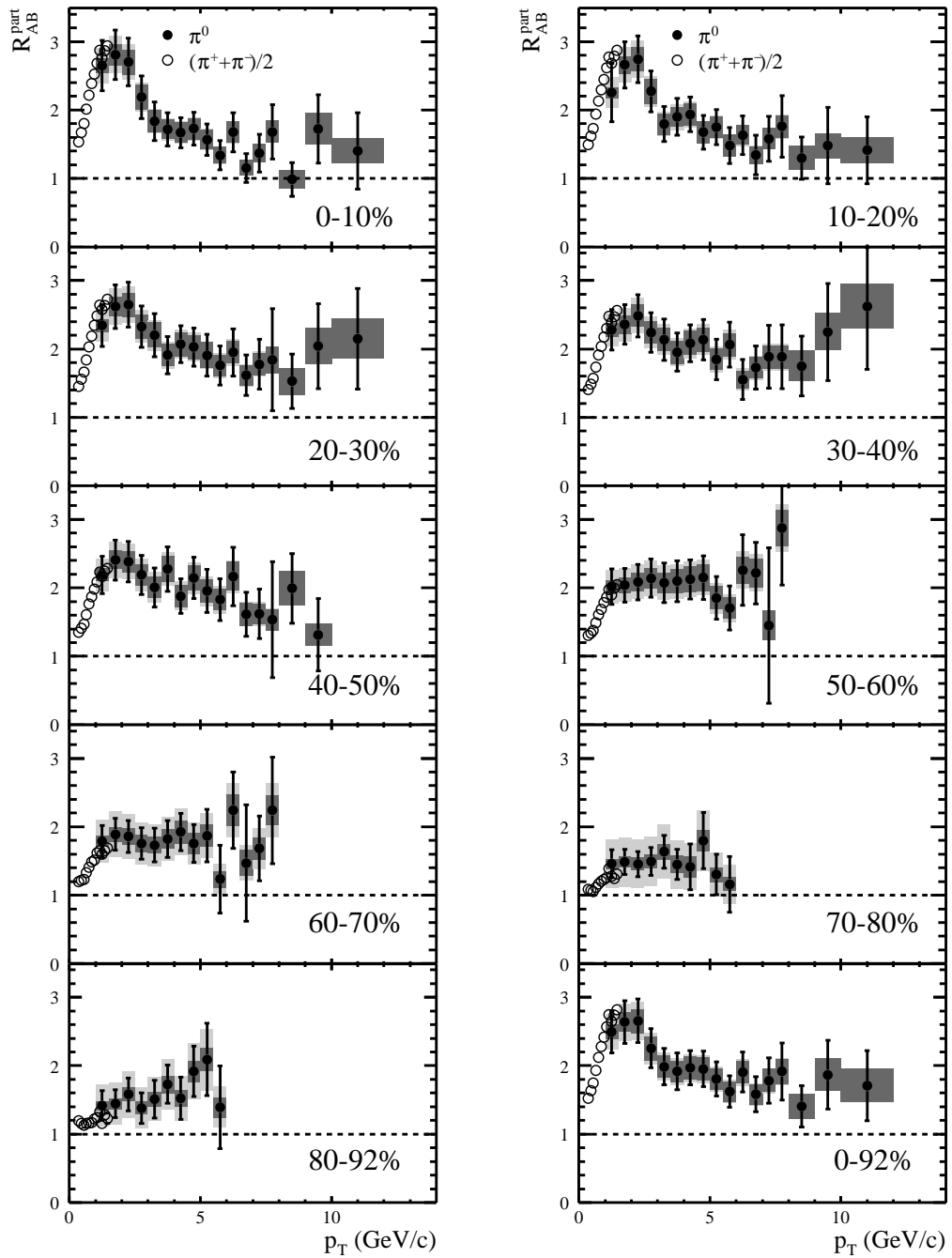


Figure 6.34: The dependence of R_{AB}^{part} on centrality. The pion production per participant pair is enhanced in central collisions at intermediate $p_T \approx 2 \text{ GeV}/c$ compared to p + p reactions. It approaches the scaling with the number of participants at low transverse momentum for all centralities. The particle production at large p_T shows only a weak dependence on centrality when scaled with the number of participating nucleons. Point-to-point errors (type A) are shown as error bars, errors that move all points in one direction (type B) are shown as dark grey boxes, and overall scale uncertainties (type C) as light grey boxes. In the case of the charged pions the scale uncertainty is not shown for clarity. It is the same as for the π^0 's (light grey boxes).

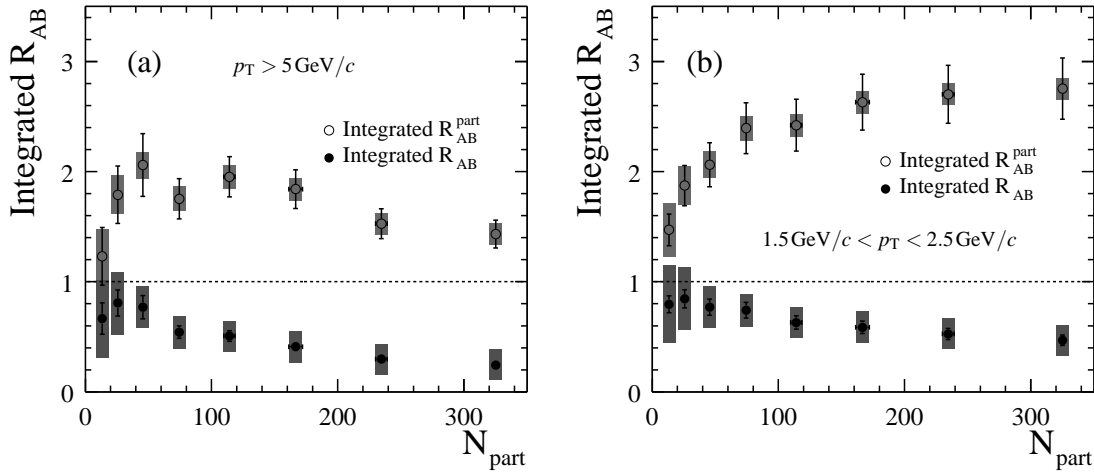


Figure 6.35: The centrality dependence of the integrated nuclear modification factor and of R_{AB}^{part} , respectively, for different p_T regions: (a) for $p_T > 5 \text{ GeV}/c$, where hard scattering is the dominant source of particle production, (b) for $1.5 \text{ GeV}/c < p_T < 2.5 \text{ GeV}/c$, which is the region of the maximum particle yield in central collisions compared to $p + p$ collisions. This region is governed by the interplay of different mechanisms of particle production and medium modification.

reactions. It is interesting to note that R_{AB}^{part} approaches unity at low transverse momenta, as expected if the particle production is dominated by soft processes. The suppression of the particle production at large transverse momenta that is observed in the nuclear modification factor is not obvious when the scaling with the number of participants is examined. Instead R_{AB}^{part} depends only weakly on centrality for large transverse momenta and is consistent with a value of $1.5 - 2$.

The approximate scaling with the number of participants suggested by PHOBOS data in [Bac04], which is often used as an argument in favor for the existence of a color glass condensate in the initial state (see Section 1.3.3), is not supported by our data. However, the PHOBOS data does not contradict our observations, as the results are based on the comparison to peripheral data. This is often done in the absence of a $p + p$ reference. The most peripheral centrality selection provided in [Bac04] and used as the reference is 45-50%. The particle production for this centrality is already suppressed compared to $p + p$ as seen in Figure 6.33, so this particular choice of the reference is not well suited to study medium effects. As illustrated by Figure 6.34, R_{AB}^{part} does not change by a large amount when going from mid-central collisions (40-50%) to central events, which is consistent with the observation in [Bac04].

The centrality dependence of the nuclear modification factor and of R_{AB}^{part} , respectively, can be summarized, by integrating it in different regions of interest. The resulting depen-

dence of the integrated ratios on the centrality, given by the number of participants, is shown in Figure 6.35. Figure 6.35(a) illustrates the behavior for neutral pions with large transverse momentum ($p_T > 5 \text{ GeV}/c$), produced predominantly in initial hard scatterings. As discussed above, the expected scaling with the number of collisions is only seen in peripheral events, while the particle production in central events is strongly suppressed, which points to strong medium effects. The scaling with the number of participants is only consistent with unity for the most peripheral collisions. Within the errors it only shows a weak dependence on centrality, with a decrease in the most central collisions.

Figure 6.35(b) shows the centrality dependence of the integrated R_{AB} and R_{AB}^{part} for $1.5 \text{ GeV}/c < p_T < 2.5 \text{ GeV}/c$, which is the region of the maximal particle yield in central collisions compared to $p + p$ reactions. The nuclear modification factor basically shows the same centrality dependence as for particles with large transverse momentum: the particle production is consistent with the scaled reference in peripheral collisions, while it shows a substantial suppression in central events. This suppression is still about a factor of two. However, it should be noted that in this p_T region soft and semi-hard processes contribute to the particle production, so even in the absence of any medium effects the scaling with the number of binary collisions cannot be presumed. The comparison of the particle production in $\text{Au} + \text{Au}$ and $p + p$ collisions, scaled with the number of participants, shows an interesting behavior in this intermediate p_T range. The integrated R_{AB}^{part} rises quickly for peripheral events and then it saturates. However, the interpretation of this observation is not clear, due to the interplay of different effects in this range: soft processes, semi-hard processes, Cronin enhancement, and the suppression of the particle production due to medium effects.

6.8.1 Comparison to Theoretical Descriptions

One possible explanation for the suppression of particle production in central events is the energy loss of hard-scattered partons prior to their fragmentation, induced by a dense and colored medium. This jet quenching has been discussed as a signature for the creation of a QGP phase in Section 1.3. We will compare the results for the π^0 production in $\text{Au} + \text{Au}$ collisions to different theoretical models that try to explain the observed suppression. Those models involve various scenarios: parton energy loss in a hot and dense phase, initial state effects, or strong hadronic final state effects.

Figure 6.36(a) shows the nuclear modification factor for neutral pions in central events compared to different theoretical calculations. It is seen that the calculation which includes only the known nuclear modifications, Cronin enhancement and nuclear shadowing, leads to a nuclear modification factor that is larger than unity. This points to an even larger suppression when comparing to cold nuclear matter instead of $p + p$ collisions.

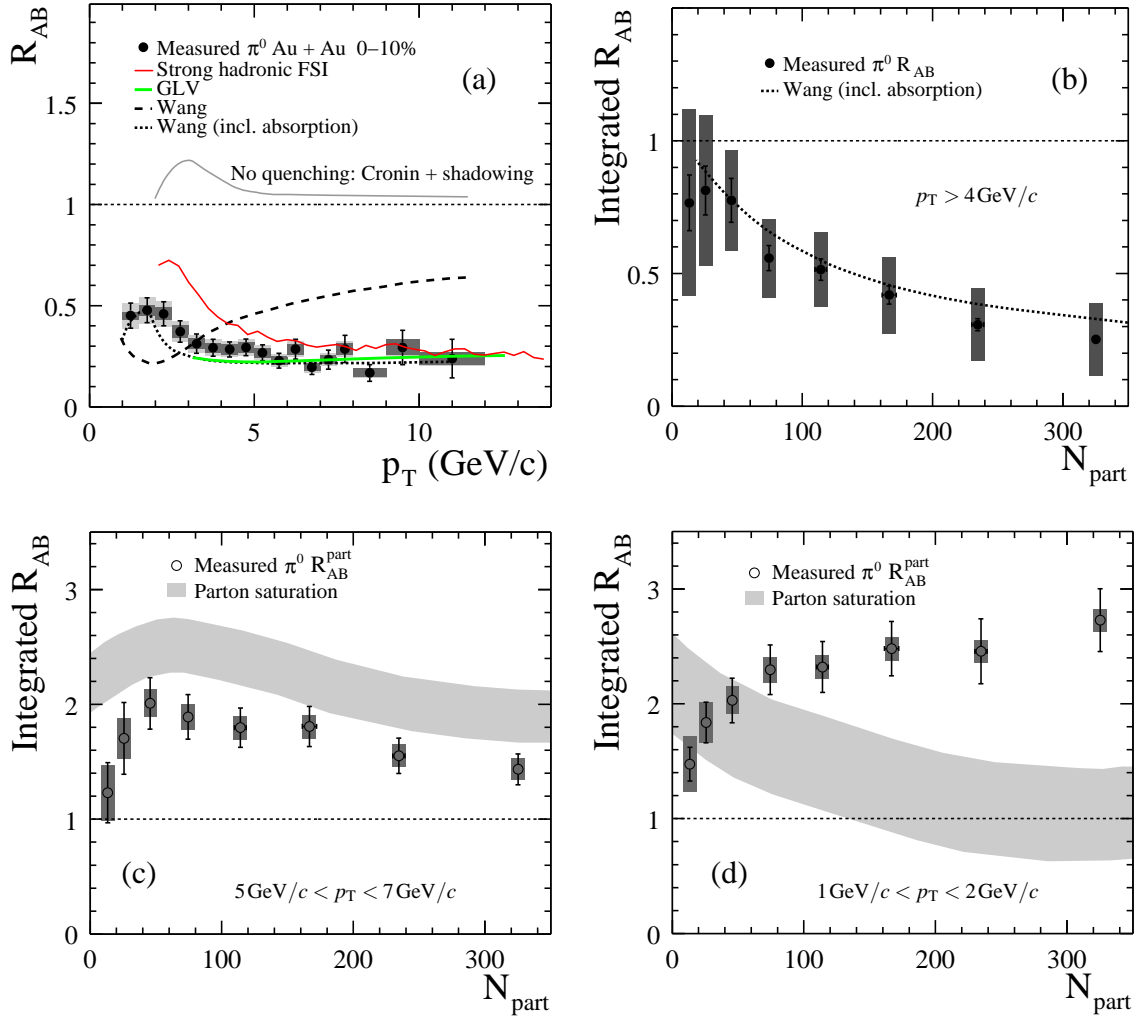


Figure 6.36: Comparison of the scaling behavior measured for neutral pions in Au + Au collisions at $\sqrt{s_{NN}} = 200$ GeV to different theoretical models. (a) The nuclear modification factor for central events compared to a model without jet quenching, only the known nuclear effects are considered [Bar02], a model with strong hadronic final state interactions [Gal03, Cas04], a parton energy loss calculation based on the GLV approach [Vit04], the parton energy loss calculation in [Wan02] without gluon absorption, and from [Wan04] including gluon absorption. (b) The centrality dependence of the nuclear modification factor for $p_T > 5$ GeV/c compared to the calculation in [Wan04]. (c) and (d) The centrality dependence of R_{AB}^{part} compared to the expectation from the parton saturation model in [Kha03] for two different p_T regions.

The order of magnitude of the suppression and the p_T dependence above $3 \text{ GeV}/c$ is well reproduced by the calculation presented in [Vit04], which employs the GLV formalism described in Section 1.3.4 for the parton energy loss in a dense, colored medium, and considers the Cronin effect as well as nuclear shadowing. The observed constant suppression pattern in this approach is a consequence of the interplay between Cronin enhancement, nuclear shadowing, and parton energy loss at RHIC energies. For LHC a rise of the nuclear modification factor with increasing p_T is predicted [Vit02]. Under the assumption of a longitudinally expanding fireball the initial gluon density needed to reproduce the observed R_{AB} is $dN^g/dy \approx 800 - 1200$. This is consistent with the gluon density inferred independently from other observables, such as the multiplicity and the elliptic flow (see [Gyu04]). It also allows to estimate the maximum initial energy density in central collisions to $\epsilon_0 \approx 20 \text{ GeV}/\text{fm}^3$, which is hundred times the energy density of cold nuclear matter [Gyu04].

A second approach to describe the parton energy loss in dense nuclear matter is followed by Wang et al. [Wan02]. It allows to relate the energy loss of partons in cold nuclear matter, which is determined by the medium modification of the parton fragmentation observed in deep inelastic $e + A$ collisions [Air01], to the parton energy loss in central $\text{Au} + \text{Au}$ collisions. The prediction shown in Figure 6.36(a) corresponds to a parton energy loss of $-7.3 \text{ GeV}/\text{fm}$ in a static medium, which is 15 times large than the energy loss derived for cold nuclear matter [Wan02]. However, the calculation fails to describe the p_T dependence of the data. As argued in [Gyu03, Wan04] this might be the indication that the absorption of thermally produced gluons and the stimulated emission of gluons in the QGP phase need to be considered in addition to the induced gluon radiation [Wan01]. This leads to an increased energy loss for large transverse momenta and the data is described well, as seen in Figure 6.36(a). The centrality dependence of the nuclear modification factor at large transverse momenta is also reproduced by this calculation as shown in Figure 6.36(b).

The last curve shown in Figure 6.36(a) corresponds to a scenario, where not the parton energy loss is considered as the source of the observed suppression but strong hadronic final state effects [Gal03, Cas04]. It is argued that the formation of most hadrons from fragmenting partons occurs within the fireball, or that at least the hadron wave function is already partially established in the hot and dense phase as a *pre-hadron*. Inelastic collisions of these particles with the bulk of hadrons in the fireball should then lead to a suppression of the particle production. The observed suppression at large transverse momenta is reproduced in by this approach as seen in Figure 6.36(a), while the calculation does not follow the data at lower transverse momentum $p_T < 4 \text{ GeV}/c$. This discrepancy should be even more pronounced when the Cronin enhancement is taken into account, which is only done for inclusive charged hadrons in [Cas04], not for identified pions. In

addition, the observed yield and width of jet-like correlations in Au + Au collisions is not consistent with the scenario of strong hadronic final state interactions [Adc04].

As discussed in Section 1.3.1 initial state effects can also influence the particle production. While the current knowledge of nuclear shadowing effects does not explain the observed suppression in central Au + Au collisions, the existence of the color glass condensate in the initial state can reproduce some of the observed suppression patterns, provided the saturation scale is large enough (see Section 1.3.3). As discussed in [Kha03] a sufficiently large saturation scale ($Q_s \approx 4 \text{ GeV}$) leads to an approximate scaling of the particle production with the number of participants in central collisions. The influence of the color glass condensate weakens as the transverse momentum of the produced particle gets larger. The centrality dependence of the integrated R_{AB}^{part} as calculated in [Kha03] is shown as grey band in Figure 6.36(c) and (d) for two different p_T regions. It is seen that the shape of the model expectation follows the data for large transverse momenta (Figure 6.36(c)), while the magnitude is overestimated. The predicted scaling with the number of participants in central Au + Au collisions at low transverse momentum is shown in Figure 6.36(d). It is clearly at variance with our data, which instead shows the opposite dependence on the number of participants.

6.8.2 Control Measurement in d + Au Collisions

Though the suppressed production of high p_T particles in central Au + Au collisions is not fully explained by the initial state effects discussed above, the measurement of the particle production in d + Au collisions provides the experimental verification of this assumption. Initial state effects such as Cronin enhancement, shadowing, or the formation of a color glass condensate are also present in d + Au collisions, while no large volumes with increased energy density are formed.

The interpretation of the suppression pattern in Au + Au collisions as a consequence of parton saturation effects, the color glass condensate, also predicted a suppression of the hadron production at large transverse momenta in d + Au collisions [Kha03]. Theoretical descriptions that incorporated only the effects nuclear shadowing and Cronin enhancement, which are also considered in the parton energy loss calculations presented above, predicted an enhancement. These predictions are shown together with the nuclear modification factor determined for neutral pions in d + Au collisions, R_{dAu} , in Figure 6.37(a) (see also [Adl03b]). The absence of suppression is clearly seen. The data show the best agreement with the prediction that incorporates HIJING shadowing and the Cronin effect. The calculation with the EKS shadowing parameterization [Esk99], which contains an anti-shadowing contribution that enhances R_{dAu} , is disfavored.

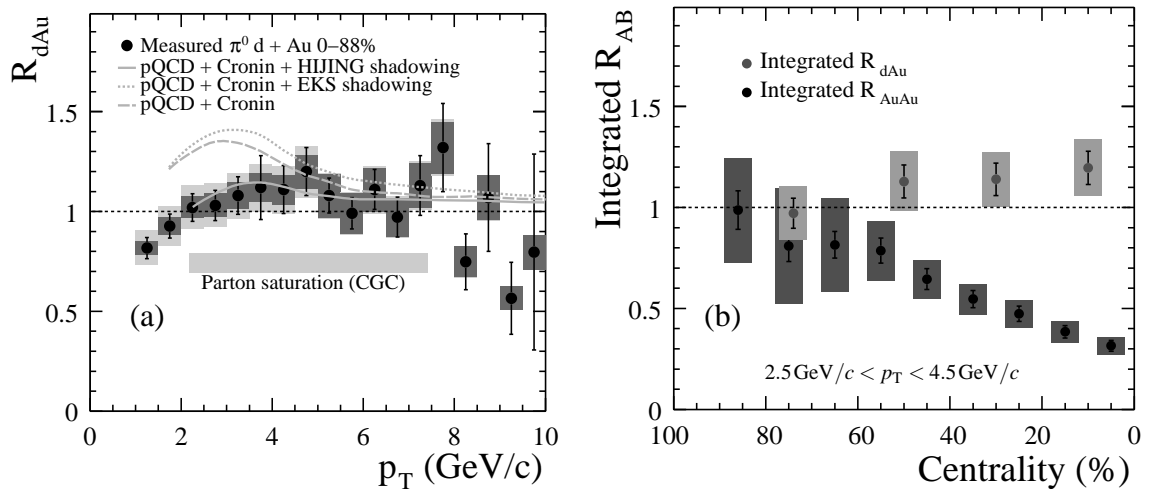


Figure 6.37: (a) The nuclear modification factor for neutral pions in minimum bias d + Au collisions compared to theoretical predictions from the parton saturation model (CGC) in [Kha03] and to the expectation for nuclear shadowing and Cronin enhancement [Lev03], with different shadowing parameterizations. (b) The centrality dependence of the nuclear modification factor in d + Au compared to Au + Au collisions [KB04a].

In addition, the centrality dependence of the nuclear modification factor in d + Au collisions shows the opposite trend as in the case of Au + Au reactions (see Figure 6.37(b) and [KB04a]). This is also not expected from the saturation model and from the pQCD calculation that employs the EKS parameterization, which provides a nuclear shadowing that depends on the impact parameter (see [Lev03]).

The observation supports the scenario that the suppression in central Au + Au collisions is not an initial state effect and that it does not arise from the saturation of the parton density. However, this does not rule out the possible existence of the color glass condensate in the initial state with a smaller saturation scale, e.g. in a different x region of the parton distribution function, which is tested by particles that are produced at forward and backward rapidity, respectively (see e.g. [JM04, Mur04]).

7. Measurement of Direct Photons

As discussed in Chapter 2 direct photons are well suited to study different stages of a heavy ion collision, as they are produced throughout all phases of the reaction and can escape without strong interactions. In this chapter the first measurement of direct photons at RHIC is presented, which allows for the first time in heavy ion collisions to test the production of direct photons in a transverse momentum region where hard scattering is the dominant source of particle production.

7.1 Inclusive Photons

The main problem in the measurement of direct photons is to separate the signal from the contribution of radiative decays (mainly $\pi^0, \eta \rightarrow \gamma\gamma$) in the inclusive photon spectrum.

A widely used strategy in nucleon-nucleon collisions is to identify direct photons at large transverse momenta via the jet topology: A cone of hadronic particles back-to-back with an isolated photon is characteristic for hard Compton scattering or $q\bar{q}$ annihilation. However, such requirements bias the measurement and basically exclude other processes, such as Bremsstrahlung. In the low multiplicity environment of nucleon-nucleon collisions it is also possible to identify photons from hadronic decays directly by an invariant mass analysis of photon pairs.

In heavy ion collisions the situation is more complicated, besides the increased number of possible sources of direct photons, the large multiplicity especially in central events does not allow to use the techniques mentioned above for elementary reactions. Instead the inclusive photons are measured and on a statistical basis compared to the expectation from hadronic decays, which is determined based on the measurement of π^0 s in the same event sample (see Chapter 6). This eliminates a large fraction of the systematic errors, e.g. for normalization and centrality selection. Also, the simultaneous measurement of π^0 s provides a good internal verification of the energy scale as already discussed in Section 6.5.

The determination of the inclusive photon yield is in many respects similar to the π^0 measurement. Since the two analyses are performed in the same computer code, in particular the particle identification criteria and the cuts on bad modules are identical. The correction for the detection efficiency for photons is also determined within the same framework, as discussed for the π^0 analysis in Au + Au in Section 6.4. One difference is that photons do not have a signature, such as the invariant mass peak in the case of

the π^0 s, to exclude background contributions from other particles. For this reason the raw inclusive photon yield is contaminated by mis-identified charged particles and neutral hadrons, which makes additional corrections necessary. Equivalent to Equation (6.11) the fully corrected inclusive photon yield is given by:

$$\frac{1}{2\pi p_T N_{\text{in}}} \left. \frac{d^2 N_\gamma}{dp_T dy} \right|_{\text{incl}} = \frac{1}{2\pi p_T N_{\text{in}}} \cdot \frac{(1 - X_{n^0}) \cdot (1 - X_{\text{ch}})}{\epsilon_\gamma \cdot a_\gamma \cdot c_{\text{conv}}} \cdot \frac{\Delta N_{\text{cluster}}}{\Delta p_T \Delta y}, \quad (7.1)$$

where a_γ is the acceptance and ϵ_γ the efficiency correction. The newly introduced factors X_{ch} and X_{n^0} are the contributions of charged particles and neutral hadrons to the raw yield of photon-like clusters measured with the EMCal, $\frac{\Delta N_{\text{cluster}}}{\Delta p_T \Delta y}$. The determination of the correction factors is discussed in the following.

Similar to the measurement of π^0 s an event sample enriched with highly energetic photons, the LVL2-triggered data, is incorporated into the measurement of the raw inclusive photons spectrum. The LVL2 data for the photon measurement is combined with the minimum bias data above $p_T = 5.5 \text{ GeV}/c$. More details on the determination of the trigger efficiency for single photons are given in the context of the π^0 measurement in Section 6.1.3.

7.1.1 Single Photon Acceptance and Efficiency

As already discussed in Section 6.3 the geometrical acceptance for single particles is basically determined by the phase-space coverage of the detector. It is calculated via a Fast Monte Carlo simulation that determines the fraction of single particles hitting the detector surface, which have been emitted in the rapidity interval $-0.45 \leq y \leq 0.45$ and $\Delta\phi = 2\pi$ with the following characteristics:

- Flat transverse momentum distribution $0 < p_T \leq 20 \text{ GeV}/c$,
- Uniform vertex distribution $|z_{\text{vtx}}| \leq 30 \text{ cm}$,
- Gaussian rapidity distribution around zero with width $\sigma_{\text{rap}} = 3$,
- Uniform ϕ distribution.

The particles have to be weighted according to their measured p_T distribution as described in Section 6.3. The resulting acceptance is shown in Figure 7.1 for the PbPb and the PbSc, respectively. As for the π^0 s the effect of the bad module and edge cut is taken into account in the efficiency calculation.

For the single photon efficiency a similar algorithm as for the π^0 efficiency is used (see Section 6.4). Photons converted into an e^+e^- pair are excluded. In addition, only

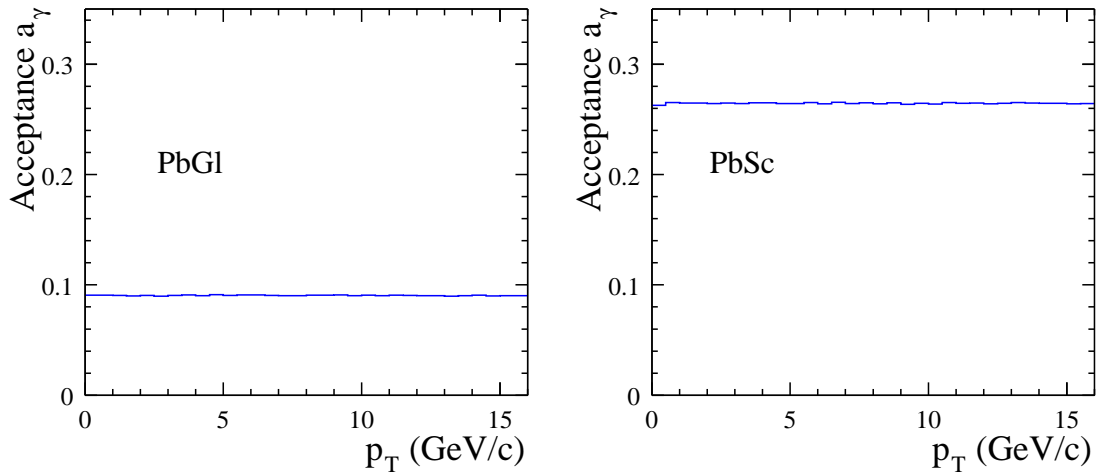


Figure 7.1: Geometrical acceptance of the PbGl and the PbSc for single particles within the rapidity interval $|y| < 0.45$.

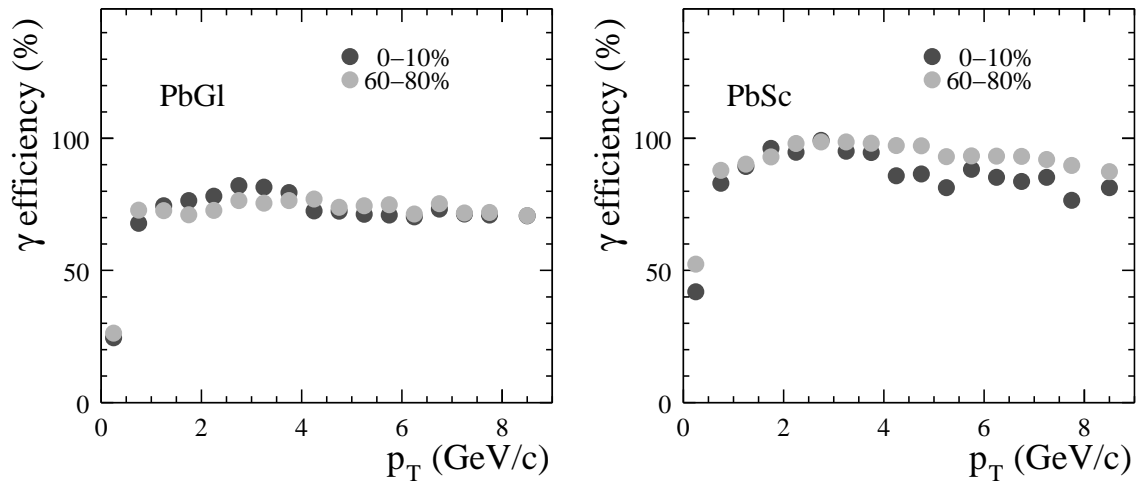


Figure 7.2: Single photon efficiency for peripheral and central events for PbGl and PbSc (PID 3). The efficiency includes the effect of the dead and bad modules.

events with a single simulated cluster on the empty detector are considered. In the merged event the hit closest to this cluster is selected. The photon is considered as reconstructed if the cluster energy did not change by more than a factor two, otherwise the photon is counted as lost to avoid double counting. The efficiency for single photons is shown for two different centralities in Figure 7.2. It includes the effect of the edge and bad module cut, which is tantamount to an additional photon loss of approximately 10% for the PbSc and 25% for the PbGl.

7.1.2 Charged Particle Background

A large source of background for the inclusive photon measurement especially at low p_T arises from charged particles. Charged hadrons deposit on the average only a fraction of their energy in the EMCal and dominate the charged particle background at low energies or transverse momenta. At higher p_T the charged particle background should be dominated by photon conversions.

The contamination of the raw inclusive photon spectrum from charged particles can be determined by employing the PHENIX tracking system as a charged particle veto (CPV). In the analysis we either use the complete information of the track reconstruction, which is basically determined by the tracking of the drift chamber, or the information on charged particles hitting the PC3, which has the advantage that it is positioned directly in front of the EMCal (see Section 3.3.2).

The fraction of charged particles contributing to the raw cluster spectrum can only be determined on a statistical basis. This is done by calculating the distance of each EMCal hit to the closest projection of a charged track onto the calorimeter surface. In the case of the DC the track projection includes the bending in the magnetic field, for the PC3 only a straight-line projection vertex–PC3–EMCal is used. The distribution of the distances to the closest track r_{CPV} is determined for different p_T ranges, particle identification criteria and centralities. It is compared to the distribution obtained via a mixed-event technique, similar to the π^0 analysis (Section 6.1.2), to eliminate the combinatorial background. The background is scaled to match the real event distribution for $r_{CPV} > 30$ cm. In the case of too few entries in the real and mixed distributions, which is the case for large transverse momenta, the scaling factor is determined by integration of the real and mixed distribution above $r_{CPV} = 30$ cm. One example for a scaled distribution of veto radii determined via the projection of PC3 tracks is shown together with the distribution from real events in Figure 7.3.

The number of EMCal clusters originating from charged particles is now given by background subtraction, integration of the remaining peak for $r_{CPV} < 30$ cm, and correct-

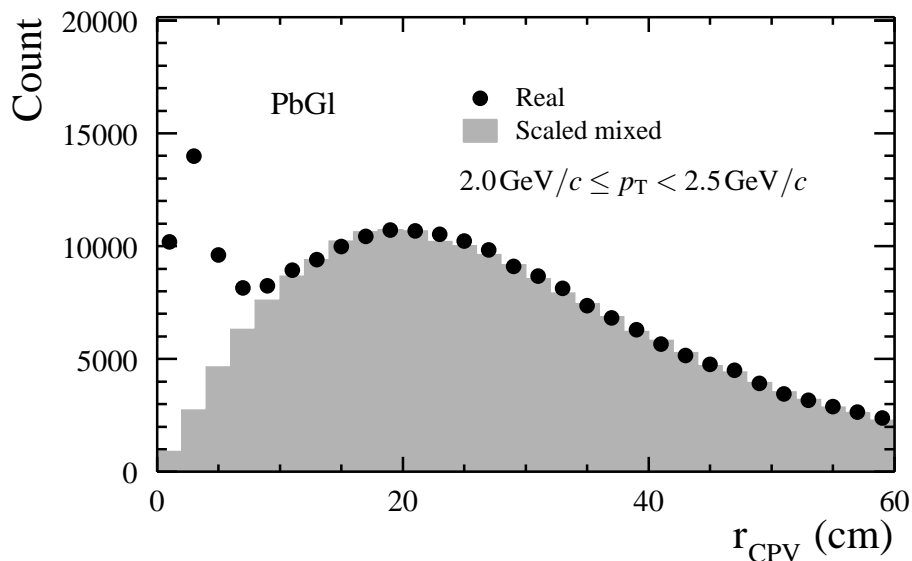


Figure 7.3: Veto radius for PbG1 hits with $2.0 \text{ GeV}/c \leq p_T < 2.5 \text{ GeV}/c$ in real and scaled mixed minimum bias events determined with the PC3 (PID2).

ing for the tracking efficiency¹. It gives the charged fraction relative to the total number of EMCal clusters for the relevant p_T range. The resulting p_T dependence of the charged particle contamination in minimum bias events determined with PC3 and DC, respectively, is shown in Figure 7.4 for the PbG1 and the PbSc. It illustrates several interesting properties of the two EMCal detectors, which shall be addressed in the following.

The hadron rejection by the different PID criteria is nicely seen for both calorimeters, going from the loosest cut (PID0) to the tightest (PID3). It is also seen that the shower shape cut is most powerful for rejecting hadrons, while the time-of-flight cut has a noticeable effect only for the PbSc at intermediate p_T . In addition, Figure 7.4 illustrates the different sensitivity of the PbG1 and the PbSc to hadrons. Charged hadrons deposit only a fraction of their energy in the calorimeter as it is only as deep as one hadronic interaction length (see Section 4.1.1). However, due to the different detection mechanisms in the calorimeters the PbG1 is only sensitive to those particles in a hadronic shower which travel faster than the speed of light in the lead-glass, leading to a smaller contribution at low detected energies compared to the PbSc.

The charged particle contamination in Figure 7.4 seems to level off at a constant value above $p_T = 2 \text{ GeV}/c$ in the case of the PbG1. This and the conversion studies below motivate the decision to fix X_{ch} to a constant value at large transverse momenta during the

¹In the current analysis the tracking efficiency and acceptance is assumed to be $\varepsilon \cdot a = (90 \pm 5)\%$.

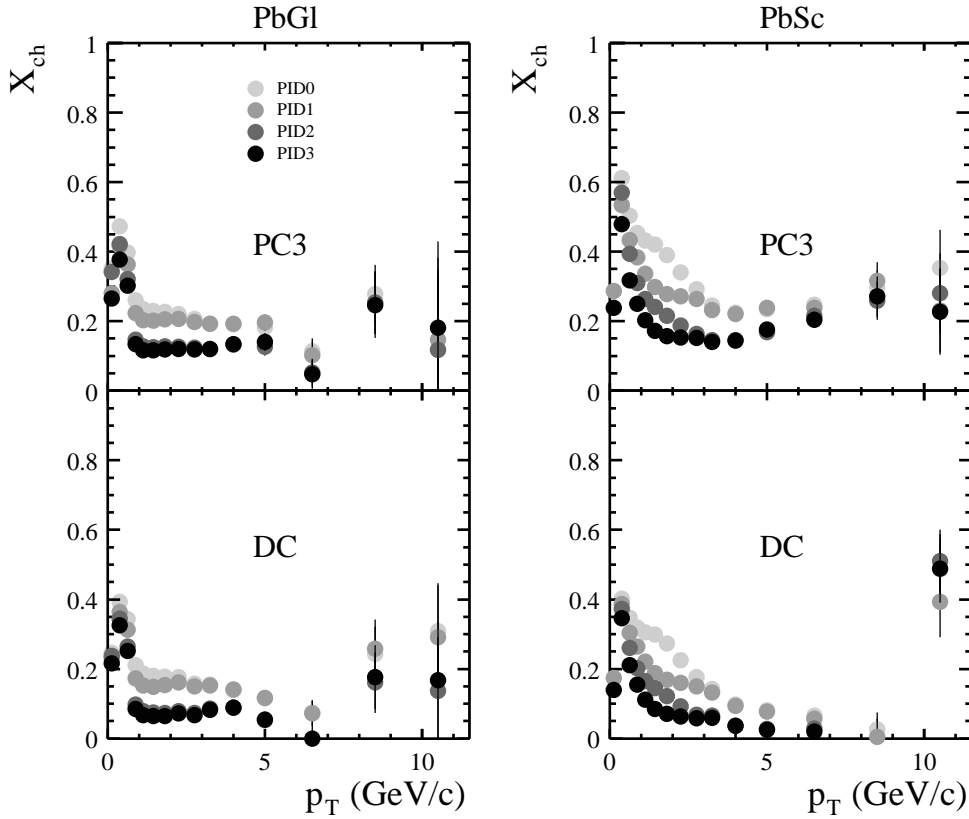


Figure 7.4: Fraction of charged particles after PID cuts in minimum bias events for PbG1 (left) and PbSc (right). The different contaminations are determined using the track projections of the PC3 and DC, respectively.

analysis, to avoid fluctuations of the correction. The value of this constant extrapolation is determined by a fit to the respective X_{ch} distributions above $p_T = 2 \text{ GeV}/c$ for the PbG1 and above $p_T = 3 \text{ GeV}/c$ for the PbSc.

Figure 7.4 not only illustrates the difference between the two employed calorimeters. There is also an obvious difference between the charged particle contamination determined with the PC3 and the DC. The main difference between the two detectors is that the DC is positioned at a radial distance of $2 \text{ m} < r < 2.4 \text{ m}$, while the PC3 is located basically in front of the calorimeters at $r \approx 5 \text{ m}$ (see Section 3.3.2). The material budget between DC and PC3 leads to additional photon conversions, which cause additional charged hits in the PC3 compared to the DC. A rough estimate based on the values given in Appendix E together with Equation (4.1) yield approximately 5% additional converted photons for the west arm and 3.6% for the east arm, respectively. The difference seen in Figure 7.4 is not fully explained by this estimate.

However, one has to consider one disadvantage of the employed mixed-event technique. It can only correct for random associations if the charged hit and the photon are uncorrelated. This is not the case for photons produced in a hadron jet or for π^0 decay photons where one photon converted. The effect of the latter shall be examined in more detail, as most of the photons are produced in π^0 decays.

As discussed in Section 6.4.1 for the efficiency calculation, the simulated detector response to single π^0 s and photons also contains information on the PC3 hits. Thus it is possible to examine the fraction of particles tagged as charged by the PC3 in a simulation, which a priori does not contain any charged hadrons, but only single photons and decay photons. The additional advantage of this method is that the simulation considers the material budget for conversions that is on the actual way of the photon to the calorimeter. The fraction of charged particles in the simulation is determined similarly to the method used in the real data by calculating the distance to the nearest projections of a PC3 hit onto the calorimeter surface. However, as random associations can be neglected due to the small number of hits in the simulation, the veto-radius can directly be used to tag an EMCal hit as charged by requiring $r_{CPV} < 30$ cm.

For photons originating from a π^0 decay one would expect that the fraction of tagged photons is larger than in the simulation of single photons, because for increasing transverse momentum the two decay photons approach each other and the conversion of one photon can tag both as charged. This is illustrated in Figure 7.5(c) and (d). The observation that the fraction of tagged photons is smaller in the PbGl compared to the PbSc reflects the finer granularity and better position resolution of the PbGl. Under the assumption that the majority of photons in peripheral events are from π^0 decays and that other overlap effects can be neglected, the fraction of charged hits determined with the PC3 should be equal to the fraction of charged hits determined with the DC plus the contribution from converted decay photons. This is shown in Figure 7.5(e) and (f), for the PbGl and the PbSc. To avoid ambiguities due to the different material budget in the two spectrometer arms, only the result for the east arm is shown.

For the final correction of the charged contamination a constant extrapolation is used above $p_T = 2 \text{ GeV}/c$ (PbGl) or $p_T = 3 \text{ GeV}/c$ (PbSc). In this region the contribution from converted single photons is at the same level as the contribution from decay photons. The constant extrapolation is justified because we only want to consider the contribution of single-photon conversions at large p_T . This loss of photons is corrected in the conversion correction described below. The fact that photons from decays are associated with a charged track more likely than single photons must not be considered, because the contribution from decay photons is considered in the background calculation described in Section 7.2.1.

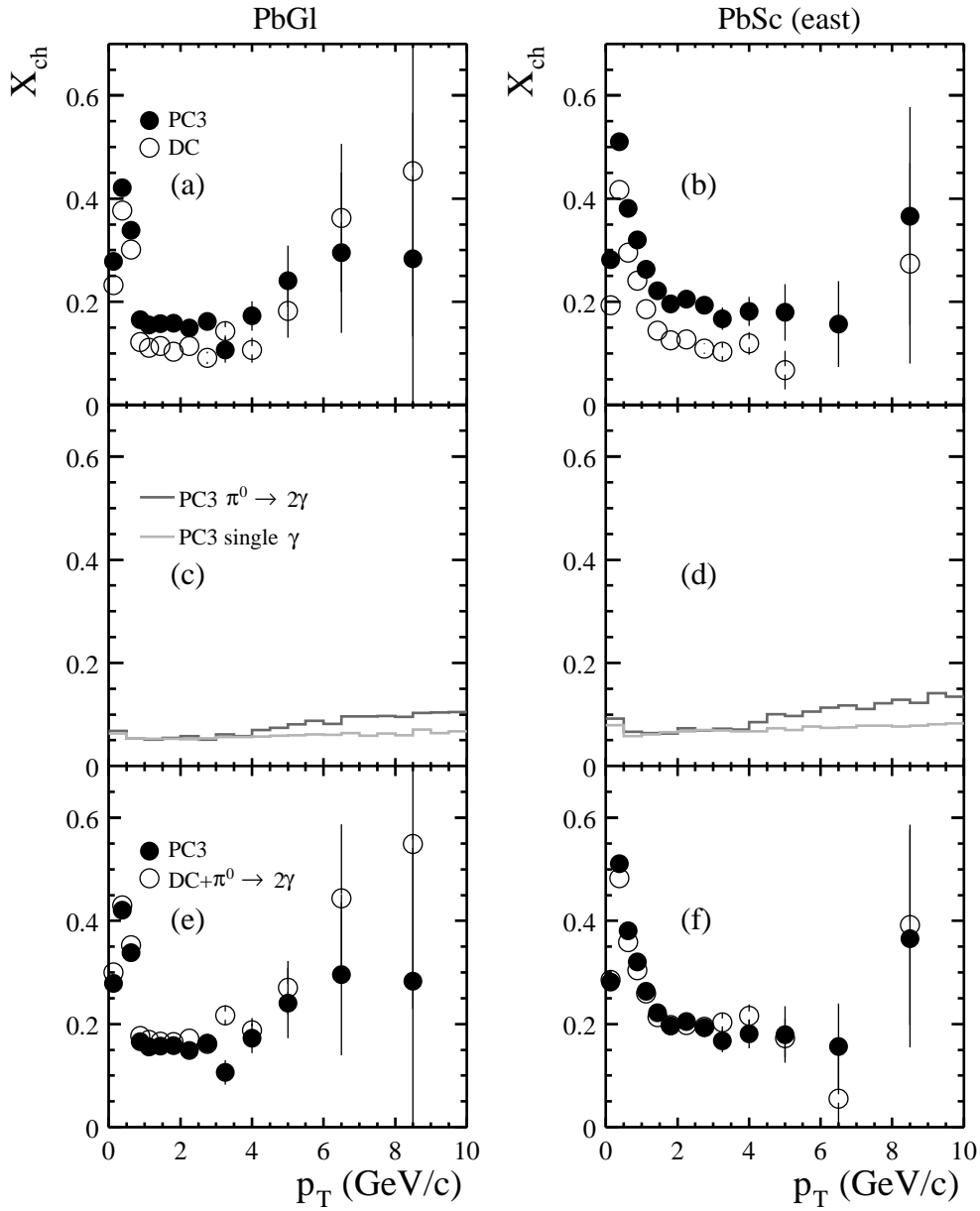


Figure 7.5: (a) and (b) comparison of the charged particle contamination in peripheral events determined with PC3 and DC in the PbG1 and the PbSc sectors of the east arm, respectively, (c) and (d) fraction of hits flagged by a veto radius of $r_{\text{CPV}} < 30\text{ cm}$ to the next PC3 hit in the simulation of single photons and π^0 s, (e) and (f) comparison of charged particle contamination determined with the PC3 to the sum of X_{ch} measured with the DC and of the expectation solely from converted decay photons. All plots are for PID1.

7.1.3 Background from Neutrons and Antineutrons

The contamination of the raw photon spectrum from neutrons and antineutrons needs to be estimated based on simulations. In the simulation, the efficiency of the calorimeter for neutrons and antineutrons $\epsilon_{n/\bar{n}}$ can be determined². Together with the geometrical acceptance for single particles $a_{n/\bar{n}} = a_\gamma$, this efficiency can be used to derive the uncorrected, raw response of the EMCal to neutrons with a given input spectrum:

$$\left. \frac{d^2N}{dp_T dy} \right|_{n/\bar{n}}^{\text{raw}} = \epsilon_{n/\bar{n}} a_{n/\bar{n}} \left. \frac{d^2N}{dp_T dy} \right|_{n/\bar{n}}. \quad (7.2)$$

It can be compared to the raw cluster spectrum after subtraction of charged particles.

Neutron Spectra

The flux of neutrons and antineutrons into the acceptance of the EMCal is estimated by a parameterization of the identified proton and antiproton cross sections measured in Au + Au collisions at PHENIX for different centrality selections [Adl04]. The basic assumption is that the production of nucleons does not depend on the isospin. Hence, the number of antineutrons and neutrons produced in the collision, not originating from the nuclei, is equal to the number of newly produced antiprotons and protons. It is also assumed that the production of nucleons and antinucleons is equivalent. The yields are then given by:

$$\left. \frac{d^2N}{dp_T dy} \right|_{\bar{n}} = \left. \frac{d^2N}{dp_T dy} \right|_{\bar{p}}, \quad (7.3)$$

$$\left. \frac{d^2N}{dp_T dy} \right|_n = \left. \frac{d^2N}{dp_T dy} \right|_p + \left(\left. \frac{d^2N}{dp_T dy} \right|_p - \left. \frac{d^2N}{dp_T dy} \right|_{\bar{p}} \right) \frac{A-Z}{Z}. \quad (7.4)$$

The second term of Equation (7.4) is the contribution of neutrons from the nucleus, with A and Z the mass number and the atomic number, respectively.

The published proton and antiproton spectra are corrected for contributions from particles decaying into p or \bar{p} , the so-called *feed-down*. However, for the background calculation the total neutron flux, including all sources, needs to be determined. The feed-down correction for neutrons is calculated based on the assumption that the main contribution from decays to the inclusive n or \bar{n} spectrum originates from λ or $\bar{\lambda}$ decays, similar to the spectrum of protons and antiprotons, respectively. The fraction of p or \bar{p} originating from λ or $\bar{\lambda}$ for the inclusive proton and antiproton spectra, $\delta_{p/\bar{p}}^{\text{feed}}(p_T)$, is known from [Adl04],

²In the following "neutrons" will be used synonymously with "antineutrons" if not stated otherwise.

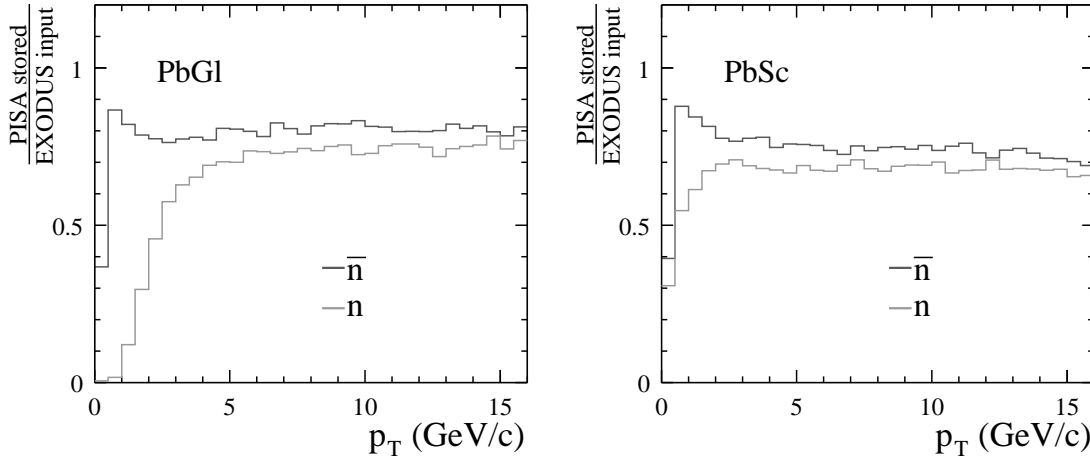


Figure 7.6: The difference between stored particles in PISA and input particles from EXODUS within the acceptance for both calorimeter types.

so that the decay contribution which needs to be added to Equation (7.3) and (7.4) is given by:

$$\left. \frac{d^2N}{dp_T dy} \right|_{n/\bar{n}}^{\text{feed-down}} = \left(\frac{\Gamma(\lambda \rightarrow n\pi^0)}{\Gamma(\lambda \rightarrow p\pi^-)} \right) \cdot \frac{1}{1 - \delta_{p/\bar{p}}^{\text{feed}}(p_T)} \cdot \left. \frac{d^2N}{dp_T dy} \right|_{p/\bar{p}}, \quad (7.5)$$

where the factor considers the different branching ratio for λ s decaying into protons and neutrons, respectively.

Neutron/Antineutron Efficiency

The efficiency calculation for neutrons is done in two different ways. The first method uses the same technique also employed for single photons and π^0 s: the embedding of simulated particles into real events. The second method involves only the pure simulation of neutrons and is used to determine the differences between different hadron packages employed for the simulation.

Before going into detail of the two different methods, one has to pay attention to a peculiarity of the GEANT simulation of neutrons. In the generation of the simulated output files only particles that interact with the calorimeter are stored. This is important in the case of neutrons, because they do not deposit energy via Cherenkov radiation or ionization and the calorimeter is only as deep as one hadronic interaction length.

The information about the non-interacting neutrons must be considered when calculating the efficiency. This is possible by going back to the EXODUS files, which are used

as input to the simulation of single particles (similar to the π^0 s and photons), and by comparison of the input particles to the stored simulated particles. The ratio between the number of input particles which fall into the EMCal acceptance and the particles which are stored in PISA is shown in Figure 7.6. A value of about 65 – 80% for large transverse momenta is observed, which is expected considering the hadronic interaction length of the calorimeters (see Section 4.1.1). The total efficiency for measuring neutrons is given by this *interaction* efficiency and the actual detection efficiency:

$$\epsilon_{n/\bar{n}} = \epsilon_{n/\bar{n}}^{\text{interaction}} \cdot \epsilon_{n/\bar{n}}^{\text{detection}}. \quad (7.6)$$

For the simulation of hadrons three different simulation packages can be employed in GEANT: GHEISHA, FLUKA, and GCALOR. The default for the GEANT simulation of the PHENIX experiment via PISA is the hadron package FLUKA [Aar87]. It uses, depending on the particle species and energy, different microscopic transport models and considers the effects of Fermi motion and binding energies. We also implemented the simulation of hadrons using GCALOR [Zei01] in the PISA framework. GCALOR is the GEANT interface to the CALOR89 program package [Gab]. The main difference to FLUKA is that it uses the transport MICAP code for thermal neutrons, the Monte Carlo package NMTC [Col78] for nucleons with energies upto 3.5 GeV, and a scaled transition from NMTC to FLUKA upto 10 GeV. The oldest implementation of hadron simulation in GEANT, GHEISHA [Fes85], is not used. A more detailed discussion of the three different packages in connection with the simulation of the PbGl is found in [KB00].

In the simulation of single neutrons the number of hits is usually greater than one. To take this cluster splitting into account in the efficiency calculation with embedding, all hits on the empty detector are considered for the search in the merged event, so that one neutron of given input p_T can have several contributions at low transverse momenta. This procedure is also employed for single photons as a cross-check, but it showed no difference in the photon efficiency. It is only important for conversion studies.

In addition to the efficiency from embedding, the efficiency from single particle simulations is determined in the same way as described in [KB00]. An *efficiency matrix* of input transverse momentum versus output transverse momentum is determined, as illustrated in Figure 7.7. It transforms a given n or \bar{n} input spectrum, described by a vector, into the raw neutron response:

$$f^{\text{raw}} = \begin{pmatrix} f_1^{\text{raw}} \\ f_2^{\text{raw}} \\ \vdots \\ f_n^{\text{raw}} \end{pmatrix} = \begin{pmatrix} a_{11} & a_{12} & \cdots & a_{1n} \\ a_{21} & a_{22} & \cdots & a_{2n} \\ \vdots & & & \vdots \\ a_{n1} & a_{n2} & \cdots & a_{nn} \end{pmatrix} \cdot \begin{pmatrix} f_1^{\text{in}} \\ f^{\text{in}} \\ \vdots \\ f_n^{\text{in}} \end{pmatrix}. \quad (7.7)$$

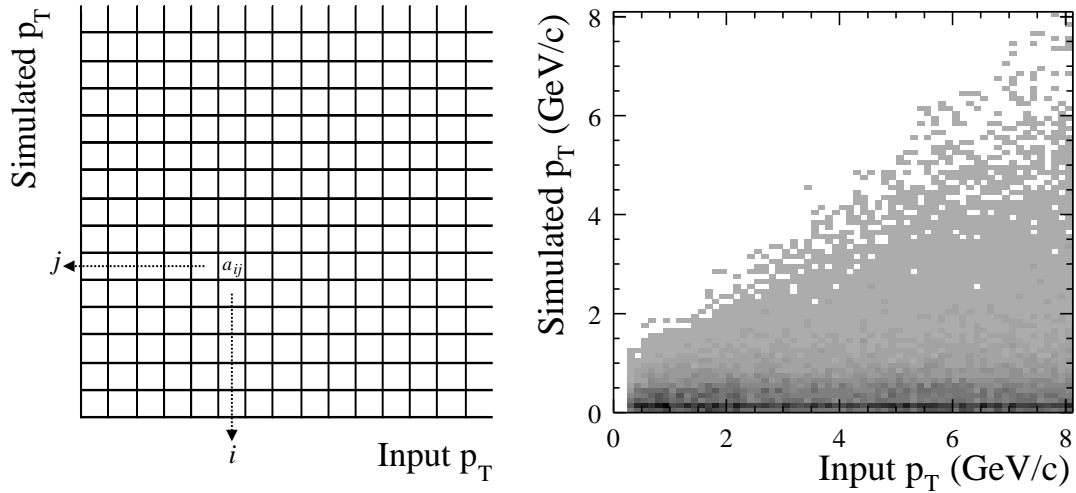


Figure 7.7: Sketch of the efficiency matrix for the determination of the raw p_T spectrum and an example of an efficiency matrix used for antineutrons in the PbG1 (PID0 FLUKA).

The neutron contamination derived in [KB00] for the direct photon measurement of the WA98 experiment and in [Rey02] for the first search for direct photons with the PHENIX experiment have been determined employing a standalone GEANT simulation of 18×12 PbG1 modules for the efficiency matrix, while for this analysis the complete PISA framework, including both EMCal detectors, PbSc and PbG1, and the generation of simulated DSTs is employed.

The efficiency determined via the embedding of neutrons and antineutrons into real events is shown in Figure 7.8 for two different PID cuts. The antineutron efficiency is large compared to the neutron efficiency, because the annihilation process can deposit an energy of twice the neutron rest-mass in the detector. Nevertheless, the efficiency is very small at large transverse momenta even without any cuts, implying that contributions from neutrons to the total neutral spectrum of the calorimeter are small. This is illustrated for two different PIDs in Figure 7.9 where the EMCal cluster spectrum, after subtraction of charged particles, is compared to the derived raw p_T -spectrum of neutrons and antineutrons determined by Equation (7.2). The contamination is largest around $p_T = 2 \text{ GeV}/c$ due to the large contribution of annihilating antineutrons. It is very effectively reduced by the shower shape cut in the PbG1 as well as in the PbSc and becomes negligible above $p_T = 5 \text{ GeV}/c$ for all PIDs.

The efficiency for neutrons and antineutrons determined within a PISA simulation employing the GCALOR hadron package instead of FLUKA has been evaluated with

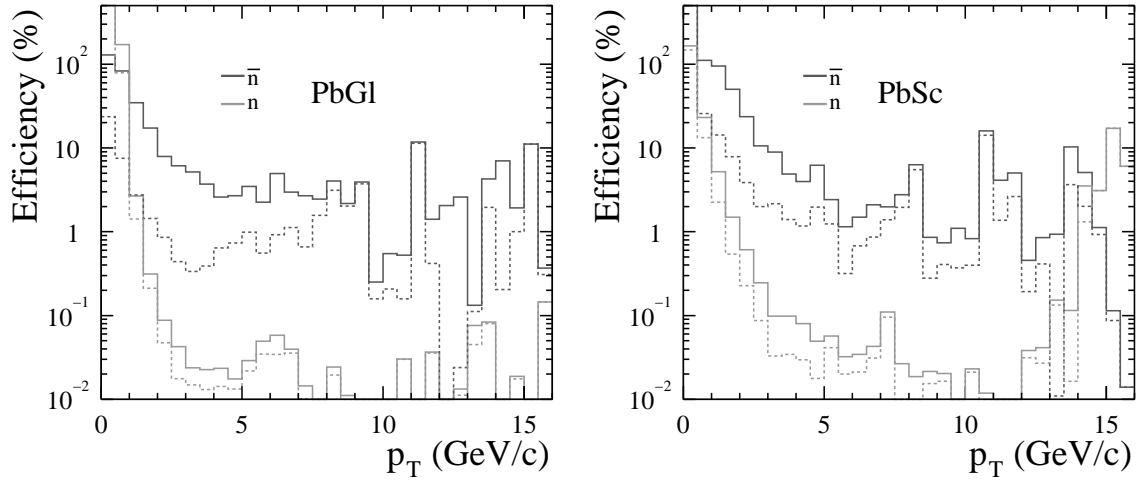


Figure 7.8: Efficiency from embedding of simulated neutrons and antineutrons into real minimum bias events for no PID cuts (PID0, solid line) and for the shower-shape cut (PID2, dashed line). The fluctuations at large p_T are due to statistical uncertainties, which are not shown in the plots.

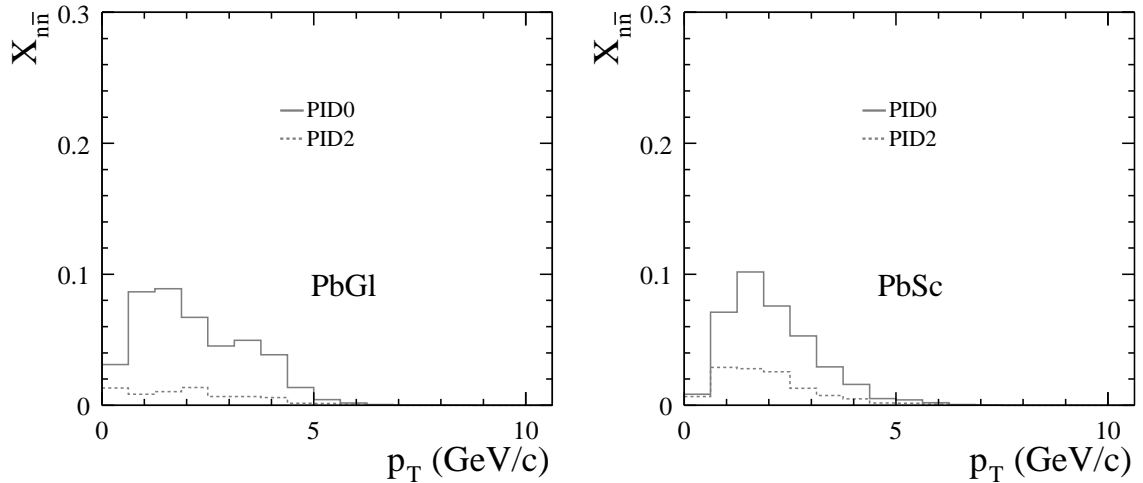


Figure 7.9: Contamination of the neutral cluster spectrum with neutrons and antineutrons in minimum bias events for two different PIDs, without any cuts and with the shower shape cut.

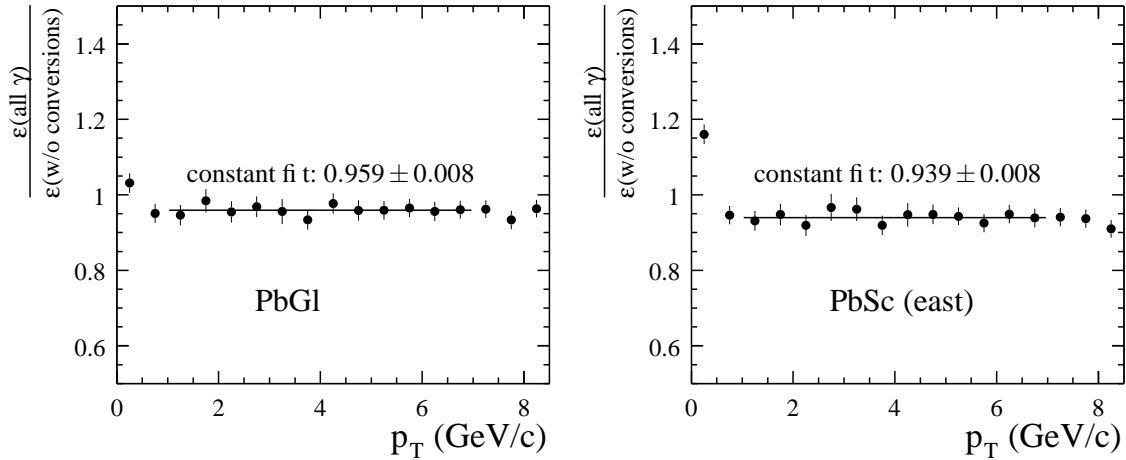


Figure 7.10: Single photon efficiencies from embedding considering all photons compared to the efficiency obtained when excluding converted photons (minimum bias events, PID0).

the method of the efficiency matrix. It is consistent within 20% with the FLUKA results determined with the same method.

7.1.4 Conversion Correction

The correction for conversion losses in the inclusive photon measurement has to consider two effects. First the loss of converted photons due to the calorimeter response or the different efficiency for converted and non-converted photons. Second the loss of photons due to the subtraction of charged particles determined with the PC3 as described in Section 7.1.2.

The efficiency loss when including converted photons is determined within the embedding framework in a similar way as for π^0 s (see Section 6.4.1). The requirement of only one hit on the empty detector is given up and all new hits in the merged event which are assigned to a hit on the empty detector are considered. The efficiencies for the case with and without the inclusion of converted photons are compared in Figure 7.10 for the PbG1 and the two sectors of PbSc in the east arm. This efficiency loss, which can be parameterized by a constant fit, is tantamount to the loss of single photons due to conversion. It is independent of the centrality selection and only sensitive to the shower shape cut. The conversion corrections derived with this method are given in Table 7.1.

The loss of inclusive photons due to the different efficiency of the detector for converted photons can be compared to the fraction of single photons tagged as charged by the PC3. It is found that this fraction of photons, approximately 5% for the PbG1 and 7% for

	PbGl	PbSc	PbSc (east)	PbSc (west)
Conversion correction c_{conv}				
PID0 and PID1	95.9%	93.4%	94.0%	93.0%
PID2 and PID3	95.3%	93.2%	93.5%	93.0%
X_0 up to PC3	5.9%	—	5.9%	7.8%
$(1 - p_{\text{conv}})$	95.5%	—	95.5%	94.1%

Table 7.1: Conversion correction from the comparison of single photon efficiencies with and without conversion. The values can be compared to the conversion determined by the material budget between the collision vertex and the PC3 as given in Appendix E.

the PbSc in the east arm, as shown in Figure 7.5(c) and (d), is very close to the employed conversion correction. This implies that the converted photons lost in the detection process are all tagged as charged particles. The conversion correction compensates for the photons subtracted already by the charged particle correction.

The conversion correction is also consistent with the rough estimate given by the material budget between the collision vertex and the PC3 in front of the EMCal (see Table 7.1). However, this estimate neglects any detector specific effects, such as position resolution and PID cuts. It is also unclear in this approach how conversions in the PC3 itself influence the photon measurement. These effects are considered with the employed efficiency comparison. Nevertheless, the estimate from the conversion probability serves as a good cross-check.

7.1.5 Spectra

The inclusive photon spectrum that is derived from the raw cluster spectrum following Equation (7.1) is determined by the corrections discussed above. The spectra have to be corrected for the bin shift effect in the same way as already discussed for the π^0 spectra (see Section 6.6.3). The averaging of the inclusive photon spectrum from the PbGl and the PbSc, needed for the calculation of the direct photon yield, is also done in the same way as described for the π^0 measurement in Section 6.6.4.

Sources of Systematic Errors

The origin of many systematic errors in the measurement of the inclusive photons is the same as for the π^0 measurement, e.g. the systematic error on the normalization, on the efficiency, and on the absolute energy scale. Other uncertainties such as the correction for mis-identified charged particles are unique to the photon measurement.

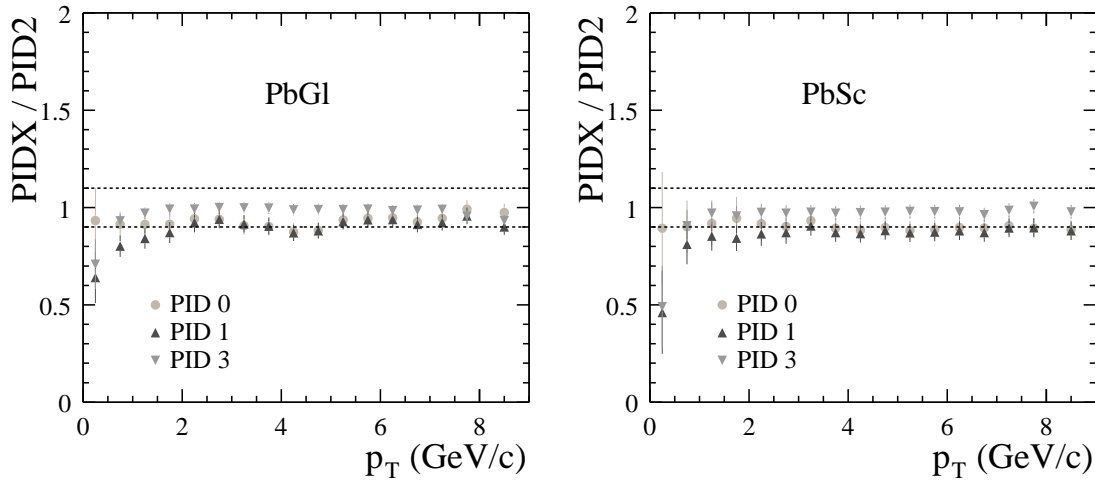


Figure 7.11: Comparison of the fully corrected inclusive photon spectra in minimum bias events for different particle identification cuts in the PbGl and the PbSc. The error bars are statistical errors plus the systematic error of the correction for charged particles and neutrons. The error estimate of 10% for the uncertainty in the efficiency calculation is indicated by the dashed lines.

The uncertainty introduced by the efficiency calculation is estimated by comparing the fully corrected inclusive photon spectra for different particle identification criteria. This is shown in Figure 7.11 for the PbGl and the PbSc, respectively. However, it should be noted that this comparison is not only sensitive to the efficiency calculations; the corrections for charged particles and neutrons also depend heavily on the PID cut. For this reason the systematic error of both corrections is considered in the error bars shown in Figure 7.11, accounting for the deviations at low transverse momentum. The systematic error due to the energy scale uncertainty in both detectors is basically determined by the shape of the spectrum and the uncertainty of the energy scale $\Delta(E)/E = 2\%$ in the PbGl and 1.6% in the PbSc as discussed in Section 6.6.2.

The correction for charged particles suffers most from the uncertainty in the drift chamber efficiency and acceptance, resulting in an overall systematic error of 15% on X_{ch} . As discussed in Section 7.1.3 the determination of the background from neutrons and antineutrons relies only on simulations, which can differ by up to 20% depending on the employed hadron package. In addition, the actual neutron and antineutron spectrum can only be estimated based on the measured $p\bar{p}$ spectrum. This results in a conservative estimate of the systematic error for $X_{n-\bar{n}}$ of 40%. However, due to the fact that the neutron contribution above $p_T = 5 \text{ GeV}/c$ is negligible, this large error does not affect the significance of the measurement at large transverse momenta.

p_T	PbGl		PbSc	
	3.25 GeV/c	8.5 GeV/c	3.25 GeV/c	8.5 GeV/c
Efficiency and acceptance	10%	10%	10%	10%
Charged particles (X_{ch})	2.4%	2.4%	3.2%	3.2%
Neutron correction ($X_{\text{n-d}}$)	0.2%	$\ll 0.1\%$	0.4%	$\ll 0.1\%$
Conversions	2%	2%	2.9%	2.9%
LVL2 data	—	6.4%	—	6.6%
Energy scale	15.7%	13.7%	12.4%	10.8%
Total syst.	18.9%	18.4%	16.5%	16.7%
Statistical	1.2%	14.1%	0.7%	7.9%

Table 7.2: Summary of the dominant sources of systematic errors on the inclusive photon yields extracted independently with the PbGl and PbSc electromagnetic calorimeters in central Au + Au events for different p_T and for PID2.

Other sources of systematic errors not discussed here are the uncertainty of the conversion correction and the normalization for the LVL2-triggered data. For the total systematic error on the measurement of the inclusive photons, the different contributions given in Table 7.2 are added in quadrature.

Combination of PbGl and PbSc

The fully corrected inclusive photon spectra for both detector types employed in the analysis is shown for different centralities in Figure 7.12, and the corresponding data are tabulated in Appendix H. For the final result the measurement employing the shower-shape cut (PID2) is chosen. The comparison of the inclusive photon measurement with the PbGl and with the PbSc is shown in Figure 7.13 for two different centrality selections. The results are consistent within 15%. However, as already seen for the π^0 results, in Au + Au collisions (Figure 6.26) as well as in d + Au collisions (Figure 6.29), the yields measured with the PbGl are systematically higher than the yields measured with the PbSc. Though the reason for this behavior is still unresolved, it nicely illustrates the importance of internal cross-checks and provides the lowest bound for the systematic error.

Since the difference between the two measurements is well covered by the assigned error, the combination of the result is justified. This is done in the same way as already described in Section 6.6.4 for the π^0 measurement by a standard weighted least-squares method. The final combined result is also given in Appendix H. It is used for the overall normalization of the direct photon cross section as described in Section 7.2

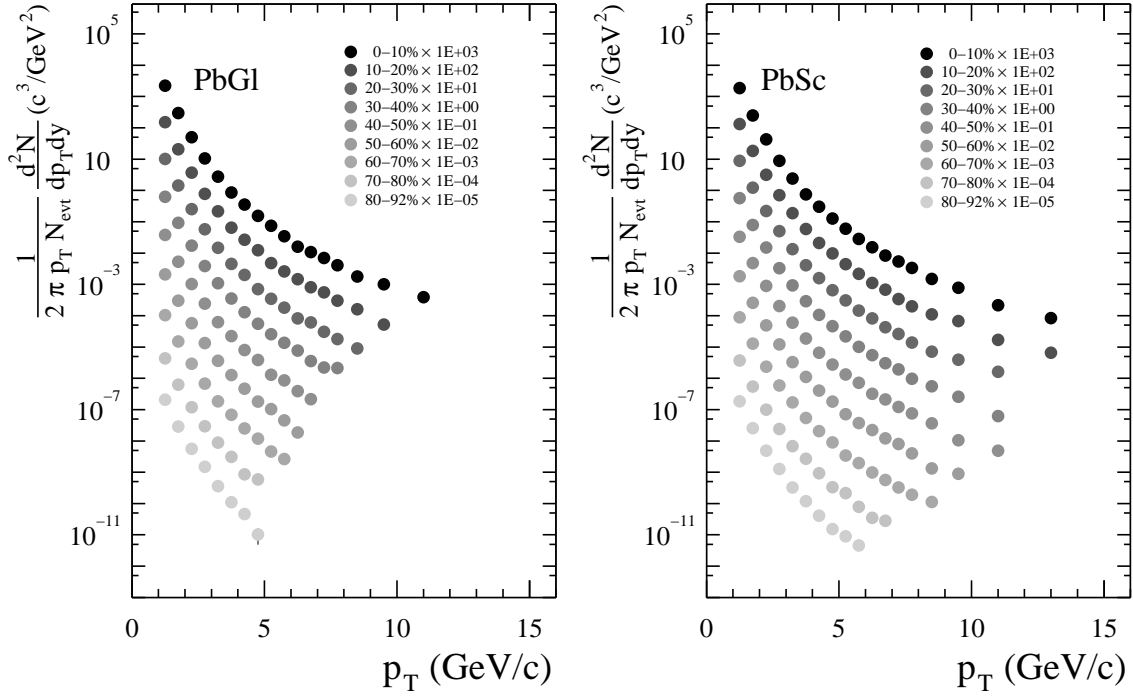


Figure 7.12: Fully corrected inclusive photon spectra for eight different centrality selections as determined with the PbGl and the PbSc, respectively. The error bars represent the combined statistical and systematic error.

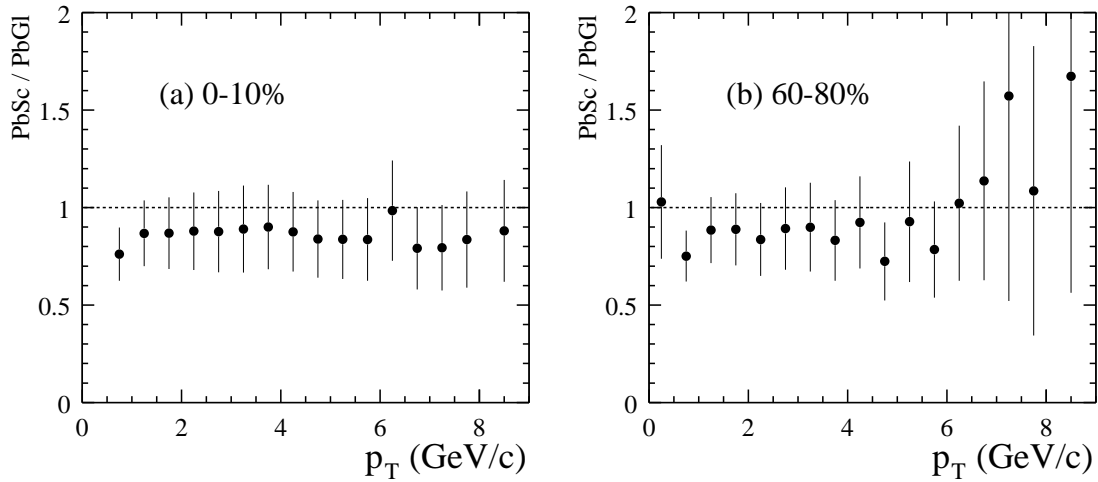


Figure 7.13: Comparison of the fully corrected inclusive photon spectra measured with the PbGl and the PbSc for two different centralities.

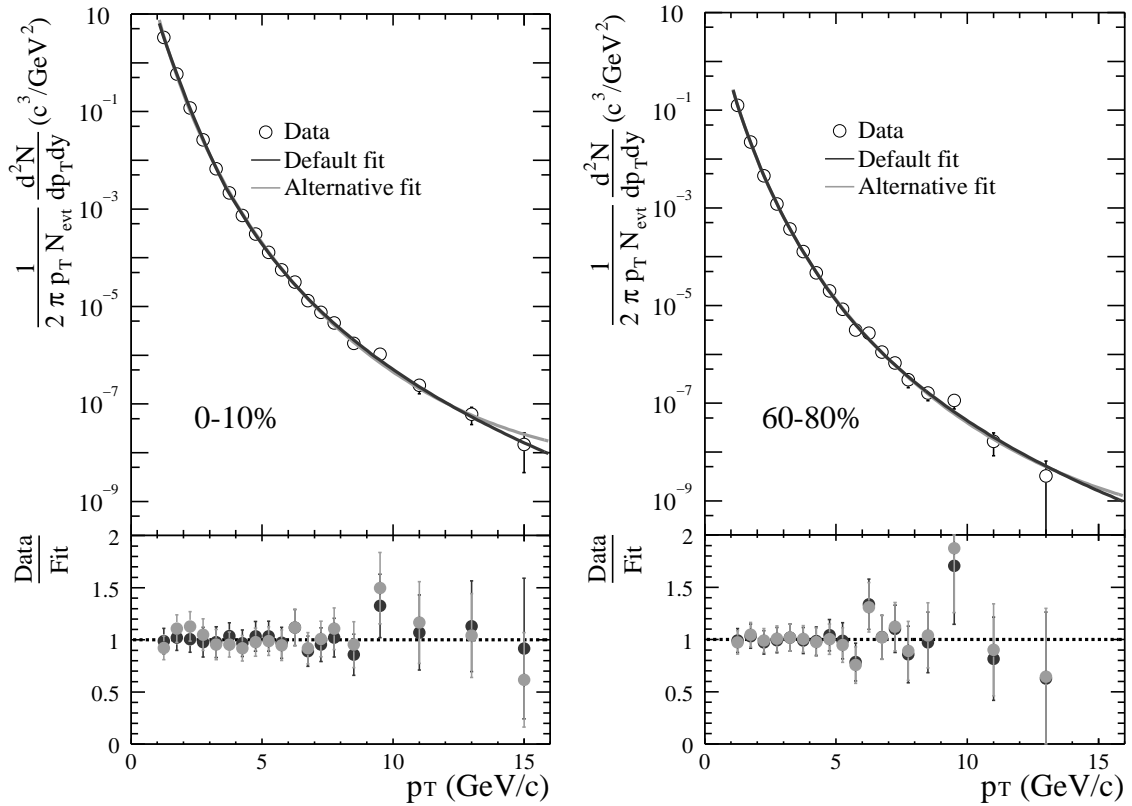


Figure 7.14: Parameterization of the combined π^0 measurement for two different centralities and comparison with the data to the default fit Equation (6.15) and to the alternative Equation (7.8).

7.2 Direct Photon Yields

As already discussed above, the direct photon yield is determined via the comparison of the inclusive photon yield to the expected yield of background photons from hadronic decays. As the main source of decay photons originates from π^0 s, the accurate determination of the π^0 yield is imperative. It is also convenient to normalize the total photon yield to this dominant source of background photons.

The comparison with the expectation from hadronic decays can then be done in terms of the ratio of N^γ/N^{π^0} , or in shorthand γ/π^0 . This has the advantage that in the measured ratio of inclusive photons to neutral pions many systematic errors cancel, such as energy-scale uncertainties and the absolute normalization. This is nicely illustrated by the fact that the inclusive photon and the π^0 measurement deviate by the same amount when comparing the PbGl and the PbSc, leading to a similar $N^\gamma/N^{\pi^0}|_{\text{meas}}$ for both detector types. For

the determination of the decay background $N^\gamma/N^{\pi^0}|_{\text{bgd}}$ only the shape of the π^0 spectrum is relevant, not the normalization.

7.2.1 Background from Radiative Decays

The expectation of photons from hadronic decays is determined within the same Monte Carlo simulation employed for the acceptance calculation. The most important input to this simulation is the parameterization of the π^0 yield as measured within the same data sample used for the direct photon analysis. The parameterization of the yield is given by Equation (6.15) and is fit to the combined result of the π^0 yield measured with the PbGl and PbSc (see Section 6.6.4).

In addition to Equation (6.15), other parameterizations of the spectrum have been tested, which avoid the need for a transition function. Most of them failed to describe the spectra over the measured p_T range and for all centralities, except one QCD-inspired parameterization [Vog04a]. It is given by:

$$\frac{dN}{dp_T} = p_T \cdot a_1 \cdot \frac{1}{p_T^{a_2 + \ln a_3 x_T}} \cdot \frac{1}{(1 - x_T^2)^{a_4}}, \quad (7.8)$$

where

$$x_T = \frac{2p_T}{\sqrt{s_{NN}}}.$$

The parameterization and the default fit are shown for two centralities in Figure 7.14; they describe the data equally well.

The decay of the π^0 is the largest contribution to the background for the direct photon measurement. It accounts for approximately 80% of the total expected background as shown in Figure 7.15. The π^0 measurement includes not only directly produced π^0 s, but also those from hadronic decays with π^0 s in their final state. Thus it is not necessary to take into account photons produced in secondary π^0 decays, e.g. from $\eta \rightarrow 3\pi^0$ with a branching ratio of 32.51% [Eid04].

The second most important contribution to the decay background after the π^0 is formed by the two photon decay of the η meson ($\eta \rightarrow \gamma\gamma$). The measurement of the η via this decay channel is complicated by the smaller production rate of the η , the smaller EMCAL acceptance for the two decay photons at low p_T , the larger decay width, and the smaller branching ratio compared to the π^0 measurement via this channel. This leads to a smaller signal to combinatorial background rate in the invariant mass analysis. Nevertheless, the η production has been measured in the PHENIX experiment for all colliding systems, p + p, d + Au, and Au + Au [Sah04, d'E04]. In Au + Au collisions the η yield

State	Mass (MeV/ c^2)	R_{h/π^0}	Decay branch	Branching ratio
π^0	134.98	–	$\gamma\gamma$	98.798%
			$e^+e^-\gamma$	1.198%
η	547.8	0.45	$\gamma\gamma$	39.43%
			$\pi^+\pi^-\gamma$	4.68%
			$e^+e^-\gamma$	$6.0 \cdot 10^{-3}$
			$\pi^0\gamma\gamma$	$7.2 \cdot 10^{-4}$
			$\mu^+\mu^-\gamma$	$3.1 \cdot 10^{-4}$
ρ^0	769.0	1.0	$\pi^+\pi^-\gamma$	$9.9 \cdot 10^{-3}$
			$\pi^0\gamma$	$6.0 \cdot 10^{-4}$
			$\eta\gamma$	$3.0 \cdot 10^{-4}$
ω	782.6	1.0	$\pi^0\gamma$	8.92%
			$\eta\gamma$	$4.9 \cdot 10^{-4}$
η'	957.8	1.0	$\rho^0\gamma$	29.5%
			$\omega\gamma$	3.0%
			$\gamma\gamma$	2.12%
			$\mu^+\mu^-\gamma$	$1.0 \cdot 10^{-4}$
K_S^0	497.65	1.0	$(\pi^0\pi^0)$	(31.05%)

Table 7.3: Dominant sources of background photons from hadronic decays and the employed m_T scaling factors relative to the π^0 measurement R_{h/π^0} . The listed masses, decay branches, and branching ratios are taken from [Eid04].

has only been determined in a limited transverse momentum region and for coarse centrality selections, thus it cannot serve as direct input to the simulation. Instead we make use of the phenomenological observation that the differential cross sections for various hadrons h have the same form when expressed as a function of the transverse mass $f(m_T)$ [Bou76]:

$$E \frac{d^3\sigma_h}{dp^3} = C_h \cdot f(m_T). \quad (7.9)$$

The η yield obeys this m_T scaling also at RHIC with a relative scaling factor of $R_{\eta/\pi^0} = C_\eta/C_{\pi^0} = (0.5 \pm 0.03)$ in p + p, (0.48 ± 0.03) in d + Au, and (0.41 ± 0.05) in Au + Au collisions [Sah04, d'E04], which is consistent with the world average of 0.45 calculated in [Kau04]. For the determination of the decay background from η s in the Fast Monte Carlo we scale the production cross section as given by Equation (7.9) with a factor of $R_{\eta/\pi^0} = 0.45 \pm 0.05$ relative to the parameterized π^0 yield.

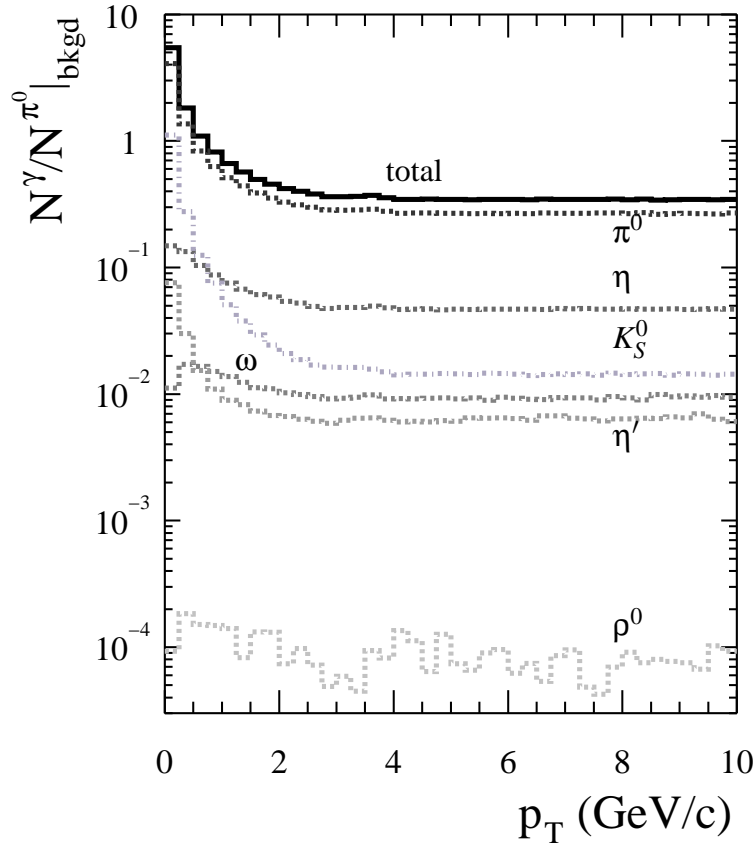


Figure 7.15: Photon background per input π^0 from hadronic decays in minimum bias events. The secondary decay photons from $K_S^0 \rightarrow \pi^0\pi^0$ are fully included.

Other hadrons that can contribute to the background photons are listed together with their relevant decay channels in Table 7.3. They have not been measured by the PHENIX experiment, and we assume m_T scaling with the same spectrum as observed for the π^0 s. The scaling factor R_{h/π^0} , which is equivalent to the ratio of the p_T spectra for $p_T \rightarrow \infty$, is reported in [Bou76, Dia80] for ω , ρ^0 , and η' . It is $R_{h/\pi^0} \approx 0.9$ for $p_T \geq 3 \text{ GeV}/c$ but consistent with unity within the experimental uncertainties.

The K_S^0 has no significant decay branch with photons in the final state. However, due to its relatively long lifetime of $\tau = 0.9 \cdot 10^{-10} \text{ s}$ and the relativistic time dilation it may decay far from the collision vertex, and the π^0 s originating from $K_S^0 \rightarrow \pi^0\pi^0$ may not be reconstructed in the invariant mass analysis. To estimate the maximum contribution due to this effect, the secondary decay photons can be included in the background calculation. As for all other hadrons m_T scaling is assumed for the K_S^0 . The scaling factor can be inferred from the ratio of identified charged pions to kaons as measured by the PHENIX experi-

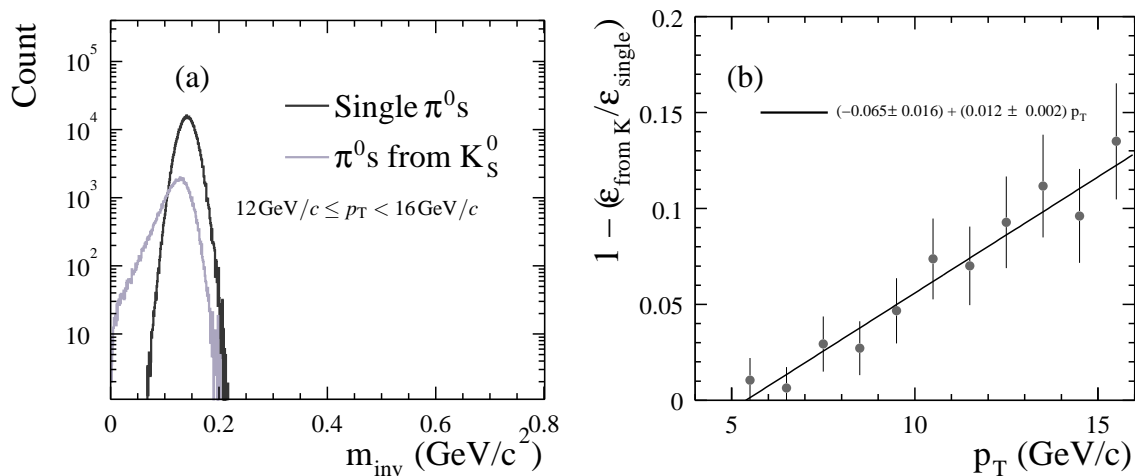


Figure 7.16: (a) Invariant mass distribution for simulated single π^0 s and for π^0 s originating from K_S^0 decays. (b) The difference in the detection efficiency between primary neutral pions and π^0 s from K_S^0 .

ment [Adl04]. It is only known up to $p_T = 2 \text{ GeV}/c$ and depends strongly on centrality with a value of $R_{K/\pi} \approx 0.7$ in central and $R_{K/\pi} \approx 0.45$ in peripheral Au + Au collisions at $p_T = 1.95 \text{ GeV}/c$. We take a scaling factor of one as an upper limit for the estimate of the photons from K_S^0 .

The contributions from the various hadronic decays, including K_S^0 , to the total photon background is shown in Figure 7.15 for minimum bias events. As already mentioned above, the largest contribution originates from the π^0 decay, which accounts for approximately 77% at large transverse momenta, followed by the η , which contributes about 14% to the background. The photons from ρ^0 decays are negligible, as expected from the branching ratio of decays with photons in the final state. The contributions from η' and ω are of the order of 2–3%, which is surpassed by the K_S^0 if all its secondary decay photons are considered.

To study the effect of K_S^0 decays, especially the question as to what extent they are included already in the π^0 measurement, we evaluated the efficiency for the detection of π^0 s originating from K_S^0 within the Fast Carlo simulation also used for the efficiency calculation in d + Au collisions. Due to the relatively long lifetime of the K_S^0 , the collision vertex used in the invariant mass analysis of photon pairs does not correspond to the π^0 decay vertex, and the invariant mass is calculated incorrectly. This essentially leads to a broadened and shifted π^0 peak as illustrated in Figure 7.16(a) for reconstructed π^0 s originating from K_S^0 with large transverse momenta, for which the effect is larger due to the relativistic time dilation. The shift and the broadening of the peak basically reduce the efficiency for the detection of π^0 s from K_S^0 decays, as they are more sensitive to the

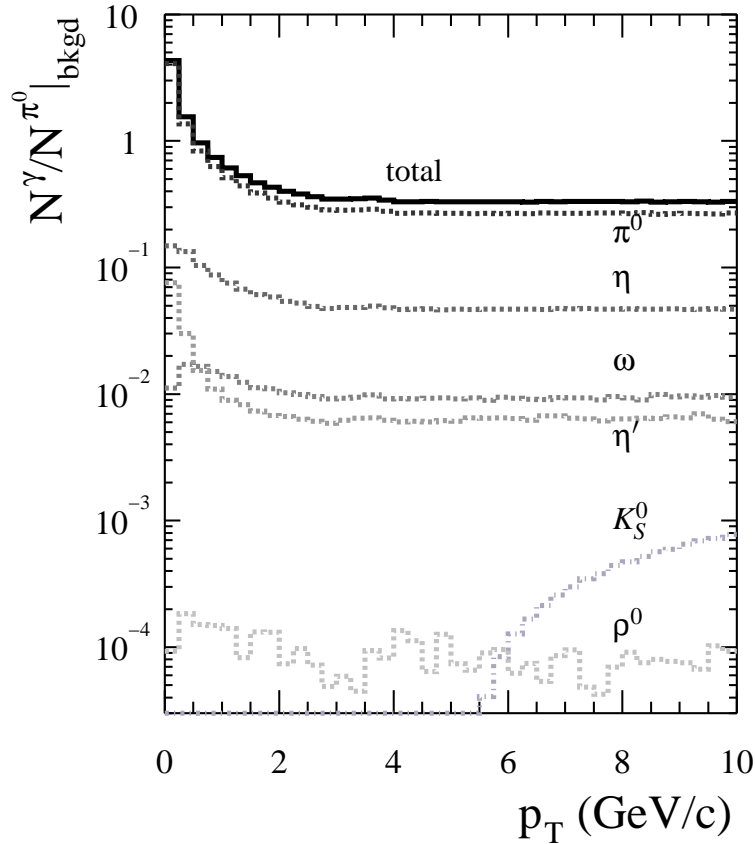


Figure 7.17: Photon background per input π^0 from hadronic decays in minimum bias events. Only those secondary decay photons from $K_S^0 \rightarrow \pi^0\pi^0$ are considered that are not included in the π^0 measurement.

employed cut of $3 \cdot \sigma_\pi$ around the π^0 peak position (see Section 6.1.2). The difference between the efficiency for primary π^0 s and for secondary π^0 s, as shown in Figure 7.16(b), determines the fraction of π^0 s from K_S^0 that are not included in the π^0 measurement. These π^0 s need to be considered in the background determination. As the decay photon spectrum at a given p_T is dominated by asymmetric π^0 decays, we assume that the decay photon contribution from K_S^0 is given by the inefficiency in the π^0 detection. The inefficiency can be parameterized by a linear function as shown in Figure 7.16(b), which is multiplied with the total photon yield from K_S^0 decays. The newly determined γ/π^0 ratio expected from hadronic decays is shown in Figure 7.17, the contribution from K_S^0 is reduced by at least one order of magnitude.

The systematic error of the decay photon simulation is basically given by the uncertainty in the m_T scaling factor employed for the determination of the η cross section. The comparison of the two different parameterizations of the π^0 cross section showed no dif-

ference at low p_T . At high transverse momenta the alternative fit leads to large feed-down contributions from the η' . The reason for this behavior lies in the fact that the fit following Equation (7.8) can show an unphysical extrapolation to p_T regions where no data are available, even though it shows a good agreement with the measured π^0 spectrum.

7.2.2 γ/π^0 Double Ratio

The expected yield of photons per π^0 originating from hadronic decays can now be compared to the measured spectra. As already mentioned many systematic errors cancel in the measured ratio of inclusive photons to neutral pions. The cancellation affects:

- The error on the energy scale, which completely cancels if it is an overall scale factor,
- The uncertainty in the efficiency calculation, which partially cancels as the single photon efficiency has a direct impact on the two-photon efficiency needed for the invariant mass analysis of the π^0 ,
- The systematic error due to the conversion correction, which partially cancels for the same reason,
- The overall normalization uncertainty of the Level-2 trigger.

The direct comparison of the point-by-point ratio of measured inclusive photons to the measured π^0 s, determined within the same detector and identical PID cuts, is shown in Figure 7.18. A clear enhancement of photons compared to the expectation from hadronic decays is seen above $p_T = 4 \text{ GeV}/c$ in central collisions, indicating a direct photon signal. For low transverse momentum as well as in peripheral events the measured ratio agrees with the calculated background.

The photon excess can be characterized more directly in the double ratio of measured photons per π^0 to the expectation from hadronic decays:

$$\frac{N^\gamma/N^{\pi^0}\big|_{\text{meas}}}{N^\gamma/N^{\pi^0}\big|_{\text{bkgd}}} = \frac{N_{\text{meas}}^\gamma}{N_{\text{bkgd}}^\gamma}. \quad (7.10)$$

This is, as indicated, equivalent to the direct comparison of measured photons to decay photons, since the measured π^0 spectrum and the input π^0 distribution for the decay photon calculation, which is derived from the combined π^0 measurement of PbPb and PbSc, should be the same, by construction, and cancel each other to a large extent. This cancellation introduces only a small systematic error of approximately 4%, as it is only sensitive

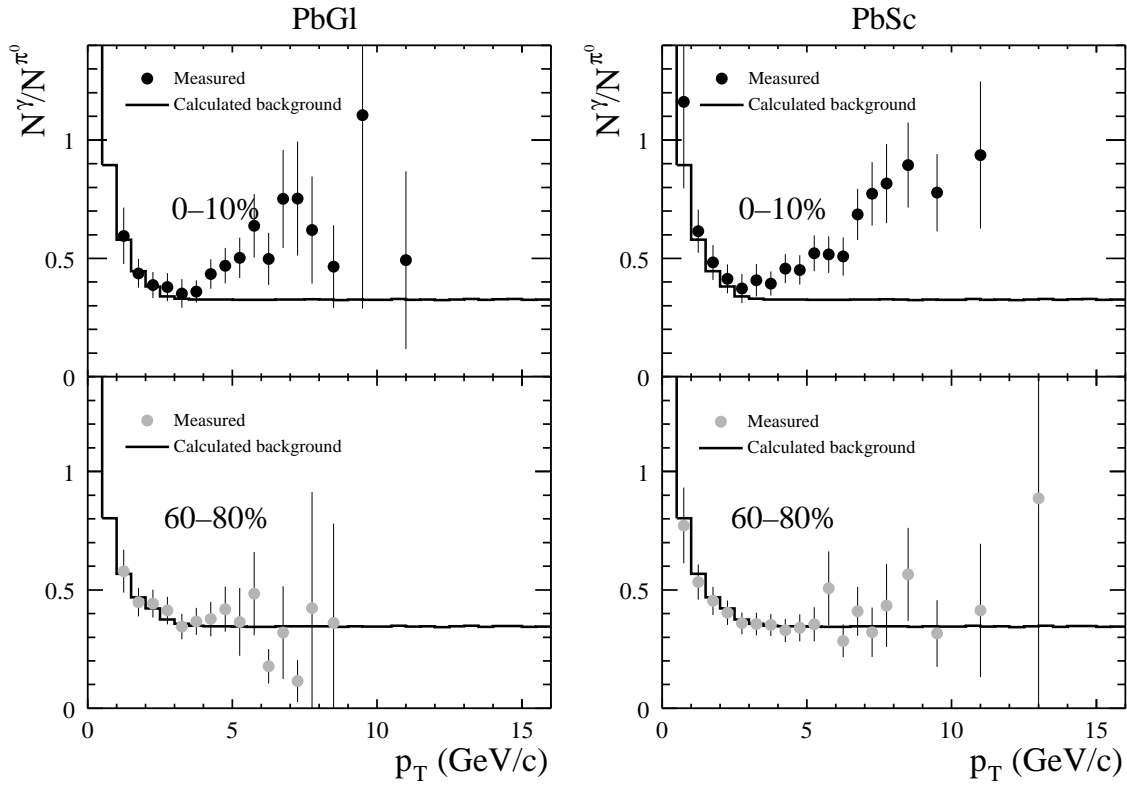


Figure 7.18: Comparison of the point-by-point photon to pion ratio determined for two different centralities with the PbGl and the PbSc, respectively. A clear enhancement over the hadronic decay background is seen in central collisions above $p_T = 4 \text{ GeV}/c$, while no significant signal is seen in peripheral events.

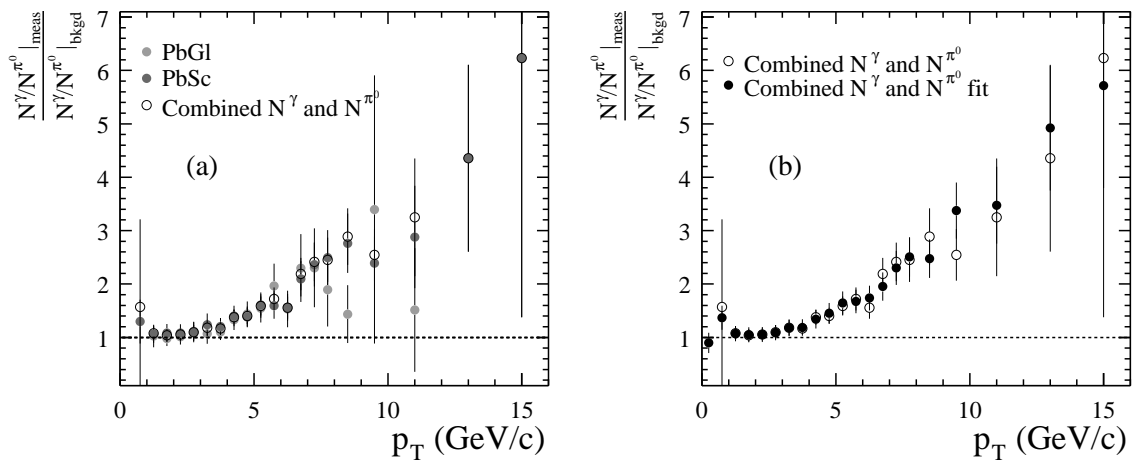


Figure 7.19: (a) Comparison of the double ratio using the point-by-point photon to pion ratio in central collisions for the PbGl, the PbSc, and the combined photon and pion result. (b) Comparison of the double ratio for the combined photon and pion result using the point-by-point ratio and a fit to the combined π^0 measurement. All statistical and systematic errors are included.

to variations of the shape of the spectrum, not to the overall normalization. The double ratio as defined by Equation (7.10) is unity in the absence of direct photons, and the direct photon signal is seen as an excess above one. Figure 7.19(a) shows the double ratio in central events for each detector type, with the photon excess above $p_T = 4 \text{ GeV}/c$ already observed in Figure 7.18.

To exploit the reduced systematic error in the combined measurement of inclusive photons and neutral pions with PbGl and PbSc, the combined result is used in the following and for the determination of the direct photon yield. The double ratio for the combined result is also shown in Figure 7.19(a) together with the individual ratios for PbGl and PbSc. As expected they show a good agreement at low p_T , while the significance of the signal is increased at large transverse momenta for the combined result. To avoid the influence of statistical fluctuations of the π^0 measurement seen in the point-by-point ratio of Figure 7.19(a) a fit to the actual π^0 spectrum is used in the further analysis. This smoothens the ratio as illustrated in Figure 7.19(b) and basically exchanges the statistical error of the π^0 measurement, contributing to the point-by-point ratio, for the systematic error introduced by the fit.

The large direct photon excess seen in the double ratio for central collisions at large transverse momenta can be understood when considering that the production of neutral pions, the main source of background photons, is suppressed by a factor of five, compared to $p + p$ collisions and to peripheral events (see Section 6.8). As already shown in Section 6.8.2 this suppression is a final state effect, most likely due to the energy loss of hard-scattered partons in the hot and dense medium produced in central collisions. As photons do not interact strongly, the hot and dense medium is transparent to them, and they penetrate the possible QGP phase without losing energy. In contrast to π^0 s, the measured direct photons originating from early hard scatterings therefore should scale with the number of binary nucleon-nucleon collisions, leading to an increase of the γ/π^0 ratio with centrality that provides the direct control measurement of the energy loss scenario in Au + Au collisions.

The effect of the suppressed π^0 background on the significance of the direct photon signal is nicely illustrated when comparing to the expectation of the photon signal from $p + p$ collisions. The production of direct photons in $p + p$ has been measured in the PHENIX experiment only with very limited accuracy, but supports the result of next-to-leading-order (NLO) pQCD calculations [Fra04a]. For this reason the pQCD calculation of the direct photon production is used for the comparison with the Au + Au data. This calculation is basically identical to the calculation also presented in [Adl03c] that shows a good agreement with the measured π^0 cross section in $p + p$ collisions (see Section 6.8). The result of this calculation is given for different factorization, renormalization

and fragmentation scales in Appendix G. The expectation can be constructed presuming two scenarios:

- The photon production is affected by the same suppression mechanism as the π^0 s, e.g. an initial state effect. Hence, the photon excess does not change compared to $p + p$:

$$\frac{N^\gamma/N^{\pi^0}}{N^\gamma/N^{\pi^0}|_{\text{bkgd}}} = 1 + \frac{N_{\text{direct,p+p}}^\gamma/N_{\text{p+p}}^{\pi^0}}{N^\gamma/N^{\pi^0}|_{\text{bkgd}}} \quad (7.11)$$

The same is true for π^0 s and for direct photons when both scale with the number of binary collisions.

- The direct photon production scales with the number of binary nucleon-nucleon collisions, while the π^0 production is suppressed compared to $p + p$, so the measured π^0 spectrum for the actual centrality has to be used:

$$\frac{N^\gamma/N^{\pi^0}}{N^\gamma/N^{\pi^0}|_{\text{bkgd}}} = 1 + \frac{N_{\text{coll}} \cdot N_{\text{direct,p+p}}^\gamma/N_{\text{Au+Au}}^{\pi^0}}{N^\gamma/N^{\pi^0}|_{\text{bkgd}}} \quad (7.12)$$

This is the expected behavior if the suppression of π^0 s is due to strong final state interactions.

The two scenarios are shown in Figure 7.20 together with the centrality evolution of the double ratio for the measured data. It is observed that the measured direct photon excess follows the expectation of the scaled $p + p$ production for all centralities. This demonstrates again that the suppression of π^0 s observed in central $\text{Au} + \text{Au}$ collisions is a strong final state effect.

As seen in Figure 7.20 the direct photon signal observed in the double ratio is explained within the experimental errors by considering only the direct photon production via initial hard scattering. However, the NLO pQCD calculation also contains the photons produced in the fragmentation process of hard-scattered partons, e.g. by conversion of a ρ into a photon [Vog04b], and photons from next-to-leading-order processes, such as Bremsstrahlung. Since those photons originate from hard-scattered partons, their production cross section is sensitive to medium effects.

Figure 7.21(a) shows the photon signals for central events in a smaller p_T range. Given the current systematic error, there is no indication for significant signal of thermal photons, to be observed as an excess above the expectation from prompt photons, at intermediate p_T . The contribution from the fragmentation of partons into photons to the total prompt photon production in the pQCD calculation is shown in Figure 7.21(b). It is about

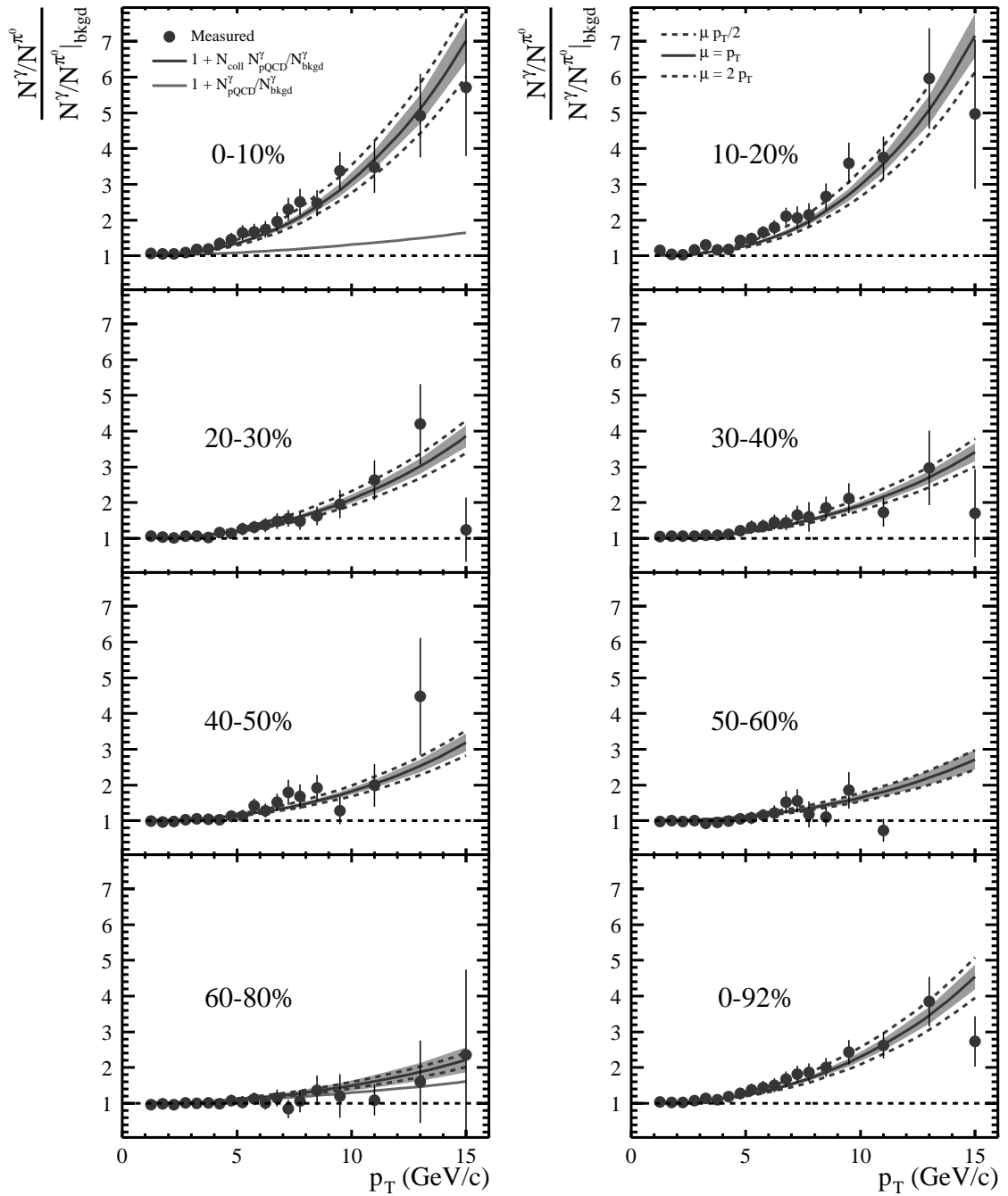


Figure 7.20: Evolution of the double ratio of the direct photon signal with centrality. The expectation based on the pQCD calculation for direct photons in p + p collisions scaled with the number of collisions is also shown for all centralities. The error band only indicates the uncertainty in the number of binary collisions. The scale uncertainty in the pQCD is illustrated by the dashed lines. They show the result for the scales $\mu = p_T/2$ and $\mu = 2p_T$ compared to the default scale $\mu = p_T$. The expected photon signal without a suppressed π^0 production is shown for the most central and the most peripheral events. It does not change with the centrality selection.

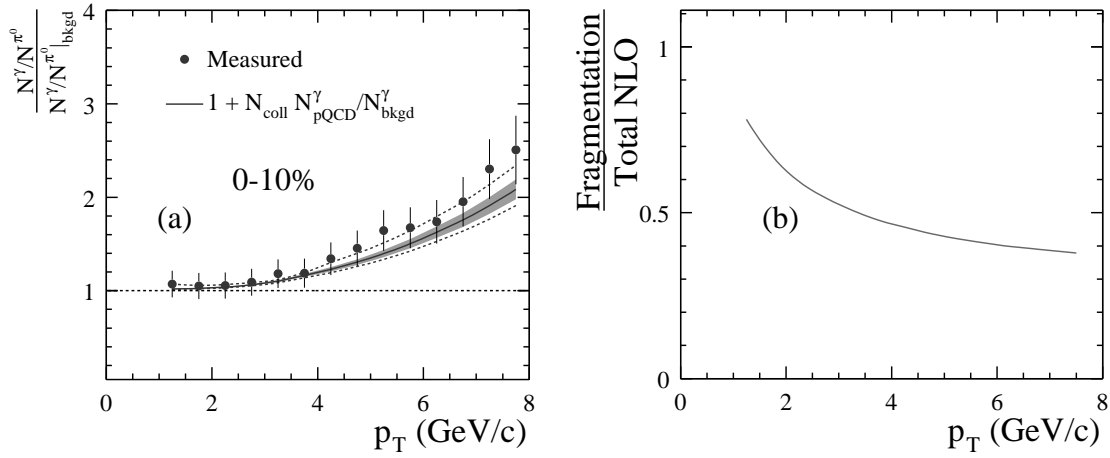


Figure 7.21: (a) The double ratio for lower transverse momenta together with the scaled expectation from the NLO pQCD calculation. The error band is the uncertainty in the number of collisions, while the dashed curves are different scales ($\mu = 0.5p_T$, $\mu = 2p_T$), (b) fraction of photons in the pQCD calculation originating from fragmentation processes.

80–40% in the region where a thermal photon signal is expected. Since this contribution may be suppressed with the possible parton energy loss in the QGP it may dilute a thermal signal, introducing an additional difficulty for discerning prompt and thermal photons.

7.3 Final Direct Photon Spectra

The comparison of the measured inclusive photons with the expectation from hadronic decays in terms of the double ratio shows a significant signal of direct photons in several centralities. This is the first observation of direct photons in heavy ion collisions at RHIC.

The final invariant yield of direct photons is obtained after the subtraction of the background from hadronic decays. This is also done via the double ratio defined in Equation (7.10):

$$\frac{1}{2\pi p_T N_{\text{in}}} \frac{d^2 N_\gamma}{dp_T dy} \Big|_{\text{direct}} = \left(1 - \frac{N^\gamma/N^{\pi^0} \Big|_{\text{bkgd}}}{N^\gamma/N^{\pi^0} \Big|_{\text{meas}}} \right) \cdot \frac{1}{2\pi p_T N_{\text{in}}} \frac{d^2 N_\gamma}{dp_T dy} \Big|_{\text{incl}}. \quad (7.13)$$

Since some of the systematic errors and the statistical uncertainty of the inclusive photon measurement are already included in the γ/π^0 ratio, we only need to consider those errors that canceled in the ratio:

- The overall normalization uncertainty of the Level-2 trigger,

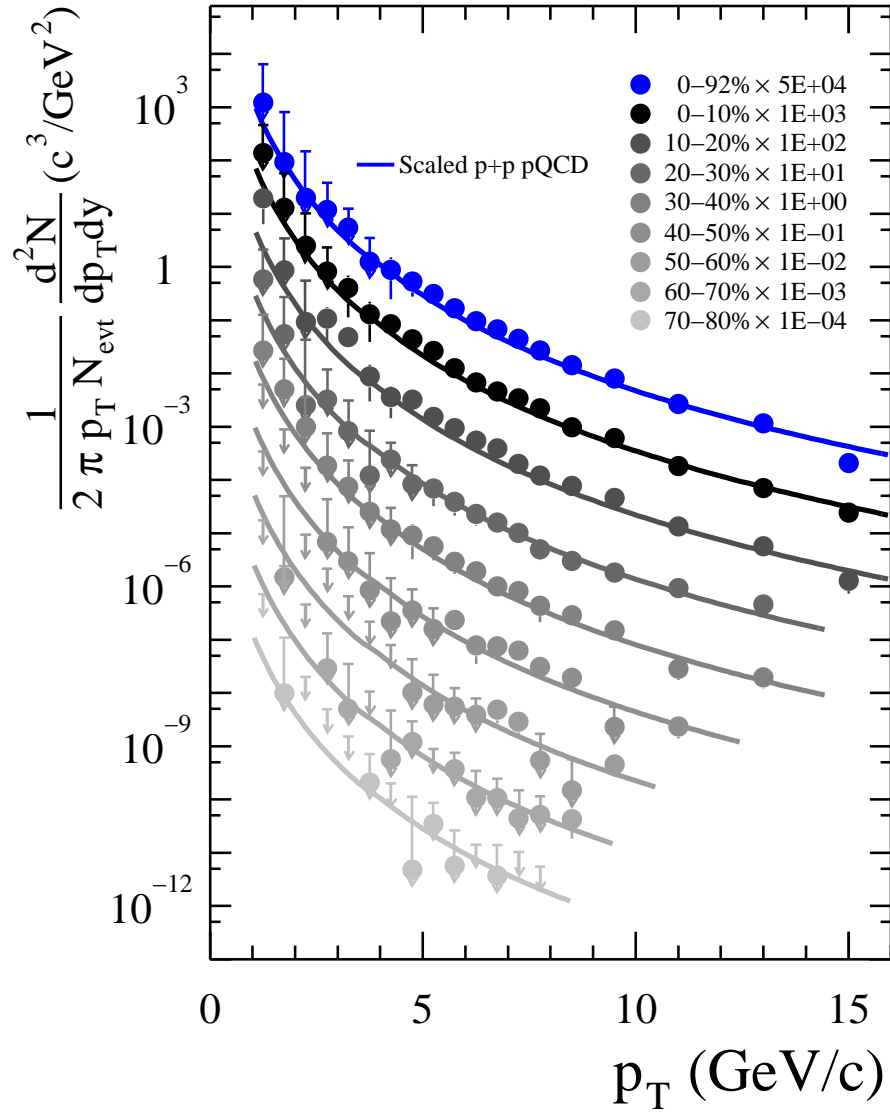


Figure 7.22: The invariant direct photon yield in Au + Au collisions at $\sqrt{s_{\text{NN}}} = 200 \text{ GeV}$ for different centralities. The downward arrows indicate the upper limits with 90% confidence level. The lines represent the NLO pQCD calculation for direct photons in p + p scaled by the appropriate number of binary nucleon-nucleon collisions.

- The error on the energy scale,
- The uncertainty in the efficiency calculation,
- The systematic error due to the conversion of photons.

For the inclusive photon yield we use again the combined result of PbPb and PbSc. The final invariant yield is tabulated in Appendix H and shown in Figure 7.22. In the case that no direct photon excess is observed in the double ratio, i.e. a double ratio lower than unity, we only give a 90% confidence level upper limit on the photon production. It is determined by the upper $1\text{-}\sigma$ error of the data point ($1.28 \cdot \sigma_{\text{up}}$) and indicated by the downward arrows in Figure 7.22. In the case the double ratio shows an excess above one, but is consistent with no signal, an upper limit is quoted ($\gamma_{\text{direct}} + 1.28 \cdot \sigma_{\text{up}}$) and the data point is provided.

The comparison with the NLO pQCD calculation scaled by the appropriate number of binary collisions is also shown Figure 7.22. As expected from the comparison already shown in Figure 7.20 the data also agree on the absolute scale with the scaled direct photon production from the calculation for $p + p$ collisions.

7.3.1 Comparison with Theoretical Models

The direct photon production from various sources has been calculated for central Au + Au collisions at $\sqrt{s_{\text{NN}}} = 200 \text{ GeV}$ in different theoretical scenarios which now can be tested against the data.

The emission of thermal photons as calculated in [Arl03] is shown in Figure 7.23(a). Two different scenarios for the QGP phase of the fireball evolution are considered: a gluon-rich QGP off chemical equilibrium, and a thermally and chemically equilibrated QGP phase. The thermal emission, which dominates at low transverse momenta over the contribution from initial hard scattering, is consistent with the upper limits imposed by the data. An additional contribution to the total photon yield is discussed in [Fri03]: the production of photons in the passage of hard-scattered partons (jets) through the QGP phase by conversion of the parton into a photon (*jet-photon conversion*). This idea is based on the properties of the production cross section for photons via Compton scattering and annihilation, respectively (see Section 2.1). They are maximal for the case the four-momentum of the outgoing photon is similar to that of the incoming quark or antiquark. The resulting additional photon yield is also shown in Figure 7.23(a). It is of the same order of magnitude as the photon production via initial hard scattering between $p_{\text{T}} = 4 \text{ GeV}/c$ and $5 \text{ GeV}/c$, which would imply a factor of two enhancement of the total rate. However, given the current theoretical and experimental uncertainties the data are consistent.

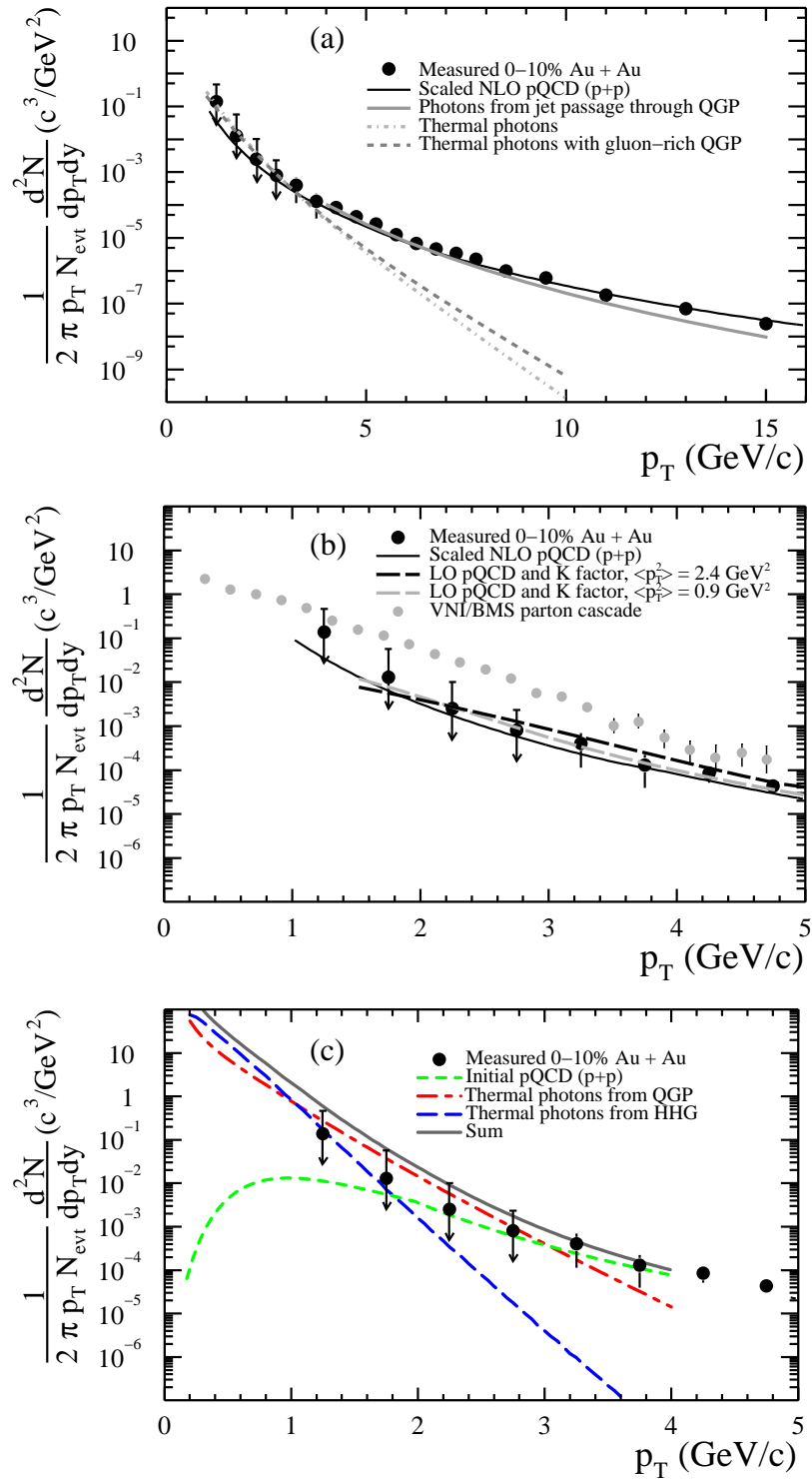


Figure 7.23: Comparison of the direct photon production in central Au + Au collisions to various theoretical calculations.

The problem of hard-scattered quarks that suffer further interactions can also be treated in parton cascade or transport simulations, which consider pQCD cross sections and the quark fragmentation via Monte Carlo techniques. This makes the treatment of many particle systems with point-like interactions feasible. The result shown in Figure 7.23(b) for the VNI/BMS parton cascade model [Bas03] considers the multiple scattering of quarks and gluons produced during the fragmentation of the hard-scattered partons. It is disfavored by our data, though it should be mentioned that the influence of quantum interference (the LPM effect) is not considered in the model. It would lead to a depletion of the photon production by multiple scattering of quarks.

Another effect important for the understanding of a photon signal at intermediate p_T is the influence of the intrinsic transverse momentum of the incoming partons. Motivated by the fact that most of the production cross sections in elementary nucleon-nucleon collisions are underestimated by pQCD calculations, an additional smearing of the parton transverse momentum $\langle p_T^2 \rangle$ can be introduced. The result for central collisions and two choices of $\langle p_T^2 \rangle$ from [Dum01] is also shown in Figure 7.23(c). It is obtained by scaling the $p + p$ photon production calculated in leading-order perturbative QCD according to the number of binary collisions. Contributions from higher order processes are taken into account by an additional scaling factor (K factor). The data are not sensitive to the choice of the intrinsic transverse momentum. As seen it is consistent with the extreme scenario of $\langle p_T^2 \rangle = 2.4 \text{ GeV}^2/c^2$ as well as with moderate and zero intrinsic p_T . The question for the amount of intrinsic p_T can only be answered in a high-precision measurement of direct photons in $p + p$ collisions. Likewise, the additional nuclear p_T broadening, the Cronin effect, which is also expected to increase the direct photon yield at intermediate p_T , can only be studied via a direct photon measurement in $d + \text{Au}$ collisions at the same energy.

Figure 7.23(c) shows the contributions to the photon yield as predicted in [Tur04] for RHIC energies: the scaled contribution from initial hard scatterings, which dominates above $p_T = 4 \text{ GeV}/c$, the thermal photons from the hot hadron gas, and the thermal radiation from the QGP phase. The static photon emission rates used in the calculation employ the complete leading-order calculation as given in [Arn01]. The hydrodynamical expansion of the fireball considers an effective chemical potential, determined by the measured antibaryon to baryon ratio, and a fixed specific entropy, which is connected to the observed multiplicity. As seen in Figure 7.23(c), the contribution from the QGP phase is largest between $p_T = 1 \text{ GeV}/c$ and $3 \text{ GeV}/c$. The total photon production in this scenario is consistent with the upper limits provided by the data.

In summary, most of the shown theoretical scenarios are consistent with the data measured in central $\text{Au} + \text{Au}$ collisions at $\sqrt{s_{\text{NN}}} = 200 \text{ GeV}$, only the photon production in the VNI/BMS parton cascade model is disfavored. In order to interpret an improved direct photon measurement in the intermediate p_T region, a consistent theoretical description,

which incorporates thermal production as well as the production of photons via the interaction of hard-scattered quarks with the plasma and the effects of nuclear p_T broadening, is still needed.

7.3.2 Comparison of the π^0 and the Direct Photon Production

As already discussed above, the analysis of the scaling behavior of the direct photon production at large transverse momenta provides a direct test of the jet quenching scenario in Au + Au collisions. It is an "in situ" control to decide whether the observed jet quenching is due to initial or final state effects, as the direct photons with large transverse momentum are predominantly produced in early hard scatterings, similar to π^0 s but without the fragmentation process and without being strongly influenced by the dense and colored medium.

We already compared the photon production to the expectation of the scaled production in p + p collisions from a NLO pQCD calculation within the double ratio of direct photons to background photons (Figure 7.20) and on the absolute scale (Figure 7.22). This comparison can also be done in terms of the familiar nuclear modification factor when employing the pQCD calculation as reference³:

$$R_{AB} = \frac{dN_{AB}^{\gamma}}{\langle N_{\text{coll}} \rangle_f \cdot dN_{\text{p+p,pQCD}}^{\gamma}}. \quad (7.14)$$

The resulting R_{AB} is shown in Figure 7.24 for five centrality selections and for minimum bias Au + Au collisions. It is consistent with unity which again stresses the fact that the observed suppression of the π^0 production in central collisions is not due to initial state effects, but a consequence of strong final state effects.

This is also illustrated when directly comparing the nuclear modification factor for the π^0 and the direct photon production in central collisions, as seen in Figure 7.25(a). The difference is apparent: while the π^0 production is strongly suppressed, the production of direct photons follows the expectation from binary scaling. A similar observation is made in the centrality dependence of the nuclear modification factor integrated for $p_T > 5 \text{ GeV}/c$. As seen in Figure 7.25(b) the π^0 as well as the photon production in peripheral collisions follow the binary-scaled p + p reference. The scaling behavior deviates when going to more central collisions. While the integrated R_{AB} for direct photons is consistent with unity or larger for all centralities, the integrated R_{AB} for neutral pions is depleted for increasing centrality.

³It should be noted that pQCD calculations reproduce the measured direct photon yields at other energies within 30%, depending on the amount of intrinsic p_T broadening. This general systematic uncertainty of pQCD calculations is not considered in the comparisons.

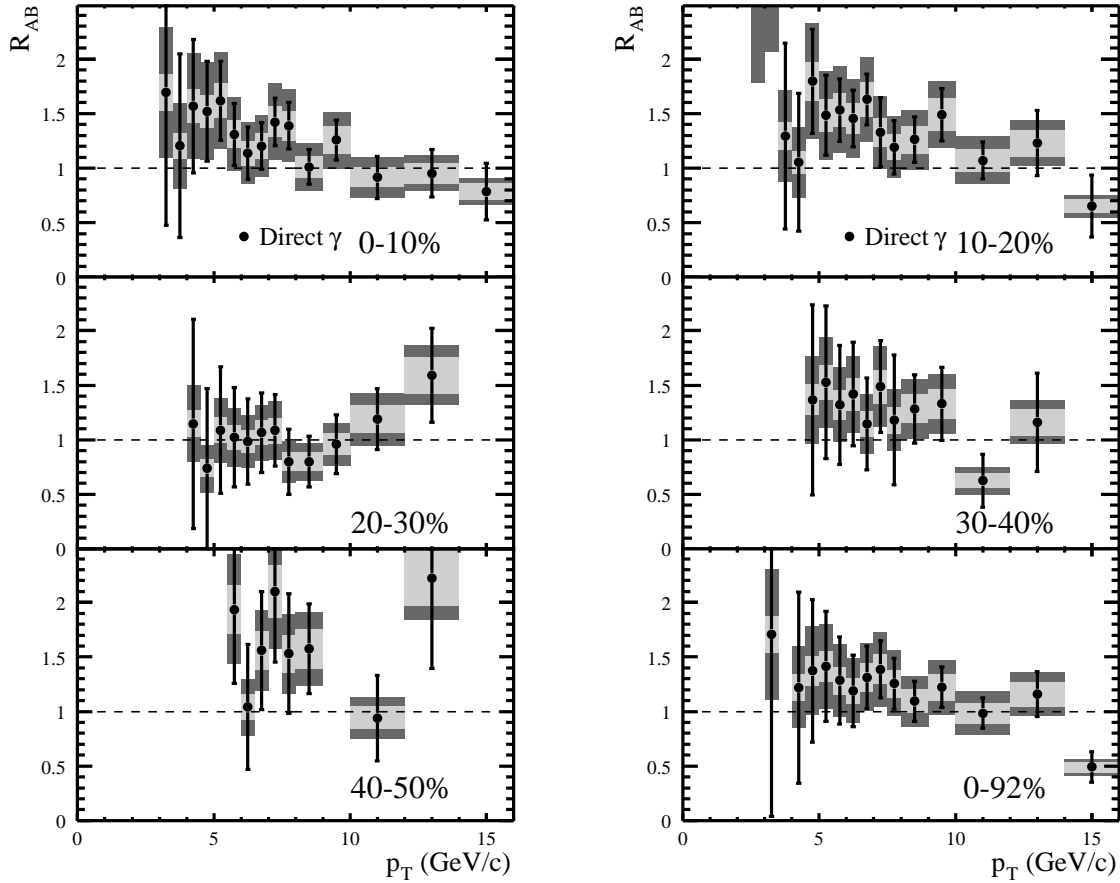


Figure 7.24: Nuclear modification factor for the production of direct photons in Au + Au collisions. All errors on the direct photon measurement are included in the error bars. The overall uncertainty in the number of collisions is given by the light grey boxes, while the dark grey boxes show the difference when using the scales $\mu = p_T/2$ or $\mu = 2p_T$ instead of the scale $\mu = p_T$ in the pQCD reference. The additional systematic uncertainty of the NLO pQCD calculation based on the comparison of pQCD calculations and direct photon production in nucleon-nucleon collisions at other energies is not included, it is of the order of 30%.

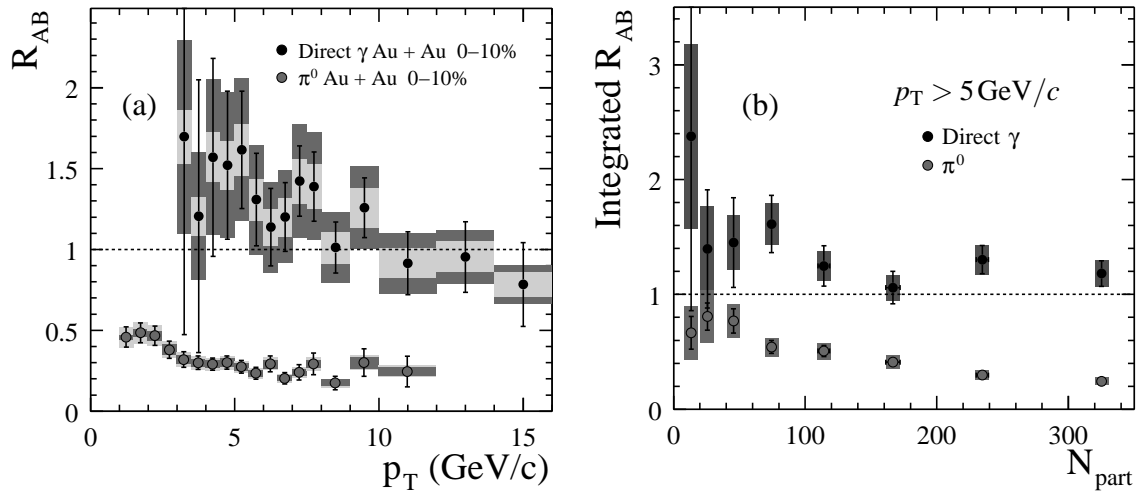


Figure 7.25: (a) Comparison of the nuclear modification factor for direct photons and neutral pions in central Au + Au collisions, (b) centrality dependence of the nuclear modification factor integrated for $p_T > 5$ GeV/c.

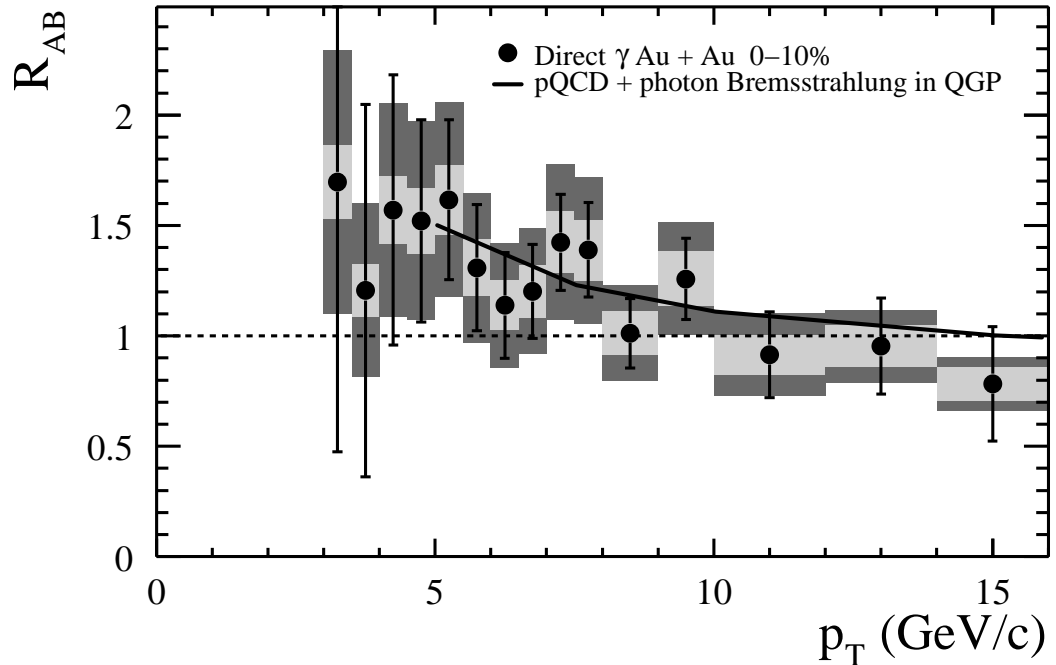


Figure 7.26: Comparison of the nuclear modification factor to a pQCD calculation that includes the induced photon Bremsstrahlung from a hard-scattered quark due to multiple scattering in the QGP [Zak04].

The nuclear modification factor expected for direct photons in central Au + Au collisions has also been calculated in [Zak04], considering the effect of the parton energy loss on the photon contribution from Bremsstrahlung. As discussed in [Zak04], the expected suppression of this contribution is compensated by the induced photon Bremsstrahlung ($q \rightarrow \gamma q$) from multiple collisions of a hard-scattered quark in the QGP. This even leads to a nuclear modification factor above unity for $p_T < 15 \text{ GeV}/c$ at RHIC energies, which is not due to Cronin enhancement that is not considered in the calculation. The comparison to our data is shown in Figure 7.26. Although it is seen that the data are well described, though, as already seen above in the comparison with other theoretical descriptions, the current magnitude of the experimental uncertainties does not allow to validate the prediction.

Summary

The main focus of this work is the measurement of neutral pions and direct photons in Au + Au collisions at a center of mass energy of $\sqrt{s_{\text{NN}}} = 200 \text{ GeV}$ in the PHENIX experiment at RHIC/BNL. In addition, the production of neutral pions was analyzed in d + Au collisions at the same energy.

One of the main goals of the PHENIX experiment is the detection of the quark-gluon plasma (QGP), which is a phase of strongly interacting matter where quarks and gluons are no longer confined in the nucleons, but instead can move freely over longer distances. Such a phase probably existed shortly after the Big Bang, and it is expected that it can be recreated for a short time in the laboratory by heavy ion collisions at a sufficiently large energy density. This new phase of matter is distinctively different from usual hadronic matter, and it is the experimental challenge to prove the fleeting existence of the QGP based on its characteristic signatures in the products of a heavy ion collision.

One possible signature is the suppression of the production of particles with large transverse momenta (p_{T}) in central Au + Au collisions compared to the expectation from scaled p + p reactions. The production of these particles is dominated by so-called *hard* processes, parton-parton interactions with large momentum transfer, and the subsequent fragmentation of partons into observable particles. These hard scatterings are identical in p + p and Au + Au reactions, hence they provide an ideal probe for the hot and dense medium created in the later stages of a central heavy ion collision. In the case that the medium has a high color-charge density, as expected for a QGP, the hard-scattered partons lose energy prior to their fragmentation, since they are also color charged. This process is similar to the energy loss of charged particles in the passage through matter and should be visible as a suppression of particle production at large transverse momenta compared to p + p reactions, the so-called *jet quenching*.

However, this is not the only effect that can lead to a suppression of particle production in Au + Au collisions compared to p + p reactions. For example, a similar effect can arise from a modification of the parton distributions in the nucleons of the gold nucleus compared to those in a free nucleon.

One aspect of this work was the analysis of the production of neutral pions for this signature. Neutral pions are reconstructed via their two decay photons, which are detected by the electromagnetic calorimeter (EMCal) of the PHENIX experiment. For this purpose an accurate and balanced energy calibration of the calorimeter is necessary. It has been verified and improved by different methods that were presented in this work. For the determination of the reconstruction efficiency of the EMCal for photons and neutral pions, a method was developed that facilitates the embedding of simulated particles into real events. This allows a detailed study of the influence of detector effects and of the event topology on the particle reconstruction. All measurements presented in this work were separately analyzed for the two detector types of the EMCal, a lead-scintillator sandwich calorimeter and a lead-glass Cherenkov calorimeter. This allows for an internal verification of the measurement and leads to a reduced systematic uncertainty for the final combined result.

The yield of neutral pions in central Au + Au collisions at $\sqrt{s_{NN}} = 200 \text{ GeV}$ exhibits a constant suppression of a factor of five above $p_T = 3 - 4 \text{ GeV}/c$ compared to the yield in p + p reactions scaled with the corresponding number of binary nucleon-nucleon collisions in the heavy ion reaction. By contrast, the yield in peripheral collisions is consistent with the expectation provided by the scaled p + p reference. A similar behavior was already observed in the first RHIC beam period with Au + Au collisions at a center of mass energy of $\sqrt{s_{NN}} = 130 \text{ GeV}$ [Adc02]. However, the results presented in this work allow for the first time a detailed study of the p_T dependence of the suppression and of its evolution with centrality. The observations are consistent with a medium-induced energy loss for a static medium of $\Delta E/\Delta x \approx -7 \text{ GeV}/\text{fm}$, which is 15 times the energy loss in cold nuclear matter, and with an initial energy density of $\epsilon_0 \approx 20 \text{ GeV}/\text{fm}^3$ in central collisions, which is hundred times the energy density of usual nuclear matter.

The decisive evidence that the observed suppression is a consequence of strong interactions of the hard-scattered partons, and not due to a modification of the initial state of the partons in nucleons of the gold nucleus, was also provided in this work. First this was demonstrated based on the analysis of neutral pions produced in d + Au collisions at $\sqrt{s_{NN}} = 200 \text{ GeV}$. In these reactions the same effects of cold nuclear matter are present as in Au + Au collisions, while at the same time no hot and dense medium is created. In contrast to the observation in Au + Au collisions, the production of neutral pions in d + Au reactions is even slightly enhanced compared to the reference measurement in p + p collisions. Thus a medium modification of the initial state of the partons in the gold nucleus cannot be responsible for the suppression of the particle production measured in central Au + Au events.

A confirmation of the jet quenching scenario directly from Au + Au collisions is provided by the measurement of direct photons. Direct photons with large p_T are likewise

produced in hard parton-parton collisions. By contrast to the hard-scattered partons they are not influenced by the strong interaction and can penetrate the hot and dense medium, which is created in central heavy ion collisions at RHIC. An additional source of direct photons is the thermal production in the QGP or in a hot hadron gas. It should be a significant contribution to the direct photon yield at intermediate p_T and is also a possible signature for the creation of a QGP.

The measurement of direct photons is complicated by the large background contribution from hadronic decays to the inclusive photon spectrum. This background is dominated by the two-photon decay of the π^0 . Based on the measured π^0 spectrum, the fraction of those photons in the inclusive photon yield was originating from π^0 , η , ω , ρ , η' , and K_S^0 decays was calculated. The comparison of the inclusive photon yield to the expectation solely from hadronic decays showed a significant excess in central Au + Au collisions, which decreased towards more peripheral collisions. The observation accords with the expectation that the production of neutral pions is suppressed by the parton energy loss, which leads to a suppression of the background from decay photons, while the yield of direct photons remains unaffected compared to the scaled expectation from p + p reactions. Within the current systematic errors of our measurement we are not sensitive to a signal of thermal photon production, which may be observed as an excess of the direct photon yield at intermediate p_T above the expectation from hard scattering processes.

The invariant yield of direct photons was determined in this work for different centralities and for a large transverse momentum range, based on the inclusive photon yield and under consideration of the background from hadronic decays. These measurements are the first observation of direct photons in heavy ion collisions at RHIC energies. The observation that their production is not suppressed in central Au + Au collisions, in contrast to the production of neutral pions, allows the direct verification that the observed suppression is due to strong final state effects, probably the parton energy loss in a dense partonic medium.

In summary, the observations of this work provide an indication that the QGP was created in central Au + Au collisions at RHIC.

Zusammenfassung

Diese Arbeit befasst sich mit der Messung neutraler Pionen und direkter Photonen in Au + Au-Kollisionen am PHENIX-Experiment des RHIC/BNL bei einer Schwerpunktsenergie von $\sqrt{s_{NN}} = 200 \text{ GeV}$. Außerdem wurde die Produktion neutraler Pionen in d + Au-Kollisionen bei identischer Schwerpunktsenergie untersucht.

Eines der Hauptziele des PHENIX Experimentes ist der Nachweis des Quark-Gluon-Plasmas (QGP), ein Zustand stark wechselwirkender Materie, in dem Quarks und Gluonen nicht mehr in Nukleonen eingeschlossen sind, sondern sich über größere Raumbereiche frei bewegen können. Dieser Zustand existierte vermutlich kurz nach dem Urknall und man erwartet, dass er bei ausreichender Energiedichte in Schwerionenkollisionen für einen kurzen Augenblick im Labor erzeugt werden kann. Diese Phase unterscheidet sich grundlegend von normaler hadronischer Materie und es ist die experimentelle Herausforderung, die flüchtige Existenz des QGP an Hand verschiedener charakteristischer Signaturen in den Reaktionsprodukten einer Schwerionenkollision nachzuweisen.

Eine mögliche Signatur ist die Unterdrückung der Produktion von Teilchen mit hohem Transversalimpuls (p_T) in zentralen Au + Au-Kollisionen im Vergleich zu der Erwartung aus skalierten p + p-Reaktionen. Die Produktion solcher Teilchen wird durch so genannte *harte* Prozesse dominiert, Parton-Parton-Kollisionen mit hohem Impulsübertrag und anschließender Fragmentation der Partonen in beobachtbare Teilchen. Diese harten Prozesse unterscheiden sich nicht für p + p- und Au + Au-Reaktionen, die so produzierten Teilchen können also als Sonde für die heiße und dichte Phase dienen, die in zentralen Schwerionenstößen erzeugt wird. Weist diese Phase eine hohe Farbladungsdichte auf, wie es beim QGP der Fall ist, so verlieren die gestreuten Partonen vor ihrer Fragmentation Energie, da auch sie eine Farbladung tragen. Dieser Prozess ist mit dem Energieverlust geladener Teilchen in Materie vergleichbar und sollte bezogen auf p + p-Reaktionen zu einer Unterdrückung der Teilchenproduktion, zum so genannten *Jet-Quenching*, führen.

Dies ist jedoch nicht das einzige Szenario, in dem es zu einer Unterdrückung der Teilchenproduktion in zentralen Au + Au-Kollisionen im Vergleich zu p + p-Reaktionen kommen kann. So kann beispielsweise eine Veränderung der Partonenverteilungen in den Nukleonen des Goldkerns im Vergleich zu denen eines freien Nukleons einen ähnlichen Effekt haben.

Im Rahmen dieser Arbeit wurde unter anderem die Produktion neutraler Pionen auf diese Signatur hin untersucht. Neutrale Pionen werden im PHENIX Experiment über die Messung ihrer Zerfallsphotonen im elektromagnetischen Kalorimeter (EMCal) nachgewiesen. Hierfür ist eine möglichst genaue und gleichmäßige Energieeichung des Kalorimeters nötig, welche an Hand verschiedener in der Arbeit vorgestellter Verfahren optimiert wurde. Zur Bestimmung der Nachweiseffizienz von Photonen sowie Pionen im EMCal wurde außerdem ein Verfahren entwickelt, bei dem simulierte Teilchen in reale Ereignisse eingebettet werden. Dies ermöglicht die detaillierte Untersuchung von Detektoreffekten und des Einflusses der Ereignistopologie auf den Teilchennachweis. Alle Messungen in dieser Arbeit wurden separat für die beiden verschiedenen Detektortypen des EMCal analysiert, einem Blei-Szintillator-Sandwichkalorimeter und einem Bleiglas-Cherenkovkalorimeter. Dies erlaubt eine interne Verifikation der Messung und führt für die kombinierten Endergebnisse zu einer reduzierten systematischen Unsicherheit.

Die Produktion neutraler Pionen in zentralen Au + Au-Kollisionen bei einer Schwerpunktsenergie von $\sqrt{s_{NN}} = 200 \text{ GeV}$ zeigt eine konstante Unterdrückung um einen Faktor fünf ab einem Transversalimpuls $p_T = 3 - 4 \text{ GeV}/c$ im Vergleich zur Produktion in p + p-Reaktionen skaliert mit der Anzahl der entsprechenden binären Nukleon-Nukleon-Kollisionen der Schwerionenreaktion. Der Vergleich in peripheren Stößen deckt sich jedoch mit der Erwartung aus skalierten p + p-Reaktionen. Eine ähnliches Verhalten wurde schon in der ersten RHIC-Strahlzeit bei einer Schwerpunktsenergie von $\sqrt{s_{NN}} = 130 \text{ GeV}$ beobachtet [Adc02]. Die im Rahmen dieser Arbeit vorgestellten Ergebnisse erlauben jedoch eine detaillierte Analyse der p_T -Abhängigkeit der Unterdrückung und ihrer Entwicklung mit der Zentralität der Reaktion. Die Beobachtungen sind konsistent mit einem mediuminduzierten Energieverlust der Partonen von $\Delta E/\Delta x \approx -7 \text{ GeV}/\text{fm}$ für ein statisches Medium, 15 mal größer als in kalter Kernmaterie, beziehungsweise mit einer anfänglichen Energiedichte von $\epsilon_0 \approx 20 \text{ GeV}/\text{fm}^3$ in zentralen Kollisionen. Dies entspricht der hundertfachen Energiedichte normaler Kernmaterie.

Der entscheidende Nachweis dafür, dass die beobachtete Unterdrückung eine Folge starker Wechselwirkungen der hart gestreuten Partonen ist und nicht eine Änderung des Anfangszustandes der Partonen in den Nukleonen des Goldkerns, gelang ebenfalls im Rahmen dieser Arbeit. Dies wurde unter anderem durch die Untersuchung der Produktion neutraler Pionen in d + Au-Kollisionen bei einer Schwerpunktsenergie von $\sqrt{s_{NN}} = 200 \text{ GeV}$ erreicht. In dieser Reaktion spielen die gleichen Effekte kalter Materie wie auch in Au + Au-Kollisionen eine Rolle, es entsteht aber kein heißes und dichtes Medium. Im Gegensatz zu zentralen Au + Au-Reaktionen wurde jedoch in d + Au-Kollisionen sogar eine leichte Erhöhung der Teilchenproduktion im Vergleich zur p + p Referenz beobachtet. Eine Modifikation des Anfangszustandes der Partonen im Goldkern

kann also nicht der Grund für die Unterdrückung der Teilchenproduktion in zentralen Au + Au Ereignissen sein.

Eine weitere Bestätigung des Jet-Quenching Szenarios erlaubt die Messung direkter Photonen. Direkte Photonen mit hohem p_T werden ebenfalls in harten Parton-Parton-Kollisionen erzeugt. Sie werden allerdings nicht durch die starke Wechselwirkung beeinflusst und können die heiße und dichte Kernmaterie, die in zentralen Schwerionenkollisionen am RHIC entsteht, quasi ungestört durchdringen. Eine weitere mögliche Quelle direkter Photonen in zentralen Schwerionenkollisionen ist die thermische Erzeugung im Quark-Gluon-Plasma oder in einem heißen Hadronengas, die im mittleren Transversalimpulsbereich die Photonproduktion aus harten Kollisionen übertreffen könnte. Der Nachweis thermischer Photonen ist ebenfalls eine mögliche Signatur für die Erzeugung eines QGP.

Die Messung direkter Photonen wird durch den großen Untergrund von Photonen aus hadronischen Zerfällen erschwert, wobei der Hauptbeitrag vom Zerfall des π^0 stammt. An Hand des gemessenen π^0 -Spektrums wurde der Anteil der Photonen aus π^0 , η , ω , ρ , η' und K_S^0 -Zerfällen am inklusiven Photonenspektrum bestimmt. Der Vergleich des inklusiven Photonenspektrums mit der Erwartung aus hadronischen Zerfällen zeigte einen signifikanten Überschuss in zentralen Au + Au-Kollisionen, der zu peripheren Reaktionen hin abnimmt. Diese Beobachtung stimmt mit der Erwartung überein, dass die Produktion neutraler Pionen durch den Energieverlust im Medium unterdrückt ist und sich somit auch der Untergrund durch Zerfallsphotonen verringert, während sich die Anzahl der direkten Photonen bei hohem p_T im Vergleich zu denen aus skalierten p + p-Reaktionen nicht ändert. Im Rahmen der Fehler läßt sich jedoch keine Aussage über ein Signal thermischer Photonen machen, welches bei mittlerem Transversalimpuls als Überschuß direkter Photonen über der Erwartung aus harten Prozessen zu beobachten wäre.

Die Produktion direkter Photonen für verschiedene Zentralitäten konnte im Rahmen dieser Arbeit über einen breiten Transversalimpulsbereich nach Berücksichtigung des Untergrundes aus den inklusiven Photonenspektren bestimmt werden. Diese Messungen stellen den ersten Nachweis direkter Photonen in Schwerionenkollisionen am RHIC dar. Die Beobachtung, dass ihre Produktion nicht wie die Produktion neutraler Pionen in zentralen Au + Au-Kollisionen unterdrückt ist, ermöglicht die direkte Verifikation, dass die Unterdrückung eine Folge starker Endzustandswechselwirkungen ist, wahrscheinlich der Energieverlust von Partonen in einem dichten Medium aus freien Farbladungen.

Zusammengefasst sind die Beobachtungen dieser Arbeit Hinweise darauf, dass es in zentralen Au + Au-Kollisionen am RHIC tatsächlich zur Ausbildung eines Quark-Gluon-Plasmas gekommen ist.

A. Kinematic Variables

When studying ultra-relativistic heavy ion collisions it is useful to choose the kinematic variables in a way that they are subject to simple transformations when changing the reference frame. According to the rules of special relativity a particle is characterized by its *four-momentum*¹:

$$P^\mu = (E, \vec{p}) = (E, p_x, p_y, p_z), \quad (\text{A.1})$$

with the energy E and the usual three-momentum of the particle \vec{p} . The absolute value of the four-momentum, called invariant mass m_{inv} , is the same in all reference frames or invariant under Lorentz transformation:

$$m_{\text{inv}}^2 = P^2 = P^\mu P_\mu = E^2 - \vec{p} \cdot \vec{p}. \quad (\text{A.2})$$

For a free particle the invariant mass is identical to its rest mass m_0 and Equation (A.2) becomes the well-known relativistic energy-momentum relation.

In high energy physics the sum of the four-momenta of two colliding particles leads to the definition of the *Mandelstam* variable s :

$$s = (P_1 + P_2)^2, \quad (\text{A.3})$$

with \sqrt{s} determining the center of mass energy of the reaction.

The beam is usually considered to point into the z -directions. Thus the transverse momentum component p_T and the longitudinal component p_L can be written as:

$$p_T = p \cdot \sin(\vartheta), \quad (\text{A.4})$$

$$p_L = p \cdot \cos(\vartheta), \quad (\text{A.5})$$

where p is the absolute value of the momentum $|\vec{p}|$ and ϑ is the angle with respect to the beam axis.

The transverse momentum p_T is invariant under Lorentz transformation in z -direction, while p_L is not invariant. Therefore the dimensionless rapidity y is defined. It is directly related to the transverse velocity $\beta_L = p_L/E$ of a particle:

$$\begin{aligned} y &= \text{atanh } \beta_L \\ &= \frac{1}{2} \ln \left(\frac{E + p_L}{E - p_L} \right). \end{aligned} \quad (\text{A.6})$$

¹Here, as well as in the following we will use the convention $\hbar = c = 1$.

It has the advantage to be additive under Lorentz transformation into a reference frame that moves at a velocity β with respect to the old reference frame in longitudinal direction:

$$y' = y + \operatorname{atanh}(\beta). \quad (\text{A.7})$$

For this reason the shape of a distribution is independent of the reference frame when it is given in units of the rapidity. The rapidity is connected to the energy of a particle and to its longitudinal momentum via the transverse mass $m_T = \sqrt{p_T^2 + m_0^2}$:

$$E = m_T \cdot \cosh(y), \quad (\text{A.8})$$

$$p_L = m_T \cdot \sinh(y). \quad (\text{A.9})$$

In the limit $E \gg m_0$ the rapidity can be approximated by the *pseudo-rapidity* η :

$$\eta = \frac{1}{2} \ln \left(\frac{p + p_L}{p - p_L} \right) \quad (\text{A.10})$$

$$= -\ln \left[\tan \left(\frac{\vartheta}{2} \right) \right]. \quad (\text{A.11})$$

The pseudo-rapidity is only determined by the angle ϑ of the particle direction of motion with respect to the beam axis. For this reason it is usually easier to determine the pseudo-rapidity than the rapidity of a particle. Similar to Equation (A.8) and (A.9) holds:

$$E = p_T \cdot \cosh(\eta), \quad (\text{A.12})$$

$$p_L = p_T \cdot \sinh(\eta). \quad (\text{A.13})$$

B. Lists of Analyzed Runs

69502	69650	69654	70087	70451	70456	72119	72361	72669	74413
74428	74443	74463	74691	74857	74865	74868	76692	76693	76797
76864	76985	76995	77380	77391	77392	78033	78035	78182	78210
78435									

Table B.1: List of runs containing all triggers used in the analysis of the $d + Au$ data.

77094	77096	77247	77252	77255	77266	77312	77313	77314	77320
77322	77374	77380	77389	77390	77391	77392	77394	77414	77415
77520	77521	77530	77531	77533	77547	77678	77683	77686	77687
77688	78029	78030	78033	78034	78035	78179	78181	78207	78553
78578	78632	78633	78808	78810	78817	78838	78839	79047	79048
79050	79066	79067	79340	79341	79343	79560	79579	79603	79615
79621	79622	79624	79626	79628	79629	79630	79632	79641	79642
79643	79644	79740	79749	79750	79753	79762	79764	79765	79863
79872	79873	79875	79885	79888	80151	80158	80161	80172	80304

Table B.2: List of filtered runs containing only Γ_{11} triggers used in the analysis of the $d + Au$ data.

27808	27823	27825	27826	27827	27831	27835	27836	27839	27896
27898	27913	27925	28004	28006	28008	28056	28063	28065	28068
28070	28075	28123	28126	28127	28135	28163	28170	28199	28209
28212	28284	28286	28302	28375	28377	28381	28414	28415	28418
28419	28447	28450	28479	28488	28490	28546	28552	28558	28573
28579	29116	29122	29146	29171	29178	29179	29183	29184	29185
29186	29190	29197	29212	29213	29218	29236	29238	29240	29241
29252	29253	29255	29268	29362	29372	29380	29386	29392	29393
29404	29445	29446	29454	29459	29461	29510	29512	29514	29515
29529	29534	29537	29557	29561	29562	29566	29888	30060	30062
30069	30074	30089	30112	30113	30117	30119	30126	30149	30157
30159	30193	30196	30197	30218	30318	30326	30328	30329	30358
30631	30637	30650	30807	30812	30813	30814	30820	30910	30911
30913	30916	30917	30920	31009	31013	31014	31021	31024	31025
31058	31060	31075	31076	31080	31143	31145	31147	31148	31152
31230	31232	31233	31240	31249	31252	31343	31459	31460	31463
31464	31497	31500	31501	31503	31509	31517	31520	31631	31633
31637	31807	31811	31814	31815	31824	31831	31836	31837	31868
32010	32011	32017	32043	32120	32123	32127	32128	32217	32218
32222	32239	32242	32271	32272	32275	32280	32367	32382	32385
32387	32435	32437	32438	32524	32525	32526	32543	32546	32709
32713	32717	32720	32721	32722	32747	32748	32763	32765	32766
32770	32771	32774	32776	32777	32779	32780	32781	32782	32908
32911	32912	32913	32914	32929	32932	32933	32934	32948	32949
33049	33050	33051	33055	33056	33064	33065	33068	33082	33083
33085	33086	33113	33116	33123	33124	33125	33149	33153	33157
33158	33161	33166	33168	33169	33295	33298	33299	33309	33314
33318	33321	33323	33327	33337	33341	33345	33392	33393	33458
33460	33463	33467	33468	33521	33526	33527	33535	33542	33545
33547	33550	33558	33575	33577	33609	33610	33611	33612	33614

Table B.3: List of runs used in the analysis of the Au + Au data.

C. Excluded Modules and FEMs

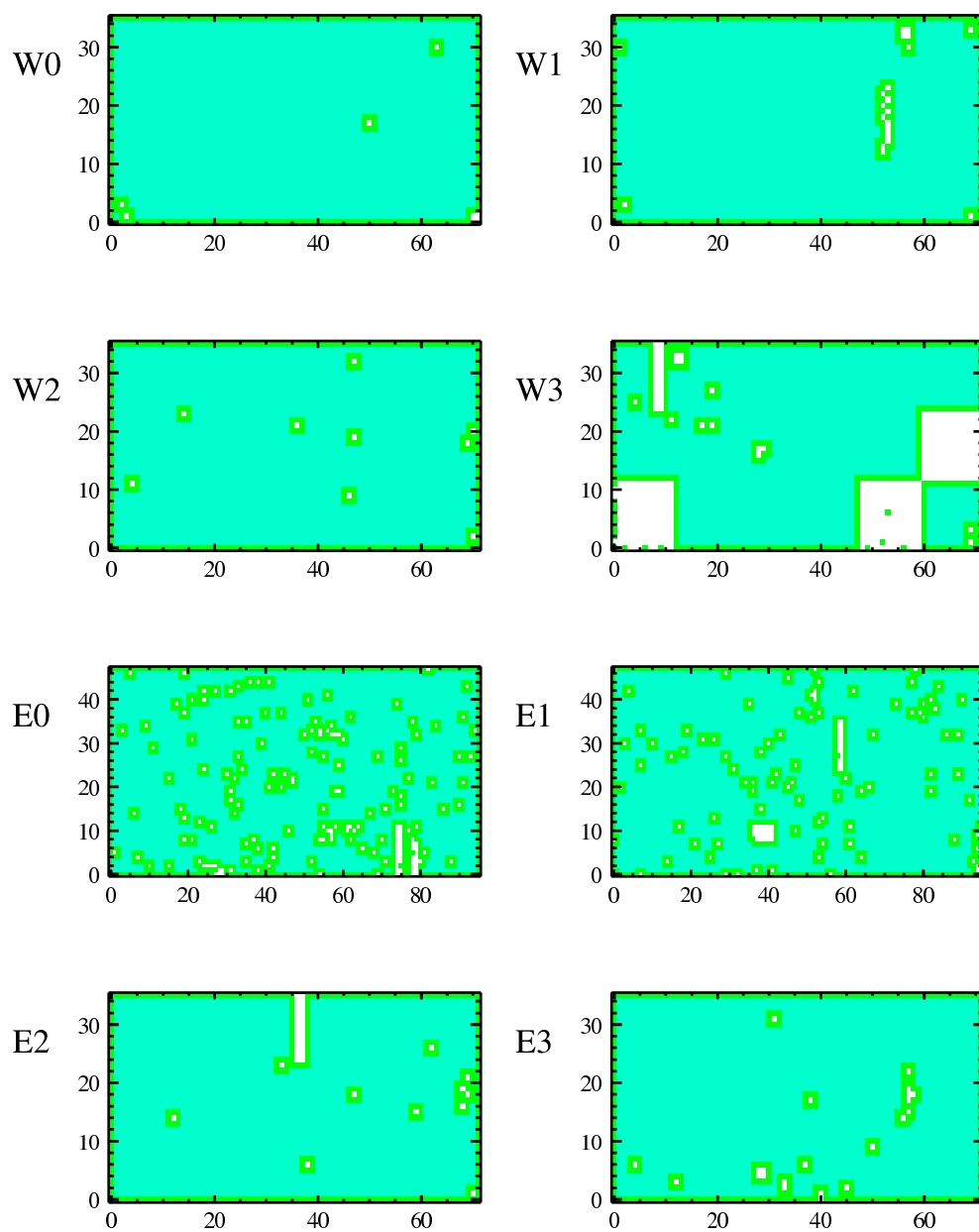


Figure C.1: Modules flagged as bad or dead for the analysis of the Au + Au data (white) and the excluded area around it. The regions excluded on the edge of the calorimeter sectors are also shown.

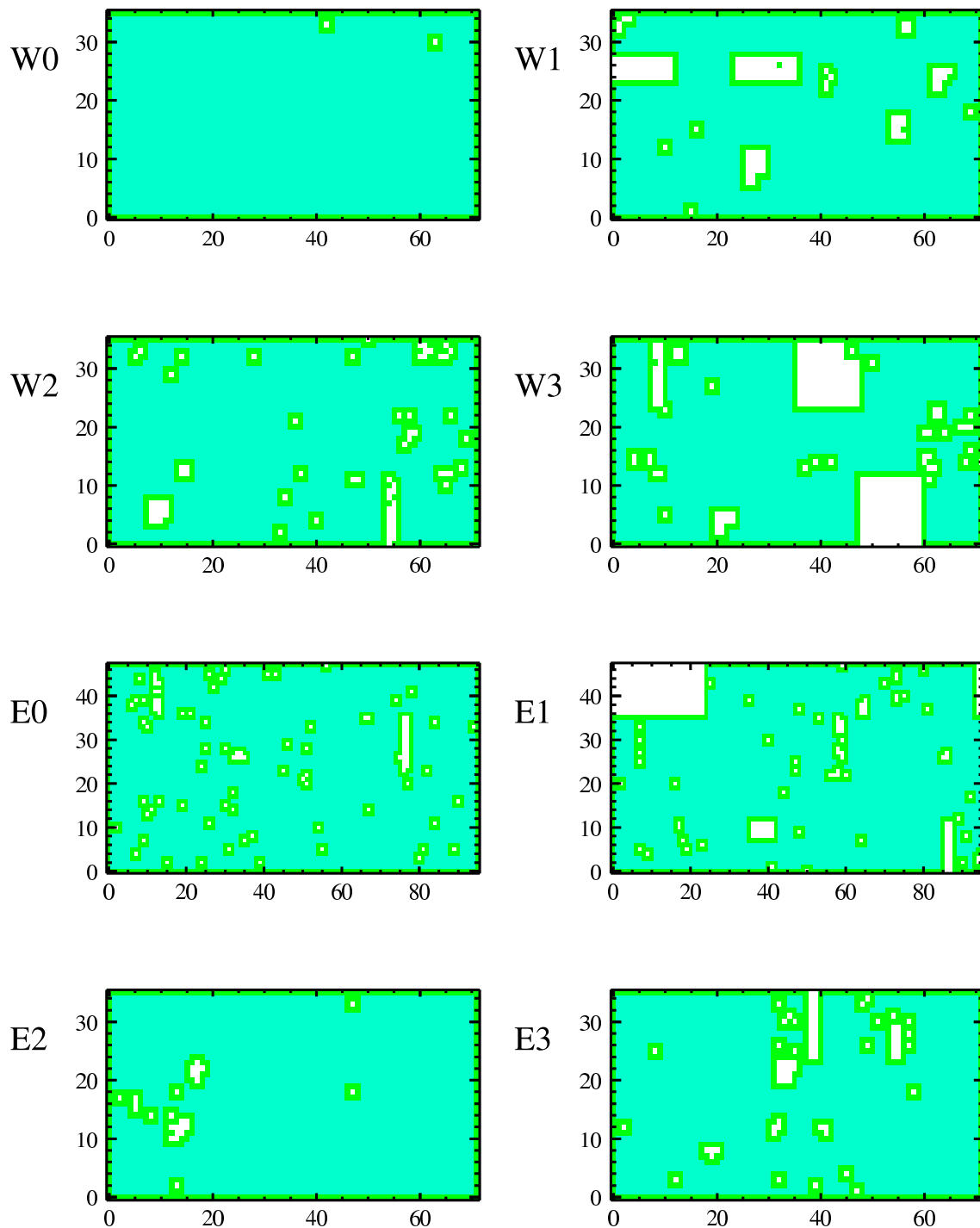


Figure C.2: Modules flagged as bad or dead for the analysis of the $d + Au$ data (white) and the excluded area around it. The regions excluded on the edge of the calorimeter sectors are also shown.

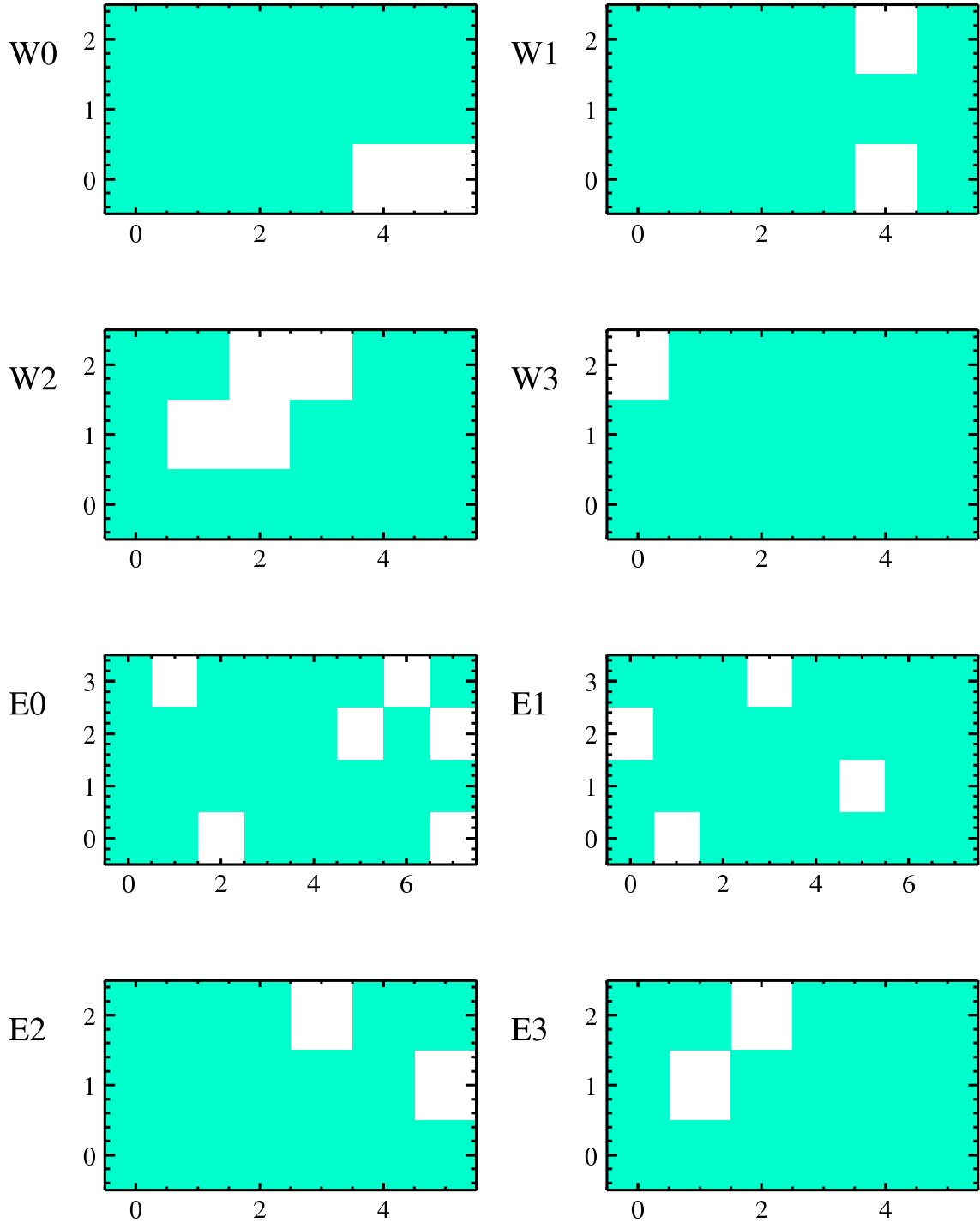


Figure C.3: FEMs masked for the 4×4 ERT trigger during the $d + \text{Au}$ run (white).

D. Countsheets

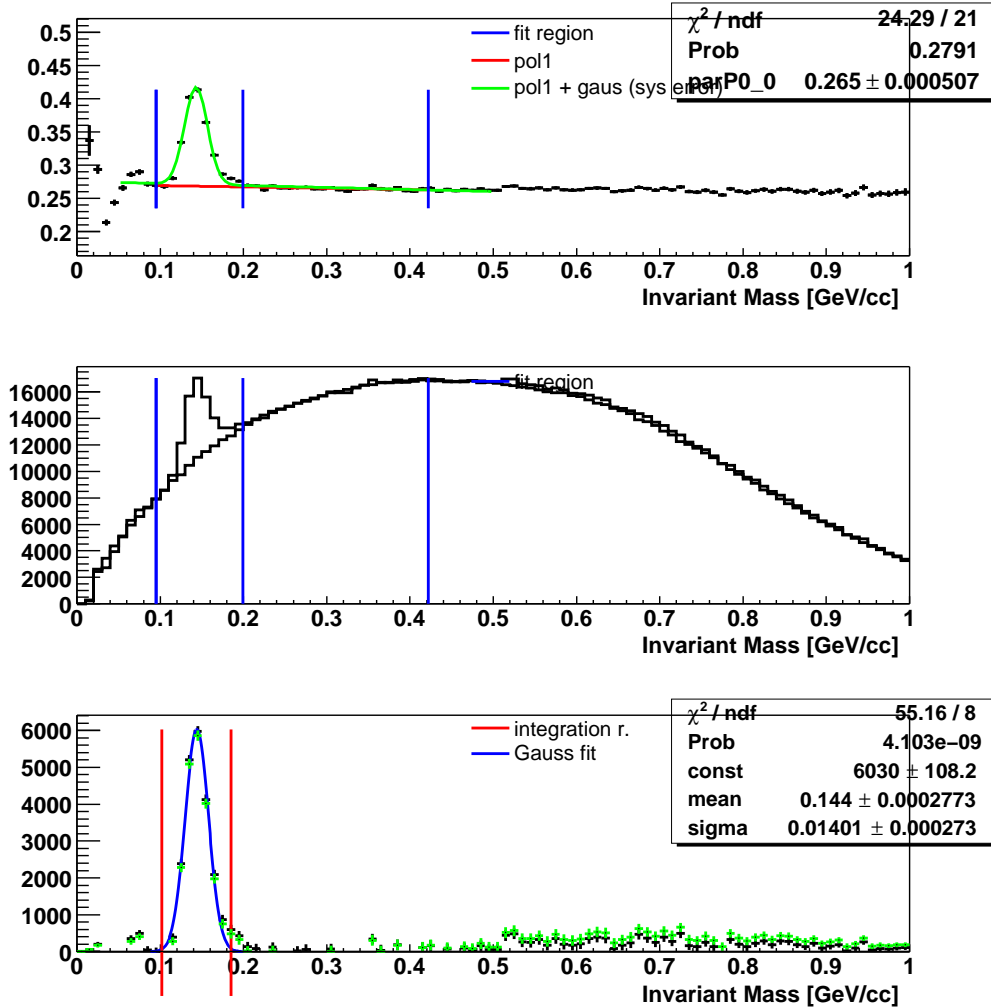
The basic idea of the countsheets is to document each step of the peak extraction process for π^0 s in each individual p_T bin, to be able to track down problems in the raw yield extraction visually.

The countsheets are PostScript files generated during the peak extraction for the selected centrality, PID, sector combination, peak extraction window and bin width. They contain the following information for each p_T bin:

- The ratio plot of real over mixed invariant mass distribution, together with the fitted scaling function used for the peak extraction and the systematic error estimate,
- A comparison plot of the scaled mixed event background with the real invariant mass distribution,
- The real event invariant mass distribution corrected for the mixed event background for both employed scaling functions,
- A table with information on the filename, the summed p_T bins, the photon pair p_T , the number of π^0 s with the peak extraction error, the integration and normalization region.

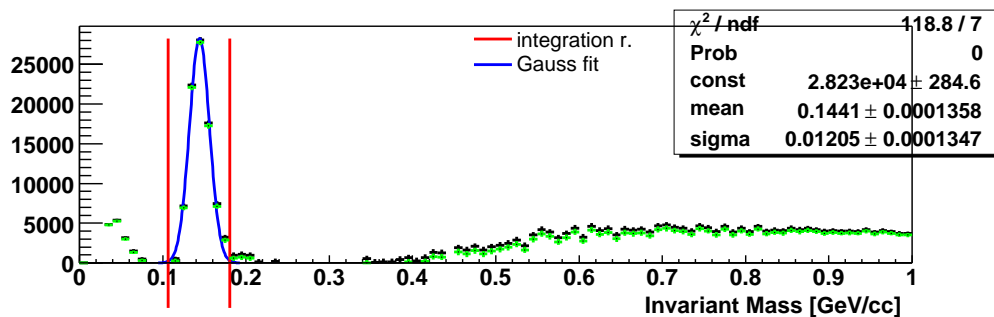
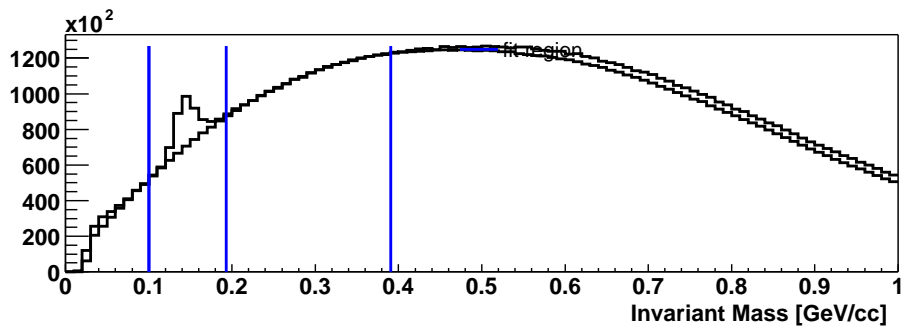
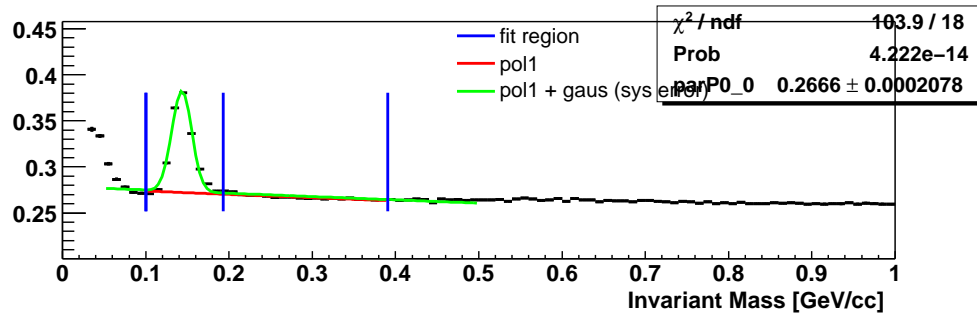
Additionally, each countsheet file contains plots of the p_T dependence of the π^0 peak position, π^0 peak width, and the raw yields.

In the following some examples for countsheets in one p_T bin will be given for the Au + Au and d + Au analysis. Those examples illustrate the different combinatorial background in both analyses as well as the gain in statistics by the Gamma1 trigger in the d + Au analysis.



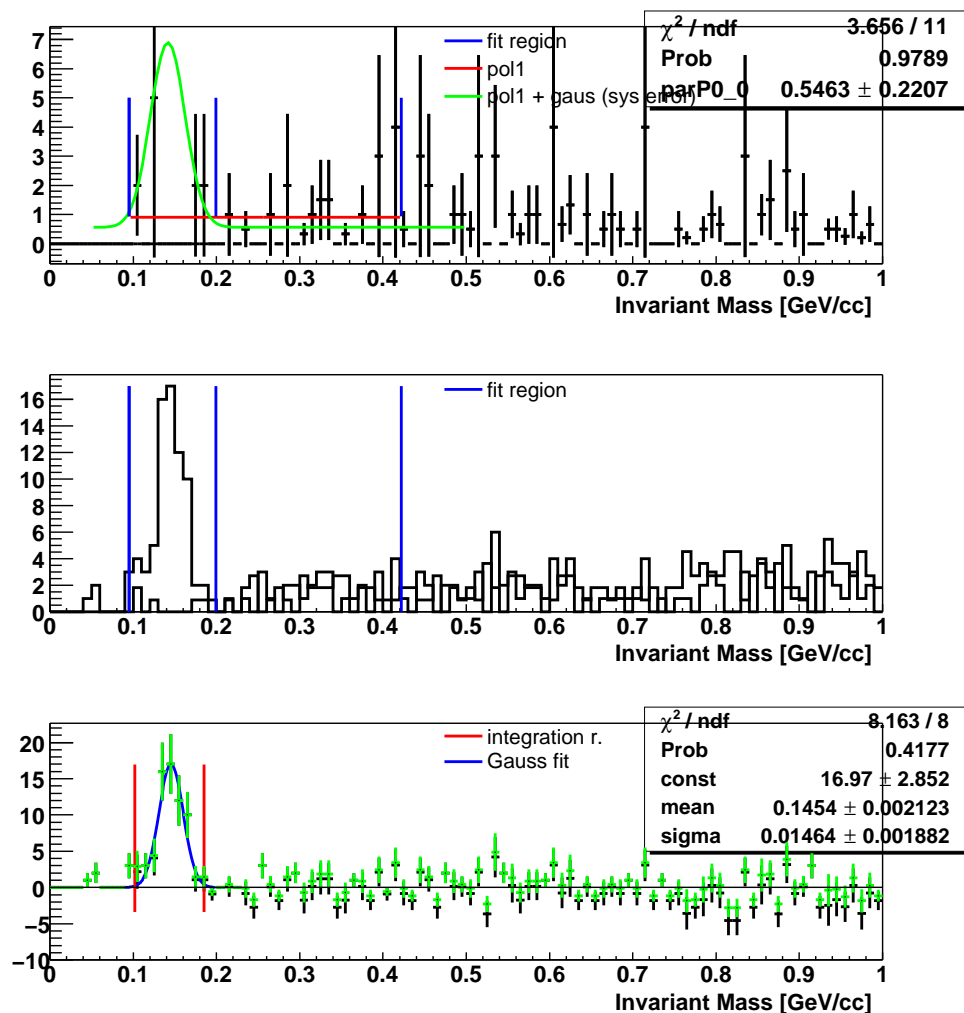
pi0_scan153_pid0_C0-10_bins32_rebin2_nSigEx3.0_E0_E1_E0E1_date190704
 bin: 13 - 14
 pT-range: $3.00 < pT < 3.50$
 number of pi0s: 21595.9 ± 1420.5 (1017.3 stat, 991.4 sys)
 bckgd, unscaled (bu): 363972
 97648
 (stat² = sig + bu*bsf + bsfE²*bu² + bsf²*bu)
 integration region: $0.1018 < \text{Minv} < 0.1853$
 normalization region: $0.095 < \text{Minv} < 0.095 \ \&\& \ 0.199 < \text{Minv} < 0.422$

Figure D.1: Example countsheet for minimum bias events measured with the PbGl in Au + Au collisions.



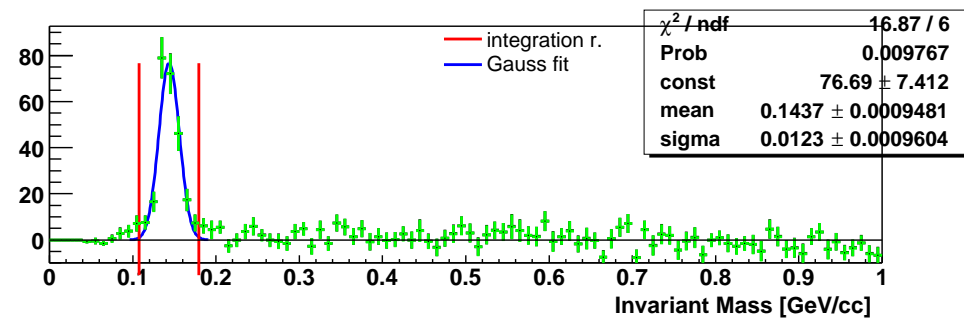
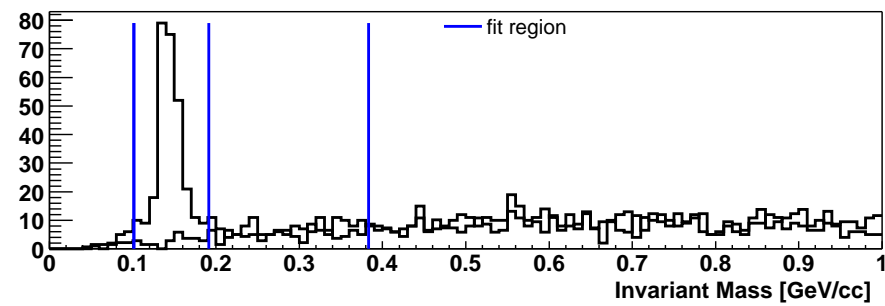
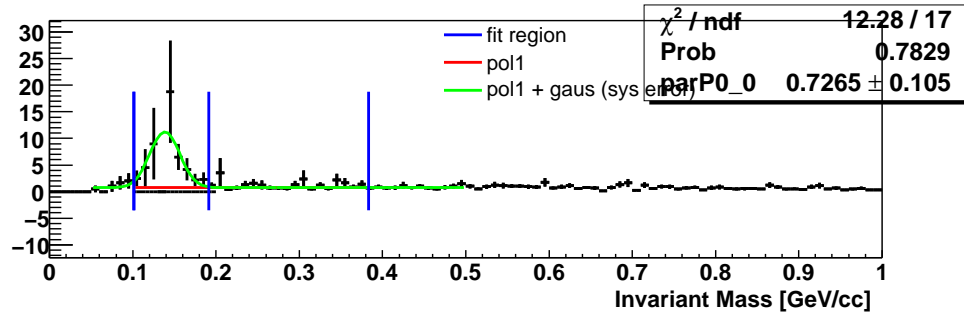
pi0_scan153_pid0_C0-10_bins32_rebin2_nSigEx3.0_W0_W1_W2_W0W1W2_ScE_date000000
 bin: 13 - 14
 pT-range: 3.00 < pT < 3.50
 number of pi0s: 86896.9 +- 4058.7 (2884.4 stat, 2855.3 sys)
 bckgd, unscaled (bu): 2319878
 631086
 (stat^2 = sig + bu*bsf + bsfE^2*bu^2 + bsf^2*bu)
 integration region: 0.1064 < Minv < 0.1805
 normalization region: 0.100 < Minv < 0.100 && 0.193 < Minv < 0.391

Figure D.2: Example countsheet for minimum bias events measured with the PbSc in Au + Au collisions.



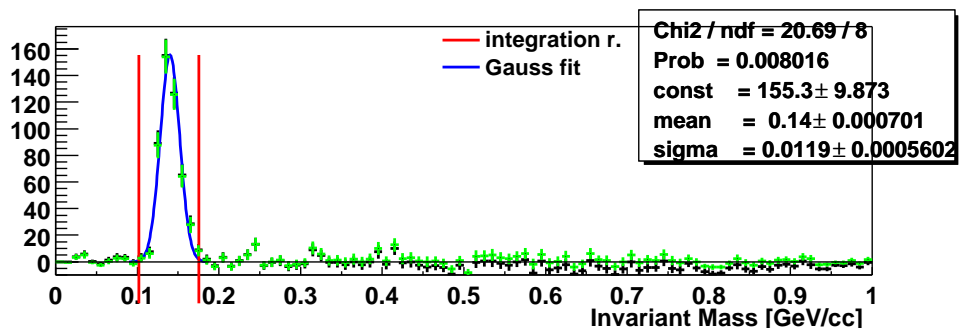
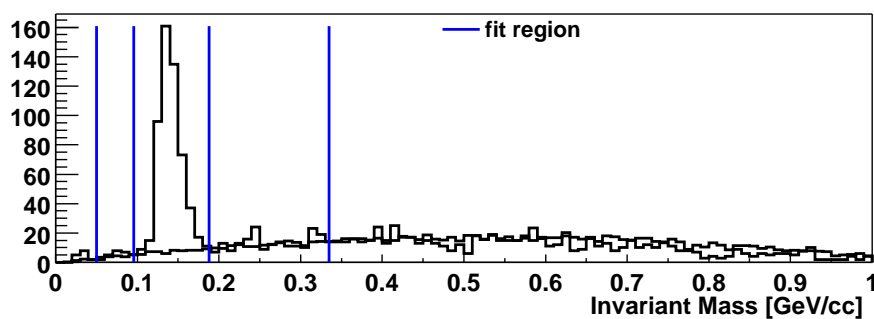
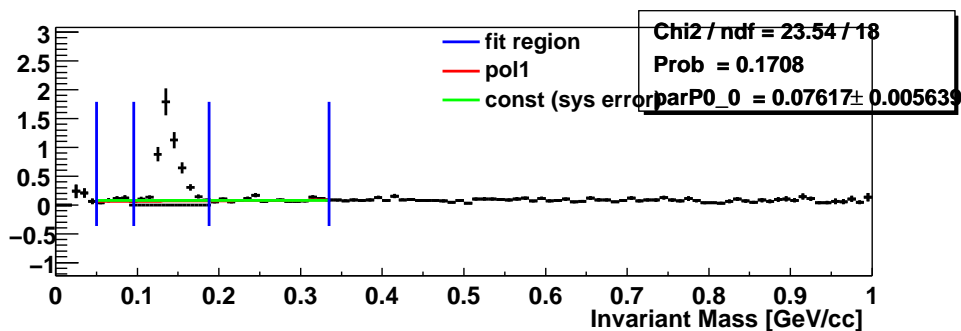
pi0_scan153_pid0_C11-21_bins32_rebin2_nSigEx3.0_E0_E1_E0E1_date190704
 bin: 31 - 32
 pT-range: $7.50 < pT < 8.00$
 number of pi0s: 66.4 ± 8.9 (8.7 stat, 1.7 sys)
 bckgd, unscaled (bu): 5
 4
 (stat² = sig + bu*bsf + bsfE²*bu² + bsf²*bu)
 integration region: $0.1018 < \text{Minv} < 0.1853$
 normalization region: $0.095 < \text{Minv} < 0.095 \ \&\& \ 0.199 < \text{Minv} < 0.422$

Figure D.3: Example countsheet for LVL2-triggered events measured with the PbG1 in Au + Au collisions (centrality class 0-93%).



pi0_scan153_pid0_C11-21_bins32_rebin2_nSigEx3.0_W0_W1_W2_W0W1W2_ScE_date000000
 bin: 31 - 32
 pT-range: 7.50 < pT < 8.00
 number of pi0s: 253.2 +/- 17.3 (17.3 stat, 0.2 sys)
 bckgd, unscaled (bu): 30
 21
 (stat^2 = sig + bu*bsf + bsfE^2*bu^2 + bsf^2*bu)
 integration region: 0.1075 < Minv < 0.1795
 normalization region: 0.101 < Minv < 0.101 && 0.191 < Minv < 0.383

Figure D.4: Example countsheet for LVL2-triggered events measured with the PbSc in Au + Au collisions (centrality class 0-93%).



pi0dAu_all_scan56_pid0_Sum0_bins32_rebin2_nSigEx3.0_E0_E1_E0E1_date061003

bin: 13 – 14

pT-range: 3.00 < pT < 3.50

number of pi0s: 484.6 ± 29.8 (28.8 stat, 7.8 sys)

bckgd, unscaled (bu): 869

(stat² = sig + bu*bsf + bsfE²*bu² + bsf²*bu)

integration region: 0.1016 < Minv < 0.1753

normalization region: 0.050 < Minv < 0.095 && 0.188 < Minv < 0.335

Figure D.5: Example countsheet for minimum bias events measured with the PbG1 in d + Au collisions.

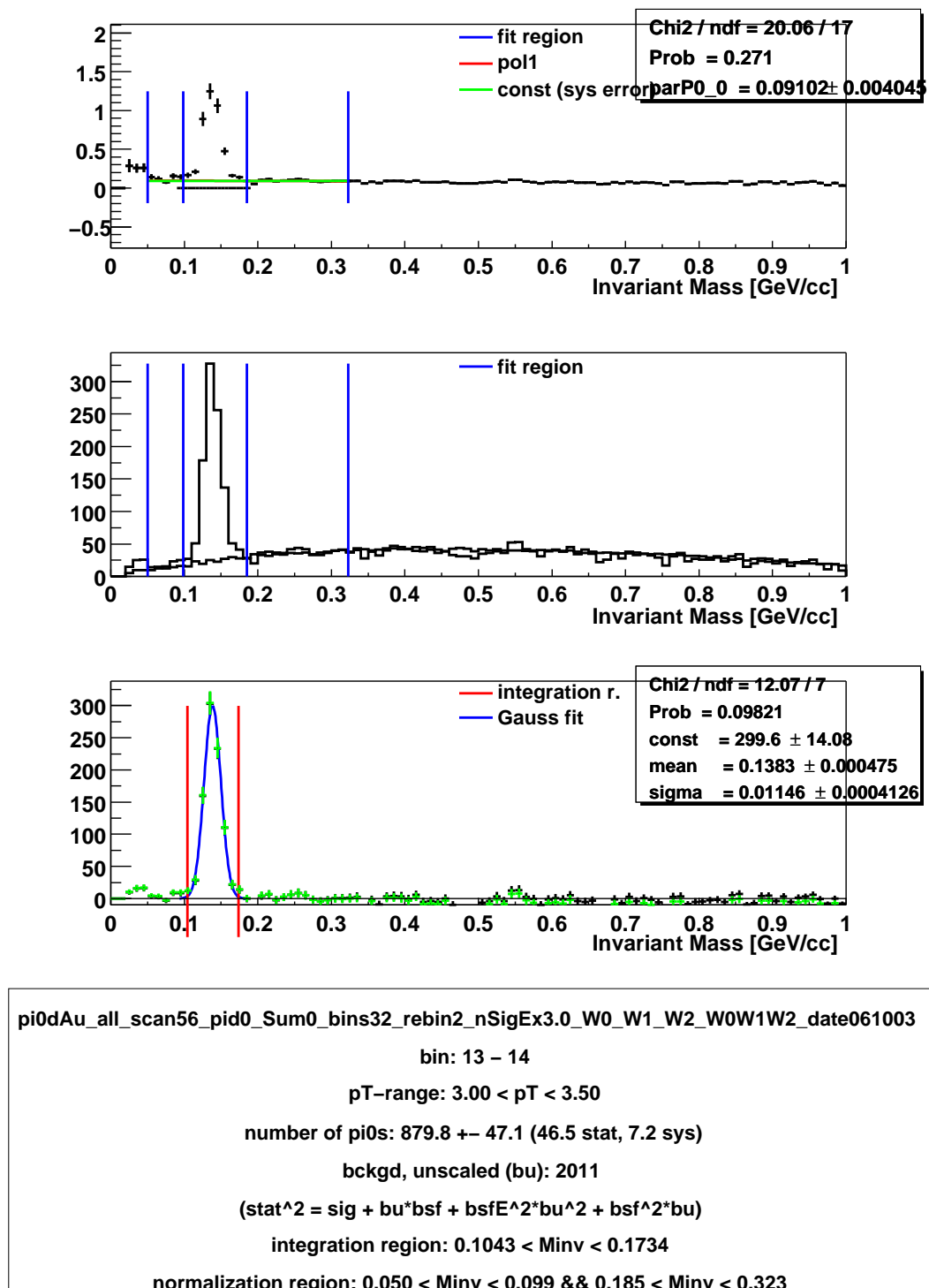
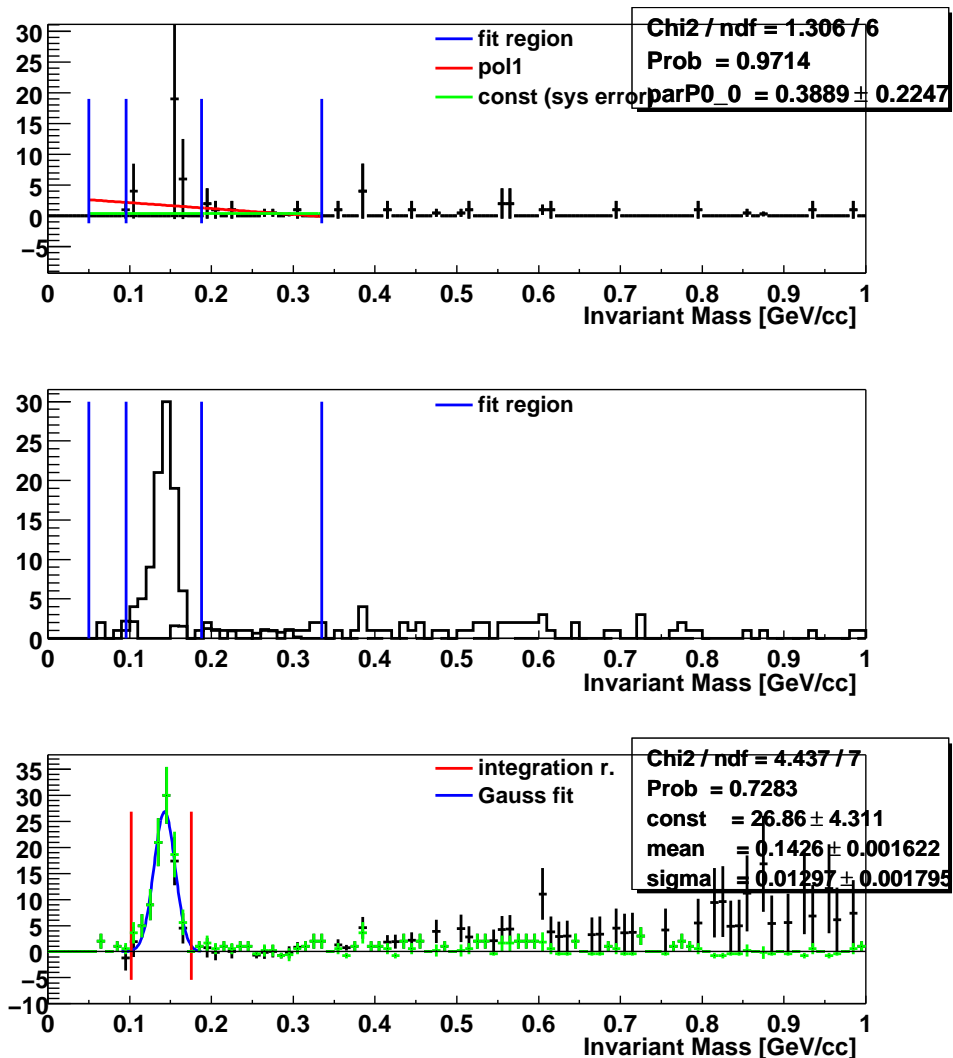


Figure D.6: Example countsheet for minimum bias events measured with the PbSc in d + Au collisions.



pi0dAu_gamma1_scan56_pid0_Sum1_bins32_rebin2_nSigEx3.0_E0_E1_E0E1_date061003

bin: 31 - 32

pT-range: 7.50 < pT < 8.00

number of pi0s: 88.7 ± 14.8 (14.2 stat, 4.1 sys)

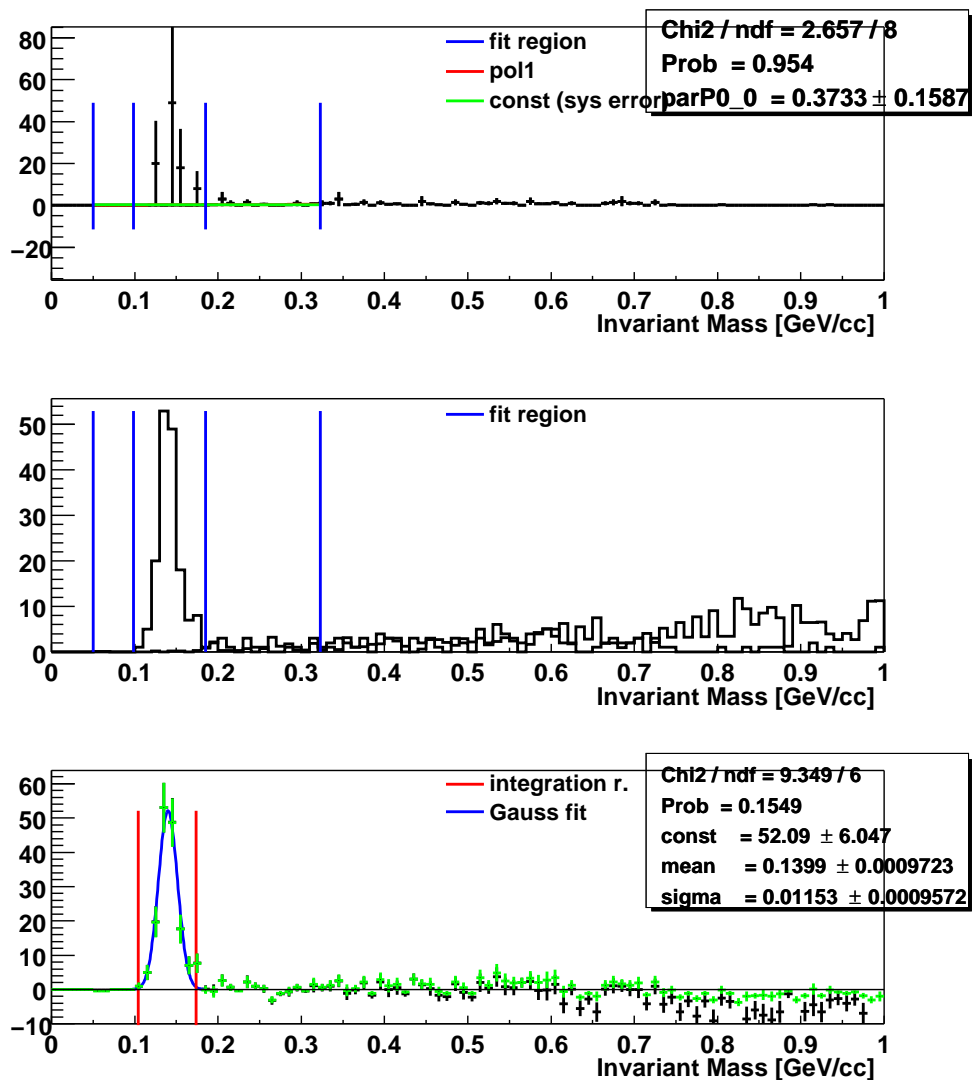
bckgd, unscaled (bu): 3

(stat² = sig + bu*bsf + bsfE²*bu² + bsf²*bu)

integration region: 0.1016 < Minv < 0.1753

normalization region: 0.050 < Minv < 0.095 && 0.188 < Minv < 0.335

Figure D.7: Example countsheet for Gamma1-triggered events measured with the PbGl in d + Au collisions.



pi0dAu_gamma1_scan56_pid0_Sum1_bins32_rebin2_nSigEx3.0_W0_W1_W2_W0W1W2_date061003

bin: 31 - 32

pT-range: 7.50 < pT < 8.00

number of pi0s: 160.0 ± 13.1 (13.1 stat, 0.5 sys)

bckgd, unscaled (bu): 4

(stat² = sig + bu*bsf + bsfE²*bu² + bsf²*bu)

integration region: 0.1043 < Minv < 0.1734

normalization region: 0.050 < Minv < 0.099 && 0.185 < Minv < 0.323

Figure D.8: Example countsheet for Gamma1-triggered events measured with the PbSc in d + Au collisions.

E. Conversion Studies

	Material budget in front of EMCal (% X_0)							
	MVD+air+DC	PC1	RICH	PC2+air	TEC	PC3	TOF	total
Run 2								
PbSc (W)	0.28% + 0.8% + 0.66%			2.4% + 0.3%	—		—	10.2%
PbSc (E)	$\approx 1.8\%$	1.2%	2.1%	—	0.8%	2.4%	—	8.3%
PbGl (E)				—			6%	14.3%
Run 3								
PbSc (W)	1.8%			2.7%	—		—	8.3%
PbSc (E)		1.2%	2.1%	—	6.4%	2.4%	—	13.9%
PbGl (E)				—			6%	19.9%

Table E.1: Radiation length of material in front of the EMCal.

F. Results of the Glauber Calculations

Centrality Class	N_{part}	N_{coll}	T_{AB} (mb $^{-1}$)
0 – 5%	351.4 ± 2.9	1065.4 ± 105.3	25.37 ± 1.77
0 – 10%	325.2 ± 3.3	955.4 ± 93.6	22.75 ± 1.56
0 – 92%	109.1 ± 4.1	257.8 ± 25.4	6.14 ± 0.45
5 – 10%	299.0 ± 3.8	845.4 ± 82.1	20.13 ± 1.36
10 – 15%	253.9 ± 4.3	672.4 ± 66.8	16.01 ± 1.15
10 – 20%	234.6 ± 4.7	602.6 ± 59.3	14.35 ± 1.00
15 – 20%	215.3 ± 5.3	532.7 ± 52.1	12.68 ± 0.86
20 – 30%	166.6 ± 5.4	373.8 ± 39.6	8.90 ± 0.72
20 – 60%	100.2 ± 3.4	193.7 ± 19.1	4.61 ± 0.36
30 – 40%	114.2 ± 4.4	219.8 ± 22.6	5.23 ± 0.44
40 – 50%	74.4 ± 3.8	120.3 ± 13.7	2.86 ± 0.28
50 – 60%	45.5 ± 3.3	61.0 ± 9.9	1.45 ± 0.23
60 – 70%	25.7 ± 3.8	28.5 ± 7.6	0.68 ± 0.18
60 – 80%	19.5 ± 3.3	20.4 ± 5.9	0.49 ± 0.14
70 – 80%	13.4 ± 3.0	12.4 ± 4.2	0.30 ± 0.10
70 – 92%	9.5 ± 1.9	8.3 ± 2.4	0.20 ± 0.06
80 – 92%	6.3 ± 1.2	4.9 ± 1.2	0.12 ± 0.03

Table F.1: The different centrality classes used in the analysis, together with the results from the Glauber calculation [Rey03b].

G. NLO pQCD results for direct photons in p + p collisions

For the comparison of the direct photon production in Au + Au to the expectation solely from hard scattering a NLO pQCD calculation of p + p collisions is used [Vog04a]. The calculation is the same as already employed for the comparison with the invariant cross section for the π^0 production in p + p collisions measured in PHENIX [Adl03c]. In particular, the employed parameter set is the same that showed the best agreement with the π^0 measurement: factorization, renormalization, and fragmentation scale $\mu = p_T$ and parton distribution functions from [Pum02] (CTEQ06M). The parton fragmentation into photons is given by the fragmentation functions from Gück, Reya, and Vogt [Glu93]. We provide the invariant cross section for direct photon production in p + p collisions at $\sqrt{s} = 200$ GeV calculated for three different scales: $2p_T$, p_T and $p_T/2$. The cross section is divided into the contribution from photons directly produced in hard scatterings and in those from fragmentation of hard-scattered partons. To obtain the invariant yield, the cross section is divided by the total inelastic cross section for p + p at $\sqrt{s} = 200$ GeV of $\sigma_{in} = 42.2$ mb.

p_T (GeV/c)	$E \cdot \frac{d^3\sigma}{dp^3} \left(\frac{\text{mb}c^3}{\text{GeV}^2} \right)$		
	Total	Direct	Fragmentation
1.25	1.534E-01	3.357E-02	1.199E-01
1.75	2.793E-02	9.253E-03	1.867E-02
2.25	7.520E-03	3.057E-03	4.464E-03
2.75	2.589E-03	1.179E-03	1.410E-03
3.25	1.046E-03	5.148E-04	5.312E-04
3.75	4.740E-04	2.476E-04	2.264E-04
4.25	2.367E-04	1.287E-04	1.080E-04
4.75	1.263E-04	7.112E-05	5.518E-05
5.25	7.154E-05	4.136E-05	3.018E-05
5.75	4.247E-05	2.509E-05	1.738E-05
6.25	2.620E-05	1.576E-05	1.044E-05
6.75	1.674E-05	1.020E-05	6.534E-06
7.50	9.108E-06	5.654E-06	3.451E-06
8.50	4.252E-06	2.703E-06	1.548E-06
9.50	2.143E-06	1.387E-06	7.563E-07
11.00	8.774E-07	5.787E-07	2.987E-07
13.50	2.358E-07	1.599E-07	7.585E-08

Table G.1: Differential cross section for the direct photon production in p + p collisions from NLO pQCD ($\mu = p_T$).

p_T (GeV/c)	$E \cdot \frac{d^3\sigma}{dp^3} \left(\frac{\text{mb}c^3}{\text{GeV}^2} \right)$		
	Total	Direct	Fragmentation
1.25	1.250E-01	2.471E-02	1.003E-01
1.75	2.299E-02	6.912E-03	1.608E-02
2.25	6.167E-03	2.290E-03	3.877E-03
2.75	2.147E-03	8.911E-04	1.257E-03
3.25	8.761E-04	3.933E-04	4.827E-04
3.75	3.994E-04	1.907E-04	2.087E-04
4.25	2.002E-04	9.983E-05	1.003E-04
4.75	1.072E-04	5.552E-05	5.170E-05
5.25	6.052E-05	3.236E-05	2.816E-05
5.75	3.581E-05	1.969E-05	1.612E-05
6.25	2.205E-05	1.241E-05	9.636E-06
6.75	1.405E-05	8.048E-06	6.006E-06
7.50	7.645E-06	4.476E-06	3.172E-06
8.50	3.580E-06	2.146E-06	1.434E-06
9.50	1.798E-06	1.104E-06	6.944E-07
11.00	7.333E-07	4.618E-07	2.716E-07
13.50	1.970E-07	1.279E-07	6.903E-08

Table G.2: Differential cross section for the direct photon production in p + p collisions from NLO pQCD ($\mu = 2p_T$).

p_T (GeV/c)	$E \cdot \frac{d^3\sigma}{dp^3} \left(\frac{\text{mb}c^3}{\text{GeV}^2} \right)$		
	Total	Direct	Fragmentation
1.25	9.620E-01	5.126E-02	9.107E-01
1.75	5.330E-02	1.453E-02	3.877E-02
2.25	1.139E-02	4.875E-03	6.517E-03
2.75	3.597E-03	1.837E-03	1.759E-03
3.25	1.414E-03	7.959E-04	6.179E-04
3.75	6.288E-04	3.771E-04	2.517E-04
4.25	3.094E-04	1.927E-04	1.168E-04
4.75	1.636E-04	1.048E-04	5.879E-05
5.25	9.103E-05	5.995E-05	3.104E-05
5.75	5.345E-05	3.584E-05	1.761E-05
6.25	3.268E-05	2.222E-05	1.045E-05
6.75	2.071E-05	1.422E-05	6.484E-06
7.50	1.117E-05	7.768E-06	3.401E-06
8.50	5.161E-06	3.654E-06	1.508E-06
9.50	2.579E-06	1.848E-06	7.312E-07
11.00	1.056E-06	7.625E-07	2.929E-07
13.50	2.830E-07	2.074E-07	7.560E-08

Table G.3: Differential cross section for the direct photon production in p + p collisions from NLO pQCD ($\mu = p_T/2$).

H. Data Tables

H.1 π^0 Production in Au + Au Collisions

p_T (GeV/c)	$\frac{1}{2\pi p_T N_{\text{evt}}} \frac{d^2N}{dp_T dy} \left(\frac{c^3}{\text{GeV}^2} \right)$	Stat. error	Total syst. error	Syst. error A	Syst. error B	Syst. error C
1.25	3.751E+00	3.132E-01	7.408E-01	7.076E-01	1.903E-01	1.092E-01
1.75	6.816E-01	4.265E-02	1.053E-01	8.939E-02	5.195E-02	1.984E-02
2.25	1.323E-01	8.907E-03	2.257E-02	1.752E-02	1.370E-02	3.849E-03
2.75	2.804E-02	2.382E-03	5.434E-03	3.908E-03	3.686E-03	8.160E-04
3.25	7.987E-03	8.471E-04	1.635E-03	1.144E-03	1.145E-03	2.324E-04
3.75	2.428E-03	1.235E-04	4.419E-04	3.133E-04	3.034E-04	7.066E-05
4.25	8.285E-04	5.664E-05	1.569E-04	1.072E-04	1.121E-04	2.411E-05
4.75	3.332E-04	2.850E-05	6.559E-05	4.510E-05	4.662E-05	9.695E-06
5.25	1.498E-04	1.483E-05	2.905E-05	1.952E-05	2.106E-05	4.359E-06
5.75	5.510E-05	8.282E-06	1.118E-05	7.903E-06	7.750E-06	1.603E-06
6.25	3.240E-05	5.469E-06	6.260E-06	4.186E-06	4.558E-06	9.430E-07
6.75	1.456E-05	3.353E-06	2.820E-06	1.891E-06	2.049E-06	4.238E-07
7.25	9.319E-06	2.556E-06	1.802E-06	1.206E-06	1.311E-06	2.712E-07
7.75	6.724E-06	2.118E-06	1.299E-06	8.687E-07	9.459E-07	1.957E-07
8.50	3.841E-06	1.249E-06	7.334E-07	5.130E-07	5.120E-07	1.118E-07
9.50	9.167E-07	6.482E-07	1.720E-07	1.181E-07	1.222E-07	2.667E-08

Table H.1: π^0 production in Au + Au collisions measured with the PbG1 (centrality 0-10%).

p_T (GeV/c)	$\frac{1}{2\pi p_T N_{evt}} \frac{d^2N}{dp_T dy} \left(\frac{c^3}{\text{GeV}^2} \right)$	Stat. error	Total syst. error	Syst. error A	Syst. error B	Syst. error C
1.25	2.197E+00	2.132E-01	4.173E-01	4.028E-01	1.093E-01	6.393E-02
1.75	4.667E-01	2.551E-02	6.967E-02	6.033E-02	3.484E-02	1.358E-02
2.25	9.146E-02	5.733E-03	1.547E-02	1.238E-02	9.278E-03	2.662E-03
2.75	2.179E-02	1.776E-03	4.095E-03	2.990E-03	2.797E-03	6.341E-04
3.25	5.104E-03	5.616E-04	9.713E-04	6.791E-04	6.944E-04	1.485E-04
3.75	1.888E-03	9.312E-05	3.276E-04	2.438E-04	2.189E-04	5.493E-05
4.25	6.739E-04	3.892E-05	1.229E-04	8.685E-05	8.690E-05	1.961E-05
4.75	2.641E-04	2.068E-05	4.924E-05	3.424E-05	3.539E-05	7.686E-06
5.25	1.222E-04	1.248E-05	2.281E-05	1.579E-05	1.645E-05	3.555E-06
5.75	6.090E-05	7.325E-06	1.223E-05	9.063E-06	8.206E-06	1.772E-06
6.25	2.487E-05	4.496E-06	4.711E-06	3.311E-06	3.351E-06	7.236E-07
6.75	8.634E-06	2.912E-06	1.720E-06	1.267E-06	1.163E-06	2.512E-07
7.25	8.255E-06	2.859E-06	1.602E-06	1.153E-06	1.112E-06	2.402E-07
7.75	3.355E-06	1.541E-06	6.341E-07	4.447E-07	4.521E-07	9.762E-08
8.50	1.621E-06	7.249E-07	3.026E-07	2.089E-07	2.190E-07	4.717E-08
9.50	7.961E-07	5.629E-07	1.486E-07	1.026E-07	1.075E-07	2.317E-08

Table H.2: π^0 production in Au + Au collisions measured with the PbGl (centrality 10-20%).

p_T (GeV/c)	$\frac{1}{2\pi p_T N_{evt}} \frac{d^2N}{dp_T dy} \left(\frac{c^3}{\text{GeV}^2} \right)$	Stat. error	Total syst. error	Syst. error A	Syst. error B	Syst. error C
1.25	1.701E+00	1.337E-01	2.605E-01	2.365E-01	9.737E-02	4.950E-02
1.75	3.098E-01	1.671E-02	4.781E-02	4.000E-02	2.458E-02	9.016E-03
2.25	6.290E-02	4.106E-03	1.068E-02	8.464E-03	6.248E-03	1.830E-03
2.75	1.515E-02	1.200E-03	2.732E-03	2.035E-03	1.769E-03	4.407E-04
3.25	4.770E-03	4.257E-04	9.684E-04	7.361E-04	6.136E-04	1.388E-04
3.75	1.236E-03	6.555E-05	2.307E-04	1.592E-04	1.630E-04	3.597E-05
4.25	5.178E-04	3.076E-05	9.808E-05	6.675E-05	7.027E-05	1.507E-05
4.75	1.980E-04	1.684E-05	3.770E-05	2.551E-05	2.715E-05	5.761E-06
5.25	1.045E-04	1.025E-05	2.079E-05	1.473E-05	1.436E-05	3.042E-06
5.75	3.332E-05	5.615E-06	6.355E-06	4.300E-06	4.578E-06	9.695E-07
6.25	1.984E-05	4.318E-06	3.848E-06	2.653E-06	2.727E-06	5.774E-07
6.75	1.137E-05	2.851E-06	2.171E-06	1.471E-06	1.562E-06	3.307E-07
7.25	6.289E-06	1.978E-06	1.200E-06	8.118E-07	8.643E-07	1.830E-07
7.75	1.365E-06	1.142E-06	4.688E-07	4.278E-07	1.876E-07	3.972E-08
8.50	1.947E-06	7.948E-07	4.231E-07	3.312E-07	2.572E-07	5.665E-08
9.50	7.852E-07	5.552E-07	1.467E-07	1.012E-07	1.037E-07	2.285E-08

Table H.3: π^0 production in Au + Au collisions measured with the PbGl (centrality 20-30%).

p_T (GeV/c)	$\frac{1}{2\pi p_T N_{\text{evt}}} \frac{d^2N}{dp_T dy} \left(\frac{c^3}{\text{GeV}^2} \right)$	Stat. error	Total syst. error	Syst. error A	Syst. error B	Syst. error C
1.25	1.146E+00	8.430E-02	2.035E-01	1.857E-01	7.642E-02	3.334E-02
1.75	1.847E-01	1.051E-02	2.954E-02	2.453E-02	1.554E-02	5.376E-03
2.25	3.884E-02	2.538E-03	6.496E-03	5.162E-03	3.778E-03	1.130E-03
2.75	9.749E-03	7.715E-04	1.666E-03	1.266E-03	1.046E-03	2.837E-04
3.25	3.189E-03	2.703E-04	6.076E-04	4.645E-04	3.804E-04	9.280E-05
3.75	9.213E-04	4.719E-05	1.745E-04	1.187E-04	1.250E-04	2.681E-05
4.25	3.493E-04	2.294E-05	6.613E-05	4.503E-05	4.735E-05	1.017E-05
4.75	1.588E-04	1.340E-05	3.035E-05	2.106E-05	2.135E-05	4.622E-06
5.25	4.762E-05	7.717E-06	9.256E-06	6.547E-06	6.395E-06	1.386E-06
5.75	3.376E-05	5.129E-06	6.402E-06	4.413E-06	4.532E-06	9.823E-07
6.25	1.354E-05	3.165E-06	2.728E-06	1.995E-06	1.819E-06	3.942E-07
6.75	1.015E-05	2.762E-06	2.234E-06	1.746E-06	1.363E-06	2.954E-07
7.25	2.958E-06	1.323E-06	5.571E-07	3.811E-07	3.972E-07	8.608E-08
7.75	3.400E-06	1.388E-06	6.405E-07	4.381E-07	4.566E-07	9.895E-08

Table H.4: π^0 production in Au + Au collisions measured with the PbG1 (centrality 30-40%).

p_T (GeV/c)	$\frac{1}{2\pi p_T N_{\text{evt}}} \frac{d^2N}{dp_T dy} \left(\frac{c^3}{\text{GeV}^2} \right)$	Stat. error	Total syst. error	Syst. error A	Syst. error B	Syst. error C
1.25	6.874E-01	5.212E-02	1.054E-01	9.516E-02	4.054E-02	2.000E-02
1.75	1.257E-01	6.352E-03	2.011E-02	1.701E-02	1.008E-02	3.656E-03
2.25	2.418E-02	1.471E-03	4.068E-03	3.218E-03	2.387E-03	7.037E-04
2.75	7.001E-03	4.912E-04	1.332E-03	1.047E-03	7.981E-04	2.037E-04
3.25	1.632E-03	1.674E-04	3.114E-04	2.336E-04	2.003E-04	4.748E-05
3.75	7.076E-04	3.747E-05	1.302E-04	9.135E-05	9.050E-05	2.059E-05
4.25	1.859E-04	1.606E-05	3.496E-05	2.397E-05	2.487E-05	5.411E-06
4.75	9.765E-05	1.015E-05	1.851E-05	1.266E-05	1.321E-05	2.842E-06
5.25	3.457E-05	5.771E-06	6.543E-06	4.457E-06	4.683E-06	1.006E-06
5.75	1.967E-05	3.801E-06	3.725E-06	2.538E-06	2.666E-06	5.725E-07
6.25	1.317E-05	2.809E-06	2.493E-06	1.697E-06	1.785E-06	3.834E-07
6.75	6.719E-06	1.940E-06	1.272E-06	8.657E-07	9.105E-07	1.955E-07
7.25	2.783E-06	1.245E-06	5.267E-07	3.586E-07	3.771E-07	8.099E-08

Table H.5: π^0 production in Au + Au collisions measured with the PbG1 (centrality 40-50%).

p_T (GeV/c)	$\frac{1}{2\pi p_T N_{\text{evt}}} \frac{d^2N}{dp_T dy} \left(\frac{c^3}{\text{GeV}^2} \right)$	Stat. error	Total syst. error	Syst. error A	Syst. error B	Syst. error C
1.25	3.666E-01	2.903E-02	5.704E-02	5.084E-02	2.356E-02	1.067E-02
1.75	6.515E-02	3.492E-03	1.023E-02	8.533E-03	5.312E-03	1.896E-03
2.25	1.266E-02	8.576E-04	2.095E-03	1.681E-03	1.195E-03	3.683E-04
2.75	3.718E-03	2.815E-04	6.259E-04	4.869E-04	3.781E-04	1.082E-04
3.25	1.197E-03	1.024E-04	2.196E-04	1.773E-04	1.249E-04	3.482E-05
3.75	4.060E-04	2.539E-05	7.568E-05	5.234E-05	5.338E-05	1.181E-05
4.25	1.405E-04	1.249E-05	2.788E-05	1.832E-05	2.062E-05	4.089E-06
4.75	5.558E-05	7.734E-06	1.104E-05	7.217E-06	8.202E-06	1.617E-06
5.25	2.018E-05	3.977E-06	3.998E-06	2.604E-06	2.977E-06	5.872E-07
5.75	1.019E-05	2.630E-06	2.220E-06	1.606E-06	1.503E-06	2.965E-07
6.25	5.371E-06	2.219E-06	1.067E-06	6.969E-07	7.922E-07	1.563E-07
6.75	4.041E-06	1.527E-06	8.002E-07	5.207E-07	5.961E-07	1.176E-07

Table H.6: π^0 production in Au + Au collisions measured with the PbGl (centrality 50-60%).

p_T (GeV/c)	$\frac{1}{2\pi p_T N_{\text{evt}}} \frac{d^2N}{dp_T dy} \left(\frac{c^3}{\text{GeV}^2} \right)$	Stat. error	Total syst. error	Syst. error A	Syst. error B	Syst. error C
1.25	1.803E-01	1.513E-02	2.787E-02	2.520E-02	1.069E-02	5.246E-03
1.75	3.393E-02	2.113E-03	5.353E-03	4.504E-03	2.719E-03	9.874E-04
2.25	6.645E-03	4.620E-04	1.093E-03	8.564E-04	6.508E-04	1.934E-04
2.75	1.646E-03	1.519E-04	2.842E-04	2.128E-04	1.822E-04	4.790E-05
3.25	5.459E-04	5.574E-05	9.485E-05	7.242E-05	5.916E-05	1.588E-05
3.75	1.920E-04	1.663E-05	3.485E-05	2.626E-05	2.223E-05	5.587E-06
4.25	6.993E-05	8.667E-06	1.310E-05	9.025E-06	9.272E-06	2.035E-06
4.75	2.988E-05	5.000E-06	5.666E-06	3.859E-06	4.056E-06	8.696E-07
5.25	1.135E-05	4.434E-06	2.199E-06	1.529E-06	1.545E-06	3.304E-07
5.75	6.212E-06	2.071E-06	1.178E-06	8.004E-07	8.456E-07	1.808E-07

Table H.7: π^0 production in Au + Au collisions measured with the PbGl (centrality 60-70%).

p_T (GeV/c)	$\frac{1}{2\pi p_T N_{\text{evt}}} \frac{d^2N}{dp_T dy} \left(\frac{c^3}{\text{GeV}^2} \right)$	Stat. error	Total syst. error	Syst. error A	Syst. error B	Syst. error C
1.25	7.709E-02	6.524E-03	1.442E-02	1.330E-02	5.098E-03	2.243E-03
1.75	1.428E-02	9.769E-04	2.286E-03	1.925E-03	1.162E-03	4.156E-04
2.25	2.895E-03	2.224E-04	4.664E-04	3.731E-04	2.668E-04	8.423E-05
2.75	7.458E-04	6.753E-05	1.307E-04	1.055E-04	7.400E-05	2.170E-05
3.25	2.807E-04	3.210E-05	5.283E-05	4.134E-05	3.186E-05	8.167E-06
3.75	8.814E-05	1.132E-05	1.771E-05	1.137E-05	1.333E-05	2.565E-06
4.25	1.854E-05	6.219E-06	4.311E-06	3.155E-06	2.888E-06	5.396E-07
4.75	1.031E-05	6.195E-06	3.313E-06	2.899E-06	1.574E-06	3.000E-07

Table H.8: π^0 production in Au + Au collisions measured with the PbGl (centrality 70-80%).

p_T (GeV/c)	$\frac{1}{2\pi p_T N_{\text{evt}}} \frac{d^2N}{dp_T dy} \left(\frac{c^3}{\text{GeV}^2} \right)$	Stat. error	Total syst. error	Syst. error A	Syst. error B	Syst. error C
1.25	3.433E-02	6.984E-03	5.365E-03	4.785E-03	2.212E-03	9.991E-04
1.75	6.619E-03	9.990E-04	1.041E-03	8.762E-04	5.277E-04	1.926E-04
2.25	1.277E-03	2.201E-04	2.069E-04	1.673E-04	1.160E-04	3.716E-05
2.75	3.827E-04	7.167E-05	6.490E-05	5.172E-05	3.760E-05	1.114E-05
3.25	1.196E-04	2.582E-05	2.317E-05	1.913E-05	1.259E-05	3.481E-06
3.75	5.255E-05	7.992E-06	9.530E-06	6.810E-06	6.488E-06	1.529E-06
4.25	1.170E-05	3.870E-06	2.381E-06	1.812E-06	1.507E-06	3.405E-07
4.75	8.401E-06	2.498E-06	1.549E-06	1.084E-06	1.079E-06	2.445E-07

Table H.9: π^0 production in Au + Au collisions measured with the PbGl (centrality 80-92%).

p_T (GeV/c)	$\frac{1}{2\pi p_T N_{\text{evt}}} \frac{d^2N}{dp_T dy} \left(\frac{c^3}{\text{GeV}^2} \right)$	Stat. error	Total syst. error	Syst. error A	Syst. error B	Syst. error C
1.25	1.138E+00	4.500E-02	1.796E-01	1.639E-01	6.542E-02	3.311E-02
1.75	2.088E-01	5.692E-03	3.227E-02	2.690E-02	1.676E-02	6.076E-03
2.25	4.164E-02	1.312E-03	7.033E-03	5.501E-03	4.212E-03	1.212E-03
2.75	9.701E-03	3.774E-04	1.784E-03	1.327E-03	1.159E-03	2.823E-04
3.25	2.758E-03	1.299E-04	5.382E-04	3.938E-04	3.580E-04	8.025E-05
3.75	8.639E-04	1.984E-05	1.597E-04	1.113E-04	1.118E-04	2.514E-05
4.25	3.116E-04	9.007E-06	5.882E-05	4.016E-05	4.200E-05	9.067E-06
4.75	1.281E-04	4.847E-06	2.437E-05	1.651E-05	1.753E-05	3.728E-06
5.25	5.389E-05	2.740E-06	1.033E-05	7.037E-06	7.393E-06	1.568E-06
5.75	2.368E-05	1.604E-06	4.527E-06	3.076E-06	3.250E-06	6.891E-07
6.25	1.368E-05	1.063E-06	2.714E-06	1.919E-06	1.877E-06	3.981E-07
6.75	6.488E-06	7.336E-07	1.238E-06	8.396E-07	8.904E-07	1.888E-07
7.25	3.559E-06	5.392E-07	6.871E-07	4.721E-07	4.884E-07	1.036E-07
7.75	1.877E-06	3.718E-07	3.575E-07	2.419E-07	2.576E-07	5.462E-08
8.50	1.180E-06	2.257E-07	2.248E-07	1.527E-07	1.614E-07	3.434E-08
9.50	4.151E-07	1.384E-07	7.893E-08	5.349E-08	5.677E-08	1.208E-08
11.00	3.032E-07	6.957E-08	1.376E-07	1.297E-07	4.327E-08	1.552E-08

Table H.10: π^0 production in minimum bias Au + Au collisions measured with the PbGl.

p_T (GeV/c)	$\frac{1}{2\pi p_T N_{\text{evt}}} \frac{d^2N}{dp_T dy} \left(\frac{c^3}{\text{GeV}^2} \right)$	Stat. error	Total syst. error	Syst. error A	Syst. error B	Syst. error C
1.25	3.151E+00	1.735E-01	4.579E-01	4.244E-01	1.453E-01	9.171E-02
1.75	5.359E-01	2.131E-02	8.720E-02	7.835E-02	3.496E-02	1.560E-02
2.25	1.089E-01	4.828E-03	1.821E-02	1.538E-02	9.220E-03	3.170E-03
2.75	2.498E-02	1.430E-03	4.781E-03	3.967E-03	2.567E-03	7.270E-04
3.25	6.135E-03	4.968E-04	1.152E-03	9.247E-04	6.638E-04	1.785E-04
3.75	2.001E-03	6.390E-05	3.327E-04	2.583E-04	2.014E-04	5.822E-05
4.25	6.893E-04	2.840E-05	1.195E-04	8.986E-05	7.620E-05	2.006E-05
4.75	2.906E-04	1.484E-05	5.076E-05	3.754E-05	3.310E-05	8.457E-06
5.25	1.206E-04	6.851E-06	2.138E-05	1.595E-05	1.379E-05	3.510E-06
5.75	5.687E-05	4.368E-06	9.939E-06	7.328E-06	6.507E-06	1.655E-06
6.25	3.127E-05	2.787E-06	5.465E-06	4.030E-06	3.578E-06	9.100E-07
6.75	1.263E-05	1.003E-06	2.324E-06	1.629E-06	1.445E-06	8.129E-07
7.25	7.209E-06	7.299E-07	1.331E-06	9.341E-07	8.248E-07	4.682E-07
7.75	4.271E-06	5.731E-07	8.159E-07	5.821E-07	4.887E-07	2.966E-07
8.50	1.759E-06	2.302E-07	3.335E-07	2.369E-07	2.048E-07	1.147E-07
9.50	1.052E-06	1.405E-07	1.953E-07	1.355E-07	1.225E-07	6.912E-08
11.00	2.427E-07	4.874E-08	6.544E-08	5.702E-08	2.687E-08	1.758E-08
13.00	6.156E-08	2.052E-08	1.194E-08	7.931E-09	6.814E-09	5.758E-09

Table H.11: π^0 production in Au + Au collisions measured with the PbSc (centrality 0-10%).

p_T (GeV/c)	$\frac{1}{2\pi p_T N_{\text{evt}}} \frac{d^2N}{dp_T dy} \left(\frac{c^3}{\text{GeV}^2} \right)$	Stat. error	Total syst. error	Syst. error A	Syst. error B	Syst. error C
1.25	1.821E+00	9.610E-02	5.247E-01	5.191E-01	7.633E-02	5.300E-02
1.75	3.695E-01	1.465E-02	5.370E-02	4.885E-02	2.230E-02	1.075E-02
2.25	8.294E-02	3.311E-03	1.269E-02	1.079E-02	6.680E-03	2.413E-03
2.75	1.860E-02	8.869E-04	3.040E-03	2.399E-03	1.867E-03	5.412E-04
3.25	4.560E-03	2.783E-04	7.671E-04	5.937E-04	4.858E-04	1.327E-04
3.75	1.611E-03	4.097E-05	2.637E-04	2.085E-04	1.615E-04	4.689E-05
4.25	5.827E-04	1.972E-05	9.972E-05	7.520E-05	6.549E-05	1.696E-05
4.75	1.927E-04	9.093E-06	3.350E-05	2.492E-05	2.239E-05	5.608E-06
5.25	9.641E-05	5.624E-06	1.678E-05	1.244E-05	1.125E-05	2.805E-06
5.75	4.026E-05	3.066E-06	7.012E-06	5.203E-06	4.701E-06	1.171E-06
6.25	2.117E-05	2.005E-06	3.684E-06	2.731E-06	2.472E-06	6.161E-07
6.75	1.227E-05	9.044E-07	2.244E-06	1.580E-06	1.433E-06	7.554E-07
7.25	6.042E-06	6.442E-07	1.128E-06	7.793E-07	7.057E-07	4.379E-07
7.75	3.517E-06	4.447E-07	6.374E-07	4.536E-07	4.108E-07	1.954E-07
8.50	1.674E-06	1.949E-07	3.108E-07	2.170E-07	1.920E-07	1.211E-07
9.50	6.505E-07	1.758E-07	1.216E-07	9.231E-08	7.465E-08	2.702E-08
11.00	1.767E-07	3.534E-08	3.302E-08	2.277E-08	2.177E-08	1.258E-08
13.00	1.962E-08	1.133E-08	3.558E-09	2.528E-09	2.417E-09	8.683E-10

Table H.12: π^0 production in Au + Au collisions measured with the PbSc (centrality 10-20%).

p_T (GeV/c)	$\frac{1}{2\pi p_T N_{\text{evt}}} \frac{d^2N}{dp_T dy} \left(\frac{c^3}{\text{GeV}^2} \right)$	Stat. error	Total syst. error	Syst. error A	Syst. error B	Syst. error C
1.25	1.391E+00	5.807E-02	2.097E-01	1.955E-01	6.429E-02	4.048E-02
1.75	2.656E-01	9.497E-03	3.912E-02	3.453E-02	1.667E-02	7.728E-03
2.25	5.667E-02	2.048E-03	8.703E-03	7.302E-03	4.439E-03	1.649E-03
2.75	1.378E-02	5.927E-04	2.249E-03	1.808E-03	1.277E-03	4.010E-04
3.25	3.854E-03	1.979E-04	6.667E-04	5.186E-04	4.038E-04	1.121E-04
3.75	1.218E-03	2.977E-05	2.061E-04	1.573E-04	1.284E-04	3.543E-05
4.25	4.424E-04	1.428E-05	7.483E-05	5.728E-05	4.640E-05	1.287E-05
4.75	1.759E-04	7.981E-06	2.977E-05	2.268E-05	1.859E-05	5.119E-06
5.25	7.324E-05	4.575E-06	1.242E-05	9.461E-06	7.752E-06	2.131E-06
5.75	4.141E-05	2.944E-06	7.027E-06	5.357E-06	4.385E-06	1.205E-06
6.25	1.849E-05	1.772E-06	3.130E-06	2.383E-06	1.958E-06	5.381E-07
6.75	8.947E-06	8.013E-07	1.592E-06	1.160E-06	9.473E-07	5.405E-07
7.25	4.818E-06	5.066E-07	8.768E-07	6.207E-07	5.101E-07	3.511E-07
7.75	2.948E-06	3.928E-07	5.436E-07	3.804E-07	3.122E-07	2.310E-07
8.50	1.398E-06	2.190E-07	2.560E-07	1.840E-07	1.543E-07	8.865E-08
9.50	6.372E-07	1.034E-07	1.163E-07	8.209E-08	7.032E-08	4.279E-08
11.00	1.908E-07	3.672E-08	3.570E-08	2.459E-08	2.262E-08	1.260E-08

Table H.13: π^0 production in Au + Au collisions measured with the PbSc (centrality 20-30%).

p_T (GeV/c)	$\frac{1}{2\pi p_T N_{\text{evt}}} \frac{d^2N}{dp_T dy} \left(\frac{c^3}{\text{GeV}^2} \right)$	Stat. error	Total syst. error	Syst. error A	Syst. error B	Syst. error C
1.25	9.450E-01	3.640E-02	1.330E-01	1.221E-01	4.509E-02	2.750E-02
1.75	1.681E-01	5.859E-03	2.472E-02	2.173E-02	1.071E-02	4.891E-03
2.25	3.743E-02	1.265E-03	5.746E-03	4.822E-03	2.928E-03	1.089E-03
2.75	9.218E-03	3.684E-04	1.493E-03	1.204E-03	8.416E-04	2.682E-04
3.25	2.545E-03	1.340E-04	4.288E-04	3.310E-04	2.623E-04	7.407E-05
3.75	8.230E-04	2.149E-05	1.380E-04	1.060E-04	8.496E-05	2.395E-05
4.25	3.091E-04	1.046E-05	5.143E-05	3.984E-05	3.126E-05	8.994E-06
4.75	1.221E-04	5.962E-06	2.035E-05	1.574E-05	1.240E-05	3.553E-06
5.25	5.815E-05	3.562E-06	9.698E-06	7.496E-06	5.915E-06	1.692E-06
5.75	2.891E-05	2.314E-06	4.924E-06	3.859E-06	2.941E-06	8.412E-07
6.25	9.517E-06	1.298E-06	1.599E-06	1.241E-06	9.683E-07	2.770E-07
6.75	6.462E-06	6.521E-07	1.147E-06	8.330E-07	6.575E-07	4.353E-07
7.25	3.918E-06	4.372E-07	7.032E-07	5.058E-07	3.987E-07	2.824E-07
7.75	1.706E-06	2.732E-07	2.952E-07	2.199E-07	1.736E-07	9.310E-08
8.50	1.097E-06	1.552E-07	1.980E-07	1.414E-07	1.145E-07	7.807E-08
9.50	4.811E-07	8.783E-08	8.495E-08	6.198E-08	5.020E-08	2.923E-08
11.00	1.594E-07	3.323E-08	2.873E-08	2.054E-08	1.853E-08	7.773E-09

Table H.14: π^0 production in Au + Au collisions measured with the PbSc (centrality 30-40%).

p_T (GeV/c)	$\frac{1}{2\pi p_T N_{\text{evt}}} \frac{d^2 N}{dp_T dy} \left(\frac{e^3}{\text{GeV}^2} \right)$	Stat. error	Total syst. error	Syst. error A	Syst. error B	Syst. error C
1.25	5.928E-01	2.203E-02	8.336E-02	7.638E-02	2.857E-02	1.725E-02
1.75	1.101E-01	3.599E-03	1.619E-02	1.421E-02	7.069E-03	3.204E-03
2.25	2.346E-02	7.555E-04	3.605E-03	3.024E-03	1.839E-03	6.828E-04
2.75	5.589E-03	2.183E-04	8.996E-04	7.284E-04	5.023E-04	1.626E-04
3.25	1.712E-03	7.820E-05	2.806E-04	2.229E-04	1.629E-04	4.982E-05
3.75	6.194E-04	1.636E-05	1.031E-04	8.001E-05	6.240E-05	1.802E-05
4.25	1.934E-04	7.619E-06	3.298E-05	2.493E-05	2.085E-05	5.629E-06
4.75	8.155E-05	4.253E-06	1.399E-05	1.052E-05	8.909E-06	2.373E-06
5.25	3.877E-05	2.647E-06	6.798E-06	5.190E-06	4.243E-06	1.128E-06
5.75	1.672E-05	1.687E-06	2.870E-06	2.156E-06	1.830E-06	4.866E-07
6.25	8.448E-06	1.140E-06	1.453E-06	1.094E-06	9.247E-07	2.458E-07
6.75	3.882E-06	4.292E-07	7.072E-07	5.002E-07	4.249E-07	2.636E-07
7.25	1.974E-06	2.980E-07	3.552E-07	2.544E-07	2.161E-07	1.214E-07
7.75	1.247E-06	3.490E-07	2.248E-07	1.621E-07	1.365E-07	7.492E-08
8.50	8.138E-07	1.218E-07	1.465E-07	1.054E-07	8.434E-08	5.709E-08
9.50	1.831E-07	5.659E-08	3.271E-08	2.360E-08	1.898E-08	1.236E-08
11.00	1.015E-07	2.538E-08	1.895E-08	1.308E-08	1.179E-08	7.000E-09

Table H.15: π^0 production in Au + Au collisions measured with the PbSc (centrality 40-50%).

p_T (GeV/c)	$\frac{1}{2\pi p_T N_{\text{evt}}} \frac{d^2 N}{dp_T dy} \left(\frac{e^3}{\text{GeV}^2} \right)$	Stat. error	Total syst. error	Syst. error A	Syst. error B	Syst. error C
1.25	3.441E-01	1.190E-02	5.104E-02	4.690E-02	1.745E-02	1.001E-02
1.75	5.698E-02	1.966E-03	8.395E-03	7.344E-03	3.714E-03	1.658E-03
2.25	1.276E-02	4.201E-04	1.959E-03	1.653E-03	9.828E-04	3.713E-04
2.75	3.506E-03	1.349E-04	5.744E-04	4.786E-04	3.008E-04	1.020E-04
3.25	9.974E-04	4.812E-05	1.610E-04	1.299E-04	9.059E-05	2.902E-05
3.75	3.467E-04	1.108E-05	5.782E-05	4.476E-05	3.519E-05	1.009E-05
4.25	1.265E-04	5.708E-06	2.163E-05	1.636E-05	1.366E-05	3.683E-06
4.75	5.203E-05	3.240E-06	9.003E-06	6.843E-06	5.650E-06	1.514E-06
5.25	2.224E-05	2.023E-06	3.806E-06	2.868E-06	2.416E-06	6.471E-07
5.75	9.945E-06	1.284E-06	1.701E-06	1.281E-06	1.081E-06	2.894E-07
6.25	6.173E-06	9.476E-07	1.066E-06	8.094E-07	6.709E-07	1.796E-07
6.75	3.433E-06	4.104E-07	6.274E-07	4.424E-07	3.731E-07	2.423E-07
7.25	1.683E-06	3.487E-07	4.070E-07	3.429E-07	1.829E-07	1.210E-07
7.75	1.107E-06	2.093E-07	2.010E-07	1.427E-07	1.203E-07	7.455E-08
8.50	3.206E-07	7.556E-08	5.789E-08	4.130E-08	3.607E-08	1.855E-08
9.50	1.855E-07	5.354E-08	3.349E-08	2.389E-08	2.087E-08	1.073E-08

Table H.16: π^0 production in Au + Au collisions measured with the PbSc (centrality 50-60%).

p_T (GeV/c)	$\frac{1}{2\pi p_T N_{\text{evt}}} \frac{d^2N}{dp_T dy} \left(\frac{c^3}{\text{GeV}^2} \right)$	Stat. error	Total syst. error	Syst. error A	Syst. error B	Syst. error C
1.25	1.741E-01	6.383E-03	2.549E-02	2.347E-02	8.570E-03	5.065E-03
1.75	2.988E-02	9.837E-04	4.496E-03	3.955E-03	1.954E-03	8.695E-04
2.25	6.228E-03	2.481E-04	9.603E-04	8.027E-04	4.949E-04	1.812E-04
2.75	1.676E-03	7.934E-05	2.683E-04	2.174E-04	1.496E-04	4.878E-05
3.25	4.771E-04	2.702E-05	7.593E-05	6.202E-05	4.154E-05	1.388E-05
3.75	1.736E-04	7.128E-06	2.854E-05	2.241E-05	1.693E-05	5.052E-06
4.25	6.568E-05	4.051E-06	1.145E-05	8.486E-06	7.440E-06	1.911E-06
4.75	2.257E-05	2.308E-06	3.971E-06	2.914E-06	2.616E-06	6.569E-07
5.25	1.250E-05	1.577E-06	2.207E-06	1.621E-06	1.453E-06	3.639E-07
5.75	2.998E-06	1.607E-06	6.183E-07	5.034E-07	3.484E-07	8.723E-08
6.25	3.013E-06	6.283E-07	5.301E-07	3.882E-07	3.501E-07	8.768E-08
6.75	1.635E-06	2.847E-07	3.012E-07	2.107E-07	1.901E-07	1.011E-07
7.25	7.099E-07	1.833E-07	1.336E-07	9.147E-08	8.250E-08	5.164E-08
7.75	4.783E-07	1.442E-07	8.948E-08	6.162E-08	5.558E-08	3.347E-08
8.50	1.777E-07	5.619E-08	3.272E-08	2.290E-08	2.014E-08	1.185E-08

Table H.17: π^0 production in Au + Au collisions measured with the PbSc (centrality 60-70%).

p_T (GeV/c)	$\frac{1}{2\pi p_T N_{\text{evt}}} \frac{d^2N}{dp_T dy} \left(\frac{c^3}{\text{GeV}^2} \right)$	Stat. error	Total syst. error	Syst. error A	Syst. error B	Syst. error C
1.25	7.417E-02	2.770E-03	1.145E-02	1.045E-02	4.159E-03	2.158E-03
1.75	1.216E-02	4.479E-04	1.813E-03	1.575E-03	8.255E-04	3.540E-04
2.25	2.445E-03	1.168E-04	3.782E-04	3.212E-04	1.865E-04	7.114E-05
2.75	7.330E-04	3.675E-05	1.163E-04	9.736E-05	5.997E-05	2.133E-05
3.25	2.324E-04	1.516E-05	3.711E-05	3.032E-05	2.031E-05	6.764E-06
3.75	7.000E-05	4.464E-06	1.175E-05	9.052E-06	7.208E-06	2.037E-06
4.25	3.001E-05	2.709E-06	5.108E-06	3.866E-06	3.222E-06	8.732E-07
4.75	1.353E-05	1.596E-06	2.300E-06	1.744E-06	1.447E-06	3.938E-07
5.25	4.066E-06	9.022E-07	7.382E-07	5.851E-07	4.342E-07	1.183E-07
5.75	2.304E-06	5.949E-07	3.913E-07	2.969E-07	2.460E-07	6.705E-08
6.25	1.938E-06	5.003E-07	3.291E-07	2.497E-07	2.069E-07	5.639E-08
6.75	5.403E-07	1.629E-07	9.800E-08	6.962E-08	5.769E-08	3.781E-08
7.25	5.157E-07	1.489E-07	9.260E-08	6.644E-08	5.506E-08	3.362E-08
7.75	1.226E-07	7.078E-08	2.416E-08	1.580E-08	1.309E-08	1.277E-08

Table H.18: π^0 production in Au + Au collisions measured with the PbSc (centrality 70-80%).

p_T (GeV/c)	$\frac{1}{2\pi p_T N_{\text{evt}}} \frac{d^2N}{dp_T dy} \left(\frac{c^3}{\text{GeV}^2} \right)$	Stat. error	Total syst. error	Syst. error A	Syst. error B	Syst. error C
1.25	3.432E-02	2.912E-03	4.948E-03	4.522E-03	1.743E-03	9.987E-04
1.75	5.572E-03	4.658E-04	8.437E-04	7.422E-04	3.669E-04	1.621E-04
2.25	1.374E-03	1.278E-04	2.168E-04	1.839E-04	1.076E-04	3.998E-05
2.75	2.966E-04	3.746E-05	4.716E-05	3.847E-05	2.587E-05	8.632E-06
3.25	1.019E-04	1.464E-05	1.731E-05	1.467E-05	8.707E-06	2.965E-06
3.75	3.836E-05	3.215E-06	6.471E-06	5.391E-06	3.400E-06	1.116E-06
4.25	1.363E-05	1.851E-06	2.354E-06	1.879E-06	1.362E-06	3.966E-07
4.75	6.136E-06	1.005E-06	1.028E-06	7.946E-07	6.269E-07	1.786E-07
5.25	3.366E-06	7.723E-07	5.680E-07	4.406E-07	3.447E-07	9.795E-08
5.75	1.131E-06	4.354E-07	2.270E-07	1.924E-07	1.159E-07	3.291E-08

Table H.19: π^0 production in Au + Au collisions measured with the PbSc (centrality 80-92%).

p_T (GeV/c)	$\frac{1}{2\pi p_T N_{\text{evt}}} \frac{d^2N}{dp_T dy} \left(\frac{c^3}{\text{GeV}^2} \right)$	Stat. error	Total syst. error	Syst. error A	Syst. error B	Syst. error C
1.25	9.919E-01	2.091E-02	1.417E-01	1.306E-01	4.688E-02	2.886E-02
1.75	1.728E-01	3.206E-03	2.547E-02	2.231E-02	1.122E-02	5.028E-03
2.25	3.694E-02	6.850E-04	5.758E-03	4.784E-03	3.019E-03	1.075E-03
2.75	8.683E-03	1.972E-04	1.439E-03	1.141E-03	8.387E-04	2.527E-04
3.25	2.282E-03	6.409E-05	3.827E-04	2.951E-04	2.345E-04	6.640E-05
3.75	7.709E-04	9.174E-06	1.282E-04	9.940E-05	7.772E-05	2.243E-05
4.25	2.792E-04	4.319E-06	4.765E-05	3.605E-05	3.008E-05	8.125E-06
4.75	1.088E-04	2.276E-06	1.871E-05	1.403E-05	1.197E-05	3.165E-06
5.25	4.799E-05	1.243E-06	8.263E-06	6.188E-06	5.295E-06	1.396E-06
5.75	2.227E-05	7.732E-07	3.834E-06	2.870E-06	2.458E-06	6.480E-07
6.25	1.131E-05	4.953E-07	1.948E-06	1.459E-06	1.249E-06	3.291E-07
6.75	5.790E-06	2.033E-07	1.051E-06	7.466E-07	6.392E-07	3.720E-07
7.25	3.204E-06	1.413E-07	5.970E-07	4.260E-07	3.537E-07	2.232E-07
7.75	1.717E-06	1.081E-07	3.149E-07	2.246E-07	1.895E-07	1.129E-07
8.50	8.424E-07	4.739E-08	1.548E-07	1.086E-07	9.453E-08	5.673E-08
9.50	3.817E-07	2.946E-08	6.960E-08	4.931E-08	4.283E-08	2.404E-08
11.00	9.906E-08	1.012E-08	1.905E-08	1.277E-08	1.259E-08	6.426E-09
13.00	2.281E-08	4.033E-09	4.354E-09	2.939E-09	2.900E-09	1.382E-09
15.00	7.780E-09	2.460E-09	1.556E-09	1.002E-09	9.889E-10	6.623E-10

Table H.20: π^0 production in minimum bias Au + Au collisions measured with the PbSc.

p_T (GeV/c)	$\frac{1}{2\pi p_T N_{\text{evt}}} \frac{d^2N}{dp_T dy} \left(\frac{c^3}{\text{GeV}^2} \right)$	Stat. error	Total syst. error	Syst. error A	Syst. error B	Syst. error C
1.25	3.314E+00	1.500E-01	3.774E-01	3.542E-01	1.111E-01	6.818E-02
1.75	5.920E-01	2.097E-02	6.723E-02	5.923E-02	2.935E-02	1.226E-02
2.25	1.177E-01	4.506E-03	1.403E-02	1.149E-02	7.676E-03	2.422E-03
2.75	2.625E-02	1.300E-03	3.571E-03	2.804E-03	2.144E-03	5.401E-04
3.25	6.722E-03	4.263E-04	9.190E-04	7.054E-04	5.726E-04	1.383E-04
3.75	2.151E-03	6.033E-05	2.616E-04	1.964E-04	1.671E-04	4.427E-05
4.25	7.382E-04	2.734E-05	9.354E-05	6.787E-05	6.255E-05	1.519E-05
4.75	3.057E-04	1.413E-05	3.951E-05	2.840E-05	2.674E-05	6.289E-06
5.25	1.300E-04	6.717E-06	1.680E-05	1.210E-05	1.134E-05	2.675E-06
5.75	5.620E-05	4.392E-06	7.389E-06	5.347E-06	4.967E-06	1.156E-06
6.25	3.167E-05	2.760E-06	4.064E-06	2.888E-06	2.784E-06	6.517E-07
6.75	1.311E-05	1.244E-06	1.729E-06	1.198E-06	1.127E-06	5.342E-07
7.25	7.612E-06	8.099E-07	1.003E-06	6.972E-07	6.452E-07	3.218E-07
7.75	4.612E-06	5.578E-07	6.239E-07	4.413E-07	3.861E-07	2.131E-07
8.50	1.759E-06	2.302E-07	3.335E-07	2.369E-07	2.048E-07	1.147E-07
9.50	1.052E-06	1.405E-07	1.953E-07	1.355E-07	1.225E-07	6.912E-08
11.00	2.427E-07	4.874E-08	6.544E-08	5.702E-08	2.687E-08	1.758E-08
13.00	6.156E-08	2.052E-08	1.194E-08	7.931E-09	6.814E-09	5.758E-09

Table H.21: Combined result for π^0 production in Au + Au collisions (centrality 0-10%).

p_T (GeV/c)	$\frac{1}{2\pi p_T N_{\text{evt}}} \frac{d^2N}{dp_T dy} \left(\frac{c^3}{\text{GeV}^2} \right)$	Stat. error	Total syst. error	Syst. error A	Syst. error B	Syst. error C
1.25	2.033E+00	1.162E-01	3.418E-01	3.352E-01	6.686E-02	4.184E-02
1.75	4.045E-01	1.369E-02	4.402E-02	3.934E-02	1.976E-02	8.323E-03
2.25	8.624E-02	3.048E-03	9.725E-03	8.060E-03	5.441E-03	1.774E-03
2.75	1.967E-02	8.502E-04	2.392E-03	1.833E-03	1.537E-03	4.047E-04
3.25	4.748E-03	2.733E-04	5.915E-04	4.405E-04	3.948E-04	9.770E-05
3.75	1.716E-03	4.420E-05	2.033E-04	1.570E-04	1.292E-04	3.532E-05
4.25	6.177E-04	1.946E-05	7.666E-05	5.634E-05	5.198E-05	1.271E-05
4.75	2.139E-04	9.867E-06	3.013E-05	2.194E-05	2.065E-05	4.805E-06
5.25	1.046E-04	5.547E-06	1.317E-05	9.547E-06	9.071E-06	2.152E-06
5.75	4.488E-05	3.563E-06	7.308E-06	5.421E-06	4.901E-06	1.219E-06
6.25	2.225E-05	1.986E-06	2.811E-06	2.049E-06	1.925E-06	4.579E-07
6.75	1.104E-05	1.601E-06	1.472E-06	1.055E-06	9.612E-07	4.229E-07
7.25	6.343E-06	7.246E-07	8.416E-07	5.852E-07	5.354E-07	3.074E-07
7.75	3.488E-06	5.560E-07	4.505E-07	3.197E-07	2.965E-07	1.295E-07
8.50	1.674E-06	1.949E-07	3.108E-07	2.170E-07	1.920E-07	1.211E-07
9.50	6.505E-07	1.758E-07	1.216E-07	9.231E-08	7.465E-08	2.702E-08
11.00	1.767E-07	3.534E-08	3.302E-08	2.277E-08	2.177E-08	1.258E-08
13.00	1.962E-08	1.133E-08	3.558E-09	2.528E-09	2.417E-09	8.683E-10

Table H.22: Combined result for π^0 production in Au + Au collisions (centrality 10-20%).

p_T (GeV/c)	$\frac{1}{2\pi p_T N_{evt}} \frac{d^2N}{dp_T dy} \left(\frac{c^3}{\text{GeV}^2} \right)$	Stat. error	Total syst. error	Syst. error A	Syst. error B	Syst. error C
1.25	1.501E+00	6.117E-02	1.610E-01	1.486E-01	5.352E-02	3.089E-02
1.75	2.827E-01	8.736E-03	3.000E-02	2.592E-02	1.392E-02	5.817E-03
2.25	5.903E-02	2.056E-03	6.675E-03	5.470E-03	3.627E-03	1.215E-03
2.75	1.430E-02	6.001E-04	1.718E-03	1.338E-03	1.036E-03	2.942E-04
3.25	4.130E-03	1.903E-04	5.332E-04	4.113E-04	3.286E-04	8.499E-05
3.75	1.225E-03	3.411E-05	1.533E-04	1.118E-04	1.019E-04	2.522E-05
4.25	4.691E-04	1.455E-05	5.859E-05	4.289E-05	3.873E-05	9.653E-06
4.75	1.838E-04	8.128E-06	2.302E-05	1.675E-05	1.532E-05	3.782E-06
5.25	8.093E-05	4.886E-06	1.188E-05	8.864E-06	7.673E-06	1.952E-06
5.75	3.780E-05	3.325E-06	4.795E-06	3.454E-06	3.233E-06	7.777E-07
6.25	1.887E-05	1.879E-06	2.355E-06	1.737E-06	1.542E-06	3.883E-07
6.75	9.427E-06	9.166E-07	1.204E-06	8.637E-07	7.521E-07	3.708E-07
7.25	5.054E-06	5.672E-07	6.556E-07	4.606E-07	3.987E-07	2.422E-07
7.75	2.588E-06	8.584E-07	4.752E-07	3.870E-07	2.347E-07	1.448E-07
8.50	1.398E-06	2.190E-07	2.560E-07	1.840E-07	1.543E-07	8.865E-08
9.50	6.372E-07	1.034E-07	1.163E-07	8.209E-08	7.032E-08	4.279E-08
11.00	1.908E-07	3.672E-08	3.570E-08	2.459E-08	2.262E-08	1.260E-08

Table H.23: Combined result for π^0 production in Au + Au collisions (centrality 20-30%).

p_T (GeV/c)	$\frac{1}{2\pi p_T N_{evt}} \frac{d^2N}{dp_T dy} \left(\frac{c^3}{\text{GeV}^2} \right)$	Stat. error	Total syst. error	Syst. error A	Syst. error B	Syst. error C
1.25	1.002E+00	3.604E-02	1.077E-01	9.859E-02	3.806E-02	2.061E-02
1.75	1.747E-01	5.547E-03	1.881E-02	1.614E-02	8.958E-03	3.594E-03
2.25	3.801E-02	1.329E-03	4.284E-03	3.509E-03	2.329E-03	7.822E-04
2.75	9.437E-03	3.959E-04	1.106E-03	8.693E-04	6.552E-04	1.942E-04
3.25	2.747E-03	1.252E-04	3.412E-04	2.625E-04	2.105E-04	5.652E-05
3.75	8.597E-04	2.281E-05	1.070E-04	7.834E-05	7.077E-05	1.769E-05
4.25	3.236E-04	1.094E-05	4.003E-05	2.949E-05	2.624E-05	6.658E-06
4.75	1.328E-04	5.754E-06	1.634E-05	1.220E-05	1.052E-05	2.732E-06
5.25	5.369E-05	4.376E-06	6.795E-06	5.034E-06	4.428E-06	1.105E-06
5.75	3.039E-05	2.305E-06	3.792E-06	2.851E-06	2.421E-06	6.253E-07
6.25	1.030E-05	1.166E-06	1.275E-06	9.756E-07	7.932E-07	2.120E-07
6.75	6.909E-06	6.541E-07	8.950E-07	6.589E-07	5.189E-07	3.124E-07
7.25	3.679E-06	6.333E-07	4.727E-07	3.356E-07	2.881E-07	1.667E-07
7.75	1.816E-06	2.566E-07	2.395E-07	1.773E-07	1.433E-07	7.332E-08
8.50	1.097E-06	1.552E-07	1.980E-07	1.414E-07	1.145E-07	7.807E-08
9.50	4.811E-07	8.783E-08	8.495E-08	6.198E-08	5.020E-08	2.923E-08
11.00	1.594E-07	3.323E-08	2.873E-08	2.054E-08	1.853E-08	7.773E-09

Table H.24: Combined result for π^0 production in Au + Au collisions (centrality 30-40%).

p_T (GeV/c)	$\frac{1}{2\pi p_T N_{\text{evt}}} \frac{d^2N}{dp_T dy} \left(\frac{c^3}{\text{GeV}^2} \right)$	Stat. error	Total syst. error	Syst. error A	Syst. error B	Syst. error C
1.25	6.259E-01	2.387E-02	6.425E-02	5.855E-02	2.311E-02	1.288E-02
1.75	1.161E-01	3.320E-03	1.249E-02	1.079E-02	5.806E-03	2.388E-03
2.25	2.377E-02	7.804E-04	2.688E-03	2.196E-03	1.471E-03	4.890E-04
2.75	6.010E-03	2.141E-04	7.235E-04	5.795E-04	4.152E-04	1.237E-04
3.25	1.679E-03	8.806E-05	2.082E-04	1.611E-04	1.273E-04	3.456E-05
3.75	6.522E-04	1.775E-05	7.986E-05	5.956E-05	5.148E-05	1.342E-05
4.25	1.902E-04	8.641E-06	2.398E-05	1.733E-05	1.611E-05	3.913E-06
4.75	8.677E-05	4.483E-06	1.090E-05	7.930E-06	7.259E-06	1.785E-06
5.25	3.704E-05	3.123E-06	4.746E-06	3.454E-06	3.165E-06	7.622E-07
5.75	1.755E-05	1.656E-06	2.194E-06	1.600E-06	1.457E-06	3.611E-07
6.25	9.369E-06	1.147E-06	1.313E-06	9.678E-07	8.604E-07	2.177E-07
6.75	4.202E-06	4.872E-07	6.266E-07	4.411E-07	3.859E-07	2.215E-07
7.25	2.059E-06	2.965E-07	2.635E-07	1.877E-07	1.638E-07	8.581E-08
7.75	9.640E-07	4.934E-07	1.376E-07	9.696E-08	8.998E-08	3.773E-08
8.50	8.138E-07	1.218E-07	1.465E-07	1.054E-07	8.434E-08	5.709E-08
9.50	1.831E-07	5.659E-08	3.271E-08	2.360E-08	1.898E-08	1.236E-08
11.00	1.015E-07	2.538E-08	1.895E-08	1.308E-08	1.179E-08	7.000E-09

Table H.25: Combined result for π^0 production in Au + Au collisions (centrality 40-50%).

p_T (GeV/c)	$\frac{1}{2\pi p_T N_{\text{evt}}} \frac{d^2N}{dp_T dy} \left(\frac{c^3}{\text{GeV}^2} \right)$	Stat. error	Total syst. error	Syst. error A	Syst. error B	Syst. error C
1.25	3.531E-01	1.420E-02	3.777E-02	3.428E-02	1.412E-02	7.266E-03
1.75	6.016E-02	1.827E-03	6.430E-03	5.517E-03	3.062E-03	1.238E-03
2.25	1.271E-02	4.606E-04	1.429E-03	1.178E-03	7.650E-04	2.616E-04
2.75	3.596E-03	1.458E-04	4.215E-04	3.412E-04	2.362E-04	7.400E-05
3.25	1.062E-03	4.720E-05	1.269E-04	1.024E-04	7.168E-05	2.185E-05
3.75	3.676E-04	1.174E-05	4.521E-05	3.354E-05	2.936E-05	7.564E-06
4.25	1.314E-04	5.938E-06	1.682E-05	1.205E-05	1.142E-05	2.704E-06
4.75	5.322E-05	3.583E-06	6.850E-06	4.928E-06	4.630E-06	1.095E-06
5.25	2.148E-05	2.123E-06	2.758E-06	1.959E-06	1.889E-06	4.419E-07
5.75	1.001E-05	1.237E-06	1.311E-06	9.731E-07	8.545E-07	2.060E-07
6.25	5.972E-06	1.039E-06	7.584E-07	5.522E-07	5.051E-07	1.229E-07
6.75	3.530E-06	4.652E-07	4.624E-07	3.216E-07	2.889E-07	1.641E-07
7.25	1.127E-06	8.451E-07	2.626E-07	2.031E-07	1.529E-07	6.563E-08
7.75	1.105E-06	2.343E-07	1.434E-07	1.007E-07	8.898E-08	5.004E-08
8.50	3.206E-07	7.556E-08	5.789E-08	4.130E-08	3.607E-08	1.855E-08
9.50	1.855E-07	5.354E-08	3.349E-08	2.389E-08	2.087E-08	1.073E-08

Table H.26: Combined result for π^0 production in Au + Au collisions (centrality 50-60%).

p_T (GeV/c)	$\frac{1}{2\pi p_T N_{\text{evt}}} \frac{d^2 N}{dp_T dy} \left(\frac{e^3}{\text{GeV}^2} \right)$	Stat. error	Total syst. error	Syst. error A	Syst. error B	Syst. error C
1.25	1.766E-01	7.557E-03	1.871E-02	1.709E-02	6.687E-03	3.634E-03
1.75	3.146E-02	1.037E-03	3.411E-03	2.948E-03	1.591E-03	6.473E-04
2.25	6.399E-03	2.446E-04	7.172E-04	5.832E-04	3.961E-04	1.317E-04
2.75	1.663E-03	8.265E-05	1.948E-04	1.523E-04	1.165E-04	3.423E-05
3.25	5.011E-04	2.682E-05	5.825E-05	4.639E-05	3.368E-05	1.031E-05
3.75	1.803E-04	7.884E-06	2.179E-05	1.683E-05	1.334E-05	3.711E-06
4.25	6.727E-05	4.288E-06	8.527E-06	6.143E-06	5.749E-06	1.384E-06
4.75	2.455E-05	2.139E-06	3.119E-06	2.240E-06	2.110E-06	5.051E-07
5.25	1.224E-05	1.886E-06	1.563E-06	1.132E-06	1.048E-06	2.518E-07
5.75	4.100E-06	1.510E-06	6.365E-07	4.934E-07	3.913E-07	9.227E-08
6.25	3.349E-06	6.426E-07	5.034E-07	3.652E-07	3.365E-07	8.249E-08
6.75	1.322E-06	7.306E-07	2.374E-07	1.645E-07	1.566E-07	6.888E-08
7.25	7.390E-07	1.632E-07	9.837E-08	6.733E-08	6.153E-08	3.686E-08
7.75	4.857E-07	1.382E-07	6.432E-08	4.425E-08	4.048E-08	2.324E-08
8.50	1.777E-07	5.619E-08	3.272E-08	2.290E-08	2.014E-08	1.185E-08
9.50	1.793E-07	5.408E-08	3.522E-08	2.311E-08	2.033E-08	1.712E-08

Table H.27: Combined result for π^0 production in Au + Au collisions (centrality 60-70%).

p_T (GeV/c)	$\frac{1}{2\pi p_T N_{\text{evt}}} \frac{d^2 N}{dp_T dy} \left(\frac{e^3}{\text{GeV}^2} \right)$	Stat. error	Total syst. error	Syst. error A	Syst. error B	Syst. error C
1.25	7.521E-02	3.124E-03	8.869E-03	8.132E-03	3.183E-03	1.548E-03
1.75	1.293E-02	4.620E-04	1.400E-03	1.201E-03	6.676E-04	2.660E-04
2.25	2.611E-03	1.111E-04	2.900E-04	2.409E-04	1.523E-04	5.373E-05
2.75	7.382E-04	3.628E-05	8.647E-05	7.122E-05	4.662E-05	1.519E-05
3.25	2.467E-04	1.446E-05	2.942E-05	2.366E-05	1.673E-05	5.077E-06
3.75	7.478E-05	4.531E-06	9.368E-06	6.833E-06	6.220E-06	1.539E-06
4.25	2.578E-05	4.738E-06	4.290E-06	3.192E-06	2.795E-06	6.386E-07
4.75	1.309E-05	2.295E-06	1.830E-06	1.468E-06	1.058E-06	2.694E-07
5.25	4.443E-06	7.854E-07	5.818E-07	4.442E-07	3.644E-07	9.142E-08
5.75	2.008E-06	6.471E-07	2.565E-07	1.829E-07	1.751E-07	4.131E-08
6.25	1.928E-06	4.782E-07	2.413E-07	1.757E-07	1.606E-07	3.967E-08
6.75	5.760E-07	1.461E-07	8.519E-08	6.033E-08	5.067E-08	3.240E-08
7.25	5.418E-07	1.215E-07	6.917E-08	4.936E-08	4.176E-08	2.456E-08
7.75	1.226E-07	7.078E-08	2.416E-08	1.580E-08	1.309E-08	1.277E-08
8.50	1.458E-07	5.155E-08	2.778E-08	1.879E-08	1.864E-08	8.435E-09

Table H.28: Combined result for π^0 production in Au + Au collisions (centrality 70-80%).

p_T (GeV/c)	$\frac{1}{2\pi p_T N_{\text{evt}}} \frac{d^2N}{dp_T dy} \left(\frac{c^3}{\text{GeV}^2} \right)$	Stat. error	Total syst. error	Syst. error A	Syst. error B	Syst. error C
1.25	3.432E-02	3.201E-03	3.589E-03	3.254E-03	1.340E-03	7.063E-04
1.75	5.895E-03	4.540E-04	6.387E-04	5.542E-04	2.935E-04	1.213E-04
2.25	1.334E-03	1.240E-04	1.505E-04	1.252E-04	7.895E-05	2.745E-05
2.75	3.207E-04	3.309E-05	3.674E-05	2.976E-05	2.051E-05	6.599E-06
3.25	1.072E-04	1.278E-05	1.344E-05	1.129E-05	6.961E-06	2.206E-06
3.75	4.194E-05	3.123E-06	5.100E-06	4.088E-06	2.924E-06	8.631E-07
4.25	1.304E-05	1.978E-06	1.684E-06	1.321E-06	1.010E-06	2.684E-07
4.75	6.573E-06	9.147E-07	7.943E-07	6.015E-07	5.008E-07	1.353E-07
5.25	3.358E-06	7.167E-07	4.105E-07	3.096E-07	2.606E-07	6.910E-08
5.75	1.131E-06	4.354E-07	2.270E-07	1.924E-07	1.159E-07	3.291E-08
6.25	1.166E-07	1.166E-07	1.949E-08	1.502E-08	1.194E-08	3.392E-09
6.75	2.899E-07	1.374E-07	5.524E-08	4.271E-08	2.970E-08	1.859E-08
7.25	1.487E-07	7.434E-08	2.724E-08	1.916E-08	1.523E-08	1.196E-08
7.75	7.042E-08	4.980E-08	1.229E-08	9.074E-09	7.215E-09	4.074E-09
8.50	4.580E-08	2.645E-08	8.831E-09	5.902E-09	4.517E-09	4.770E-09

Table H.29: Combined result for π^0 production in Au + Au collisions (centrality 80-92%).

p_T (GeV/c)	$\frac{1}{2\pi p_T N_{\text{evt}}} \frac{d^2N}{dp_T dy} \left(\frac{c^3}{\text{GeV}^2} \right)$	Stat. error	Total syst. error	Syst. error A	Syst. error B	Syst. error C
1.25	1.047E+00	2.175E-02	1.100E-01	1.009E-01	3.799E-02	2.153E-02
1.75	1.865E-01	2.937E-03	1.980E-02	1.701E-02	9.382E-03	3.837E-03
2.25	3.880E-02	6.728E-04	4.422E-03	3.582E-03	2.468E-03	7.985E-04
2.75	9.078E-03	1.929E-04	1.110E-03	8.572E-04	6.808E-04	1.868E-04
3.25	2.438E-03	6.121E-05	3.056E-04	2.309E-04	1.938E-04	5.018E-05
3.75	8.071E-04	9.749E-06	9.915E-05	7.357E-05	6.437E-05	1.661E-05
4.25	2.919E-04	4.492E-06	3.674E-05	2.664E-05	2.459E-05	6.007E-06
4.75	1.158E-04	2.318E-06	1.465E-05	1.056E-05	9.870E-06	2.383E-06
5.25	5.023E-05	1.328E-06	6.386E-06	4.602E-06	4.306E-06	1.033E-06
5.75	2.283E-05	8.160E-07	2.906E-06	2.087E-06	1.966E-06	4.698E-07
6.25	1.207E-05	4.865E-07	1.546E-06	1.133E-06	1.022E-06	2.485E-07
6.75	6.039E-06	3.122E-07	7.895E-07	5.513E-07	5.151E-07	2.323E-07
7.25	3.321E-06	2.214E-07	4.429E-07	3.120E-07	2.816E-07	1.395E-07
7.75	1.764E-06	1.494E-07	2.314E-07	1.625E-07	1.483E-07	7.165E-08
8.50	8.424E-07	4.739E-08	1.548E-07	1.086E-07	9.453E-08	5.673E-08
9.50	3.817E-07	2.946E-08	6.960E-08	4.931E-08	4.283E-08	2.404E-08
11.00	9.906E-08	1.012E-08	1.905E-08	1.277E-08	1.259E-08	6.426E-09
13.00	2.281E-08	4.033E-09	4.354E-09	2.939E-09	2.900E-09	1.382E-09
15.00	7.780E-09	2.460E-09	1.556E-09	1.002E-09	9.889E-10	6.623E-10

Table H.30: Combined result for π^0 production in minimum bias Au + Au collisions.

H.2 π^0 Production in d + Au Collisions

p_T (GeV/c)	$\frac{1}{2\pi p_T N_{\text{evt}}} \frac{d^2N}{dp_T dy} \left(\frac{c^3}{\text{GeV}^2} \right)$	Stat. error	Total syst. error	Syst. error A	Syst. error B	Syst. error C
1.25	5.621E-02	1.127E-03	4.306E-03	2.810E-03	2.858E-03	1.574E-03
1.75	1.067E-02	2.025E-04	8.754E-04	5.337E-04	6.262E-04	2.989E-04
2.25	2.390E-03	5.532E-05	2.118E-04	1.195E-04	1.615E-04	6.691E-05
2.75	6.739E-04	2.036E-05	6.368E-05	3.370E-05	5.063E-05	1.887E-05
3.25	2.199E-04	8.812E-06	2.186E-05	1.099E-05	1.787E-05	6.156E-06
3.75	8.356E-05	4.115E-06	8.663E-06	4.178E-06	7.220E-06	2.340E-06
4.25	2.946E-05	2.606E-06	3.165E-06	1.473E-06	2.677E-06	8.249E-07
4.75	1.180E-05	1.445E-06	1.308E-06	5.902E-07	1.120E-06	3.305E-07
5.25	5.028E-06	1.422E-07	8.576E-07	2.514E-07	7.676E-07	2.881E-07
5.75	2.344E-06	7.779E-08	3.865E-07	1.172E-07	3.429E-07	1.343E-07
6.25	1.152E-06	5.220E-08	1.854E-07	5.758E-08	1.634E-07	6.599E-08
6.75	6.042E-07	3.657E-08	9.571E-08	3.021E-08	8.396E-08	3.462E-08
7.25	3.251E-07	3.726E-08	5.098E-08	1.625E-08	4.458E-08	1.863E-08
7.75	1.898E-07	1.681E-08	2.960E-08	9.492E-09	2.584E-08	1.088E-08
8.25	8.409E-08	1.336E-08	1.308E-08	4.205E-09	1.141E-08	4.819E-09
8.75	6.473E-08	1.997E-08	1.007E-08	3.237E-09	8.782E-09	3.709E-09
9.25	2.309E-08	4.751E-09	3.596E-09	1.155E-09	3.138E-09	1.323E-09
9.75	1.507E-08	3.292E-09	2.352E-09	7.535E-10	2.054E-09	8.636E-10

Table H.31: π^0 production measured with the PbGl in minimum bias d + Au collisions.

p_T (GeV/c)	$\frac{1}{2\pi p_T N_{\text{evt}}} \frac{d^2N}{dp_T dy} \left(\frac{c^3}{\text{GeV}^2} \right)$	Stat. error	Total syst. error	Syst. error A	Syst. error B	Syst. error C
1.25	4.975E-02	7.904E-04	3.811E-03	2.487E-03	2.529E-03	1.393E-03
1.75	9.561E-03	1.538E-04	7.841E-04	4.780E-04	5.609E-04	2.677E-04
2.25	2.186E-03	4.102E-05	1.938E-04	1.093E-04	1.478E-04	6.122E-05
2.75	6.105E-04	1.422E-05	5.768E-05	3.052E-05	4.586E-05	1.709E-05
3.25	1.914E-04	6.022E-06	1.903E-05	9.570E-06	1.555E-05	5.359E-06
3.75	6.503E-05	2.893E-06	6.743E-06	3.252E-06	5.619E-06	1.821E-06
4.25	2.296E-05	1.520E-06	2.466E-06	1.148E-06	2.086E-06	6.428E-07
4.75	1.035E-05	8.525E-07	1.147E-06	5.174E-07	9.815E-07	2.898E-07
5.25	4.346E-06	9.165E-08	6.128E-07	2.173E-07	5.160E-07	2.491E-07
5.75	2.017E-06	5.183E-08	2.851E-07	1.009E-07	2.403E-07	1.156E-07
6.25	1.030E-06	3.259E-08	1.465E-07	5.150E-08	1.238E-07	5.902E-08
6.75	5.450E-07	2.305E-08	7.821E-08	2.725E-08	6.632E-08	3.123E-08
7.25	3.194E-07	1.534E-08	4.629E-08	1.597E-08	3.940E-08	1.830E-08
7.75	1.834E-07	1.188E-08	2.685E-08	9.171E-09	2.295E-08	1.051E-08
8.25	1.041E-07	9.729E-09	1.540E-08	5.207E-09	1.321E-08	5.968E-09
8.75	7.146E-08	1.024E-08	1.067E-08	3.573E-09	9.188E-09	4.095E-09
9.25	4.070E-08	1.705E-08	6.137E-09	2.035E-09	5.299E-09	2.332E-09
9.75	2.834E-08	5.184E-09	4.310E-09	1.417E-09	3.732E-09	1.624E-09

Table H.32: π^0 production measured with the PbSc in minimum bias d + Au collisions.

p_T (GeV/c)	$\frac{1}{2\pi p_T N_{\text{evt}}} \frac{d^2N}{dp_T dy} \left(\frac{c^3}{\text{GeV}^2} \right)$	Stat. error	Total syst. error	Syst. error A	Syst. error B	Syst. error C
1.25	5.255E-02	6.725E-04	2.852E-03	1.861E-03	1.893E-03	1.042E-03
1.75	1.005E-02	1.251E-04	5.838E-04	3.559E-04	4.176E-04	1.993E-04
2.25	2.278E-03	3.393E-05	1.429E-04	8.062E-05	1.090E-04	4.515E-05
2.75	6.385E-04	1.217E-05	4.271E-05	2.260E-05	3.396E-05	1.266E-05
3.25	2.033E-04	5.174E-06	1.433E-05	7.204E-06	1.171E-05	4.034E-06
3.75	7.187E-05	2.401E-06	5.310E-06	2.561E-06	4.425E-06	1.434E-06
4.25	2.512E-05	1.379E-06	1.922E-06	8.948E-07	1.626E-06	5.011E-07
4.75	1.086E-05	7.755E-07	8.525E-07	3.847E-07	7.296E-07	2.154E-07
5.25	4.576E-06	7.868E-08	4.984E-07	1.622E-07	4.331E-07	1.859E-07
5.75	2.132E-06	4.397E-08	2.293E-07	7.557E-08	1.984E-07	8.661E-08
6.25	1.076E-06	2.907E-08	1.148E-07	3.809E-08	9.906E-08	4.366E-08
6.75	5.680E-07	2.054E-08	6.040E-08	2.011E-08	5.209E-08	2.304E-08
7.25	3.215E-07	1.825E-08	3.401E-08	1.137E-08	2.928E-08	1.303E-08
7.75	1.862E-07	1.004E-08	1.984E-08	6.583E-09	1.713E-08	7.544E-09
8.25	9.438E-08	8.229E-09	1.013E-08	3.355E-09	8.746E-09	3.846E-09
8.75	6.941E-08	9.858E-09	7.420E-09	2.456E-09	6.411E-09	2.815E-09
9.25	2.481E-08	4.937E-09	2.770E-09	8.964E-10	2.411E-09	1.027E-09
9.75	1.858E-08	2.747E-09	2.120E-09	6.889E-10	1.843E-09	7.896E-10

Table H.33: Combined result for π^0 production measured in minimum bias d + Au collisions.

H.3 Reference Data: π^0 Production in p + p Collisions

p_T (GeV/c)	$E \frac{d^3\sigma}{dp^3} \left(\frac{\text{mb}c^3}{\text{GeV}^2} \right)$	Stat. error	Total syst. error
1.250	3.245E-01	5.316E-03	2.373E-02
1.750	5.471E-02	9.715E-04	3.872E-03
2.250	1.131E-02	2.789E-04	8.006E-04
2.750	3.114E-03	1.112E-04	2.236E-04
3.250	9.503E-04	5.383E-05	6.931E-05
3.750	3.252E-04	2.359E-05	2.488E-05
4.250	1.148E-04	2.810E-06	9.559E-06
4.750	4.592E-05	1.933E-06	3.887E-06
5.250	2.151E-05	1.069E-06	1.882E-06
5.750	1.089E-05	4.898E-07	1.006E-06
6.250	4.904E-06	3.112E-07	4.669E-07
6.750	2.953E-06	2.266E-07	2.901E-07
7.250	1.442E-06	1.552E-07	1.433E-07
7.750	7.123E-07	1.043E-07	7.232E-08
8.500	4.633E-07	5.567E-08	5.015E-08
9.500	1.581E-07	3.046E-08	1.745E-08
11.000	4.495E-08	1.001E-08	5.244E-09
13.500	8.090E-09	3.337E-09	1.265E-09

Table H.34: Differential cross section for π^0 production in p + p collisions. The overall scale uncertainty of 9.6% is not included in the error.

H.4 Inclusive Photon Production in Au + Au Collisions

p_T (GeV/c)	$\frac{1}{2\pi p_T N_{\text{evt}}} \frac{d^2N}{dp_T dy} \left(\frac{c^3}{\text{GeV}^2} \right)$	Stat. error	Total syst. error
1.25	2.233E+00	1.525E-03	3.065E-01
1.75	2.979E-01	4.689E-04	4.570E-02
2.25	5.123E-02	1.711E-04	8.522E-03
2.75	1.061E-02	6.954E-05	1.882E-03
3.25	2.811E-03	3.309E-05	5.301E-04
3.75	8.748E-04	1.760E-05	1.573E-04
4.25	3.596E-04	1.121E-05	6.191E-05
4.75	1.564E-04	6.979E-06	2.694E-05
5.25	7.522E-05	4.683E-06	1.297E-05
5.75	3.514E-05	1.931E-06	6.417E-06
6.25	1.613E-05	1.263E-06	2.932E-06
6.75	1.094E-05	9.827E-07	1.988E-06
7.25	7.016E-06	7.702E-07	1.284E-06
7.75	4.167E-06	5.779E-07	7.630E-07
8.50	1.786E-06	2.526E-07	3.285E-07
9.50	1.013E-06	1.820E-07	1.865E-07
11.00	3.908E-07	7.257E-08	7.208E-08

Table H.35: Inclusive photon production measured with the PbGl in Au + Au collisions (centrality 0-10%).

p_T (GeV/c)	$\frac{1}{2\pi p_T N_{\text{evt}}} \frac{d^2N}{dp_T dy} \left(\frac{c^3}{\text{GeV}^2} \right)$	Stat. error	Total syst. error
1.25	1.538E+00	1.275E-03	1.367E-01
1.75	2.086E-01	3.956E-04	2.340E-02
2.25	3.715E-02	1.469E-04	4.796E-03
2.75	7.814E-03	6.004E-05	1.118E-03
3.25	2.197E-03	3.004E-05	3.446E-04
3.75	6.562E-04	1.493E-05	9.591E-05
4.25	2.687E-04	9.373E-06	3.672E-05
4.75	1.242E-04	6.218E-06	1.699E-05
5.25	4.832E-05	3.673E-06	6.617E-06
5.75	2.610E-05	1.660E-06	3.575E-06
6.25	1.467E-05	1.186E-06	2.009E-06
6.75	8.197E-06	8.546E-07	1.123E-06
7.25	5.586E-06	6.875E-07	7.651E-07
7.75	3.047E-06	4.943E-07	4.174E-07
8.50	1.610E-06	2.428E-07	2.206E-07
9.50	5.234E-07	1.308E-07	7.169E-08

Table H.36: Inclusive photon production measured with the PbGl in Au + Au collisions (centrality 10-20%).

p_T (GeV/c)	$\frac{1}{2\pi p_T N_{\text{evt}}} \frac{d^2N}{dp_T dy} \left(\frac{c^3}{\text{GeV}^2} \right)$	Stat. error	Total syst. error
1.25	1.025E+00	1.051E-03	1.403E-01
1.75	1.459E-01	3.404E-04	2.235E-02
2.25	2.571E-02	1.242E-04	4.273E-03
2.75	5.825E-03	5.383E-05	1.033E-03
3.25	1.495E-03	2.438E-05	2.819E-04
3.75	4.573E-04	1.281E-05	8.219E-05
4.25	2.016E-04	8.212E-06	3.470E-05
4.75	7.185E-05	4.759E-06	1.237E-05
5.25	3.504E-05	3.159E-06	6.038E-06
5.75	1.813E-05	1.370E-06	3.354E-06
6.25	8.300E-06	8.899E-07	1.511E-06
6.75	6.228E-06	7.552E-07	1.146E-06
7.25	3.119E-06	5.060E-07	5.784E-07
7.75	1.829E-06	3.815E-07	3.294E-07
8.50	9.161E-07	1.797E-07	1.677E-07

Table H.37: Inclusive photon production measured with the PbGl in Au + Au collisions (centrality 20-30%).

p_T (GeV/c)	$\frac{1}{2\pi p_T N_{\text{evt}}} \frac{d^2N}{dp_T dy} \left(\frac{c^3}{\text{GeV}^2} \right)$	Stat. error	Total syst. error
1.25	6.389E-01	8.231E-04	8.747E-02
1.75	9.330E-02	2.727E-04	1.428E-02
2.25	1.747E-02	1.049E-04	2.897E-03
2.75	3.858E-03	4.372E-05	6.825E-04
3.25	1.092E-03	2.148E-05	2.055E-04
3.75	3.585E-04	1.158E-05	6.431E-05
4.25	1.300E-04	6.658E-06	2.232E-05
4.75	5.619E-05	4.188E-06	9.655E-06
5.25	2.598E-05	2.708E-06	4.467E-06
5.75	1.376E-05	1.216E-06	2.507E-06
6.25	7.724E-06	8.690E-07	1.437E-06
6.75	3.603E-06	5.770E-07	6.441E-07
7.25	2.235E-06	4.383E-07	4.082E-07
7.75	2.143E-06	4.125E-07	3.953E-07

Table H.38: Inclusive photon production measured with the PbGl in Au + Au collisions (centrality 30-40%).

p_T (GeV/c)	$\frac{1}{2\pi p_T N_{\text{evt}}} \frac{d^2 N}{d p_T dy} \left(\frac{c^3}{\text{GeV}^2} \right)$	Stat. error	Total syst. error
1.25	3.880E-01	6.462E-04	5.311E-02
1.75	5.366E-02	2.027E-04	8.220E-03
2.25	1.030E-02	7.926E-05	1.711E-03
2.75	2.448E-03	3.517E-05	4.334E-04
3.25	6.262E-04	1.613E-05	1.179E-04
3.75	2.275E-04	9.301E-06	4.083E-05
4.25	8.013E-05	5.141E-06	1.377E-05
4.75	3.897E-05	3.458E-06	6.702E-06
5.25	1.315E-05	1.898E-06	2.263E-06
5.75	8.613E-06	9.342E-07	1.554E-06
6.25	3.945E-06	6.087E-07	7.184E-07
6.75	2.177E-06	4.355E-07	3.890E-07

Table H.39: Inclusive photon production measured with the PbG1 in Au + Au collisions (centrality 40-50%).

p_T (GeV/c)	$\frac{1}{2\pi p_T N_{\text{evt}}} \frac{d^2 N}{d p_T dy} \left(\frac{c^3}{\text{GeV}^2} \right)$	Stat. error	Total syst. error
1.25	2.110E-01	4.806E-04	2.885E-02
1.75	3.046E-02	1.561E-04	4.659E-03
2.25	5.820E-03	6.066E-05	9.656E-04
2.75	1.343E-03	2.587E-05	2.377E-04
3.25	3.650E-04	1.234E-05	6.870E-05
3.75	1.279E-04	6.998E-06	2.295E-05
4.25	4.706E-05	4.021E-06	8.087E-06
4.75	1.815E-05	2.363E-06	3.120E-06
5.25	1.058E-05	1.717E-06	1.821E-06
5.75	4.624E-06	6.893E-07	8.649E-07
6.25	1.897E-06	4.242E-07	3.600E-07

Table H.40: Inclusive photon production measured with the PbG1 in Au + Au collisions (centrality 50-60%).

p_T (GeV/c)	$\frac{1}{2\pi p_T N_{\text{evt}}} \frac{d^2N}{dp_T dy} \left(\frac{c^3}{\text{GeV}^2} \right)$	Stat. error	Total syst. error
1.25	1.053E-01	3.432E-04	1.440E-02
1.75	1.514E-02	1.115E-04	2.313E-03
2.25	2.970E-03	4.363E-05	4.917E-04
2.75	6.809E-04	1.862E-05	1.203E-04
3.25	1.871E-04	9.096E-06	3.517E-05
3.75	6.971E-05	5.153E-06	1.249E-05
4.25	2.531E-05	2.922E-06	4.341E-06
4.75	1.192E-05	1.933E-06	2.045E-06
5.25	4.616E-06	1.154E-06	7.927E-07
5.75	2.670E-06	5.237E-07	4.839E-07

Table H.41: Inclusive photon production measured with the PbGl in Au + Au collisions (centrality 60-70%).

p_T (GeV/c)	$\frac{1}{2\pi p_T N_{\text{evt}}} \frac{d^2N}{dp_T dy} \left(\frac{c^3}{\text{GeV}^2} \right)$	Stat. error	Total syst. error
1.25	4.390E-02	2.209E-04	6.008E-03
1.75	6.372E-03	7.312E-05	9.744E-04
2.25	1.210E-03	2.777E-05	2.006E-04
2.75	2.953E-04	1.236E-05	5.224E-05
3.25	8.907E-05	6.176E-06	1.676E-05
3.75	3.158E-05	3.531E-06	5.663E-06
4.25	8.711E-06	1.708E-06	1.496E-06
4.75	6.016E-06	1.380E-06	1.033E-06

Table H.42: Inclusive photon production measured with the PbGl in Au + Au collisions (centrality 70-80%).

p_T (GeV/c)	$\frac{1}{2\pi p_T N_{\text{evt}}} \frac{d^2N}{dp_T dy} \left(\frac{c^3}{\text{GeV}^2} \right)$	Stat. error	Total syst. error
1.25	2.107E-02	1.405E-04	2.870E-03
1.75	2.916E-03	4.459E-05	4.454E-04
2.25	5.644E-04	1.746E-05	9.342E-05
2.75	1.514E-04	8.224E-06	2.675E-05
3.25	3.667E-05	3.667E-06	6.890E-06
3.75	1.118E-05	1.945E-06	2.002E-06
4.25	4.700E-06	1.175E-06	8.059E-07
4.75	1.051E-06	5.253E-07	1.803E-07

Table H.43: Inclusive photon production measured with the PbGl in Au + Au collisions (centrality 80-92%).

p_T (GeV/ c)	$\frac{1}{2\pi p_T N_{\text{evt}}} \frac{d^2 N}{d p_T dy} \left(\frac{c^3}{\text{GeV}^2} \right)$	Stat. error	Total syst. error
1.25	6.775E-01	2.798E-04	9.282E-02
1.75	9.269E-02	8.755E-05	1.420E-02
2.25	1.661E-02	3.271E-05	2.757E-03
2.75	3.587E-03	1.361E-05	6.351E-04
3.25	9.740E-04	6.563E-06	1.834E-04
3.75	3.077E-04	3.470E-06	5.522E-05
4.25	1.253E-04	2.171E-06	2.154E-05
4.75	5.358E-05	1.358E-06	9.212E-06
5.25	2.399E-05	8.707E-07	4.127E-06
5.75	1.220E-05	3.764E-07	2.232E-06
6.25	6.015E-06	2.537E-07	1.100E-06
6.75	3.734E-06	1.913E-07	6.768E-07
7.25	2.316E-06	1.465E-07	4.262E-07
7.75	1.364E-06	1.095E-07	2.503E-07
8.50	6.394E-07	5.024E-08	1.160E-07
9.50	2.683E-07	3.099E-08	4.890E-08
11.00	9.870E-08	1.206E-08	1.818E-08

Table H.44: Inclusive photon production measured with the PbGl in minimum bias Au + Au collisions.

p_T (GeV/c)	$\frac{1}{2\pi p_T N_{\text{evt}}} \frac{d^2 N}{dp_T dy} \left(\frac{c^3}{\text{GeV}^2} \right)$	Stat. error	Total syst. error
1.25	1.938E+00	6.812E-04	2.662E-01
1.75	2.589E-01	2.134E-04	3.766E-02
2.25	4.501E-02	8.136E-05	6.868E-03
2.75	9.304E-03	3.392E-05	1.469E-03
3.25	2.502E-03	1.680E-05	4.125E-04
3.75	7.875E-04	8.907E-06	1.252E-04
4.25	3.149E-04	5.580E-06	4.833E-05
4.75	1.311E-04	3.407E-06	2.013E-05
5.25	6.295E-05	2.305E-06	9.670E-06
5.75	2.938E-05	9.102E-07	4.833E-06
6.25	1.588E-05	6.571E-07	2.629E-06
6.75	8.659E-06	4.655E-07	1.427E-06
7.25	5.570E-06	3.581E-07	9.096E-07
7.75	3.485E-06	2.855E-07	5.806E-07
8.50	1.573E-06	1.243E-07	2.627E-07
9.50	8.178E-07	8.480E-08	1.363E-07
11.00	2.273E-07	2.887E-08	3.774E-08
13.00	8.807E-08	1.635E-08	1.418E-08

Table H.45: Inclusive photon production measured with the PbSc in Au + Au collisions (centrality 0-10%).

p_T (GeV/c)	$\frac{1}{2\pi p_T N_{\text{evt}}} \frac{d^2 N}{dp_T dy} \left(\frac{c^3}{\text{GeV}^2} \right)$	Stat. error	Total syst. error
1.25	1.383E+00	5.906E-04	9.755E-02
1.75	1.914E-01	1.901E-04	1.701E-02
2.25	3.309E-02	7.093E-05	3.380E-03
2.75	7.370E-03	3.129E-05	8.333E-04
3.25	1.955E-03	1.496E-05	2.420E-04
3.75	6.104E-04	7.953E-06	7.067E-05
4.25	2.188E-04	4.413E-06	2.367E-05
4.75	1.019E-04	3.055E-06	1.103E-05
5.25	4.596E-05	1.940E-06	4.980E-06
5.75	2.247E-05	7.995E-07	2.435E-06
6.25	1.152E-05	5.603E-07	1.249E-06
6.75	7.142E-06	4.223E-07	7.740E-07
7.25	3.519E-06	2.893E-07	3.814E-07
7.75	2.074E-06	2.151E-07	2.248E-07
8.50	1.143E-06	1.056E-07	1.239E-07
9.50	6.958E-07	7.981E-08	7.541E-08
11.00	1.758E-07	2.511E-08	1.905E-08
13.00	6.854E-08	1.461E-08	7.429E-09

Table H.46: Inclusive photon production measured with the PbSc (centrality 10-20%).

p_T (GeV/c)	$\frac{1}{2\pi p_T N_{\text{evt}}} \frac{d^2N}{dp_T dy} \left(\frac{c^3}{\text{GeV}^2} \right)$	Stat. error	Total syst. error
1.25	9.227E-01	4.877E-04	1.239E-01
1.75	1.275E-01	1.558E-04	1.824E-02
2.25	2.305E-02	6.009E-05	3.456E-03
2.75	5.221E-03	2.671E-05	8.172E-04
3.25	1.406E-03	1.277E-05	2.309E-04
3.75	4.238E-04	6.457E-06	6.708E-05
4.25	1.642E-04	3.831E-06	2.508E-05
4.75	6.739E-05	2.381E-06	1.030E-05
5.25	3.236E-05	1.602E-06	4.949E-06
5.75	1.532E-05	6.660E-07	2.512E-06
6.25	8.638E-06	4.769E-07	1.433E-06
6.75	4.425E-06	3.317E-07	7.300E-07
7.25	2.710E-06	2.494E-07	4.437E-07
7.75	1.450E-06	1.771E-07	2.380E-07
8.50	7.368E-07	8.452E-08	1.209E-07
9.50	4.060E-07	5.922E-08	6.603E-08
11.00	1.693E-07	2.470E-08	2.793E-08

Table H.47: Inclusive photon production measured with the PbSc in Au + Au collisions (centrality 20-30%).

p_T (GeV/c)	$\frac{1}{2\pi p_T N_{\text{evt}}} \frac{d^2N}{dp_T dy} \left(\frac{c^3}{\text{GeV}^2} \right)$	Stat. error	Total syst. error
1.25	5.900E-01	3.903E-04	7.891E-02
1.75	8.266E-02	1.258E-04	1.179E-02
2.25	1.569E-02	5.041E-05	2.348E-03
2.75	3.425E-03	2.129E-05	5.360E-04
3.25	9.649E-04	1.049E-05	1.588E-04
3.75	3.028E-04	5.450E-06	4.805E-05
4.25	1.108E-04	3.118E-06	1.697E-05
4.75	4.834E-05	2.041E-06	7.408E-06
5.25	2.295E-05	1.325E-06	3.520E-06
5.75	1.055E-05	5.357E-07	1.737E-06
6.25	5.699E-06	3.842E-07	9.375E-07
6.75	3.140E-06	2.693E-07	5.218E-07
7.25	2.011E-06	2.096E-07	3.286E-07
7.75	1.016E-06	1.437E-07	1.653E-07
8.50	5.824E-07	7.338E-08	9.532E-08
9.50	2.699E-07	4.698E-08	4.547E-08
11.00	6.495E-08	1.490E-08	1.065E-08

Table H.48: Inclusive photon production measured with the PbSc in Au + Au collisions (centrality 30-40%).

p_T (GeV/c)	$\frac{1}{2\pi p_T N_{\text{evt}}} \frac{d^2 N}{dp_T dy} \left(\frac{c^3}{\text{GeV}^2} \right)$	Stat. error	Total syst. error
1.25	3.450E-01	2.941E-04	4.608E-02
1.75	4.947E-02	9.705E-05	7.033E-03
2.25	9.344E-03	3.840E-05	1.399E-03
2.75	2.117E-03	1.660E-05	3.311E-04
3.25	6.238E-04	8.436E-06	1.023E-04
3.75	1.938E-04	4.378E-06	3.063E-05
4.25	6.905E-05	2.428E-06	1.053E-05
4.75	2.852E-05	1.540E-06	4.352E-06
5.25	1.382E-05	1.016E-06	2.110E-06
5.75	7.553E-06	4.580E-07	1.227E-06
6.25	3.361E-06	2.948E-07	5.515E-07
6.75	2.216E-06	2.274E-07	3.645E-07
7.25	1.279E-06	1.679E-07	2.084E-07
7.75	7.829E-07	1.270E-07	1.319E-07
8.50	3.823E-07	5.900E-08	6.335E-08
9.50	1.088E-07	3.018E-08	1.762E-08
11.00	5.100E-08	1.317E-08	8.367E-09

Table H.49: Inclusive photon production measured with the PbSc in Au + Au collisions (centrality 40-50%).

p_T (GeV/c)	$\frac{1}{2\pi p_T N_{\text{evt}}} \frac{d^2 N}{dp_T dy} \left(\frac{c^3}{\text{GeV}^2} \right)$	Stat. error	Total syst. error
1.25	1.886E-01	2.189E-04	2.514E-02
1.75	2.713E-02	7.233E-05	3.849E-03
2.25	5.166E-03	2.867E-05	7.719E-04
2.75	1.254E-03	1.308E-05	1.962E-04
3.25	3.456E-04	6.284E-06	5.683E-05
3.75	1.162E-04	3.380E-06	1.841E-05
4.25	4.237E-05	1.944E-06	6.482E-06
4.75	1.872E-05	1.232E-06	2.866E-06
5.25	7.433E-06	7.433E-07	1.138E-06
5.75	3.849E-06	3.164E-07	6.382E-07
6.25	2.317E-06	2.403E-07	3.911E-07
6.75	1.264E-06	1.704E-07	2.054E-07
7.25	8.358E-07	1.356E-07	1.385E-07
7.75	4.152E-07	9.061E-08	7.103E-08
8.50	1.370E-07	3.538E-08	2.254E-08
9.50	9.251E-08	2.789E-08	1.648E-08

Table H.50: Inclusive photon production measured with the PbSc in Au + Au collisions (centrality 50-60%).

p_T (GeV/c)	$\frac{1}{2\pi p_T N_{\text{evt}}} \frac{d^2N}{dp_T dy} \left(\frac{c^3}{\text{GeV}^2} \right)$	Stat. error	Total syst. error
1.25	9.350E-02	1.549E-04	1.246E-02
1.75	1.342E-02	5.124E-05	1.905E-03
2.25	2.475E-03	1.961E-05	3.693E-04
2.75	6.197E-04	9.120E-06	9.661E-05
3.25	1.771E-04	4.495E-06	2.911E-05
3.75	5.617E-05	2.343E-06	8.897E-06
4.25	2.158E-05	1.379E-06	3.300E-06
4.75	9.425E-06	8.640E-07	1.442E-06
5.25	3.595E-06	5.189E-07	5.502E-07
5.75	2.033E-06	2.348E-07	3.440E-07
6.25	1.036E-06	1.599E-07	1.741E-07
6.75	5.916E-07	1.160E-07	9.678E-08
7.25	3.381E-07	8.452E-08	5.514E-08
7.75	2.001E-07	6.329E-08	3.090E-08
8.50	1.170E-07	3.244E-08	1.930E-08

Table H.51: Inclusive photon production measured with the PbSc in Au + Au collisions (centrality 60-70%).

p_T (GeV/c)	$\frac{1}{2\pi p_T N_{\text{evt}}} \frac{d^2N}{dp_T dy} \left(\frac{c^3}{\text{GeV}^2} \right)$	Stat. error	Total syst. error
1.25	3.892E-02	1.004E-04	5.194E-03
1.75	5.667E-03	3.355E-05	8.028E-04
2.25	1.047E-03	1.275E-05	1.572E-04
2.75	2.520E-04	5.794E-06	3.940E-05
3.25	7.061E-05	2.800E-06	1.159E-05
3.75	2.819E-05	1.735E-06	4.461E-06
4.25	9.689E-06	9.367E-07	1.480E-06
4.75	3.446E-06	5.255E-07	5.267E-07
5.25	2.227E-06	4.135E-07	3.405E-07
5.75	8.163E-07	1.443E-07	1.330E-07
6.25	3.671E-07	9.479E-08	6.125E-08
6.75	2.942E-07	8.159E-08	4.938E-08

Table H.52: Inclusive photon production measured with the PbSc in Au + Au collisions (centrality 70-80%).

p_T (GeV/c)	$\frac{1}{2\pi p_T N_{\text{evt}}} \frac{d^2N}{dp_T dy} \left(\frac{c^3}{\text{GeV}^2} \right)$	Stat. error	Total syst. error
1.25	1.910E-02	6.524E-05	2.508E-03
1.75	2.695E-03	2.127E-05	3.786E-04
2.25	5.071E-04	8.354E-06	7.533E-05
2.75	1.323E-04	4.025E-06	2.050E-05
3.25	3.414E-05	1.838E-06	5.567E-06
3.75	1.248E-05	1.078E-06	1.959E-06
4.25	4.269E-06	5.757E-07	6.468E-07
4.75	1.602E-06	3.341E-07	2.428E-07
5.25	9.452E-07	2.526E-07	1.433E-07
5.75	4.742E-07	1.060E-07	7.735E-08

Table H.53: Inclusive photon production measured with the PbSc in Au + Au collisions (centrality 80-92%).

p_T (GeV/c)	$\frac{1}{2\pi p_T N_{\text{evt}}} \frac{d^2N}{dp_T dy} \left(\frac{c^3}{\text{GeV}^2} \right)$	Stat. error	Total syst. error
1.25	6.041E-01	1.283E-04	8.152E-02
1.75	8.313E-02	4.104E-05	1.192E-02
2.25	1.497E-02	1.590E-05	2.249E-03
2.75	3.271E-03	6.853E-06	5.122E-04
3.25	9.018E-04	3.388E-06	1.478E-04
3.75	2.836E-04	1.786E-06	4.480E-05
4.25	1.089E-04	1.066E-06	1.660E-05
4.75	4.642E-05	6.760E-07	7.079E-06
5.25	2.189E-05	4.478E-07	3.341E-06
5.75	1.034E-05	1.801E-07	1.693E-06
6.25	5.514E-06	1.284E-07	9.091E-07
6.75	3.138E-06	9.291E-08	5.156E-07
7.25	1.838E-06	6.862E-08	2.996E-07
7.75	1.079E-06	5.192E-08	1.773E-07
8.50	5.345E-07	2.402E-08	8.829E-08
9.50	2.768E-07	1.645E-08	4.565E-08
11.00	8.020E-08	5.671E-09	1.312E-08
13.00	3.112E-08	3.245E-09	5.206E-09
15.00	6.568E-09	1.400E-09	1.046E-09

Table H.54: Inclusive photon production measured with the PbSc in minimum bias Au + Au collisions.

p_T (GeV/c)	$\frac{1}{2\pi p_T N_{\text{evt}}} \frac{d^2N}{dp_T dy} \left(\frac{c^3}{\text{GeV}^2} \right)$	Stat. error	Total syst. error
1.25	2.065E+00	7.601E-04	2.005E-01
1.75	2.747E-01	2.303E-04	2.889E-02
2.25	4.746E-02	8.470E-05	5.307E-03
2.75	9.800E-03	3.431E-05	1.147E-03
3.25	2.618E-03	1.659E-05	3.225E-04
3.75	8.212E-04	8.898E-06	9.716E-05
4.25	3.316E-04	5.552E-06	3.769E-05
4.75	1.400E-04	3.336E-06	1.587E-05
5.25	6.715E-05	2.231E-06	7.610E-06
5.75	3.140E-05	9.104E-07	3.798E-06
6.25	1.598E-05	6.747E-07	1.950E-06
6.75	9.376E-06	4.455E-07	1.129E-06
7.25	6.002E-06	3.421E-07	7.192E-07
7.75	3.699E-06	2.698E-07	4.497E-07
8.50	1.643E-06	1.206E-07	2.007E-07
9.50	8.715E-07	7.956E-08	1.058E-07
11.00	2.564E-07	3.658E-08	4.451E-08
13.00	8.807E-08	1.635E-08	1.418E-08

Table H.55: Combined result for inclusive photon production in Au + Au collisions (centrality 0-10%).

p_T (GeV/c)	$\frac{1}{2\pi p_T N_{\text{evt}}} \frac{d^2N}{dp_T dy} \left(\frac{c^3}{\text{GeV}^2} \right)$	Stat. error	Total syst. error
1.25	1.435E+00	6.027E-04	7.837E-02
1.75	1.974E-01	1.918E-04	1.361E-02
2.25	3.444E-02	6.997E-05	2.722E-03
2.75	7.529E-03	3.042E-05	6.634E-04
3.25	2.035E-03	1.445E-05	1.951E-04
3.75	6.264E-04	7.561E-06	5.635E-05
4.25	2.332E-04	4.633E-06	2.144E-05
4.75	1.083E-04	2.942E-06	9.348E-06
5.25	4.674E-05	1.844E-06	3.921E-06
5.75	2.355E-05	7.618E-07	1.958E-06
6.25	1.233E-05	5.932E-07	1.178E-06
6.75	7.438E-06	3.924E-07	6.160E-07
7.25	3.887E-06	4.547E-07	5.707E-07
7.75	2.257E-06	2.529E-07	2.472E-07
8.50	1.235E-06	1.188E-07	1.278E-07
9.50	6.352E-07	7.843E-08	5.355E-08
11.00	1.838E-07	2.224E-08	1.495E-08
13.00	6.854E-08	1.461E-08	7.429E-09

Table H.56: Combined result for inclusive photon production in Au + Au collisions (centrality 10-20%).

p_T (GeV/ c)	$\frac{1}{2\pi p_T N_{\text{evt}}} \frac{d^2N}{dp_T dy} \left(\frac{c^3}{\text{GeV}^2} \right)$	Stat. error	Total syst. error
1.25	9.673E-01	5.376E-04	9.265E-02
1.75	1.349E-01	1.672E-04	1.404E-02
2.25	2.410E-02	6.225E-05	2.668E-03
2.75	5.453E-03	2.698E-05	6.356E-04
3.25	1.442E-03	1.273E-05	1.777E-04
3.75	4.371E-04	6.565E-06	5.165E-05
4.25	1.768E-04	3.789E-06	1.994E-05
4.75	6.912E-05	2.428E-06	7.852E-06
5.25	3.335E-05	1.589E-06	3.781E-06
5.75	1.627E-05	6.498E-07	1.973E-06
6.25	8.494E-06	4.896E-07	1.039E-06
6.75	4.884E-06	3.487E-07	6.658E-07
7.25	2.834E-06	2.364E-07	3.420E-07
7.75	1.547E-06	1.633E-07	1.843E-07
8.50	7.843E-07	7.815E-08	9.387E-08
9.50	3.756E-07	5.928E-08	4.518E-08
11.00	1.497E-07	2.526E-08	1.852E-08

Table H.57: Combined result for inclusive photon production in Au + Au collisions (centrality 20-30%).

p_T (GeV/ c)	$\frac{1}{2\pi p_T N_{\text{evt}}} \frac{d^2N}{dp_T dy} \left(\frac{c^3}{\text{GeV}^2} \right)$	Stat. error	Total syst. error
1.25	6.120E-01	4.297E-04	5.849E-02
1.75	8.697E-02	1.353E-04	9.035E-03
2.25	1.639E-02	5.253E-05	1.811E-03
2.75	3.590E-03	2.167E-05	4.177E-04
3.25	1.012E-03	1.057E-05	1.244E-04
3.75	3.225E-04	5.484E-06	3.793E-05
4.25	1.176E-04	3.156E-06	1.330E-05
4.75	5.107E-05	2.009E-06	5.776E-06
5.25	2.399E-05	1.303E-06	2.713E-06
5.75	1.151E-05	5.237E-07	1.384E-06
6.25	6.239E-06	3.733E-07	7.770E-07
6.75	3.286E-06	2.662E-07	3.956E-07
7.25	2.077E-06	2.029E-07	2.488E-07
7.75	1.161E-06	2.252E-07	2.503E-07
8.50	6.197E-07	6.830E-08	7.345E-08
9.50	2.825E-07	4.321E-08	3.417E-08
11.00	6.818E-08	1.330E-08	8.059E-09

Table H.58: Combined result for inclusive photon production in Au + Au collisions (centrality 30-40%).

p_T (GeV/ c)	$\frac{1}{2\pi p_T N_{\text{evt}}} \frac{d^2N}{dp_T dy} \left(\frac{c^3}{\text{GeV}^2} \right)$	Stat. error	Total syst. error
1.25	3.634E-01	3.257E-04	3.469E-02
1.75	5.124E-02	1.041E-04	5.324E-03
2.25	9.728E-03	4.001E-05	1.076E-03
2.75	2.238E-03	1.696E-05	2.600E-04
3.25	6.248E-04	8.702E-06	7.722E-05
3.75	2.057E-04	4.413E-06	2.413E-05
4.25	7.294E-05	2.445E-06	8.231E-06
4.75	3.137E-05	1.713E-06	4.146E-06
5.25	1.356E-05	1.022E-06	1.539E-06
5.75	7.917E-06	4.496E-07	9.452E-07
6.25	3.540E-06	2.813E-07	4.250E-07
6.75	2.203E-06	2.250E-07	2.641E-07
7.25	1.428E-06	1.937E-07	2.208E-07
7.75	7.640E-07	1.238E-07	9.311E-08
8.50	3.994E-07	5.414E-08	4.869E-08
9.50	1.050E-07	2.833E-08	1.282E-08
11.00	4.750E-08	1.286E-08	5.726E-09

Table H.59: Combined result for inclusive photon production in Au + Au collisions (centrality 40-50%).

p_T (GeV/ c)	$\frac{1}{2\pi p_T N_{\text{evt}}} \frac{d^2N}{dp_T dy} \left(\frac{c^3}{\text{GeV}^2} \right)$	Stat. error	Total syst. error
1.25	1.983E-01	2.430E-04	1.890E-02
1.75	2.848E-02	7.766E-05	2.949E-03
2.25	5.421E-03	2.996E-05	5.981E-04
2.75	1.290E-03	1.336E-05	1.506E-04
3.25	3.534E-04	6.404E-06	4.358E-05
3.75	1.206E-04	3.473E-06	1.422E-05
4.25	4.406E-05	1.964E-06	4.985E-06
4.75	1.850E-05	1.257E-06	2.102E-06
5.25	8.151E-06	7.467E-07	1.005E-06
5.75	4.076E-06	3.063E-07	4.966E-07
6.25	2.147E-06	2.478E-07	2.696E-07
6.75	1.415E-06	2.020E-07	2.239E-07
7.25	7.987E-07	1.315E-07	9.806E-08
7.75	3.468E-07	9.743E-08	4.472E-08
8.50	1.492E-07	3.048E-08	1.762E-08
9.50	9.888E-08	2.421E-08	1.273E-08

Table H.60: Combined result for inclusive photon production in Au + Au collisions (centrality 50-60%).

p_T (GeV/c)	$\frac{1}{2\pi p_T N_{\text{evt}}} \frac{d^2N}{dp_T dy} \left(\frac{c^3}{\text{GeV}^2} \right)$	Stat. error	Total syst. error
1.25	9.857E-02	1.723E-04	9.389E-03
1.75	1.411E-02	5.522E-05	1.462E-03
2.25	2.653E-03	2.036E-05	2.913E-04
2.75	6.435E-04	9.358E-06	7.476E-05
3.25	1.811E-04	4.663E-06	2.229E-05
3.75	6.046E-05	2.310E-06	7.065E-06
4.25	2.277E-05	1.350E-06	2.561E-06
4.75	1.008E-05	8.162E-07	1.127E-06
5.25	3.826E-06	4.705E-07	4.260E-07
5.75	2.195E-06	2.180E-07	2.675E-07
6.25	1.024E-06	1.556E-07	1.264E-07
6.75	5.953E-07	1.073E-07	7.290E-08
7.25	3.154E-07	8.382E-08	3.780E-08
7.75	2.079E-07	5.577E-08	2.358E-08
8.50	1.150E-07	3.048E-08	1.362E-08
9.50	5.158E-08	2.443E-08	6.118E-09

Table H.61: Combined result for inclusive photon production in Au + Au collisions (centrality 60-70%).

p_T (GeV/c)	$\frac{1}{2\pi p_T N_{\text{evt}}} \frac{d^2N}{dp_T dy} \left(\frac{c^3}{\text{GeV}^2} \right)$	Stat. error	Total syst. error
1.25	4.105E-02	1.110E-04	3.916E-03
1.75	5.951E-03	3.621E-05	6.157E-04
2.25	1.108E-03	1.337E-05	1.225E-04
2.75	2.674E-04	5.867E-06	3.099E-05
3.25	7.630E-05	2.736E-06	9.277E-06
3.75	2.934E-05	1.704E-06	3.438E-06
4.25	9.324E-06	9.373E-07	1.055E-06
4.75	3.850E-06	6.218E-07	5.809E-07
5.25	2.029E-06	4.068E-07	2.292E-07
5.75	8.579E-07	1.305E-07	1.026E-07
6.25	3.710E-07	8.689E-08	4.454E-08
6.75	2.561E-07	8.508E-08	3.111E-08
7.25	6.416E-08	3.704E-08	1.172E-08
7.75	6.017E-08	3.474E-08	9.202E-09

Table H.62: Combined result for inclusive photon production in Au + Au collisions (centrality 70-80%).

p_T (GeV/ c)	$\frac{1}{2\pi p_T N_{\text{evt}}} \frac{d^2N}{dp_T dy} \left(\frac{c^3}{\text{GeV}^2} \right)$	Stat. error	Total syst. error
1.25	1.995E-02	7.172E-05	1.883E-03
1.75	2.787E-03	2.281E-05	2.872E-04
2.25	5.294E-04	8.681E-06	5.816E-05
2.75	1.391E-04	3.996E-06	1.604E-05
3.25	3.505E-05	1.831E-06	4.274E-06
3.75	1.197E-05	1.083E-06	1.405E-06
4.25	4.385E-06	5.383E-07	4.873E-07
4.75	1.406E-06	3.400E-07	1.580E-07
5.25	9.999E-07	2.200E-07	1.102E-07
5.75	4.377E-07	1.045E-07	5.209E-08
6.25	2.183E-07	5.643E-08	2.676E-08
6.75	1.258E-07	5.136E-08	2.177E-08
7.25	3.799E-08	2.687E-08	6.068E-09
7.75	1.806E-08	1.806E-08	2.739E-09

Table H.63: Combined result for inclusive photon production in Au + Au collisions (centrality 80-92%).

p_T (GeV/ c)	$\frac{1}{2\pi p_T N_{\text{evt}}} \frac{d^2N}{dp_T dy} \left(\frac{c^3}{\text{GeV}^2} \right)$	Stat. error	Total syst. error
1.25	6.360E-01	1.421E-04	6.110E-02
1.75	8.708E-02	4.405E-05	9.085E-03
2.25	1.562E-02	1.649E-05	1.732E-03
2.75	3.396E-03	6.930E-06	3.960E-04
3.25	9.303E-04	3.382E-06	1.144E-04
3.75	2.931E-04	1.787E-06	3.458E-05
4.25	1.150E-04	1.066E-06	1.301E-05
4.75	4.906E-05	6.679E-07	5.548E-06
5.25	2.271E-05	4.452E-07	2.577E-06
5.75	1.101E-05	1.806E-07	1.331E-06
6.25	5.714E-06	1.300E-07	6.960E-07
6.75	3.351E-06	9.178E-08	4.041E-07
7.25	1.989E-06	6.631E-08	2.391E-07
7.75	1.168E-06	4.966E-08	1.409E-07
8.50	5.705E-07	2.369E-08	6.896E-08
9.50	2.733E-07	1.682E-08	3.329E-08
11.00	8.576E-08	5.418E-09	1.031E-08
13.00	3.112E-08	3.245E-09	5.206E-09
15.00	6.568E-09	1.400E-09	1.046E-09

Table H.64: Combined result for the inclusive photon production in minimum bias Au + Au collisions.

H.5 Direct Photon Yield in Au + Au Collisions

The direct photon yield presented in the following are derived from the combined results of single inclusive photons and neutral pions. The quoted errors are one σ uncertainties. In the case that the direct photon yield is consistent with zero within $1.28 \cdot \sigma$ (90% confidence level) the upper limit is given. For data points without a direct photon signal only the upper limit is quoted.

p_T (GeV/c)	$\frac{1}{2\pi p_T N_{\text{evt}}} \frac{d^2N}{dp_T dy} \left(\frac{c^3}{\text{GeV}^2} \right)$	Total error	Upper limit (90% CL)
1.25	1.388E-01	—	4.669E-01
1.75	1.297E-02	—	5.744E-02
2.25	2.496E-03	—	1.011E-02
2.75	8.133E-04	—	2.325E-03
3.25	4.038E-04	2.910E-04	—
3.75	1.300E-04	9.093E-05	—
4.25	8.454E-05	3.297E-05	—
4.75	4.370E-05	1.316E-05	—
5.25	2.630E-05	5.899E-06	—
5.75	1.264E-05	2.756E-06	—
6.25	6.783E-06	1.425E-06	—
6.75	4.575E-06	8.094E-07	—
7.25	3.395E-06	5.173E-07	—
7.75	2.223E-06	3.424E-07	—
8.50	9.790E-07	1.529E-07	—
9.50	6.132E-07	9.004E-08	—
11.00	1.826E-07	3.882E-08	—
13.00	7.018E-08	1.604E-08	—
15.00	2.460E-08	8.125E-09	—

Table H.65: Direct photon production measured with the PbGl and the PbSc in Au + Au collisions (centrality 0-10%).

p_T (GeV/c)	$\frac{1}{2\pi p_T N_{\text{evt}}} \frac{d^2N}{dp_T dy} \left(\frac{c^3}{\text{GeV}^2} \right)$	Total error	Upper limit (90% CL)
1.25	1.949E-01	1.317E-01	—
1.75	8.659E-03	—	3.453E-02
2.25	9.203E-04	—	5.526E-03
2.75	1.082E-03	6.885E-04	—
3.25	4.779E-04	1.695E-04	—
3.75	8.804E-05	5.785E-05	—
4.25	3.581E-05	2.147E-05	—
4.75	3.254E-05	8.645E-06	—
5.25	1.524E-05	3.767E-06	—
5.75	9.342E-06	1.744E-06	—
6.25	5.475E-06	9.721E-07	—
6.75	3.915E-06	5.576E-07	—
7.25	2.002E-06	4.762E-07	—
7.75	1.204E-06	2.470E-07	—
8.50	7.703E-07	1.267E-07	—
9.50	4.584E-07	7.409E-08	—
11.00	1.348E-07	2.111E-08	—
13.00	5.704E-08	1.391E-08	—
15.00	1.292E-08	5.629E-09	—

Table H.66: Direct photon production measured with the PbGl and the PbSc in Au + Au collisions (centrality 10-20%).

p_T (GeV/c)	$\frac{1}{2\pi p_T N_{\text{evt}}} \frac{d^2N}{dp_T dy} \left(\frac{c^3}{\text{GeV}^2} \right)$	Total error	Upper limit (90% CL)
1.25	5.891E-02	—	2.126E-01
1.75	5.459E-03	—	2.733E-02
2.25	2.536E-04	—	4.278E-03
2.75	3.209E-04	—	1.182E-03
3.25	8.301E-05	—	3.112E-04
3.75	1.207E-05	—	8.389E-05
4.25	2.414E-05	—	5.002E-05
4.75	8.295E-06	—	1.883E-05
5.25	6.929E-06	3.700E-06	—
5.75	3.874E-06	1.721E-06	—
6.25	2.293E-06	9.109E-07	—
6.75	1.588E-06	5.414E-07	—
7.25	1.014E-06	3.059E-07	—
7.75	5.004E-07	1.875E-07	—
8.50	3.029E-07	8.824E-08	—
9.50	1.833E-07	5.146E-08	—
11.00	9.286E-08	2.172E-08	—
13.00	4.584E-08	1.244E-08	—

Table H.67: Direct photon production measured with the PbGl and the PbSc in Au + Au collisions (centrality 20-30%).

p_T (GeV/c)	$\frac{1}{2\pi p_T N_{\text{evt}}} \frac{d^2N}{dp_T dy} \left(\frac{c^3}{\text{GeV}^2} \right)$	Total error	Upper limit (90% CL)
1.25	2.704E-02	—	1.260E-01
1.75	5.014E-03	—	1.883E-02
2.25	1.002E-03	—	3.586E-03
2.75	1.871E-04	—	7.580E-04
3.25	7.523E-05	—	2.328E-04
3.75	2.549E-05	—	7.568E-05
4.25	1.187E-05	—	2.994E-05
4.75	9.027E-06	5.757E-06	—
5.25	5.718E-06	2.621E-06	—
5.75	2.933E-06	1.212E-06	—
6.25	1.946E-06	6.530E-07	—
6.75	1.004E-06	3.683E-07	—
7.25	8.157E-07	2.308E-07	—
7.75	4.349E-07	2.191E-07	—
8.50	2.858E-07	6.952E-08	—
9.50	1.491E-07	3.769E-08	—
11.00	2.868E-08	1.109E-08	—
13.00	1.966E-08	7.602E-09	—

Table H.68: Direct photon production measured with the PbGl and the PbSc in Au + Au collisions (centrality 30-40%).

p_T (GeV/c)	$\frac{1}{2\pi p_T N_{\text{evt}}} \frac{d^2N}{dp_T dy} \left(\frac{c^3}{\text{GeV}^2} \right)$	Total error	Upper limit (90% CL)
1.25	—	—	6.222E-02
1.75	—	—	8.953E-03
2.25	—	—	1.688E-03
2.75	6.924E-05	—	4.340E-04
3.25	2.978E-05	—	1.300E-04
3.75	8.535E-06	—	4.202E-05
4.25	2.203E-06	—	1.445E-05
4.75	3.530E-06	—	8.863E-06
5.25	1.593E-06	—	3.907E-06
5.75	2.353E-06	8.213E-07	—
6.25	7.810E-07	4.289E-07	—
6.75	7.479E-07	2.597E-07	—
7.25	6.307E-07	1.938E-07	—
7.75	3.084E-07	1.104E-07	—
8.50	1.920E-07	5.000E-08	—
9.50	2.308E-08	—	5.556E-08
11.00	2.365E-08	9.839E-09	—

Table H.69: Direct photon production measured with the PbGl and the PbSc in Au + Au collisions (centrality 40-50%).

p_T (GeV/c)	$\frac{1}{2\pi p_T N_{\text{evt}}} \frac{d^2N}{dp_T dy} \left(\frac{c^3}{\text{GeV}^2} \right)$	Total error	Upper limit (90% CL)
1.25	—	—	3.417E-02
1.75	1.474E-04	—	4.933E-03
2.25	—	—	9.417E-04
2.75	—	—	2.180E-04
3.25	—	—	6.504E-05
3.75	—	—	2.188E-05
4.25	—	—	7.915E-06
4.75	1.026E-06	—	4.326E-06
5.25	6.025E-07	—	2.188E-06
5.75	5.500E-07	—	1.233E-06
6.25	3.904E-07	—	7.877E-07
6.75	4.851E-07	2.102E-07	—
7.25	2.868E-07	1.200E-07	—
7.75	5.335E-08	—	1.714E-07
8.50	1.487E-08	—	5.678E-08
9.50	4.554E-08	1.907E-08	—

Table H.70: Direct photon production measured with the PbGl and the PbSc in Au + Au collisions (centrality 50-60%).

p_T (GeV/c)	$\frac{1}{2\pi p_T N_{\text{evt}}} \frac{d^2N}{dp_T dy} \left(\frac{c^3}{\text{GeV}^2} \right)$	Total error	Upper limit (90% CL)
1.25	—	—	1.235E-02
1.75	—	—	1.720E-03
2.25	—	—	3.331E-04
2.75	8.059E-06	—	8.388E-05
3.25	2.202E-07	—	2.253E-05
3.75	3.590E-07	—	8.127E-06
4.25	—	—	2.975E-06
4.75	4.987E-07	—	1.812E-06
5.25	8.353E-08	—	7.145E-07
5.75	1.744E-07	—	4.519E-07
6.25	4.651E-09	—	1.714E-07
6.75	5.507E-08	—	1.563E-07
7.25	—	—	8.323E-08
7.75	7.221E-09	—	5.340E-08
8.50	2.075E-08	—	4.440E-08
9.50	4.698E-09	—	1.990E-08

Table H.71: Direct photon production measured with the PbGl and the PbSc in Au + Au collisions (centrality 60-80%).

p_T (GeV/c)	$\frac{1}{2\pi p_T N_{\text{evt}}} \frac{d^2N}{dp_T dy} \left(\frac{c^3}{\text{GeV}^2} \right)$	Total error	Upper limit (90% CL)
1.25	2.445E-02	—	1.283E-01
1.75	1.880E-03	—	1.631E-02
2.25	3.964E-04	—	2.964E-03
2.75	2.370E-04	—	7.661E-04
3.25	1.097E-04	—	2.469E-04
3.75	2.533E-05	—	7.013E-05
4.25	1.772E-05	1.273E-05	—
4.75	1.065E-05	5.063E-06	—
5.25	6.210E-06	2.210E-06	—
5.75	3.348E-06	1.041E-06	—
6.25	1.915E-06	5.282E-07	—
6.75	1.349E-06	2.925E-07	—
7.25	8.923E-07	1.693E-07	—
7.75	5.422E-07	1.009E-07	—
8.50	2.856E-07	4.811E-08	—
9.50	1.609E-07	2.419E-08	—
11.00	5.306E-08	7.567E-09	—
13.00	2.302E-08	4.075E-09	—
15.00	4.163E-09	1.190E-09	—

Table H.72: Direct photon production measured with the PbGl and the PbSc in minimum bias Au + Au collisions.

Bibliography

- [Aar87] P. A. Aarnio *et al.* *FLUKA User's Guide*. Technical Report TIS RP 190, CERN, 1987.
- [Ack03] K. H. Ackermann *et al.* *Nucl. Instrum. Meth.* **A499** (2003) 624.
- [Ada03] M. Adamczyk *et al.* *Nucl. Instrum. Meth.* **A499** (2003) 437.
- [Adc01a] K. Adcox *et al.* *Phys. Rev. Lett.* **86** (2001) 3500.
- [Adc01b] K. Adcox *et al.* *Phys. Rev. Lett.* **87** (2001) 052301.
- [Adc02] K. Adcox *et al.* *Phys. Rev. Lett.* **88** (2002) 022301.
- [Adc03a] K. Adcox *et al.* *Nucl. Instrum. Meth.* **A499** (2003) 489.
- [Adc03b] K. Adcox *et al.* *Nucl. Instrum. Meth.* **A499** (2003) 469.
- [Adc04] K. Adcox. *Formation of Dense Partonic Matter in Relativistic Nucleus Nucleus Collisions at RHIC: Experimental Evaluation by the PHENIX collaboration*. nucl-ex/0410003, 2004.
- [Adl03a] C. Adler *et al.* *Nucl. Instrum. Meth.* **A499** (2003) 433.
- [Adl03b] S. S. Adler *et al.* *Phys. Rev. Lett.* **91** (2003) 072303.
- [Adl03c] S. S. Adler *et al.* *Phys. Rev. Lett.* **91** (2003) 241803.
- [Adl03d] S. S. Adler *et al.* *Nucl. Instrum. Meth.* **A499** (2003) 560.
- [Adl03e] S. S. Adler *et al.* *Phys. Rev. Lett.* **91** (2003) 072301.
- [Adl04] S. S. Adler *et al.* *Phys. Rev.* **C69** (2004) 034909.
- [Agg00] M. M. Aggarwal *et al.* *Phys. Rev. Lett.* **85** (2000) 3595.
- [Agg01] M. M. Aggarwal *et al.* *Eur. Phys. J.* **C18** (2001) 651.

- [Air01] A. Airapetian *et al.* *Eur. Phys. J.* **C20** (2001) 479.
- [Aiz03] M. Aizawa *et al.* *Nucl. Instrum. Meth.* **A499** (2003) 508.
- [Aki03] H. Akikawa *et al.* *Nucl. Instrum. Meth.* **A499** (2003) 537.
- [All03] M. Allen *et al.* *Nucl. Instrum. Meth.* **A499** (2003) 549.
- [Aph03a] L. Aphecetche *et al.* *Nucl. Instrum. Meth.* **A499** (2003) 521.
- [Aph03b] L. Apheceteche, T. C. Awes, S. Bathe, *et al.* *Neutral Pion Spectra Measured with the EMCal in $\sqrt{s_{NN}} = 200$ GeV d+Au-Collisions*. PHENIX Internal Analysis Note 203, 2003.
- [Arl03] F. Arleo *et al.* *Photon Physics in Heavy Ion Collisions at the LHC*. hep-ph/0311131, 2003.
- [Arn01] P. Arnold, G. D. Moore, and L. G. Yaffe. *JHEP* **12** (2001) 009.
- [Aro03] S. H. Aronson *et al.* *Nucl. Instrum. Meth.* **A499** (2003) 480.
- [Aub83] J. J. Aubert *et al.* *Phys. Lett.* **B123** (1983) 275.
- [Aur98] P. Aurenche, F. Gelis, R. Kobes, *et al.* *Phys. Rev.* **D58** (1998) 085003.
- [Aur00] P. Aurenche, F. Gelis, and H. Zaraket. *Phys. Rev.* **D61** (2000) 116001.
- [Ave03] R. Averbeck. *EXODUS Event Generator*. PHENIX CVS Repository offline-analysis/exodus, 2003.
- [Awe01] T. C. Awes, S. Bathe, H. Büsching, *et al.* *Neutral Pion Spectra from the Lead-glass Calorimeter*. PHENIX Internal Analysis Note 69, 2001.
- [Awe02] T. C. Awes *et al.* *High Energy Beam Test of the PHENIX Lead-scintillator EM Calorimeter*. nucl-ex/0202009, 2002.
- [Bac03] B. B. Back *et al.* *Nucl. Instrum. Meth.* **A499** (2003) 603.
- [Bac04] B. B. Back *et al.* *Phys. Lett.* **B578** (2004) 297.
- [Bai95] R. Baier, Y. L. Dokshitzer, S. Peigne, *et al.* *Phys. Lett.* **B345** (1995) 277.
- [Bai97] R. Baier, Y. L. Dokshitzer, A. H. Mueller, *et al.* *Nucl. Phys.* **B483** (1997) 291.
- [Bar02] G. G. Barnafoldi, P. Levai, G. Papp, *et al.* *High p_T Pion Production in Heavy-Ion Collisions at RHIC Energies*. nucl-th/0212111, 2002.

- [Bas03] S. A. Bass, B. Muller, and D. K. Srivastava. *Phys. Rev. Lett.* **90** (2003) 082301.
- [Bat02] S. Bathe. *Impulsfluktuationen und Produktion neutraler Pionen in ultrarelativistischen Schwerionenstößen*. Ph.D. thesis, Institut für Kernphysik, Münster, 2002.
- [Baz99] A. V. Bazilevsky, V. I. Kochetkov, V. K. Semenov, *et al.* *Instrum. Exp. Tech.* **42** (1999) 167.
- [Baz01] S. Bazilevsky and M. Volkov. *PHENIX PbGl Cluster Identification*. PHENIX Internal Technical Note 386, 2001.
- [Baz03a] A. Bazilevsky and M. Volkov. *PbGl Reconstruction Routine EmcGlSector.cxx Rev. 2.14*. PHENIX CVS Repository offline/packages/emc, 2003.
- [Baz03b] A. Bazilevsky and M. Volkov. *PbSc reconstruction routine EmcScSector.cxx Rev. 2.10*. PHENIX CVS Repository offline/packages/emc, 2003.
- [Bel03] S. Belikov, G. Bunce, M. Chiu, *et al.* *Determination of the Absolute Luminosity for the Proton-Proton Data at $\sqrt{s} = 200$ GeV Recorded by PHENIX During RHIC Run-02*. PHENIX Internal Analysis Note 184, 2003.
- [Bjo83] J. D. Bjorken. *Phys. Rev.* **D27** (1983) 140.
- [Bla90] J.-P. Blaizot and J.-Y. Ollitrault. In R. C. Hwa (Editor) *Quark-Gluon Plasma*, World Scientific, Singapore. 1990.
- [Bla02] J.-P. Blaizot. *Lect. Notes Phys.* **583** (2002) 117.
- [Bou76] M. Bourquin and J. M. Gaillard. *Nucl. Phys.* **B114** (1976) 334.
- [Bra90] E. Braaten and R. D. Pisarski. *Nucl. Phys.* **B337** (1990) 569.
- [Bru93] R. Brun and F. Carminati. *GEANT, Detector Description and Simulation Tool*. CERN Program Library Long Writeup W5013, 1993.
- [Buc99] D. Bucher. *Produktion direkter Photonen in ultrarelativistischen Schwerionenstößen*. Ph.D. thesis, Institut für Kernphysik, Münster, 1999.
- [Büs97] H. Büsching. *Untersuchung nichtlinearer Effekte im BleiglasKalorimeter LEDA – Eine Computersimulation –*. Diplomarbeit, Institut für Kernphysik, Münster, 1997.

- [Büs02] H. Büsching. *Azimuthale Photonen-Korrelationen in ultrarelativistischen $p+A$ -, $Pb+Pb$ und $Au+Au$ Reaktionen*. Ph.D. thesis, Institut für Kernphysik, Münster, 2002.
- [Cas98] C. Caso *et al.* *Eur. Phys. J.* **C3** (1998) 1.
- [Cas04] W. Cassing, K. Gallmeister, and C. Greiner. *Nucl. Phys.* **A735** (2004) 277.
- [Che03] S. Chekanov *et al.* *Phys. Rev.* **D67** (2003) 012007.
- [Chi02] M. Chiu, G. David, J. Frantz, *et al.* *EMCal Calibration in Preparation for QM 2002*. PHENIX Internal Technical Note 400, 2002.
- [Cho74] A. Chodos, R. L. Jaffe, K. Johnson, *et al.* *Phys. Rev.* **D9** (1974) 3471.
- [Col78] W. A. Coleman and T. W. Armstrong. *The Nucleon - Meson Transport Code NMTC*, 1978.
- [Col85] J. C. Collins, D. E. Soper, and G. Sterman. *Nucl. Phys.* **B261** (1985) 104.
- [Cre77] M. Creutz. *Phys. Rev.* **D15** (1977) 1128.
- [Cro75] J. W. Cronin *et al.* *Phys. Rev.* **D11** (1975) 3105.
- [Dav98] G. David *et al.* *IEEE Trans. Nucl. Sci.* **45** (1998) 692.
- [d'E03] D. d'Enterria, G. David, S. Mioduszewski, *et al.* *Neutral Pion Measurement in the PbSc Calorimeter in Au + Au Collisions at $\sqrt{s_{NN}} = 200$ GeV*. PHENIX Internal Analysis Note 166, 2003.
- [d'E04] D. d'Enterria, J. Frantz, and S. Mioduszewski. *Final Au + Au $\rightarrow \eta + X$ Measurement at $\sqrt{s_{NN}} = 200$ GeV in the PbSc Calorimeter*. PHENIX Internal Analysis Note 3XX, 2004.
- [Dia80] M. Diakonou *et al.* *Phys. Lett.* **B89** (1980) 432.
- [Dum01] A. Dumitru, L. Frankfurt, L. Gerland, *et al.* *Phys. Rev.* **C64** (2001) 054909.
- [dV04] Z. del Valle and G. Martinez. *Glauber Calculation of N_{coll} and N_{part} in $d+Au$ Collisions at $\sqrt{s_{NN}} = 200$ GeV*. PHENIX Internal Analysis Note 295, 2004.
- [Eid04] S. Eidelman *et al.* *Physics Letters B* **592** (2004) 1+.
- [Esk99] K. J. Eskola, V. J. Kolhinen, and C. A. Salgado. *Eur. Phys. J.* **C9** (1999) 61.

- [Fes85] H. Fesefeldt. *The Simulation of Hadronic Showers: Physics and Applications*. Report PITHA-85-02, 1985.
- [Fod02] Z. Fodor and S. D. Katz. *JHEP* **03** (2002) 014.
- [Fra04a] J. Frantz. *J. Phys.* **G30** (2004) S1003.
- [Fra04b] J. Frantz, B. A. Cole, J. L. Nagle, *et al.* *Run2 Level2 High Pt Tile Trigger Photon Analysis Note*. PHENIX Internal Analysis Note 278, 2004.
- [Fri03] R. J. Fries, B. Muller, and D. K. Srivastava. *Phys. Rev. Lett.* **90** (2003) 132301.
- [Fro61] M. Froissart. *Phys. Rev.* **123** (1961) 1053.
- [Gab] T. A. Gabriel. *CALOR89: A Monte Carlo Program Package for the Design and Analysis of Calorimeter Systems*. ORNL/TM-11185 in preparation.
- [Gal91] C. Gale and J. I. Kapusta. *Nucl. Phys.* **B357** (1991) 65.
- [Gal03] K. Gallmeister, C. Greiner, and Z. Xu. *Phys. Rev.* **C67** (2003) 044905.
- [Glu93] M. Gluck, E. Reya, and A. Vogt. *Phys. Rev.* **D48** (1993) 116.
- [GM64] M. Gell-Mann. *Phys. Lett.* **8** (1964) 214.
- [Gyu90] M. Gyulassy and M. Plumer. *Phys. Lett.* **B243** (1990) 432.
- [Gyu94a] M. Gyulassy and X.-N. Wang. *Comput. Phys. Commun.* **83** (1994) 307.
- [Gyu94b] M. Gyulassy and X.-n. Wang. *Nucl. Phys.* **B420** (1994) 583.
- [Gyu00] M. Gyulassy, P. Levai, and I. Vitev. *Phys. Rev. Lett.* **85** (2000) 5535.
- [Gyu03] M. Gyulassy, I. Vitev, X.-N. Wang, *et al.* *Jet Quenching and Radiative Energy Loss in Dense Nuclear Matter*. nucl-th/0302077, 2003.
- [Gyu04] M. Gyulassy and L. McLerran. *New Forms of QCD Matter Discovered at RHIC*. nucl-th/0405013, 2004.
- [Hah03] H. Hahn *et al.* *Nucl. Instrum. Meth.* **A499** (2003) 245.
- [Hir04] T. Hirano. *J. Phys.* **G30** (2004) S845.
- [Hop04] M. Hoppe. *Aufbau und Inbetriebnahme einer Funkenkammer*. Diplomarbeit, Institut für Kernphysik, Münster, 2004.

- [Ian03] E. Iancu and R. Venugopalan. *The Color Glass Condensate and High Energy Scattering in QCD*. hep-ph/0303204, 2003.
- [Jac80] M. Jacob and P. Landshoff. *Sci. Am.* **242** (1980) 46.
- [JM04] J. Jalilian-Marian. *J. Phys.* **G30** (2004) S751.
- [Kap91] J. I. Kapusta, P. Lichard, and D. Seibert. *Phys. Rev.* **D44** (1991) 2774.
- [Kar88] F. Karsch. *Z. Phys.* **C38** (1988) 147.
- [Kar02] F. Karsch. *Lect. Notes Phys.* **583** (2002) 209.
- [Kau04] M. Kaufmann and D. d’Enterria. *Systematics of η/π^0 at High p_T in Hadronic Collisions*. PHENIX Internal Analysis Note 337, 2004.
- [KB00] C. Klein-Bösing. *Simulation der Detektoreigenschaften des Bleiglaskalorimeters in den Experimenten WA98 und PHENIX*. Diplomarbeit, Institut für Kernphysik, Münster, 2000.
- [KB03] C. Klein-Bösing, K. Reygers, T. C. Awes, *et al.* *Neutral Pion Spectra Measured with the PbGl in $\sqrt{s_{NN}} = 200$ GeV Au+Au Collisions*. PHENIX Internal Analysis Note 167, 2003.
- [KB04a] C. Klein-Bösing. *J. Phys.* **G30** (2004) S975.
- [KB04b] C. Klein-Bösing and S. Bathe. *PbGl Reconstruction Routine EmcGlSector.cxx Rev. 2.17*. PHENIX CVS Repository offline/packages/emc, 2004.
- [Kel00] S. Kelly, D. Morrison, J. Nagle, *et al.* *Calculation of the Number of Participating Nucleons for Centrality Classes Defined with the ZDC and BBC*. PHENIX Internal Analysis Note 33, 2000.
- [Kha03] D. Kharzeev, E. Levin, and L. McLerran. *Phys. Lett.* **B561** (2003) 93.
- [Kle92] K. Kleinknecht. *Detektoren für Teilchenstrahlung*. Teubner, 1992.
- [Kni01] B. A. Kniehl, G. Kramer, and B. Potter. *Nucl. Phys.* **B597** (2001) 337.
- [Koc97] V. Koch. *Int. J. Mod. Phys.* **E6** (1997) 203.
- [Kre04] S. Kretzer, H. L. Lai, F. I. Olness, *et al.* *Phys. Rev.* **D69** (2004) 114005.
- [Lev03] P. Levai, G. Papp, G. G. Barnafoldi, *et al.* *Pion Production in d+Au Collisions at RHIC Energy*. nucl-th/0306019, 2003.

- [Mag04] C. F. Maguire. *PISA Simulation Framework*. PHENIX CVS Repository siumlation/pisa2000/, 2004.
- [Mat04] F. Matathias. *Identified Particle Production in $p + p$ and $d + Au$ Collisions at $\sqrt{s_{NN}} = 200 \text{ GeV}$ with the PHENIX Experiment at RHIC*. Ph.D. thesis, State University of New York, Stony Brook, 2004. In preparation.
- [Mex99] V. Mexner. *Hochenergiestests eines elektromagnetischen Kalorimeters für das PHENIX Experiment*. Diplomarbeit, Institut für Kernphysik, Münster, 1999.
- [Mig56] A. B. Migdal. *Phys. Rev.* **103** 6 (1956) 1811.
- [Mit02] J. T. Mitchell *et al.* *Nucl. Instrum. Meth.* **A482** (2002) 491.
- [Mur04] M. Murray. *J. Phys.* **G30** (2004) S667.
- [Neu95] S. Neumaier *et al.* *Nucl. Instrum. Meth.* **A360** (1995) 593.
- [Nys01] J. Nystrand, R. du Rietz, and D. Silvermyr. *Coherent Peripheral Collisions in PHENIX*. PHENIX Internal Analysis Note 63, 2001.
- [Pei96] T. Peitzmann *et al.* *Nucl. Instrum. Meth.* **A376** (1996) 368.
- [Pei97] T. Peitzmann. *Kernmaterie unter extremen Bedingungen – Die experimentelle Suche nach dem Quark-Gluon-Plasma*. Habilitation, Institut für Kernphysik, Münster, 1997.
- [Pei02] T. Peitzmann and M. H. Thoma. *Phys. Rept.* **364** (2002) 175.
- [Per00] D. H. Perkins. *Introduction to High Energy Physics*. Cambridge University Press, Cambridge, 2000.
- [Pil00] G. Piller and W. Weise. *Phys. Rept.* **330** (2000) 1.
- [Pin03] C. Pinkenburg. *Ezdst Framework*. PHENIX CVS Repository offline/-framework/ezdst, 2003.
- [Pin04] C. Pinkenburg. *J. Phys.* **G30** (2004) S1201.
- [Pum02] J. Pumplin *et al.* *JHEP* **07** (2002) 012.
- [Rap04] R. Rapp. *Mod. Phys. Lett.* **A19** (2004) 1717.
- [Rey99] K. Reygers. *Teilchenproduktion in ultrarelativistischen $p + Pb$ - und $Pb + Pb$ -Reaktionen*. Ph.D. thesis, Institut für Kernphysik, Münster, 1999.

- [Rey02] K. Reygers, C. Klein-Bösing, T. C. Awes, *et al.* *Direct Photon Search in Au+Au Reactions at $\sqrt{s_{NN}} = 200$ GeV: Results of the QM02 Analysis.* PHENIX Internal Analysis Note 141, 2002.
- [Rey03a] K. Reygers. *Fast Monte-Carlo Simulation for π^0 and Photon Analysis.* PHENIX CVS Repository offline/analysis/PbGl/gampi0v2/acceptance/, 2003.
- [Rey03b] K. Reygers. *Glauber Monte-Carlo Calculation for Au+Au Collisions at $\sqrt{s_{NN}} = 200$ GeV.* PHENIX Internal Analysis Note 169, 2003.
- [Rey03c] K. Reygers, C. Klein-Bösing, T. C. Awes, *et al.* *Measurement of Neutral Pion Spectra in $\sqrt{s_{NN}} = 200$ GeV p+p-Collisions with the PbGl Calorimeter.* PHENIX Internal Analysis Note 175, 2003.
- [Roe96] B. P. Roe. *Particle Physics at the New Millennium.* Springer, New York, 1996.
- [Sah04] B. Sahlmüller. *Production of η Mesons in $\sqrt{s_{NN}} = 200$ GeV d+Au and p+p Collisions Measured by the PHENIX Experiment.* Diplomarbeit, Institut für Kernphysik, Münster, 2004.
- [Sch94a] G. Schepers. *Entwicklung und Erprobung eines LED-gestützten Monitorsystems für ein modulares Bleiglasspektrometer.* Diplomarbeit, Institut für Kernphysik, Münster, 1994.
- [Sch94b] H. Schlagheck. *Konstruktion und Kalibration eines Bleiglasskalorimeters für ultrarelativistische Schwerionenreaktionen.* Diplomarbeit, Institut für Kernphysik, Münster, 1994.
- [Sjo01] T. Sjostrand *et al.* *Comput. Phys. Commun.* **135** (2001) 238.
- [Son93] C. Song. *Phys. Rev.* **C47** (1993) 2861.
- [Son98] C.-S. Song and G. I. Fai. *Phys. Rev.* **C58** (1998) 1689.
- [Sri98] D. K. Srivastava and K. Geiger. *Phys. Rev.* **C58** (1998) 1734.
- [Ste94] K. Steffens. *Untersuchungen zur korrelierten Produktion von Photonen und neutralen Pionen in Schwerionenreaktionen bei 200 AGeV Projektilenergie.* Ph.D. thesis, Institut für Kernphysik, Münster, 1994.
- [Ste99] F. D. Steffen. *Bremsstrahlung out of the Quark-Gluon Plasma.* Diplomarbeit, Institut für Theoretische Physik, Giessen, 1999.
- [Ste01] F. D. Steffen and M. H. Thoma. *Phys. Lett.* **B510** (2001) 98.

- [Ste02] J. Stewering. *Messung der transversalen Energie mit dem Bleiglaskalorimeter des PHENIX-Experiments*. Diplomarbeit, Institut für Kernphysik, Münster, 2002.
- [Tan03] M. J. Tannenbaum. *The Centrality Bias in High p_T Particle Production and How to Correct it*. PHENIX Internal Analysis Note 209, 2003.
- [Tho00] M. H. Thoma. *New Developments and Applications of Thermal Field Theory*. hep-ph/0010164, 2000.
- [Tho01] A. W. Thomas and W. Weise. *The Structure of the Nucleon*. WILEY-VCH, Berlin, 2001.
- [Tur04] S. Turbide, R. Rapp, and C. Gale. *Phys. Rev.* **C69** (2004) 014903.
- [Vit02] I. Vitev and M. Gyulassy. *Phys. Rev. Lett.* **89** (2002) 252301.
- [Vit04] I. Vitev. *AIP Conf. Proc.* **698** (2004) 721.
- [Vog04a] W. Vogelsang. Private communications, August 2004.
- [Vog04b] W. Vogelsang. Private communications, May 2004.
- [Wan92] X.-N. Wang and M. Gyulassy. *Phys. Rev. Lett.* **68** (1992) 1480.
- [Wan01] E. Wang and X.-N. Wang. *Phys. Rev. Lett.* **87** (2001) 142301.
- [Wan02] E. Wang and X.-N. Wang. *Phys. Rev. Lett.* **89** (2002) 162301.
- [Wan04] X.-N. Wang. *Phys. Lett.* **B579** (2004) 299.
- [Wil74] K. G. Wilson. *Phys. Rev.* **D10** (1974) 2445.
- [Won94] C.-Y. Wong. *Introduction to High-Energy Heavy-Ion Collisions*. World Scientific, Singapore, 1994.
- [Xio92] L. Xiong, E. V. Shuryak, and G. E. Brown. *Phys. Rev.* **D46** (1992) 3798.
- [Zak04] B. G. Zakharov. *JETP Lett.* **80** (2004) 1.
- [Zei01] C. Zeitnitz and T. A. Gabriel. *The GEANT CALOR Interface User's Guide, GCALOR Version 1.05/3*, 2001.
- [Zwe64] G. Zweig. *An $SU(3)$ Model for Strong Interaction Symmetry and its Breaking*. 2, 1964. CERN-TH-412.

Danksagung

Schließlich und endlich möchte ich mich bei all denen bedanken, die zum Gelingen dieser Arbeit beigetragen haben.

Herrn Prof. Dr. Rainer Santo und Herrn Prof. Dr. Johannes P. Wessels danke ich für die Unterstützung meiner Arbeit, die sehr guten Arbeitsbedingungen am Institut für Kernphysik, sowie für die Ermöglichung der zahlreichen Aufenthalte am BNL und der Teilnahme an zahlreichen nationalen und internationalen Konferenzen und Workshops.

Bei Dr. Klaus Reygers möchte ich mich für die Betreuung meiner Arbeit bedanken. Seine unermüdliche Diskussionsbereitschaft, die zahlreichen Anregungen und die Hilfestellung bei physikalischen und technischen Fragestellungen haben diese Arbeit entscheidend vorangebracht. Außerdem danke ich für die sehr gute Arbeits- und Wohnatmosphäre während unserer Aufenthalte am BNL.

Bei Justin Frantz und Dr. David d'Enterria möchte ich mich für die sehr gute Zusammenarbeit bei der Analyse direkter Photonen und neutraler Pionen sowie bei der Entwicklung des Embedding-Frameworks bedanken.

Dr. Terry Awes danke ich für die lehrreichen Diskussionen während zahlreicher Aufenthalte am BNL, seinen unermüdlichen Einsatz für das Bleigaskalorimeter des EMCal und sein Interesse an dieser Arbeit.

Für die fruchtbare Kooperation zur Veröffentlichung der Ergebnisse der Analyse direkter Photonen und neutraler Pionen danke ich Dr. T. Awes, Dr. G. David, Dr. D. d'Enterria, J. Frantz, Dr. S. Mioduszewski, Dr. K. Reygers und Dr. T. Sakaguchi.

Für die angenehme Arbeitsatmosphäre und ihre Unterstützung gilt mein Dank der gesamten PHENIX Kollaboration sowie allen aktuellen und ehemaligen Mitgliedern der Arbeitsgruppe: H.-H. Adam, J. Auffenberg, Dr. S. Bathe, C. Baumann, Dr. D. Bucher, Dr. H. Büsching, Dr. R. Glasow, H. Gottschlag, M. Hoppe, S. Keßen, PD Dr. A. Khoukaz, T. Korfsmeier, Dr. N. Lang, Dr. J. Langheinrich, Dr. T. Lister, R. Menke, T. Mersmann, Dr. T. Peitzmann, Dr. C. Quentmeier, T. Rausmann, Dr. K. Reygers, B. Sahlmüller, S. Steltenkamp, J. Stewering, A. Täschner, A. Wilk, O. Winkelmann und O. Zaudtke.

Für die kritische Durchsicht meiner Arbeit und viele hilfreiche Anregungen danke ich Dr. Terry Awes, Dr. Henner Büsching, Melanie Hoppe, Dr. Saskia Mioduszewski, Dr. Klaus Reygers und Kathrin Schröer.

Ein dickes Dankeschön geht außerdem an all jene, die mich während der letzten Jahre auch außerhalb des Studiums begleitet haben und für die oftmals nötige Ablenkung von der Physik gesorgt haben: Alex, André, Anja, Christian, Daniel, Ingrid, Jens, Kathrin R., Kathrin S., Marcus, Mareike, Markus, Michaela, Olaf, den Ringgeistern, Ricki und Tobi.

Ein ganz besonderer Dank gilt meinen Eltern für ihre große Unterstützung in allen Lebenslagen und dafür, dass sie mir das Studium der Physik ermöglicht haben.

Zu guter Letzt möchte ich Melanie danken, für die Unterstützung, die Ermutigungen und die vielen anderen kleinen und großen Dinge: Danke Mela!

PHENIX Collaboration

S.S. ADLER⁴, S. AFANASIEV¹⁹, C. AIDALA⁹, N.N. AJITANAND⁴³, Y. AKIBA^{20,39},
A. AL-JAMEL³⁴, J. ALEXANDER⁴³, K. AOKI²⁴, L. APHECETCHE⁴⁵, R. ARMENDARIZ³⁴,
S.H. ARONSON⁴, R. AVERBECK⁴⁴, T.C. AWES³⁵, V. BABINTSEV¹⁶, A. BALDISSERI¹⁰,
K.N. BARISH⁵, P.D. BARNES²⁷, B. BASSALLECK³³, S. BATHE^{5,30}, S. BATSOULI⁹,
V. BAUBLIS³⁸, F. BAUER⁵, A. BAZILEVSKY^{4,40}, S. BELIKOV^{18,16}, M.T. BJORN DAL⁹,
J.G. BOISSEVAIN²⁷, H. BOREL¹⁰, M.L. BROOKS²⁷, D.S. BROWN³⁴, N. BRUNER³³,
D. BUCHER³⁰, H. BÜSCHING^{4,30}, V. BUMAZHNOV¹⁶, G. BUNCE^{4,40},
J.M. BURWARD-HOY^{27,26}, S. BUTSYK⁴⁴, X. CAMARD⁴⁵, P. CHAND³, W.C. CHANG²,
S. CHERNICHENKO¹⁶, C.Y. CHI⁹, J. CHIBA²⁰, M. CHIU⁹, I.J. CHOI⁵², R.K. CHOUDHURY³,
T. CHUJO⁴, V. CIANCIOLO³⁵, Y. COBIGO¹⁰, B.A. COLE⁹, M.P. COMETS³⁶,
P. CONSTANTIN¹⁸, M. CSANÁD¹², T. CSÖRGŐ²¹, J.P. CUSSONNEAU⁴⁵, D. D'ENTERRIA⁹,
K. DAS¹³, G. DAVID⁴, F. DEÁK¹², H. DELAGRANGE⁴⁵, A. DENISOV¹⁶, A. DESHPANDE⁴⁰,
E.J. DESMOND⁴, A. DEVISMES⁴⁴, O. DIETZSCH⁴¹, J.L. DRACHENBERG¹, O. DRAPIER²⁵,
A. DREES⁴⁴, A. DURUM¹⁶, D. DUTTA³, V. DZHORDZHADZE⁴⁶, Y.V. EFREMENKO³⁵,
H. EN'YO^{39,40}, B. ESPAGNON³⁶, S. ESUMI⁴⁸, D.E. FIELDS^{33,40}, C. FINCK⁴⁵, F. FLEURET²⁵,
S.L. FOKIN²³, B.D. FOX⁴⁰, Z. FRAENKEL⁵¹, J.E. FRANTZ⁹, A. FRANZ⁴, A.D. FRAWLEY¹³,
Y. FUKAO^{24,39,40}, S.-Y. FUNG⁵, S. GADRAT²⁸, M. GERMAIN⁴⁵, A. GLENN⁴⁶, M. GONIN²⁵,
J. GOSSET¹⁰, Y. GOTO^{39,40}, R. GRANIER DE CASSAGNAC²⁵, N. GRAU¹⁸, S.V. GREENE⁴⁹,
M. GROSSE PERDEKAMP^{17,40}, H.-Å. GUSTAFSSON²⁹, T. HACHIYA¹⁵, J.S. HAGGERTY⁴,
H. HAMAGAKI⁷, A.G. HANSEN²⁷, E.P. HARTOUNI²⁶, M. HARVEY⁴, K. HASUKO³⁹,
R. HAYANO⁷, X. HE¹⁴, M. HEFFNER²⁶, T.K. HEMMICK⁴⁴, J.M. HEUSER³⁹, P. HIDAS²¹,
H. HIEJIMA¹⁷, J.C. HILL¹⁸, R. HOBBS³³, W. HOLZMANN⁴³, K. HOMMA¹⁵, B. HONG²²,
A. HOOVER³⁴, T. HORAGUCHI^{39,40,47}, T. ICHIHARA^{39,40}, V.V. IKONNIKOV²³, K. IMAI^{24,39},
M. INUZUKA⁷, D. ISENHOWER¹, L. ISENHOWER¹, M. ISSAH⁴³, A. ISUPOV¹⁹, B.V. JACAK⁴⁴,
J. JIA⁴⁴, O. JINNOUCHI^{39,40}, B.M. JOHNSON⁴, S.C. JOHNSON²⁶, K.S. JOO³¹, D. JOUAN³⁶,
F. KAJIHARA⁷, S. KAMETANI^{7,50}, N. KAMIHARA^{39,47}, M. KANETA⁴⁰, J.H. KANG⁵²,
K. KATOU⁵⁰, T. KAWABATA⁷, A. KAZANTSEV²³, S. KELLY^{8,9}, B. KHACHATUROV⁵¹,
A. KHANZADEEV³⁸, J. KIKUCHI⁵⁰, D.J. KIM⁵², E. KIM⁴², G.-B. KIM²⁵, H.J. KIM⁵²,
E. KINNEY⁸, A. KISS¹², E. KISTENEV⁴, A. KIYOMICHI³⁹, C. KLEIN-BÖSING³⁰,
H. KOBAYASHI⁴⁰, V. KOCHETKOV¹⁶, R. KOHARA¹⁵, B. KOMKOV³⁸, M. KONNO⁴⁸,
D. KOTCHETKOV⁵, A. KOZLOV⁵¹, P.J. KROON⁴, C.H. KUBERG¹, G.J. KUNDE²⁷,
K. KURITA³⁹, M.J. KWEON²², Y. KWON⁵², G.S. KYLE³⁴, R. LACEY⁴³, J.G. LAJOIE¹⁸,
Y. LE BORNEC³⁶, A. LEBEDEV^{18,23}, S. LECKEY⁴⁴, D.M. LEE²⁷, M.J. LEITCH²⁷,
M.A.L. LEITE⁴¹, X. LI⁶, X.H. LI⁵, H. LIM⁴², A. LITVINENKO¹⁹, M.X. LIU²⁷,
C.F. MAGUIRE⁴⁹, Y.I. MAKDISI⁴, A. MALAKHOV¹⁹, V.I. MANKO²³, Y. MAO^{37,39},
G. MARTINEZ⁴⁵, H. MASUI⁴⁸, F. MATATHIAS⁴⁴, T. MATSUMOTO^{7,50}, M.C. MCCAIN¹,
P.L. MCGAUGHEY²⁷, Y. MIAKE⁴⁸, T.E. MILLER⁴⁹, A. MILOV⁴⁴, S. MIODUSZEWSKI⁴,
G.C. MISHRA¹⁴, J.T. MITCHELL⁴, A.K. MOHANTY³, D.P. MORRISON⁴, J.M. MOSS²⁷,
D. MUKHOPADHYAY⁵¹, M. MUNIRUZZAMAN⁵, S. NAGAMIYA²⁰, J.L. NAGLE^{8,9},
T. NAKAMURA¹⁵, J. NEWBY⁴⁶, A.S. NYANIN²³, J. NYSTRAND²⁹, E. O'BRIEN⁴,
C.A. OGILVIE¹⁸, H. OHNISHI³⁹, I.D. OJHA⁴⁹, H. OKADA^{24,39}, K. OKADA^{39,40},
A. OSKARSSON²⁹, I. OTTERLUND²⁹, K. OYAMA⁷, K. OZAWA⁷, D. PAL⁵¹,

A.P.T. PALOUNEK²⁷, V. PANTUEV⁴⁴, V. PAPAVALASSILOU³⁴, J. PARK⁴², W.J. PARK²²,
S.F. PATE³⁴, H. PEI¹⁸, V. PENEV¹⁹, J.-C. PENG¹⁷, H. PEREIRA¹⁰, V. PERESODOV¹⁹,
A. PIERSON³³, C. PINKENBURG⁴, R.P. PISANI⁴, M.L. PURSCHKE⁴, A.K. PURWAR⁴⁴,
J. QUALLS¹, J. RAK¹⁸, I. RAVINOVICH⁵¹, K.F. READ^{35,46}, M. REUTER⁴⁴, K. REYGERS³⁰,
V. RIABOV³⁸, Y. RIABOV³⁸, G. ROCHE²⁸, A. ROMANA²⁵, M. ROSATI¹⁸, S. ROSENDAHL²⁹,
P. ROSNET²⁸, V.L. RYKOV³⁹, S.S. RYU⁵², N. SAITO^{24,39,40}, T. SAKAGUCHI^{7,50}, S. SAKAI⁴⁸,
V. SAMSONOV³⁸, L. SANFRATELLO³³, R. SANTO³⁰, H.D. SATO^{24,39}, S. SATO^{4,48},
S. SAWADA²⁰, Y. SCHUTZ⁴⁵, V. SEMENOV¹⁶, R. SETO⁵, T.K. SHEA⁴, I. SHEIN¹⁶,
T.-A. SHIBATA^{39,47}, K. SHIGAKI¹⁵, M. SHIMOMURA⁴⁸, A. SICKLES⁴⁴, C.L. SILVA⁴¹,
D. SILVERMYR²⁷, K.S. SIM²², A. SOLDATOV¹⁶, R.A. SOLTZ²⁶, W.E. SONNENHEIM²⁷,
S. SORENSEN⁴⁶, I.V. SOURIKOVA⁴, F. STALEY¹⁰, P.W. STANKUS³⁵, E. STENLUND²⁹,
M. STEPANOV³⁴, A. STER²¹, S.P. STOLL⁴, T. SUGITATE¹⁵, J.P. SULLIVAN²⁷, S. TAKAGI⁴⁸,
E.M. TAKAGUI⁴¹, A. TAKETANI^{39,40}, Y. TANAKA³², K. TANIDA³⁹, M.J. TANNENBAUM⁴,
A. TARANENKO⁴³, P. TARJÁN¹¹, T.L. THOMAS³³, M. TOGAWA^{24,39}, J. TOJO³⁹, H. TORII^{24,40},
R.S. TOWELL¹, V.-N. TRAM²⁵, I. TSERRUYA⁵¹, Y. TSUCHIMOTO¹⁵, H. TYDESJÖ²⁹,
N. TYURIN¹⁶, T.J. UAM³¹, H.W. VAN HECKE²⁷, J. VELKOVSKA⁴, M. VELKOVSKY⁴⁴,
V. VESZPRÉMI¹¹, A.A. VINOGRADOV²³, M.A. VOLKOV²³, E. VZNUZDAEV³⁸, X.R. WANG¹⁴,
Y. WATANABE^{39,40}, S.N. WHITE⁴, N. WILLIS³⁶, F.K. WOHN¹⁸, C.L. WOODY⁴, W. XIE⁵,
A. YANOVICH¹⁶, S. YOKKAICHI^{39,40}, G.R. YOUNG³⁵, I.E. YUSHMANOV²³, W.A. ZAJC⁹,
C. ZHANG⁹, S. ZHOU⁶, J. ZIMÁNYI²¹, L. ZOLIN¹⁹, X. ZONG¹⁸

¹ Abilene Christian University, Abilene, TX 79699, USA

² Institute of Physics, Academia Sinica, Taipei 11529, Taiwan

³ Bhabha Atomic Research Centre, Bombay 400 085, India

⁴ Brookhaven National Laboratory, Upton, NY 11973-5000, USA

⁵ University of California - Riverside, Riverside, CA 92521, USA

⁶ China Institute of Atomic Energy (CIAE), Beijing, People's Republic of China

⁷ Center for Nuclear Study, Graduate School of Science, University of Tokyo, 7-3-1 Hongo,
Bunkyo, Tokyo 113-0033, Japan

⁸ University of Colorado, Boulder, CO 80309

⁹ Columbia University, New York, NY 10027 and Nevis Laboratories, Irvington, NY 10533, USA

¹⁰ Dapnia, CEA Saclay, F-91191, Gif-sur-Yvette, France

¹¹ Debrecen University, H-4010 Debrecen, Egyetem tér 1, Hungary

¹² ELTE, Eötvös Loránd University, H - 1117 Budapest, Pázmány P. s. 1/A, Hungary

¹³ Florida State University, Tallahassee, FL 32306, USA

¹⁴ Georgia State University, Atlanta, GA 30303, USA

¹⁵ Hiroshima University, Kagamiyama, Higashi-Hiroshima 739-8526, Japan

¹⁶ Institute for High Energy Physics (IHEP), Protvino, Russia

¹⁷ University of Illinois at Urbana-Champaign, Urbana, IL 61801

¹⁸ Iowa State University, Ames, IA 50011, USA

¹⁹ Joint Institute for Nuclear Research, 141980 Dubna, Moscow Region, Russia

²⁰ KEK, High Energy Accelerator Research Organization, Tsukuba-shi, Ibaraki-ken 305-0801,
Japan

²¹ KFKI Research Institute for Particle and Nuclear Physics (RMKI), H-1525 Budapest 114,
POBox 49, Hungary

- ²² Korea University, Seoul, 136-701, Korea
- ²³ Russian Research Center “Kurchatov Institute”, Moscow, Russia
- ²⁴ Kyoto University, Kyoto 606, Japan
- ²⁵ Laboratoire Leprince-Ringuet, Ecole Polytechnique, CNRS-IN2P3, Route de Saclay, F-91128, Palaiseau, France
- ²⁶ Lawrence Livermore National Laboratory, Livermore, CA 94550, USA
- ²⁷ Los Alamos National Laboratory, Los Alamos, NM 87545, USA
- ²⁸ LPC, Université Blaise Pascal, CNRS-IN2P3, Clermont-Fd, 63177 Aubiere Cedex, France
- ²⁹ Department of Physics, Lund University, Box 118, SE-221 00 Lund, Sweden
- ³⁰ Institut für Kernphysik, University of Münster, D-48149 Münster, Germany
- ³¹ Myongji University, Yongin, Kyonggido 449-728, Korea
- ³² Nagasaki Institute of Applied Science, Nagasaki-shi, Nagasaki 851-0193, Japan
- ³³ University of New Mexico, Albuquerque, NM, USA
- ³⁴ New Mexico State University, Las Cruces, NM 88003, USA
- ³⁵ Oak Ridge National Laboratory, Oak Ridge, TN 37831, USA
- ³⁶ IPN-Orsay, Université Paris Sud, CNRS-IN2P3, BP1, F-91406, Orsay, France
- ³⁷ Peking University, Beijing, People’s Republic of China
- ³⁸ PNPI, Petersburg Nuclear Physics Institute, Gatchina, Russia
- ³⁹ RIKEN (The Institute of Physical and Chemical Research), Wako, Saitama 351-0198, Japan
- ⁴⁰ RIKEN BNL Research Center, Brookhaven National Laboratory, Upton, NY 11973-5000, USA
- ⁴¹ Universidade de São Paulo, Instituto de Física, Caixa Postal 66318, São Paulo CEP05315-970, Brazil
- ⁴² System Electronics Laboratory, Seoul National University, Seoul, South Korea
- ⁴³ Chemistry Department, Stony Brook University, Stony Brook, SUNY, NY 11794-3400, USA
- ⁴⁴ Department of Physics and Astronomy, Stony Brook University, SUNY, Stony Brook, NY 11794, USA
- ⁴⁵ SUBATECH (Ecole des Mines de Nantes, CNRS-IN2P3, Université de Nantes) BP 20722 - 44307, Nantes, France
- ⁴⁶ University of Tennessee, Knoxville, TN 37996, USA
- ⁴⁷ Department of Physics, Tokyo Institute of Technology, Tokyo, 152-8551, Japan
- ⁴⁸ Institute of Physics, University of Tsukuba, Tsukuba, Ibaraki 305, Japan
- ⁴⁹ Vanderbilt University, Nashville, TN 37235, USA
- ⁵⁰ Waseda University, Advanced Research Institute for Science and Engineering, 17 Kikui-cho, Shinjuku-ku, Tokyo 162-0044, Japan
- ⁵¹ Weizmann Institute, Rehovot 76100, Israel
- ⁵² Yonsei University, IPAP, Seoul 120-749, Korea

Lebenslauf und Bildungsgang

Name: Christian Klein-Bösing

geb.: 01.06.1976 in Rheine

Eltern: Ludger Klein-Bösing
Theresia Klein-Bösing, geb. Wilting

Familienstand: ledig

Schulbildung: Grundschule: 1982–1986
St. Josef Grundschule Borken
Realschule: 1986 – 1992
Nünning-Realschule Borken
Gymnasium: 1992 – 1995
Gymnasium Remigianum Borken

Hochschulreife: am 14.06.1995 in Borken

Studium: Okt. 1995 – Dez. 2000
Diplomstudiengang Physik an der
Westfälischen Wilhelms-Universität Münster

Prüfungen: Vordiplom: 07.06.1997
Diplom: 18.12.2000

Tätigkeiten: Okt. 1999–Dez. 2000 stud. Hilfskraft,
Jan. 2001–März 2001 wiss. Hilfskraft,
seit April 2001 wiss. Mitarbeiter

Beginn der Dissertation: 01.01.2001
am Institut für Kernphysik bei
Prof. Dr. R. Santo

